Cosmology in the Nonlinear Domain: Warm Dark Matter

Katarina Markovič

München 2012

Cosmology in the Nonlinear Domain: Warm Dark Matter

Katarina Markovič

Dissertation
an der Fakultät für Physik
der Ludwig–Maximilians–Universität
München

vorgelegt von
Katarina Markovič
aus Ljubljana, Slowenien

München, den 17.12.2012

Erstgutachter: Prof. Dr. Jochen Weller
Zweitgutachter: Prof. Dr. Andreas Burkert
Tag der mündlichen Prüfung: 01.02.2013

Abstract

The introduction of a so-called dark sector in cosmology resolved many inconsistencies between cosmological theory and observation, but it also triggered many new questions. Dark Matter (DM) explained gravitational effects beyond what is accounted for by observed luminous matter and Dark Energy (DE) accounted for the observed accelerated expansion of the universe. The most sought after discoveries in the field would give insight into the nature of these dark components. Dark Matter is considered to be the better established of the two, but the understanding of its nature may still lay far in the future.

This thesis is concerned with explaining and eliminating the discrepancies between the current theoretical model, the standard model of cosmology, containing the cosmological constant (Λ) as the driver of accelerated expansion and Cold Dark Matter (CDM) as main source of gravitational effects, and available observational evidence pertaining to the dark sector. In particular, we focus on the small, galaxy-sized scales and below, where N-body simulations of cosmological structure in the ΛCDM universe predict much more structure and therefore much more power in the matter power spectrum than what is found by a range of different observations. This discrepancy in small scale power manifests itself for example through the well known "dwarf-galaxy problem" (e.g. Klypin et al., 1999), the density profiles and concentrations of individual haloes (Donato et al., 2009) as well as the properties of voids (Tikhonov et al., 2009). A physical process that would suppress the fluctuations in the dark matter density field might be able to account for these discrepancies.

Free-streaming dark matter particles dampen the overdensities on small scales of the initial linear matter density field. This corresponds to a suppression of power in the linear matter power spectrum and can be modeled relatively straightforwardly for an early decoupled thermal relic dark matter particle. Such a particle would be neutrino-like, but heavier; an example being the gravitino in the scenario, where it is the Lightest Supersymmetric Particle and it decouples much before neutrinos, but while still relativistic. Such a particle is not classified as Hot Dark Matter, like neutrinos, because it only affects small scales as opposed to causing a suppression at all scales. However, its free-streaming prevents the smallest structures from gravitationally collapsing and does therefore not correspond to Cold Dark Matter. The effect of this Warm Dark Matter (WDM) may be observable in the statistical properties of cosmological Large Scale Structure.

The suppression of the linear matter density field at high redshifts in the WDM scenario can be calculated by solving the Boltzmann equations. A fit to the resulting linear matter power spectrum, which describes the statistical properties of this density field in the simple thermal relic scenario is provided by Viel et al. (2004). This linear matter power spectrum must then be corrected for late-time non-linear collapse. This is rather difficult already in the standard cosmological scenario, because exact solutions the the evolution of the perturbed density field in the nonlinear regime cannot be found. The widely used approaches are to the

HALOFIT method of Smith et al. (2003), which is essentially a physically motivated fit to the results of numerical simulations or using the even more physical, but slightly less accurate *halo model*. However, both of these non-linear methods were developed assuming only CDM and are therefore not necessarily appropriate for the WDM case.

In this thesis, we modify the halo model (see also Smith & Markovič, 2011) in order to better accommodate the effects of the smoothed WDM density field. Firstly, we treat the dark matter density field as made up of two components: a smooth, linear component and a non-linear component, both with power at all scales. Secondly, we introduce a cut-off mass scale, below which no haloes are found. Thirdly, we suppress the mass function also above the cut-off scale and finally, we suppress the centres of halo density profiles by convolving them with a Gaussian function, whose width depends on the WDM relic thermal velocity. The latter effect is shown to not be significant in the WDM scenario for the calculation of the non-linear matter power spectrum at the scales relevant to the present and near future capabilities of astronomical surveys in particular the EUCLID weak lensing survey.

In order to determine the validity of the different non-linear WDM models, we run cosmological simulations with WDM (see also Viel et al., 2012) using the cutting edge Lagrangian code GADGET-2 (Springel, 2005). We provide a fitting function that can be easily applied to approximate the non-linear WDM power spectrum at redshifts $z = 0.5 - 3.0$ at a range of scales relevant to the weak lensing power spectrum. We examine the simple thermal relic scenario for different WDM masses and check our results against resolution issues by varying the size and number of simulation particles.

We finally briefly discuss the possibility that the effects of WDM on the matter power spectrum might resemble the analogous, but weaker and larger scale effects of the free-streaming of massive neutrinos. We consider this with the goal of re-examining the Sloan Digital Sky Survey data (as in Thomas et al., 2010). We find that the effects of the neutrinos might just differ enough from the effects of WDM to prevent the degeneracy of the relevant parameters, namely the sum of neutrino masses and the mass of the WDM particle.

Zusammenfassung

Mit der Einführung eines so genannten "dunklen Sektors" in der Kosmologie konnten zwar Ungereimtheiten zwischen kosmologischer Theorie und Beobachtungen gelöst werden - er wirft allerdings auch viele neue Fragen auf. Dunkle Materie (DM), erklärt gravitative Effekte, die nicht durch die beobachtete leuchtende Materie verursacht werden können. Dunkle Energie (DE) erklärt die beobachtete beschleunigte Expansion des Universums. Zu den begehrenswertesten Entdeckungen des gesamten Feldes gehören jene, die unser Verständnis bezüglich der Dunklen Materie und Dunklen Energie erweitern. Obwohl die Dunkle Materie die etabliertere der beiden Theorien ist, steckt unser Verständnis auch ihrbezüglich noch in den Kinderschuhen.

Diese Doktorarbeit befasst sich mit der Erklärung und Beseitigung von Unstimmigkeiten zwischen dem gängigen theoretischem Modell, dem ΛCDM-Modell - welches die kosmologische Konstante (Λ) als Ursache für die beschleunigte Ausbreitung des Universums und kalte dunkle Materie (CDM) als die Quelle für Gravitationseffekte beinhaltet - und den verfügbaren Beobachtungsdaten ergeben. Dabei wird der Schwerpunkt auf kleine Maßstäbe - Galaxiengröße und kleiner - gelegt, wo N-Teilchensimulationen der kosmologischen Strukturbildung im ΛCDM-Modell viel mehr Struktur und folglich viel mehr Leistung im Materieleistungsspektrum voraussagten, als viele andere Beobachtungen. Diese Unstimmigkeiten im Leistungspektrum auf kleinen Maßstäben äußern sich zum Beispiel im so genannten Zwerggalaxienproblem (z.B. Klypin et al., 1999), in der Konzentration und den Dichteprofilen individueller Halos (Donato et al., 2009) und auch in den Eigenschaften so genannter Voids, großer Leerräume im Universum. (Tikhonov et al., 2009). Diese Ungereimtheiten könnten durch einen physikalischen Prozess erklärt werden, welcher die Schwankungen des DM-Dichtefeldes zu unterdrücken vermag.

Frei ströhmende dunkle Materieteilchen dämpfen auf kleinen Abständen das ursprüngliche lineare Materiedichtefeld. Dies deckt sich mit einer Unterdrückung der der Leistung im Leistungsspektrum und erlaubt eine relativ einfache Erstellung von Modellen von früh abgekoppelten thermischen Relikteilchen. Solche Teilchen wären neutrinoähnlich, allerdings schwerer. Ein Beispiel wäre das Gravitino in einem Szenarium wo es das leichteste supersymmetrische Teilchen ist und sich viel früher abkoppelte als Neutrinos, aber noch während es sich in einem relativistischen Zustand befand. Diese Teilchen können nicht wie Neutrinos als heiße dunkle Materie klassifiziert werden, da sie nur auf kleinen und nicht auf allen Abständen einen Einfluss auf das Leistungsspektrum haben. Allerdings bewahrt das freie Strömen dieser Teilchen die kleinsten Strukturen vom Gravitationskollaps, womit sie auch nicht in die Kategorie der kalten dunklen Materie fallen können. Der Einfluss dieser warmen dunklen Materie kann in den statistischen Eigenschaften von kosmologischen Strukturen beobachtet werden.

Die Unterdrückung des linearen Materiedichtefeldes bei hohen Rotverschiebungen im WDM-Szenarium kann durch Lösen der Boltzmann-Gleichungen berechnet werden. Ein Fit an das

resultierende lineare Materieleistungsspektrum, welches die statistischen Eigenschaften dieses Materiedichtefeldes im einfachen thermischen Reliktszenarium beschreibt, wird von Viel et al. (2004) bereitgestellt. Dieses lineare Materieleistungsspektrum muss als nächstes korrigiert werden um die nichtlineare Strukturbildung im heutigen Universum miteinzubeziehen. Dies erweist sich als schwierig, da schon im kosmologischen Standard-Modell exakte Lösungen für die Entwicklung von gestörten Dichtefeldern im nichtlinearen Regime nicht analytisch berechenbar sind. Die weitverbreiteten Ansätze sind die `HALOFIT`-Methode von Smith et al. (2003), welche einen physikalisch motivierten Fit an die Ergebnisse von numerischen Simulationen vornimmt, oder das noch physikalischere, jedoch weniger akurate *Halomodel*. Beide nichtlinearen Methoden wurden jedoch nur unter der Annahme von kalter dunkler Materie entwickelt und sind daher nicht unbedingt für den Fall der warmen dunklen Materie anwendbar.

In dieser Doktorarbeit wird das Halomodel abgeändert (siehe auch Smith & Markovič, 2011) um die Auswirkungen eines geglätteten WDM-Dichtefeldes miteinzubeziehen. Erstens wird das dunkle Materiedichtefeld in zwei Hauptkomponenten geteilt: einen geglätteten linearen Bestandteil und einen nichtlinearen Bestandteil, wobei jedoch beide Leistung auf allen Skalen haben. Zweitens wird eine Mindestmasse vorgeschlagen unter welcher keine Halos gefunden werden können. Drittens wird die Massenfunktion auch überhalb der Mindestmasse unterdrückt. Viertens werden die Zentren der Halodichteprofile durch eine Faltung mit einer Gaußschen Funktion geglättet, dessen Breite von der thermische WDM-Geschwindigkeit bestimmt wird. Es wird gezeigt, dass im WDM-Szenarium der letztere Effekt nicht relevant für die Berechnung des nichtlinearen Materie-Leistungsspektrums ist, auf allen Skalen relevant für aktuelle astronomische Surveys, insbesondere das EUCLID Weak-Lensing-Survey.

Um die Gültigkeit der verschiedenen nichtlinearen WDM-Modelle zu überprüfen, wurden mit Hilfe des innovativen Lagrange-Code `GADGET-2` (Springel, 2005) kosmologische N-Teilchensimulationen durchgefürt (siehe auch Viel et al., 2012). Diese Arbeit stellt eine leicht zu benutzende Fitfunktion zur Verfügung, welche das nichtlineare WDM-Leistungsspektrum bei Rotverschiebungen zwischen $z = 0.5 - 3.0$ und im Bereich der für Weak-Lensing relevanten Skalen approximiert. Dabei wird das einfache thermische Reliktszenarium für verschiedene WDM-Massen untersucht und mit unseren Ergebnissen auf Aspekte der Auflösungskraft durch Variation der Größe und Zahl der simulierten Teilchen überprüft.

Die Doktorarbeit endet mit einer Diskussion der Möglichkeit, dass die WDM-Effekte auf das Materie-Leistungsspektrum Ähnlichkeiten aufweisen können mit den schwächeren und großskaligeren Effekten von freiströmenden massiven Neutrinos. Dies dient dem Ziel, die Daten des SLOAN DIGITAL SKY SURVEY daraufhin zu untersuchen (wie in Thomas et al., 2011). Es wird ermittelt, dass Neutrinoeffekte sich gerade genug von WDM-Effekten unterscheiden um eine Entartung von relevanten Parametern - die Summe der Neutrinomassen und die WDM-Masse - zu verhindern.

Contents

The Life of our Universe

This chapter corresponds closely to a public talk I gave[1]
at the AND Festival
www.andfestival.org.uk,
entitled *The Life of Our Universe*,
on the 30th of September, 2011
at the Scandinavian Seamans Church in Liverpool, UK.

The First Hour

Inflation

Here is a story, pieced together by physicists, called *Cosmology* about a continuously expanding and cooling universe.

The very first memory of our universe is of rapidly inflating space. This means that different points in space flew away from each other unbelievably quickly, distances grew and coordinate systems expanded. This *inflation* was fueled by a strange energy field that permeated the entire embryonic universe.

This energy field is cleverly called the *inflaton* field and it had very unusual properties. Its temperature at the moment of this first memory would have been a bit less than a hundred million trillion trillion degrees. The field was also super dense: if you took everything that you see in the observable universe today, back then, it would have been squished into a tiny subatomic space with the size of what we call the *Planck Length*. If you walked in *Planck Length* paces, you would have to make a hundred million trillion trillion paces to walk just one millimetre!

The pressure of the *inflaton* field was negative. This is very weird to imagine: a substance with positive pressure contracts if you squeeze it, whereas if it has negative pressure, squeezing it makes it bigger! So, what happened was, as gravity tried to pull this incredibly dense universe together, the already expanding universe expanded even faster. In other words, the negative pressure of the *inflaton* field caused the inflation of space to continuously accelerate.

In the mean time, because of the quantum nature of our universe, the *inflaton* field also fluctuated. Its density decreased very slowly and it was nearly perfectly uniform, but not quite. Instead of the slight fluctuations in the field eventually canceling each other out, because of the rapid expansion, the slight density inhomogeneities remained and even expanded in size. So, what we had now was a nearly uniform universe, filled with a strange

---

[1] Multimedia resources can be found at `http://www.usm.uni-muenchen.de/people/markovic/docs.html`.

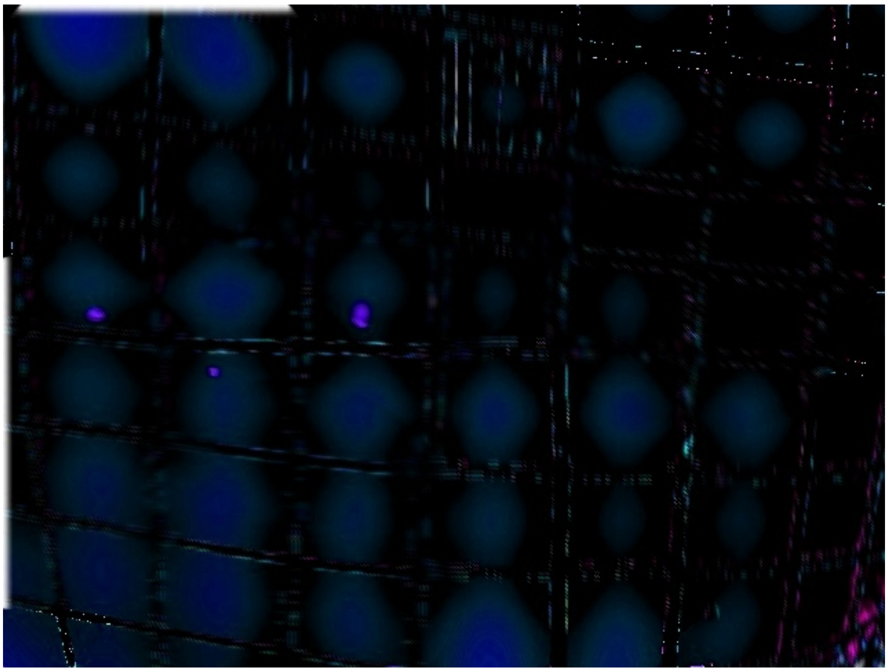

Figure 0.1: Inflation.
Image source: A doodle by Katarina Markovic.

energy field, which was a little bumpy at all different length scales, the bumps constantly emerging and growing as the universe expanded.

As the bumps were being pulled apart by the expanding space, before they could annihilate each other and fluctuate out of existence, the rapid expansion caused the universe to cool down to a “mere” thousand trillion trillion degrees. In other words the density of the universe dropped. Because of this, the *inflaton* field couldn’t fuel the acceleration any longer, and the speed of the expansion of space gradually became constant.

Reheating and Baryogenesis

Inflation happened in a tiny fraction of a second. In the time it takes me to say the word inflation, the entire process could replay itself at least a hundred million trillion trillion times! In this tiny fraction of a second the universe was obviously a very strange place. At very very early times, in the so called *Planck Epoch*, when the universe is of the size of *Planck Length*, the four forces of nature are believed to have been all one and the same. These forces were, and still are: **gravity** that holds planets in their orbits and us on the ground, **the strong nuclear force** that hold atomic nuclei together, **the weak nuclear force** that causes radioactive decay **and the electromagnetic force** that governs all of chemistry and sends electricity down wires. They ruled over the infinitely dense, infinitesimally small realm that was occupied by the embryo of our observable universe.

It was probably before or maybe during *inflation* that gravity differentiated itself from the other three forces, which was just one of many so-called *phase transitions* in the history of the universe and marked the end of the *Planck Epoch.* This transition was one of many moments in history when symmetries broke and therefore enabled the diversity of phenomena

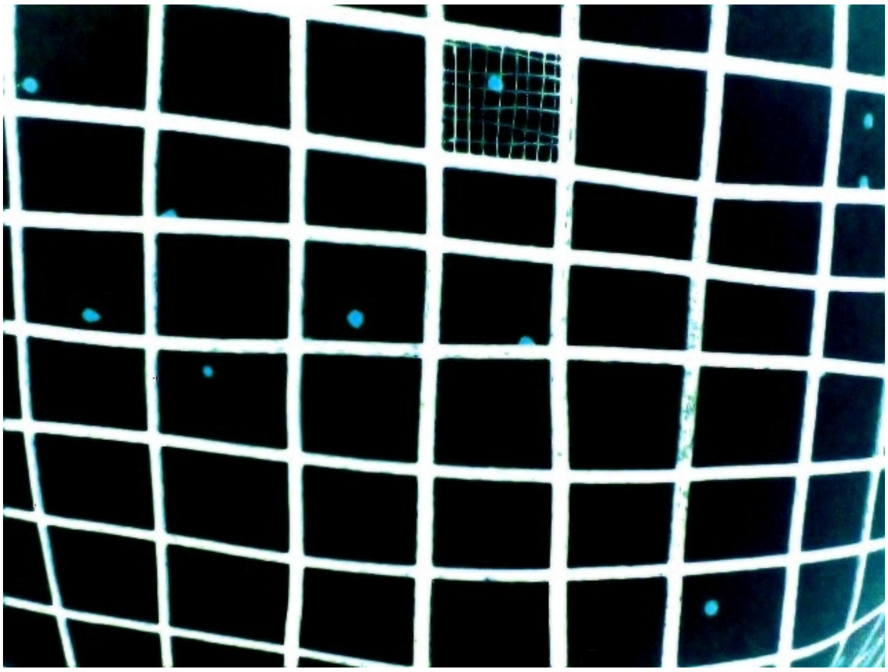

FIGURE 0.2: Reheating.
IMAGE SOURCE: A doodle by Katarina Markovic.

we observe in our universe, from *supernovae* explosions, to *black holes*, to life. A tiny fraction of a second later, the strong nuclear force also became distinct and different from the weak and electromagnetic forces. This transition is called the *Grand Unification Transition* or *GUT*, poetically.

This early, short and strange epoch has inspired many physics theories ranging from strange to mad. But the two leading candidates for the explanation of infant universe physics are String Theory and Loop Quantum Gravity. These models go beyond what I want to talk about today. They postulate about the nature of spacetime and the sources of the properties of elementary particles. They can be made to explain some of the observed particle physics phenomena, but they have not yet given any testable *predictions*. In other words, they do not postulate any phenomena that could falsify them, which means that, for now, they are little more than mathematical toys.

So, the universe had undergone the *Planck Epoch*, *Grand Unification* as well as *inflation* and was expanding and slowly cooling down. This made the *inflaton* field oscillate. But oscillation in a field is nothing else than waves. And because of *particle-wave duality*, we know that wave in a field means particles. This way the oscillation of the *inflaton* field produced vast numbers of *inflaton* particles. But this oscillation was non-uniform in space. Where quantum fluctuations produced bumps in the field during *inflation*, slightly more particles were produced, because the oscillation was a little out of phase from the rest of the universe. In this way, initial bumps in the *inflaton* field resulted in physical bumps in the density of *inflaton* particles. The *inflaton* particles were the big and heavy granddaddies of everything. But they were really unstable and as the universe cooled even more, they decayed into a myriad of new, lighter, fundamental particles, some of which are still around today and which make up the stars, the planets and you and me. With the *inflaton* field nearly gone, the

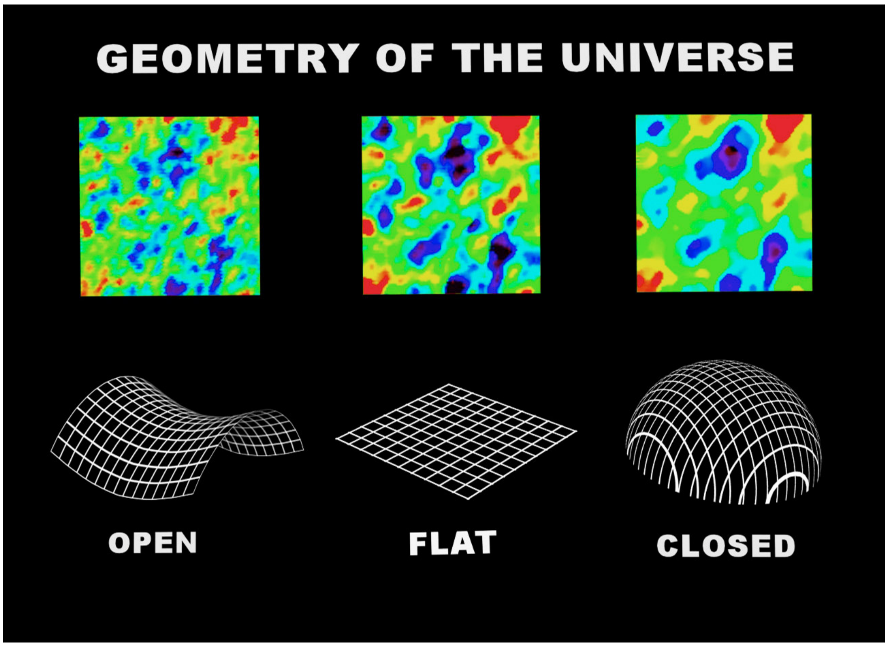

Figure 0.3: Curvature of the universe.
Image source: http://map.gsfc.nasa.gov/media/030639

energy of the new particles could now only fuel an expansion of space that was slowing down.

The new fundamental particles produced from the decay of *inflaton* particles were particles but also antiparticles. In other words matter and an equal amount of antimatter, which coexisted in equilibrium until the still expanding universe cooled down enough to destabilise the equilibrium. Now something very strange happened! A symmetry was broken! And as matter and antimatter annihilated each other in at least two distinct violent eruptions of energy a little bit of matter was left over.

Evidence for Inflation

What? You don't believe me? But it's a fact that this is *by far* the simplest way of explaining observational evidence! Why does the universe look the same in every direction? Why are the galaxies in the sky distributed in exactly the same pattern as far as we can see? How could the different sides of the sky possibly have become the same? These incredibly distant regions used to occupy a tiny space at the beginning of *inflation*. That's why they look the same, they were right next to each other at the beginning!

Why is the universe flat? You all know that if you add all the angles in a triangle together, you get 180 degrees, right? On a flat piece of paper? And if you draw it on the surface of a sphere? You get 270 degrees. This is because the surface of a sphere is curved, unlike a flat piece of paper. This is why maps of the whole world get stretched out on top and bottom as opposed to globes. So, we've drawn angles as big as the entire visible universe and they add up to 180 degrees. Precisely 180. This means that space is exactly flat. Why is that? Well, the universe needn't have always been flat. Inflation stretched it out. The universe expanded so much, we don't see the curvature anymore. It's analogous to looking at the flatness of the

Earth's surface. From our perspective it looks flat, right? But we all know that really its very nearly spherical, which means that it has a positive curvature.

We've also measured the statistics of the distances between the peaks of matter density today. In other words we've measured the distances between the places in the universe, where high concentrations of objects like galaxies can be found. They correspond exactly to the statistics of distances between the bumps in the *inflaton* field during inflation! Where there are more galaxies today, there would have been more *inflaton* particles in the early universe.

Of course what I've just told you is a postulated sequence of events at the very beginning of the life of the universe. And the physics of this early inferno are not very well understood. I've presented you with a theory about how the universe began for which there is a lot of evidence. But this evidence is not conclusive. At least not yet. Cosmology is a very young science and our capabilities in acquiring data and developing theoretical models are increasing drastically every decade.

The Electroweak Phase Transition

Now let's talk about a regime of physics that we can describe with more confidence, an environment, we can reproduce here, on Earth in our particle physics experiments like the Large Hadron Collider in Geneva.

We've just undergone the two waves of annihilation of antimatter and nearly all matter. The universe was cooling and expanding at a constant rate. Now the universe was filled with a plasma made of *quarks and leptons* - **the building blocks of everything** - and *gauge bosons* - **the messenger particles** that carry the strong, weak and electromagnetic force and hold the building blocks together. These particles, *quarks, leptons and gauge bosons*, are all of the fundamental particles of the so-called *Standard Model* of particle physics and are, in the simplest picture, all you need to build the universe we see today.

In particular, there are six different types of quarks, six different types of leptons and four different gauge bosons. The most familiar gauge boson is the photon, the particle of light, the carrier of the electromagnetic force. The most common leptons are the negatively charged electrons that, if sent through wires, give us electricity. Another omnipresent lepton is the very weakly interacting neutrino, of which there are trillions passing through us every second, most originating from the Sun.

In the not-so-simple picture there are at least three extra particles that you need to explain what we observe today: the *graviton*, which carries the gravitational force, the Higgs boson that appears at the next stage of the evolution of the universe I will talk about or the next *phase transition* and a *dark matter particle*, which I will also talk about later.

The immense release of energy at the brutal annihilation of matter and anti-matter gave the remaining matter particles a burst of kinetic energy, which made them speed up and by whizzing around very quickly the particles were able to constantly exchange energy and kept each other in equilibrium. If by coincidence a particle-antiparticle pair was produced, the antiparticle was very quickly annihilated by another particle.

This chaotic plasma of fundamental particles could only exist for another tiny fraction of a second. This short time was already orders of magnitude longer than the *Planck Epoch* or the *GUT* phase, but it was still very very short. In particular, if your heart needed such a tiny fraction of a second to beat once, it would beat a hundred thousand million times per second.

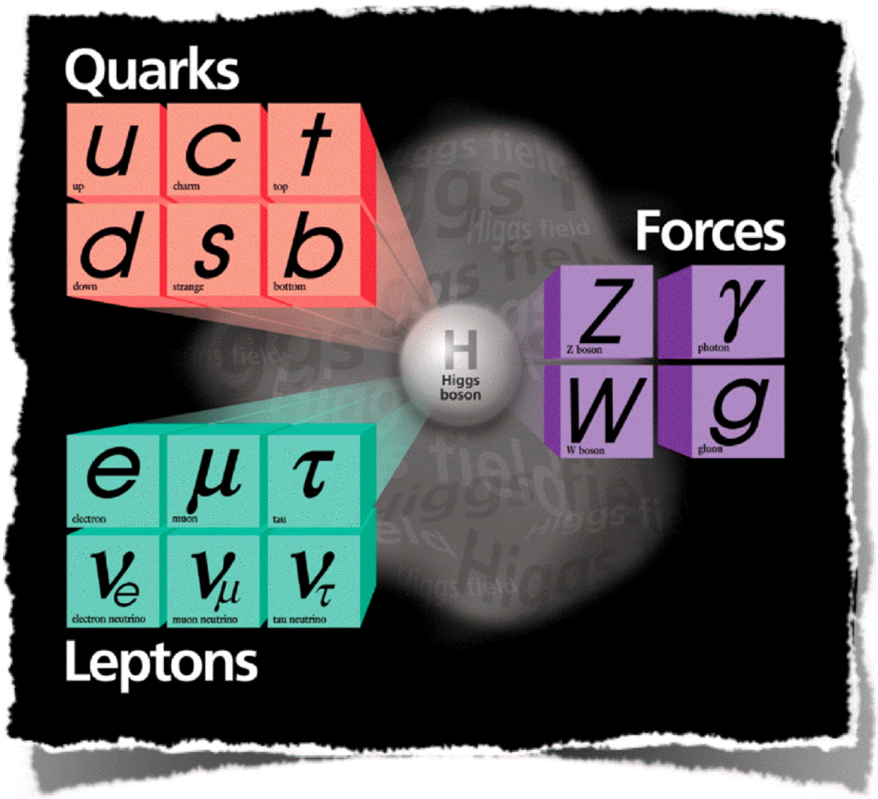

FIGURE 0.4: Standard model of particle physics.
IMAGE SOURCE: http://web.infn.it/sbuser/index.php/en/physics

At this point in cosmic time, the universe underwent another *phase transition*: the *Electroweak Phase Transition*, when the electromagnetic and weak nuclear forces finally became different. Now the four fundamental forces were distinct and the universe looked a little more familiar. This was also the time when the mysterious Higgs particles were produced. These particles are essential for our theory of particle physics, but they have perhaps been detected only recently. Their importance comes from their coupling to normal matter, which causes the *quarks*, *leptons* and some of the *gauge bosons* to attain mass at the *Electroweak Phase Transition*, but not photons. Photons remain masseless. **Without the Higgs, we would not be here today.**

Creation of Hadrons and Nucleosynthesis

A millionth of a second later the universe cooled down so much that the *quarks* didn't have enough energy to exist separately anymore. They huddled together like penguins in the winter and joined in threesomes into protons and neutrons, jointly called *baryons*. The temperature of the new plasma was ten trillion degrees and falling. The contents of the new plasma remained in equilibrium for a whole second! But this was not a boring equilibrium. The *leptons*, i.e. *electrons* and *neutrinos* took part in reactions in which protons changed into neutrons and vice versa.

After now a whole a second the temperature dropped to ten billion degrees, which meant

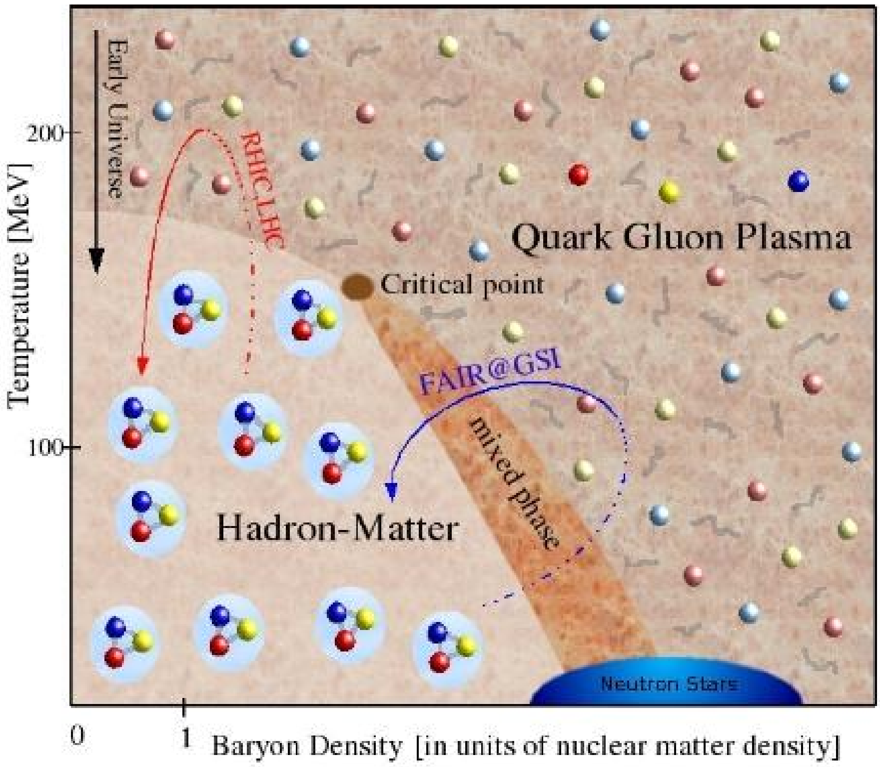

FIGURE 0.5: Phase transitions.
IMAGE SOURCE: http://www.gauss-centre.eu/quarks

that neutrinos could no longer take part in those reactions. This meant that the maximum number of neutrons was fixed, because neutrons can decay into protons, but protons are stable and do not decay. Now, the plasma was made up of mostly electrons - which are *leptons*, protons - which are *baryons* and are made up of *quarks* and photons - which are massless *gauge bosons* and are the particles of light.

Now jump with me to about a minute and a half later, when at a billion degrees, the universe was cool enough for some of the protons and *all* of neutrons to join together into atomic nuclei of Deuterium, the heavier brother of Hydrogen. Hydrogen has only one proton for a nucleus and in an everyday environment an electron orbits around the proton. The nucleus of a Deuterium atom however, contains a proton and neutron and is, just as in Hydrogen, orbited by an electron. So, once enough Deuterium nuclei were produced, they could start fusing into Helium nuclei, some of which fused into Lithium nuclei. **This stage in the evolution of the universe is called *nucleosynthesis* and it ends, when the universe is about three minutes old.**

We know this, because we know the properties of protons, neutrons and electrons very well, from observing them in physics laboratories. We can also observe the universe and measure the proportions of baryonic matter. It consists of roughly 75 percent Hydrogen and 25 percent Helium. Lithium and other elements are present in very very small quantities. Such a large amount of Helium could not have been produced in the stars that we observe. There would have to be a lot more of them and so, the night sky would have to look a lot brighter. Such an amount of Helium could only have been produced in the primordial universe.

The First 400,000 Years

Radiation-dominated Era and Baryonic Acoustic Oscillations

When the universe was only 3 minutes old, or rather, when the universe had 3 minutes of memory, it was permeated by a plasma containing mostly electrons and protons, or Hydrogen nuclei and some Helium nuclei, made up of a proton and a neutron, but by far the most dominant particles at that time were photons.

Photons are in fact a form of radiation. You are all familiar with the dangers of UV radiation from the Sun? Well UV radiation is nothing but relatively high frequency photos. In particular, their frequency lies in the Ultra-Violet part of the *electromagnetic spectrum*, which is just above our visual range which goes from red to violet - the rainbow. On the other side of the range is Infra-Red light, whose frequency is just too low for humans to see. The entire *electromagnetic spectrum*, going from low to high frequency consists of the following types of radiation: radio-waves, with the longest wavelengths and smallest frequencies, the microwaves, infrared light, visible light, ultraviolet light, X-rays and finally, the most energetic, highest frequency and shortest wavelength: Gamma-rays.

Another, entirely unrelated frequency spectrum, we are all familiar with is the spectrum of sound. Whereas a photon (or a light wave) is an oscillation of the electromagnetic field - a very fundamental phenomenon, sound is a (longitudinal) compression wave in the motion of particles in a medium, like water or air - or plasma. A sound wave can displace a membrane, like an eardrum for example.

The photon-baryon plasma that ruled the universe after the first three minutes was loud. Remember the bumps in the *inflaton* field? Remember that they produced over-densities in the numbers of *inflaton* particles? And remember that these particles decayed into familiar particles of regular matter that make up Hydrogen and Helium? Well, in fact, the over-densities or bumps, however you want to call them, were preserved through these first three minutes. Now that physics had time to kick in, these bumps realised that they were immensely over-pressurised and turned into explosive sound waves in the plasma that was made up of mostly photons and baryons (or nuclei).

The reason why the bumps became sound waves, was because the overdensity of the bumps caused them to start collapsing under gravity, but the very quickly moving particles in the plasma were too energetic to allow the collapse. So, as the bumps tried to contract, the pressure from the plasma particles caused them to expand, which created an outwardly propagating wave, sort-of like when you drop a stone into a pond (only that there was only one wave-front). In fact the universe was full of bumps of different sizes, which meant that the outwardly propagating spherical sound waves made it looked like a three dimensional pond into which many metaphorical pebbles of different sizes were dropped at the same time.

The Cosmic Microwave Background and the Size of the Sound Horizon

The (interference) pattern in the photon-baryon plasma resulting from these spherical sound waves propagated through the universe and didn't die down for four hundred thousand years. If you look at the three-dimensional wave pattern resulting from one bump or one pebble, you can calculate how far the wave front could have propagated in this time. It's simply the speed of the sound times the time. Sound speed in those times was, because of the high energies, nearly equal to the speed of light; well, about fifty percent. So, the distance the wave

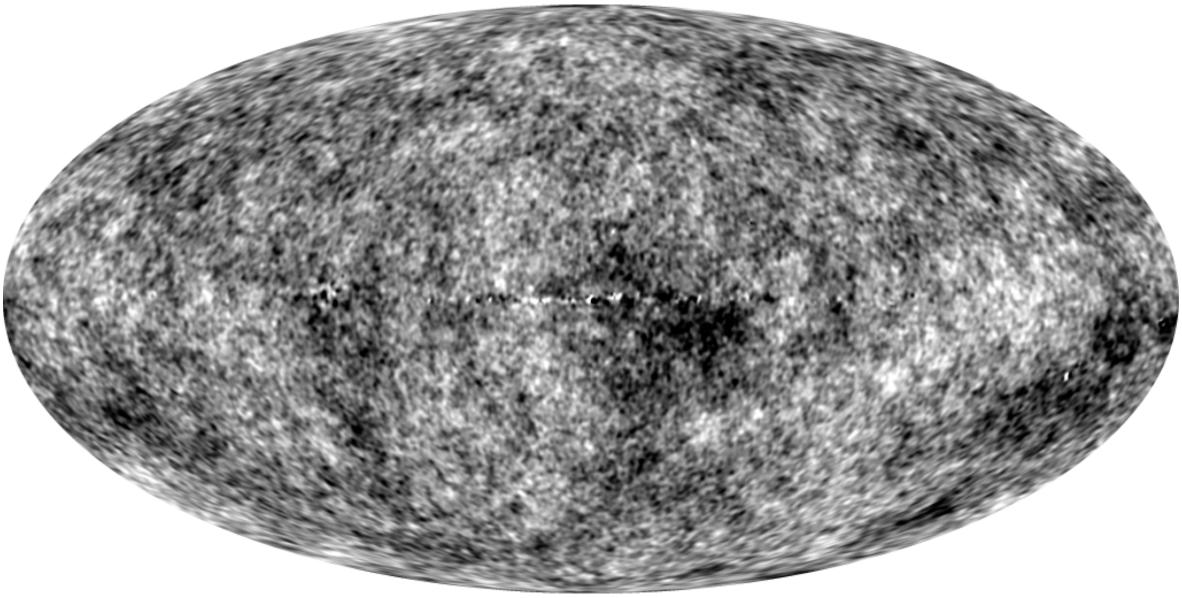

FIGURE 0.6: The Cosmic Microwave Background Anisotropy.
IMAGE SOURCE: http://map.gsfc.nasa.gov/media/101080

front travelled in those four hundred thousand years, was approximately fifty percent of four hundred thousand light years; so, two hundred thousand light years. An added complication was that the universe was still expanding, so in the end, this means that the size of the entire spherical wave front is about a million light years across. This means that the universe was filled with spherical shells of overdensity in the photon-baryon plasma. You can imagine this as millions of overlapping bubbles of equal size, filling all of space and expanding with time.

After four hundred thousand years, the universe cooled down to about three thousand degrees Kelvin, which is approximately the melting point of diamond. This meant that electrons in the plasma no longer had enough energy to travel freely. They quickly had to find a lower energy state, meaning that they had to combine with the Hydrogen and Helium nuclei, to form Hydrogen and Helium atoms! This marked another important transition in the life of the universe.

Electrons, as you might know, are negatively charged, whereas nuclei are positively charged, due to the presence of protons. When electrons combined with nuclei to form atoms, there were no more charged particles traveling freely through the universe. This meant that the photons, who would normally be absorbed by such charged particles, suddenly became free. The universe went from being filled with a glowing fog to being completely transparent and dark. There were no new photons produced and no old ones were destroyed. The photons released at this transition travelled freely from then on.

From then on, these photos of ancient light were unobstructed, their life was uninteresting. They propagated freely and slowly cooled down as the universe expanded. You can imagine this cooling as a stretching of the light's wavelength by the expanding universe, because low energy or low temperature always corresponds to a larger wavelength. This light from the infant universe is still traveling through the universe today. We've all seen it. Well if you are over 20 years old, you probably have. A few percent of the white noise in old television sets came from this very cold, very long wavelength radiation. In particular, the

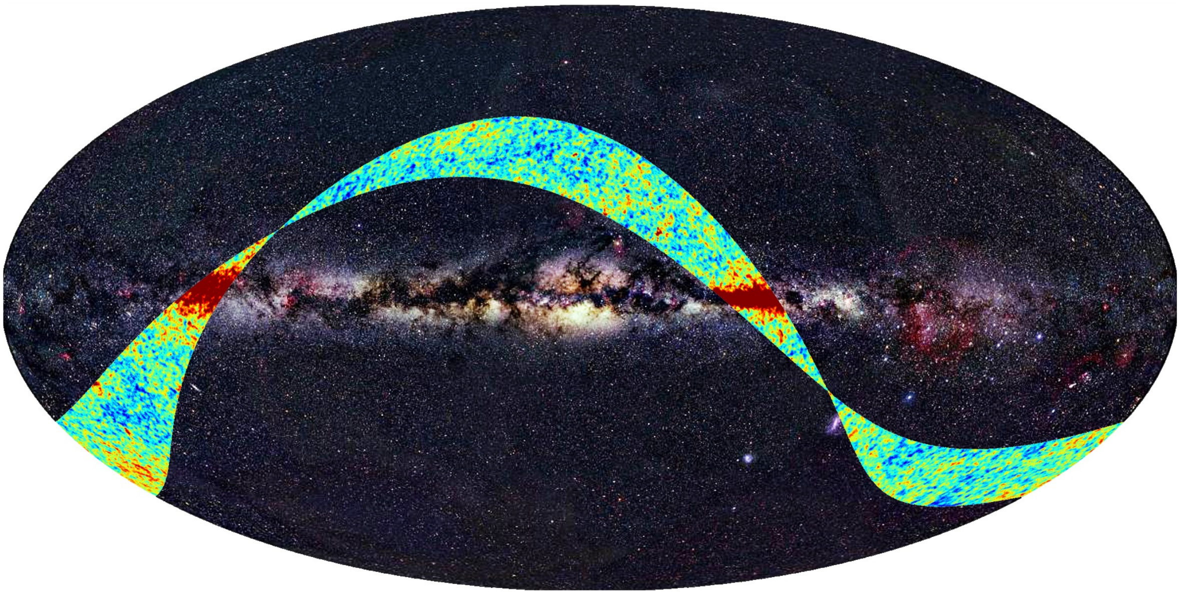

Figure 0.7: The Sky at Different Wavelengths.
Image source: `http://www.stfc.ac.uk/resources/image/jpg/planckfirstlight.jpg`

temperature today is about three degrees Kelvin or three degrees above absolute zero or minus two hundred and seventy degrees Celsius. This can be interpreted as the temperature of outer space, which is today a nearly perfect vacuum filled with extremely rarefied gas as well as ancient light. The wavelength of such low temperature radiation falls in to the microwave part of the electromagnetic spectrum and for this reason we call it **the *Cosmic Microwave Background*** or *CMB* for short.

CMB light was first detected and identified in 1964 by two radio astronomers called Arno Penzias and Robert Wilson, who serendipitously found a very long wavelength, very uniform and regular glow of exactly the same intensity coming from all directions in the sky. This was very conclusive evidence for some parts of what was called *The Big Bang Theory*, or the theory that postulates a universe starting out very small and then expanding.

Almost two decades later, in 1992, a satellite called *The Cosmic Background Explorer* or *COBE* was able to make such a precise measurement of this *Microwave Background*, that it was able to increase the contrast in image by a factor of a hundred thousand. Once they did this, the scientists, John Mather and George Smoot, saw the bubbles from the expanding sound waves and won the Nobel Prize! This measurement showed that our theories of *inflation* and sound bubbles in the primordial baryon-photon plasma were correct!

As the photons were freed, when the universe was about four hundred thousand years old, the walls of the bubbles blown by the primordial pressure of the baryon-photon plasma, were a little more dense and therefore, had a little bit more gravitational pull. When the released photons had to climb out of these gravitational wells into which they were being pulled, they lost energy. And because the photons have been traveling freely ever since, the photons coming from the points in the sky where the bubbles were located, have a little less energy than other photons, that escaped from outside these bubbles. For this reason, when looking at the *Cosmic Microwave Background* image, having increased the contrast by one hundred thousand, we can see little overlapping blobs, whose size turns out to correspond exactly to what we calculated a minute ago: a million light years! The bubbles turn out to be exactly the size our theory predicted!

The First 10 Billion Years

Dark Ages and Reionisation: The First Stars

So, we left off in a universe that was transparent and dark and whose fuzzy reddening light was slowly fading. It remained so for the next hundred million years! This epoch in the life of the universe is cheerfully called *the Dark Ages.* The universe was now undergoing a slowing expansion and cooling. The Hydrogen atoms soon became too cold to remain completely free and some of them combined in pairs into Hydrogen, or H_2 molecules. Luckily however, the cold darkness did not remain.

Before *the Dark Ages*, when the massless photons left the bubble walls, the inertia of the remaining heavy baryons stalled the bubble growth. The bubble sizes were frozen; the pressure supplied by the energy of the photons no longer could push the electrons, because now they were bound to nuclei into neutral atoms. This also meant that over-densities could suddenly be overcome by gravity. The bubble walls started to fragment into separate clouds of gas and collapse. At first, these clouds collapsed gently and slowly. They slowly became denser, smaller and hotter. But because of slight inhomogeneities in the collapse, the in-fall of gas caused it to become turbulent. Moreover, as gas turbulently flew into the centres of clouds, it accelerated, like any object falling under gravity.

Finally, in majestic swirls the clouds collapsed into extremely dense objects, whose centres were under so much pressure and at such high temperatures, that in these centres, the conditions from a much earlier time in the life of the universe were recreated. Hydrogen molecules broke up and electrons were again stripped away from atomic nuclei. The cores of these hot, dense objects ignited in nuclear fusion and the nuclei of Hydrogen and Helium from the primordial universe started joining into nuclei of heavier elements, like Carbon, Nitrogen and Oxygen! These objects were nothing but the first stars!

The first stars formed a hundred million years after the emission of the *Cosmic Microwave Background.* They were very different from the stars we see today; their masses were hundreds of times that of our Sun and they were very pure! They contained only Hydrogen and Helium (perhaps also a tiny bit of Lithium). They lived short and violent lives at the end of which they exploded as fantastic *hypernovae* and filled the universe with fireworks of Gamma radiation made up of high-frequency photons. And most importantly, they expelled the Carbon, Nitrogen and Oxygen out of their cores into the inter-stellar gas!

The appearance of the first stars lit up the universe and ended the *the Dark Ages.* The new light consisted of plenty of new, energetic photos that diffused into the surrounding Hydrogen and Helium gas. These photons heated up the gas, which *re-ionized* it. In other words, the temperature went up enough for hot gas pockets to form around the stars. The gas in these pockets was hot enough for electrons inside to become free from atomic nuclei again.

Matter-dominated Era and Non-linear Collapse: Dark Matter

The first stars were created first and in largest numbers inside the over-densities in the primordial Hydrogen and Helium gas. In particular, they formed inside the walls of the pressure bubbles originating from the very early universe. But they also formed in the centres

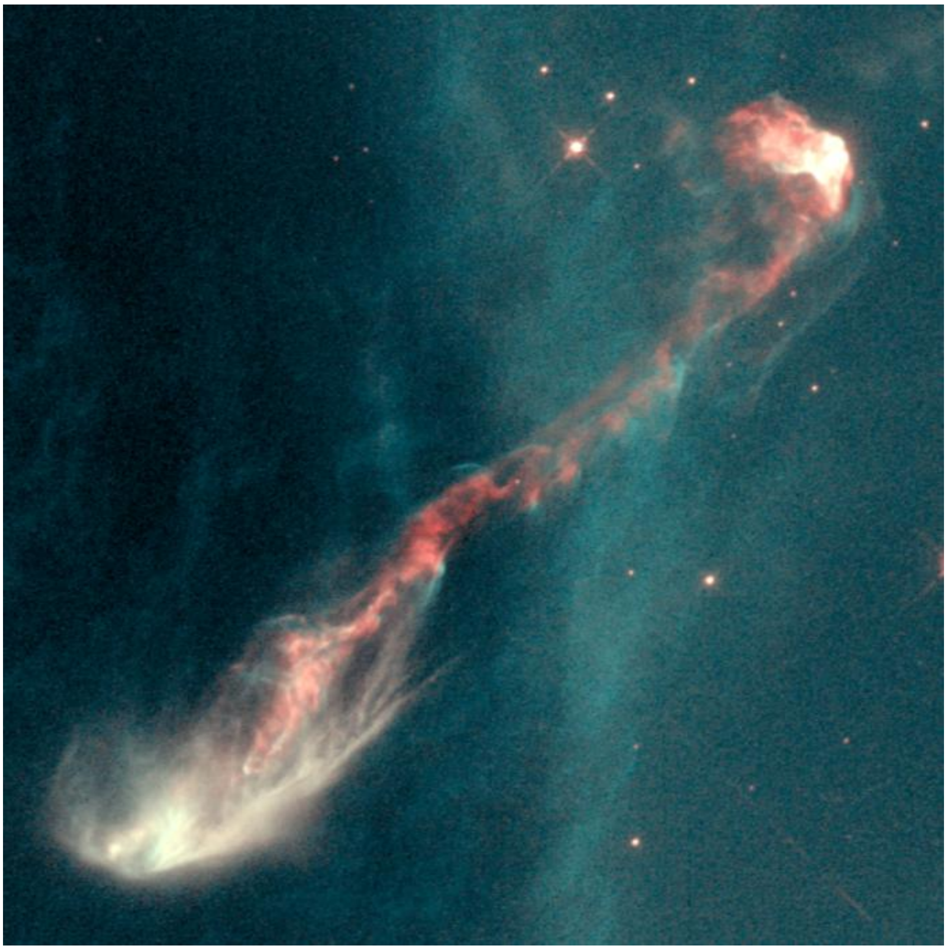

FIGURE 0.8: Population III Stars.
IMAGE SOURCE: http://www.mpa-garching.mpg.de/mpa/conferences/stars99

of these bubbles. It turns out, that the whole time, since the beginning of the universe, there was something else present. An elusive and strange type of matter, which did not let itself be known to the leptons, quarks and gauge bosons. It did not interact with any of these regular particles. It hid in the background, giving the rest of the universe a gentle gravitational tug.

The expansion of the universe diluted the density of this strange matter more slowly than that of the photons. And as the universe cooled down, it's gravitational influence became more and more important, until it overpowered the gravitational pull of the bubble walls and lured most of the baryonic matter back into the centres of the primordial bumps. At the same time, the mass of the baryonic matter in the bubble walls also attracted a little bit of this matter to itself.

The strange matter does not interact with electromagnetic radiation, in other words it is completely transparent to light and does not emit any either. **For this reason we call it *Dark Matter.*** And even though we don't see it, we know it's there. Its gravitational pull is unmistakeable.

With time, the gentle gravitational tug of *Dark Matter* grew into a fierce pull and all matter gushed towards the ancient bumps of over-density and the much less pronounced

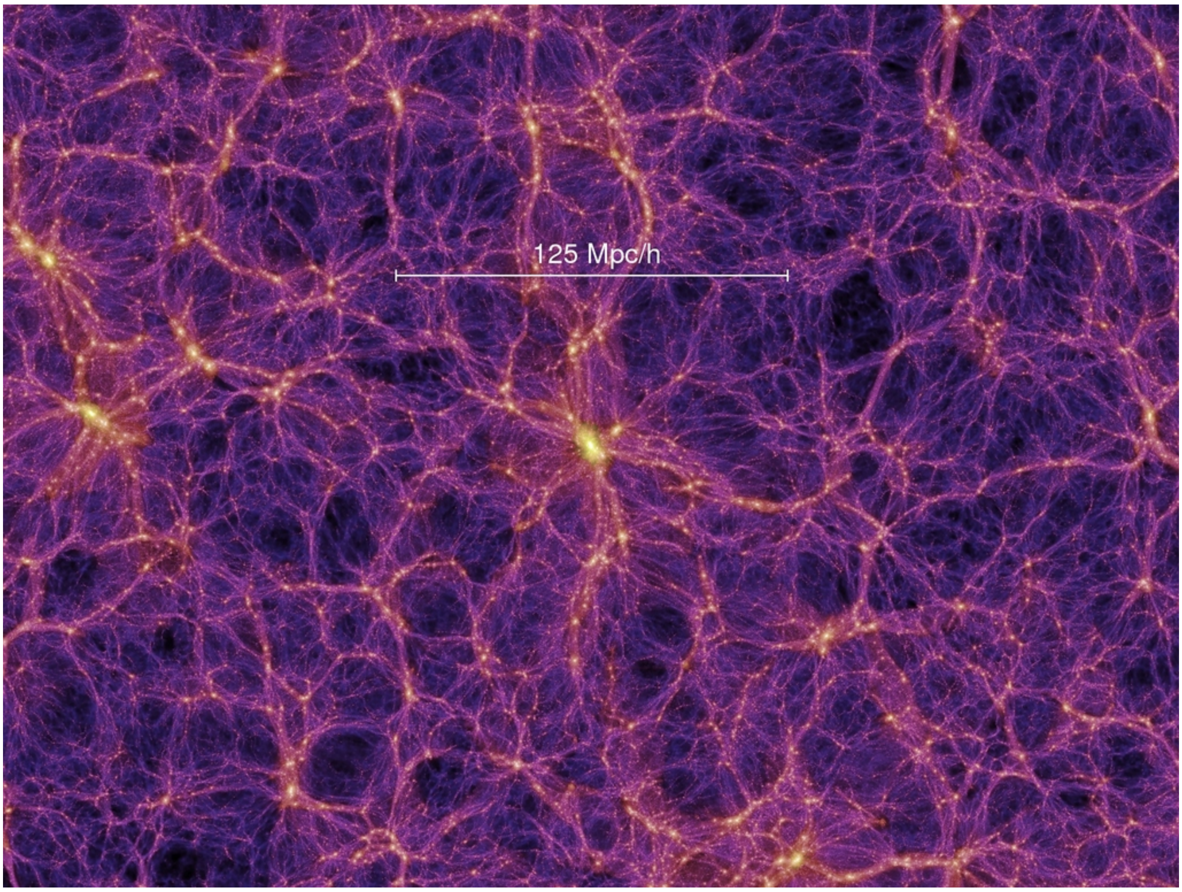

FIGURE 0.9: The Dark Matter Web.
IMAGE SOURCE: http://www.mpa-garching.mpg.de/galform/virgo/millennium

bubble walls. The gravitational instability sourced by *Dark Matter* over-densities caused all matter to collapse into majestic web-like structures, at whose nodes great gravitational wells formed and became cradles in which the first galaxies were born.

Because *Dark Matter* is undetectable directly, scientist use its gravitational effect to map out its web-like structure. Firstly, we know that regular matter, so, atomic nuclei and electrons feel gravitational attraction to the *Dark Matter*. Luckily this regular matter does interact with light. In fact, stars generate light and other matter disperses it, for this reason such matter is also referred to as *luminous matter* and most importantly, therefore we can see it. Consequently, if we follow the distribution of *luminous matter*, we can infer the underlying *Dark Matter* structure!

In addition, we can try to find the signature of the bubble walls and compare their prominence to the densities of the primordial bumps. This, of course, depends on how much *Dark Matter* there is in the universe. The more the *Dark Matter*, the more the *luminous matter* getts pulled from the bubble walls, towards the bubble centres, where the bumps are located. And if there were no *Dark Matter* at all, there would only be bubbles!

Finally there is *gravitational lensing*. Normally photos of light travel on straight lines. However, according to the theory of Albert Einstein, any kind of massive matter distorts space by curving all its paths. Therefore, close to massive objects in the universe, light cannot travel in straight lines any longer and is therefore deflected or *lensed.* This causes the images of distant bright objects, from which this deflected light is coming from, to be distorted, as if we were looking through a lens! But *Dark Matter* structures are the most massive objects in our universe and therefore can be detected by looking for the distortions in the images of far-away luminous objects like galaxies!

In the early universe, *Dark Matter* mysteriously lurked in the background, slowly creating gravitational cradles in which regular matter could safely collapse, without being blown away by it's own pressure. These *Dark Matter* cradles or *haloes* as they are better known, started out small. They first formed by collapsing around the smallest and most abundant density bumps in the universe. As time went by, these small *haloes* started moving closer together and clustering around larger bumps until these larger bumps collapsed into larger *haloes*, which then clustered and collapsed around even larger bumps. This process is known as *non-linear collapse of structure* and is, to an extent, still going on today. The largest haloes that have had time to collapse in such a way, cradle groups of hundreds of galaxies and are called *galaxy clusters.* They are the largest gravitationally bound objects today. But this process is now, after fourteen billion years (or fourteen *gigayears*), starting to halt. Why this is the case, I will keep secret for a little longer.

Galaxy Formation and Active Galactic Nuclei

The baryonic gas of Hydrogen and Helium from the early universe collapsed gradually. Like *Dark Matter* it started off with the smallest objects. This is because in the short time from the emission of the *Cosmic Microwave Backgroud*, when photos became free and baryons no longer were pushed around by them, until the beginning of collapse, only the very smallest objects had time to form. These were the giant primordial starts, who lived violently and died young in a spectacular fashion. As time went on, like in the case of *Dark Matter*, larger clouds of gas had time to collapse, protected in the wells of the forming *Dark Matter* haloes. However, unlike *Dark Matter*, baryonic or regular matter collapsed spectacularly.

So, in the first billion years after the first giant stars formed, the collapsing gas clouds formed protogalaxies. These protogalaxies were very diverse, taking different forms due to the turbulent nature of the collapsing gas. Gravity was pulling these vast amounts of material towards the centre of the gravitational wells. At the same time, the in-falling gas heated up, because it was moving faster and faster and becoming denser and denser. This heating sometimes caused it to emit photons, who took away some of its energy, which cooled it down. Sometimes it was not able to cool down so well and its pressure just increased. This created magnificent shock waves that travelled through the gas clouds. Sometimes these shock waves caused such instability in the clouds, that they fragmented further and collapsed into stars.

Some of the protogalaxies had exactly the right properties and environments for this star formation to happen relatively quickly. This means that once the stars appeared, lived their lives and died, there was nothing left to happen in the galaxy. The galaxies remained “cloud shaped”, with no particular interesting features. Their stars at the beginning were born and enthusiastically emitted high energy photos for a while. High energy photons carry high frequency light. In other words, stars emitting high energy photons appear blueish. So, these galaxies shone bright and blue for a short amount of time. Then the stars started running our of fuel, started getting old and so only could emit lower frequency, reddish light. These are *elliptical* galaxies and when observed through something like the Hubble Space Telescope, they still appear, thirteen billion years later, as featureless, fuzzy reddish blobs.

Figure 0.10: Barred Spiral Galaxy.
Image source: http://hubblesite.org/gallery/album/galaxy/pr2005001a/

Other galaxies were not so good at creating regions of star formation. These had time to collapse more gradually and could therefore form discs with beautiful spiral arms of gas, dust and stars. As the spiral arms rotate around the centre of the galaxy, they create shock waves that trigger star formation over and over again. Because young, bright stars are always present, such galaxies appear somewhat blue. Furthermore, because all the material is present in an ordered disc, there are sometimes giant dust clouds obscuring parts of the galaxy, creating morphologies that make each spiral galaxy as unique as a snowflake.

Because *Dark Matter* cradles or haloes exist in many different sizes, some contain a little bit of lonely gas, some contain little dwarf galaxies, some contain whole, large galaxies and a few even contain and protect large galaxy clusters. Galaxies always feel gravitational attraction towards the centres of these large haloes and orbit around it, like the Moon orbits the Earth. Often there is a large *elliptical* galaxy present in the centre of such a *Dark Matter* halo and other, smaller galaxies orbit around them. Every few billion years, somewhere in the universe, two galaxies follow dangerous paths and collide into each other. This is a rare and beautiful event that triggers new star formation and often turns beautiful spiral galaxies into chaotic *ellipticals* and lasts billions and billions of years.

After violently exploding into majestic *hypernovae*, the most ancient giant stars collapsed into black holes. These black holes may today be travelling through space, hidden from sight in their darkness or they may have been caught in the swirls of the largest early collapsing clouds and ended up seeding the formation of galaxies and may today be resting in the centres of these galaxies, slowly swallowing up the surrounding gas and stars growing into super-massive black holes. It is believed that most galaxies contain super-massive black holes in their centres, which are millions of times heavier than our Sun. If two such galaxies collide, their central black holes may merge in one of the most violent events possible in the universe today. Moreover, when some of these giant black holes first formed, billions of years ago, in the violent rotating in-fall of material, gigantic jets of photons and other particles were emitted perpendicularly out of the host galaxy.

So, the primordial baryonic bumps fragmented into giant clouds, when the universe was about half a billion years old. These clouds then collapsed, protected in gravitational wells of *Dark Matter*, into the gigantic and magnificent objects occupied by tens of billions of stars as well as clouds of gas and dust. On really dark nights, we can see a few of these, the ones that are very close by, as fuzzy bright spots in the sky. But the closest one of them dominates our night view upwards. Its arm is the home of our Solar System, the beautiful spiral galaxy, **the Milky Way.**

The Universe Today

Supernovae and Redshift

For the next eight billion years not much changed. Galaxies kept rotating, stars kept forming and they kept dying in brilliant supernovae explosions. These explosions could be seen extremely far away, since they, originating from single stars, could outshine an entire galaxy of billions of stars! But they could also be seen for a long time. In a way they could be seen for a time much longer than how long it took them to burn out. This is a strange idea. But in a way, it makes sense, let me try to explain why.

Photons of light are massless particles. They are infinitely light and so, they are allowed by physics to travel at the fastest speed possible through a vacuum. The fastest speed anything can ever travel at. Particles and objects that have mass are forbidden from travelling so fast, by one of Albert Einstein's famous calculations. This speed is therefore called the *speed of light* in a vacuum and equals six hundred and seventy million miles per hour or three hundred thousand kilometres per second. However, even though this speed is large, it is not infinite. This means that even though light travels human distances instantaneously, it takes a while to traverse astronomical distances. For example, it takes light eight minutes to travel from the Sun to Earth. It takes it about a day to get from the Sun to the cold, icy, rock populated edge of our Solar System, about four years to get to our closest star, *Proxima Centauri* and twenty five thousand years to get to the centre of our galaxy. The closest galaxy to us is the *Andromeda*. If our Sun went nova, the alien astronomers of Andromeda galaxy would only see it two and a half million years later!

For this reason, any bright event, like a supernova explosion, which only last a few weeks, is seen forever, its photons travelling farther and farther into the unknown, distant universe, becoming more and more rarefied and losing energy. **And more importantly, for this reason, the further away we look, the further we look into the past!** The furthest observable distance is in the earliest visible event in the past: the Cosmic Microwave Background, which is what our universe looked like in the last brief epoch before it became transparent.

Since *inflation*, the universe has been expanding rapidly. At first its expansion accelerated exponentially; then it suddenly decelerated to a constant speed whilst *inflaton* particles were produced. Then, as radiation and matter dominated it, its expansion slowed, but never ceased! Photons traveling through such an expanding space, become stretched out in wavelength and their frequency becomes lesser, it goes from the blue part of the spectrum towards the red. In

FIGURE 0.11: Supernova Remnant, the Crab Nebula.
IMAGE SOURCE: http://hubblesite.org/gallery/album/star/supernova/pr2002024a/

other words, as if they were becoming tired from having to cross growing distances, photons loose energy and therefore become *red-shifted*. The longer a photon has had to travel through expanding space, the more energy it looses, the more redshifted it becomes. This is why we say, the universe is cooling down. As the photons loose energy, they become more redshifted and cooler.

Conveniently, the phenomenon of *redshift* enables us to measure distances in the universe even for objects of unknown sizes as long as they emit, diffuse or absorb some light. Objects like galaxies and supernovae have typical frequency signatures, which are also known as *spectra*. As photons from these objects move through the expanding universe and lose energy, their signatures shift red-wards. Measuring this redshift then means measuring how long the photon has been traveling through the universe, which, knowing the speed of light, immediately betrays the distance the photon has travelled from the object to Earth!

As always however, there is a further complication. *Redshift* can be cosmological, as I have just described, but it can also come from the motions of bright objects. This effect is analogous to the *Doppler effect*, which causes the wavelength of the sound of an approaching siren have a higher frequency and so a higher pitch than the sound of a siren that is moving

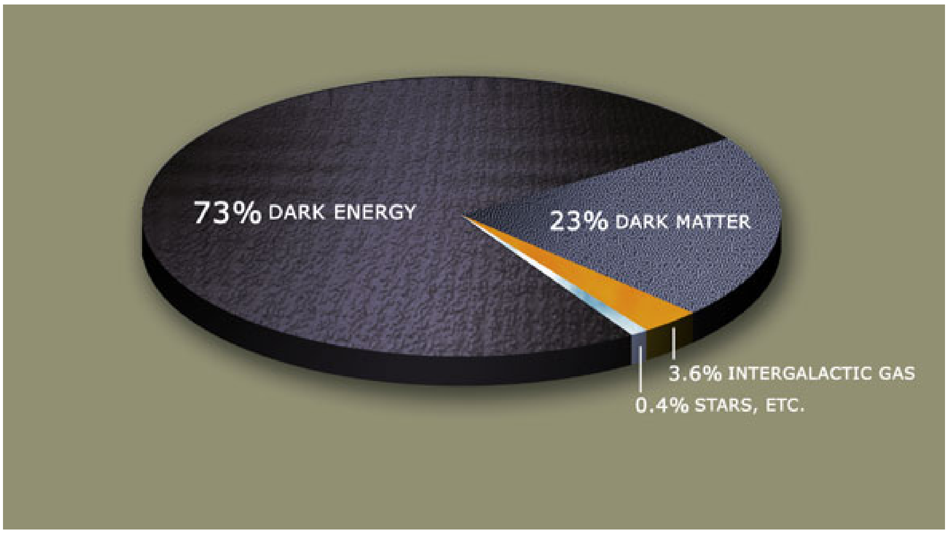

FIGURE 0.12: The Energy Budget of our Universe.
IMAGE SOURCE: http://planetquest.jpl.nasa.gov/images/darkMatterPie-590.jpg

away. Therefore if a bright object travels towards us, its light becomes *Doppler shifted* and it appears bluer. Conversely, if it is moving away from us, it appears redder! So, when measuring *redshift*, there are two competing effects, cosmological red-shifting and *Doppler* red-shifting. These can in some cases be disentangled and even used to uncover underlying physical processes in our universe.

In fact, supernovae make very good so-called *standard candles*, because their intrinsic brightness is easily predicted. Knowing the intrinsic brightness means having a distance measure independent from redshift. This is because, as we all know, as things go further away, they only become dimmer and dimming has nothing to do with wavelength. So if we know the distance to a supernova, we can figure out how quickly it is moving away from us!

Accelerated Expansion, Dark Energy and the Energy Budget of our Universe

Non-linear structure collapse is a process in which smaller *Dark Matter* haloes cluster together and contribute to the collapse of larger haloes. Until today, when the universe is fourteen billion years old, this happened in a fractal fashion; the smallest haloes clustered into mid-sized ones, mid-sized haloes clustered into large ones and so on and so forth. But lately, for the past few billion years, something strange has been happening. Five billion years ago, when the universe turned nine billion years old, the giant clusters of galaxies became unable to collapse. Anything larger that a cluster, started feeling like it's being pulled apart. This pull grew with time as the universe gradually re-started its accelerated expansion.

You see, as the universe expanded, the density of radiation fell most rapidly, this is because unlike ordinary matter, radiation lost additional energy, because the expansion stretched out its wavelength. The density of ordinary matter, as well as *Dark Matter* also fell, as you would expect, if you expand a container without injecting new matter into it. But as the densities of matter and radiation fell, one density, initially very low and hidden, now started emerging and becoming more important. Another form of strange energy emerged. **Some call it**

vacuum energy and some simply call it *Dark Energy.* Its most important feature is that its density has stayed constant, since the beginning of time, even though the universe has undergone many epochs of expansion. Five million years ago, the density of this energy became greater than the densities of matter and radiation.

Today, it is starting to dominate the budget of the universe. More than seventy percent of stuff around us is *Dark Energy*; nearly thirty percent is *Dark Matter*; only a few percent is made up of what is familiar, ions, atoms and molecules, stuff you can see, hear, smell and touch. Like the *inflaton* field, which caused the very early accelerated *inflation*, *Dark Energy* also has the strange property of negative pressure. Like the *inflaton*, it also pushes apart as it gets pulled together by gravity and just like the strange *inflaton* in the very early universe, *Dark Energy* today causes the expansion of space to accelerate!

The accelerated expansion can be seen by observing distant supernovae. In a universe expanding with a constant speed, doubling the distance, doubles the speed of recession. In other words, a galaxy cluster a hundred million light-years away will be receding from us twice as fast as a cluster at only half that distance, so fifty million light-years away. However, if we look at bright supernovae, whose light reaches us across the furthest distances and whose light signature is so well known that we can be confident about their speed of recession and whose distance is also betrayed by their brightness, because they are standard candles, it becomes clear that they are not receding linearly! Observing such supernovae proves the present day accelerated expansion of our universe.

The Future of the Universe

The Big Freeze

As time passes, and the universe expands, the already diminishing density of radiation and matter will disappear. Galaxies will merge and spiral towards their central black holes. Star formation will cease. As the expansion of space accelerates, it will be able to pull apart any gravitationally bound objects. First galaxy clusters will fly away from each other, then they will be ripped apart. All stars will die in novae and turn into dark dwarfs, neutron stars or black holes. Then individual galaxies will be ripped into pieces. After that stellar remnants will dissolve into space. Eventually all matter will either fall into black holes or become so diluted, it will disappear. The universe will become cold and dark, the only objects around will be extremely rare black holes that will be slowly radiating away their bodies.

And the universe will just keep expanding. **Forever.**

Figure 0.13: Merging Galaxies.
Image source: http://hubblesite.org/gallery/album/galaxy/interacting

CHAPTER 1

The Background Universe

In the introduction, this thesis will deal with the canonical model of cosmology. This model consists most importantly of two main ideas. The first says that our universe can be described mathematically by the Friedman-Lemaitre-Robertson-Walker *metric* quantifying the geometric properties of the space-time *manifold*. The second says that the energy-momentum *tensor* (EM) sources this geometry and describes four distinct types of "matter":

radiation - relativistic matter,

baryonic matter - confusingly called so, this is matter made up of non-relativistic particles of the standard model (SM) of particle physics, to which baryons contribute most in energy density,

dark matter (DM) - weakly or non-interacting unknown matter as well as some standard model particles in the case where their perfect fluid pressure is zero and

Λ - a property or substance that drives the accelerated expansion of space.

These types of "matter" are classified according to their cosmological effects and not their microscopic properties. We will define these effects and justify this classification below.

In this chapter we derive the equations governing the universe as a whole. These equations assume a fundamental premise, which is named after Nicolaus Copernicus, who was one of the more important proponents of the idea that the Earth is not at the centre of the universe. In the context of cosmology this principle is generalised to say that we do not occupy a special place in the universe. This is referred to as the *Copernican Principle.* Together with the observed *isotropy* of the sky, we can deduce the third important assumption: *homogeneity.* We will use these principles as absolute in this chapter, but we will weaken them to only *statistical* homogeneity and isotropy in the following chapters. These assumptions are in fact to a large extent justified by observation, but the discussion of probing homogeneity and isotropy of the universe is beyond the scope of this text.

The principles and the equations we derive for the dynamics of the universe are needed to later understand the evolution equations for the structures in our universe, which are the topic of this thesis.

1.1 Basic geometry of the spacetime continuum

1.1.1 Ricci Calculus

The mathematical objects called *tensors* are governed by the formalism formulated by Ricci & Levi-Civita (1901) and are reviewed for example by Kay (1988) (but it does utilise a slightly outdated notation).

Generally, in geometry, a *metric* tensor can be written down as the invariant infinitesimal space-time interval (or generally a "line element"), $ds^2 = g_{\mu\nu}dx^\mu dx^\nu$, using *Einstein summation convention*, $g_{\mu\nu}$ being a symmetric covariant metric tensor[1]. Note that unlike in non-relativistic physics, spatial distances are not invariant under coordinate transformations nor is there an absolute time! In relativity[2], the invariant quantity to rely upon becomes the infinitesimal space-time interval, ds^2.

Let us first define partial and covariant derivatives in a curved geometry, respectively:

$$\begin{aligned} A_{\mu\nu,\alpha} \equiv \partial_\alpha A_{\mu\nu} &\equiv \frac{\partial A_{\mu\nu}}{\partial x^\alpha} \quad \text{and} \\ A_{\mu\nu;\alpha} \equiv \nabla_\alpha A_{\mu\nu} &\equiv A_{\mu\nu,\alpha} - \Gamma^\tau_{\mu\alpha}A_{\tau\nu} - \Gamma^\tau_{\nu\alpha}A_{\mu\tau} \quad , \end{aligned} \tag{1.1}$$

where we have introduced three new mathematical objects:

1. *Christofel symbol* (generally, the Levi-Civita connection) is not a tensor:

$$\Gamma^\lambda_{\mu\nu} = \frac{1}{2}g^{\lambda\alpha}\left(g_{\mu\alpha,\nu} + g_{\nu\alpha,\mu} - g_{\mu\nu,\alpha}\right), \tag{1.2}$$

   where $g^{\lambda\alpha}$ is the *contravariant* form of the metric.

2. The *Riemann tensor*, $R^\kappa{}_{\lambda\mu\nu}$, defines the curvature of a manifold. It is dependent on the non-commutativity of covariant differentiation and vanishes if the order of two differentiations along different directions is unimportant. With these considerations it can be derived, but here, we simply write it down:

$$R^\kappa{}_{\lambda\mu\nu} \equiv \Gamma^\kappa_{\lambda\nu,\mu} - \Gamma^\kappa_{\lambda\mu,\nu} + \Gamma^\alpha_{\lambda\nu}\Gamma^\kappa_{\mu\alpha} - \Gamma^\alpha_{\lambda\mu}\Gamma^\kappa_{\nu\alpha}. \tag{1.3}$$

3. Contracting the Riemann tensor, which means summing over two of its indices, gives the *Ricci tensor*, $\delta^\mu{}_\kappa R^\kappa{}_{\lambda\mu\nu} = R^\kappa{}_{\lambda\kappa\nu} = R_{\lambda\nu}$. Contracting again gives the *Ricci scalar*, $\delta^\nu{}_\iota g^{\iota\lambda}R_{\lambda\nu} = \delta^\nu{}_\iota R^\iota{}_\nu = R$, where we have used the contravariant metric to raise the tensorial index of the Ricci tensor to prepare it for the contraction. Both of these entities; a rank-2 and a rank-0 tensor, tell us about the properties of the manifold:

$$\begin{aligned} R_{\lambda\nu} &= \Gamma^\kappa_{\lambda\nu,\kappa} - \Gamma^\kappa_{\lambda\kappa,\nu} + \Gamma^\alpha_{\lambda\nu}\Gamma^\kappa_{\kappa\alpha} - \Gamma^\alpha_{\lambda\kappa}\Gamma^\kappa_{\nu\alpha} \\ R &= g^{\lambda\nu}R_{\lambda\nu}. \end{aligned} \tag{1.4}$$

---

[1] We could also take the Minkowski metric of Special Relativity, $\eta_{\mu\nu}$ and treat gravity as a spin-2 field, $h_{\mu\nu}$ on the space described by this metric, but let us leave that for next time.

[2] This is the case in Special (Einstein, 1905) as well as General (Einstein, 1916) Relativity.

With respect to the Ricci scalar, R, we can define an extrinsic curvature of the n-dimensional manifold:

$$K = \frac{R}{n(n-1)} \quad , \tag{1.5}$$

which, taking $n = 4$, describes our universe. For example, Minkowski space gives $K = 0$ and (anti-)de-Sitter space gives $K = \pm 1$. Here we have taken the Minkowskian metric signature of $(+, -, -, -)$. This quantity is related to the spatial 3-d curvature, k that we will briefly discuss below.

The above objects all have interesting symmetries, including the *Bianchi identities* of the Riemann tensor.

Extremising the invariant interval, ds^2 according to the *variational principle* yields the Euler-Lagrange equations of motion in the space described by the metric $g_{\mu\nu}$, which describe so-called *geodesics*, shortest paths through space-time[3]:

$$\frac{d^2x^\mu}{ds^2} + \Gamma^\mu_{\alpha\beta}\frac{dx^\alpha}{ds}\frac{dx^\beta}{ds} = 0 \quad , \tag{1.6}$$

where s is the affine parameter and increases monotonically along the path.

For massless particles these paths must be "null" geodesics, where $ds^2 = 0$. Massive particles travel on *time-like* geodesics, which in our signature convention $ds^2 > 0$ if no external forces act on them. If there exist external forces, massive particles travel on time-like *world-lines*.

1.1.2 Einstein's theory

The fundamental theory of the modern canonical cosmology is defined by the *Einstein field equations*: a set of **nonlinear** coupled partial differential equations for the components of the metric, sourced by the components of the EM tensor. The theory is called *General Relativity* (Einstein, 1916) and it contains the two above-mentioned central objects of the canonical cosmology: the metric and the EM tensor. There exist three central premises for this theory. Firstly, the theory must be coordinate independent or *covariant*. In fact, the so-called *Principle of General Covariance* follows from the *Principle of Equivalence* of gravitation and inertia (e.g. Weinberg, 1972, ch. 4). Secondly, the equation of motion must be made up of terms 2nd order in derivatives of the metric to ensure the equations of gravity not vary with scale (e.g. Weinberg, 1972, ch. 7). And thirdly, the EM tensor must be covariantly conserved, which is only true for all types of matter, if the Einstein tensor (defined below, in eq. 1.16) is also covariantly conserved.

The field equations are derived from the Principle *of Least Action* applied to the so-called Einstein-Hilbert action, by varying the metric, $\delta g_{\mu\nu}$:

$$\delta S = \delta S_{\text{Hilbert}} + \delta S_{\text{“matter”}} = \delta \int d^4x\sqrt{-g}\left(\frac{c^4}{16\pi G}R + \mathcal{L}_{\text{“matter”}}\right) = 0 \quad , \tag{1.7}$$

where the Ricci Scalar, R, gives the Lagrangian density for gravitation (giving the so-called *Hilbert action*),

$$\mathcal{L}_{\text{GR}} = \sqrt{-g}\,R = \sqrt{-g}\,g^{\mu\nu}R_{\mu\nu} \quad , \tag{1.8}$$

---

[3] This equation can also be derived for example by considering a coordinate transformation of the equations of motion of a free particle in Cartesian coordinates, $d^2x^\mu/ds^2 = 0$

$g = \det(g_{\mu\nu})$ is the determinant of the metric tensor (see also Levi-Civita, 1999) and the final expression is called also the *Palatini Lagrangian*.

The $S_{\text{“matter”}}$ variation with respect to the metric gives the EM tensor. One can calculate the conserved *Noether current* resulting from the invariance of the GR action under global coordinate transformations. Such a current yields an energy-momentum tensor, but it turns out not to correspond to observables and does not equal the EM tensor for General Relativity. However the two mathematical objects are indeed related via spatial averaging as is discussed in Maggiore (2007, sec. 2.1.1).
The reason for using the Ricci scalar as the (kinetic term only) Lagrangian is beyond the scope of this thesis and will be discussed another time[4].

The field equations are then:

$$G_{\mu\nu} \equiv R_{\mu\nu} - \frac{1}{2}g_{\mu\nu}R - g_{\mu\nu}\Lambda = \frac{8\pi G}{c^2}T_{\mu\nu} \quad , \tag{1.9}$$

where $G_{\mu\nu}$ is the so-called *Einstein tensor*, which vanishes in a vacuum, $T_{\mu\nu}$ is the energy-momentum (EM) tensor, describing the properties of the contents of the universe and Λ is the cosmological constant, which can be put on the RHS of the equation, absorbed into the EM tensor and treated like a strange kind of matter, which is what we choose in this thesis[5]. From now on, we will deal mostly with so-called *mixed form* tensors, because their components are often simpler and less metric-component-dependent, namely $G^{\mu}{}_{\nu}$ and $T^{\mu}{}_{\nu}$. So, let us write the field equations in a more practical form:

$$\boxed{G^{\mu}{}_{\nu} = 8\pi G T^{\mu}{}_{\nu}} \quad . \tag{1.10}$$

As already mentioned, a result of the symmetries of the Einstein tensor it is covariantly conserved through *Bianchi identities* and the field equations imply local conservation of energy-momentum:

$$G^{\alpha}{}_{\nu;\alpha} = 0 \quad \Rightarrow \quad T^{\alpha}{}_{\nu;\alpha} = 0 \quad . \tag{1.11}$$

Several possible solutions to the field equations have been found. In a spherically symmetric system for example, with a mass at the origin of the coordinates, the Schwarzschild solution holds (Schwarzschild, 1916). This is often used to describe the space around black holes.

1.2 Homogeneous background evolution of the FLRW metric

For a universe following the Copernican principle of spatial *homogeneity* as well as *isotropy* and allowing for curvature of the space-time, the solution to the Einstein field equations is the Friedmann-Lemaitre-Robertson-Walker (FLRW) metric (Friedmann, 1924; Lemaıtre, 1927; Robertson, 1935; Walker, 1935). We will see later that the universe is indeed *spatially* “Copernican” if viewed by a far-sighted, Hubble-sized giant i.e. on the largest scales, the universe is accurately described by this metric. On smaller scales, we will have to deal with small perturbations first, which on their own would not disturb Copernicus, but that will at late times, to our fortune, grow under gravitational instability to the structures that we inhabit today.

---

[4] But we will refer to Lovelock (1972) and Misner et al. (1973) for future reading.

[5] We will also choose to work in natural units from now on, where we set $c = 1$.

Because this thesis is only concerned with a spatially flat, expanding universe, we will not use the most general FLRW metric; we will set the spatial curvature, $k = 0$. We will only be concerned with what could be considered a "temporal curvature"[6], quantified by the scale factor, $a(t)$, which quantifies the expansion of the universe, is normalised to $a(t = t_{\text{today}}) = 1$ and $a(t = 0) = 0$ at the time of the "Big Bang". A spatio-temporally curved metric describing such a space-time manifold as seen by the far-sighted giant can thus be written as:

$$\begin{aligned} ds^2 &= c^2dt^2 - a^2(t)\left(\frac{dr^2}{1-kr^2} + r^2d\theta^2 + r^2\sin^2(\theta)d\phi^2\right) \\ &= dt^2 - a^2(t)\left(\frac{dr^2}{1-kr^2} + r^2d\Omega\right) \end{aligned} \tag{1.12}$$

with $c = 1$ being the speed of light in natural units and $x^i \in \{r, \theta, \phi\}$ the standard 3-dimensional spherical coordinates with $d\Omega$ being the solid angle[7].

The metric in eq. 1.12 already assumes many properties for the spacetime it describes. Namely, it is clear that the metric is symmetric, moreover the off-diagonal components equal zero. Note also that the so-called *metric signature* we have chosen here is *Minkowskian*, i.e. the spatial part of the metric is negative. Had we chosen the temporal term in the metric to be negative, this would not have changed our calculations at all.

Note that, in terms of components, for example, the flat, spatially homogeneous and isotropic metric in Cartesian coordinates can can be written in component form:

$$g_{\mu\nu} = \begin{pmatrix} 1 & 0 & 0 & 0 \\ 0 & -a^2(t) & 0 & 0 \\ 0 & 0 & -a^2(t) & 0 \\ 0 & 0 & 0 & -a^2(t) \end{pmatrix} \quad , \tag{1.13}$$

alternatively, $g_{\mu\nu} = \text{diag}(1, -a^2(t), -a^2(t), -a^2(t))$, with the conjugate, contravariant form being $g^{\mu\nu} = \text{diag}(1, -a^{-2}(t), -a^{-2}(t), -a^{-2}(t))$, whereas as a line element it becomes:

$$ds^2 = dt^2 - a^2(t)\delta_{ij}dx^i dx^j \quad , \tag{1.14}$$

where δ_{ij} can be regarded as the Kroenecker delta, but also as the flat, 3-d *Euclidean metric* representing the spatial components of the full metric. As here, in most of this thesis, we set $k = 0$, thereby choosing a flat universe, which is a good assumption as the curvature has been measured to be close to zero (e.g. Komatsu et al., 2011)! However, if $k > 0$, the curvature is positive and the universe is finite or *closed*. Conversely, if $k < 0$, we get a hyperboloid space with negative curvature, which is infinite or *open*. However, for a little while, we keep k in our equations for the sake of generality. Here r is *comoving*, meaning that the corresponding physical distance, $\boldsymbol{x} = a(t)\boldsymbol{r}$. The 4-d coordinates can generally be denoted as $x^\mu \in \{t, r, \theta, \phi\}$.

Actually, this thesis will only be interested in the contents of the energy-momentum tensor. We will use the results from this section throughout the work, but we will leave the more subtle considerations of geometry for next time.

---

[6] Briefly, in *conformal coordinates*, i.e. using conformal time, η as the time coordinate, without spatial curvature, the space-time interval in Cartesian spatial coordinates with setting $c = 1$ (natural units) becomes $ds^2 = a^2(\eta)\left(d\eta^2 - dx^2 - dy^2 - dz^2\right)$. In fact, if we set $a(\eta) = 1$, thus ignoring the "temporal curvature" (extrinsic curvature), we obtain the Minkowski metric, which is used in *Special Relativity* and contains the Euclidean metric to describe space, plus an extra time-like dimension.

[7] Sometimes defined as $d\Omega^2 = d\theta^2 + \sin^2(\theta)d\phi^2$ in literature.

1.2.1 The Friedmann equations

Let us now attempt to solve Einstein eqns for homogeneous, isotropic, curved (for generality) metric. Using the FLRW metric from eq. 1.12 and finding its Ricci tensor and scalar using eq. 1.4,

$$\begin{aligned} R^{\mu}{}_{\nu} &= \mathrm{diag}(R^{0}{}_{0}, R^{i}{}_{j}) = \mathrm{diag}\left(-3\frac{\ddot{a}}{a},\ \delta_{ij}\left[\frac{\ddot{a}}{a}+2\frac{\dot{a}^2}{a^2}+2\frac{k}{a^2}\right]\right) \\ R &= -6\left(\frac{\ddot{a}}{a}+\frac{\dot{a}^2}{a^2}+\frac{k}{a^2}\right) \quad , \end{aligned} \tag{1.15}$$

we can try to solve the field equations (eq. 1.10) for the individual metric components, which are parametrised by the time dependent scale factor, $a(t)$ and the spatial curvature, k. Note that we use the Latin alphabet to denote spatial indices only going as $i \in \{1,2,3\}$ and dots denote derivatives with respect to time, i.e. $\dot{a} \equiv (\partial a/\partial t) \equiv \partial_0 a \equiv a_{,0}$.

We can now find the LHS of the field equations; we can calculate the purely temporal, 00, and the spatial, ij, components of the Einstein tensor in mixed form[8]:

$$G^{\mu}{}_{\nu} \equiv R^{\mu}{}_{\nu} - \frac{1}{2}\delta^{\mu}{}_{\nu}R \quad , \tag{1.16}$$

having moved the Λ term over onto the RHS of the field equations, into the EM tensor.

However, in order to solve the field equations, we need to find the appropriate EM tensor. As a first guess, it is convenient to assume that the "matter" described by this tensor behaves like a **perfect fluid** and hence, the mixed form EM tensor gains the form of[9]:

$$T^{\mu}{}_{\nu} = (\rho + P)U^{\mu}U_{\nu} - P\delta^{\mu}{}_{\nu} \quad , \tag{1.17}$$

ρ and P being the energy density and pressure and $U^{\mu} = dx^{\mu}/\sqrt{-ds^2}$ being the 4-velocity, usually $U^{\mu} = \mathrm{diag}(1, v^i)$ for massive particles generally and $U^{\mu} = \mathrm{diag}(1,0,0,0)$ in the rest frame of the fluid particles. For this reason we can simplify the EM tensor of a perfect fluid to $T^{\mu}_{\nu} = \mathrm{diag}(\rho, -\delta_{ij}P)$, which remains useful in other frames, because it transforms as a tensor. In fact, this is by far not a very general EM tensor, but it is a reasonable assumption in most regimes relevant for cosmology, because all the major components happen to behave as perfect fluids *on large scales*. However, going back in time, as the temperature increases, there exist regimes in the extreme, early universe, where a more general matter Lagrangian, $\mathcal{L}_{\text{“matter”}}$ must be used. The most general meaning the full Lagrangian, describing all the fields and interactions of the Standard Model (SM) of particle physics. In intermediate regimes, we can use the full **phase space** (momentum-position) distribution for only a few individual particle species, which we do in sec. 2.2.4.

We can now write down the Einstein field equations, where the universe is spatially homogeneous, isotropic and filled with a single (or dominant) perfect fluid, for now assuming

---

[8] Noting that for any metric $g^{\mu\alpha}g_{\alpha\nu} = \delta^{\mu}{}_{\nu} = \delta^{\mu\nu} = \delta_{\mu\nu}$, the Kroenecker delta.

[9] Derivation may be found in Landau & Lifshits (1975).

that ρ and P are global, but time dependent properties of the fluid:

$$G^0{}_0 = 3\frac{\dot{a}^2}{a^2} + 3\frac{k}{a^2} = 8\pi G\rho \tag{1.18}$$

$$\begin{aligned} G^i{}_j &= \delta_{ij}\left(\frac{\ddot{a}}{a} + 2\frac{\dot{a}^2}{a^2} + 2\frac{k}{a^2}\right) - 3\delta_{ij}\left(\frac{\ddot{a}}{a} + \frac{\dot{a}^2}{a^2} + \frac{k}{a^2}\right) \\ &= \delta_{ij}\left(-2\frac{\ddot{a}}{a} + \frac{\dot{a}^2}{a^2} + \frac{k}{a^2}\right) = -8\pi G\delta_{ij}P \quad , \end{aligned} \tag{1.19}$$

which can be rearranged in the following way to obtain the equation of motion for the FLRW universe:

$$\text{eq. 1.18} \Rightarrow \quad \boxed{\left(\frac{\dot{a}}{a}\right)^2 = \frac{8\pi G}{3}\rho - \frac{k}{a^2}} \quad , \tag{1.20}$$

$$\text{eq. 1.19 \& eq. 1.18} \Rightarrow \quad \boxed{\frac{\ddot{a}}{a} = \frac{4\pi G}{3}(\rho + 3P)} \quad . \tag{1.21}$$

These are called the **Friedmann** and **acceleration** equations and can be combined into a conservation (**fluid** or **continuity**) equation, which also directly follows from the EM conservation, $T^{\alpha}_{\nu;\alpha} = 0$; the component with $\nu = 0$:

$$\text{eq. 1.11} \quad \Rightarrow \quad \boxed{\dot{\rho} + 3\frac{\dot{a}}{a}(\rho + P) = 0} \quad , \tag{1.22}$$

which is valid for individual components, x, of the "matter" in the universe as well as for the total density of all "matter" combined.

1.2.2 Redshift

As briefly mentioned in the sec. 1.1.2, massless particles travel on 'null' geodesics. These geodesics change with time however, due to the expansion of space. We would like to described the changes in the characteristics of the massless particles (namely photons) induced by this expansion. For this reason, we define the 4-momentum for massless particles[10]:

$$P^{\mu} \equiv \frac{dx^{\mu}}{ds} \quad , \tag{1.23}$$

where s is still the affine parameter and the 4-momentum components are $P^{\mu} = (E, p^i)$, where p^i is the physical momentum.We also note that

$$\frac{d}{ds} = \frac{dx^0}{ds}\frac{d}{dx^0} = E\frac{d}{dt} \quad , \tag{1.24}$$

from the definition of the 4-momentum. We know that the magnitude of the 4-momentum for massless particles is zero (e.g. Peiris, 2009) and therefore,

$$\begin{aligned} |P|^2 = P^{\mu}P_{\mu} &= g_{\mu\nu}P^{\mu}P^{\nu} \\ &= E^2 - a^2\delta_{ij}p^i p^j = 0 \\ \Rightarrow |p|^2 &= E^2 a^{-2} \quad , \end{aligned} \tag{1.25}$$

---

[10] *Nota bene* that this and sec. 2.2.4 are the only sections in this thesis, where P denotes momentum and in most of the rest of the work, P will always stand for pressure.

where we have defined the magnitude of the *comoving* 3-momentum vector in flat space as $|p|^2 = \delta_{ij}p^ip^j$, because we consider only flat space, $k = 0$ and therefore the spatial metric is Euclidean, δ_{ij}. We now use these results to calculate the 0^{th} component of the geodesic equation (eq. 1.6) for a massless particle:

$$\begin{aligned} 0 &= E\frac{dP^0}{dt} + \Gamma^0_{ij}p^ip^j \\ &= E\frac{dE}{dt} + \dot{a}a\,|p|^2 \\ \Rightarrow \qquad 0 &= \frac{1}{E}\frac{dE}{dt} + \frac{\dot{a}}{a} \qquad , \end{aligned} \tag{1.26}$$

and so

$$E \propto \frac{1}{a} \qquad , \tag{1.27}$$

meaning that as $a \to \infty$, $E \to 0$ i.e. as the universe expands, massless particles loose energy. We know from quantum mechanics that the energy of photons, $E = \lambda^{-1}$, where λ is the wavelength and we are using natural units ($c = \hbar = 1$). This means that the expansion of the universe stretches the wavelength of photons linearly, $\lambda \propto a$ and we can define a "redshift":

$$z \equiv \frac{\lambda_{\text{observed}} - \lambda_{\text{emitted}}}{\lambda_{\text{emitted}}} = \frac{a_{\text{observed}} - a_{\text{emitted}}}{a_{\text{emitted}}} \tag{1.28}$$

and assuming we observe this photon today, when $a = 1$ then

$$\boxed{a_{\text{emitted}} = \frac{1}{1+z}} \qquad . \tag{1.29}$$

1.2.3 Distances

Let us finally take the opportunity here to discuss the cosmological horizons, in reference to Mukhanov (2005, ch. 2) and Hogg (1999). A *comoving* distance is the distance between points on an imaginary comoving grid, which expands together with the universe. In order to convert it to a physical or *proper* distance, we must multiply by the scale factor, a. We have used $x^1 = r$, the comoving distance, which makes $\boldsymbol{x} = a(t)\boldsymbol{r}$ for example, a proper distance. Because a distance is a shortest path between two points, which can be characterised by photon paths through space, we can set $ds^2 = 0$ and integrate eq. (1.14) to find a distance:

$$r = \int_0^r d\tilde{r} = \int_{t_{\text{init}}}^t \frac{dt}{a(t)} \qquad , \tag{1.30}$$

where we have chosen to integrate along the path of the photon (i.e. we've set dr parallel to the path, setting the angular part of eq. (1.14). This is the first time we have made a choice of coordinates, but we will do this once again in the next section, in the context of perturbation theory. Noting eq. (1.33), we can re-write the above equation in therms of the Hubble parameter:

$$r = \int_{a_{\text{init}}}^a \frac{da}{aH} \qquad . \tag{1.31}$$

Since a is dimensionless, we can now note that in terms of units, $[r] = [cH^{-1}] = [ct_H]$ and in recent times, when $a \sim 1$, it is also the case that $r \sim H^{-1}$, where as before we set $c = 1$. This defines a so-called *Hubble scale*, $r_H = H^{-1}$ and the *Hubble time*, t_H. The Hubble scale can be interpreted to characterise the size of the local inertial frame (Mukhanov, 2005, p.40), because it is of the order of the 4-curvature, K. We can see this by looking at equations (1.5) and (1.15), considering only regimes, where the acceleration of the expansion of the universe is small.

Secondly, taking into account the finiteness of the age of the universe, $t_{\text{age}} \approx 15\,\text{Gyrs}$, we should realise, that the maximal distance light could have travelled from its starting point is also finite. For this reason we can define horizons. The *particle horizon* is said to define volume in the universe from which we can receive information. Without taking into account the expansion of the universe a rough guess of the size of the particle horizon might then be $t_{\text{age}}c \approx 15$ million light years. In order to calculate the horizon at time, t more precisely, one should integrate the following over the different eras of expansion from the section above:

$$r(t) = \int_{a=0}^{a(t)} \frac{da}{aH(a)} \quad . \tag{1.32}$$

In the following sections, we will refer to a “Hubble horizon” several times. By this we will simply mean that we are approximating the particle horizon by the Hubble scale, because the exact value is not relevant to our calculations.

1.3 Contents of the universe: ΛCDM

So far we have only spoken abstractly of the EM tensor, density and pressure of the perfect-fluid-like “matter” in the universe. We should now discuss the three main substances: relativistic “matter” or **radiation**, non-relativistic pressureless **matter** and the strange **cosmological constant** in order to describe the dynamics of the universe[11].

As suggested in sec. 1.1.2, we will consider the geometry to conform to standard GR and classify the **cosmological constant** as a substance and as a part of the EM tensor. There is a large volume of research concerned with the nature of this substance (see for e.g. Carroll (2003); Padmanabhan (2008); Amendola et al. (2012); Carroll (2001); Li et al. (2012); Perlmutter et al. (1999); Riess et al. (1998)). It is more generally known as *dark energy*, which implies a wider variety of possible properties. Even more general is *quintessence*, which allows for a time varying equation of state. *Modified gravity* on the other hand leaves the unknown strangeness on the geometry side of the field equations. Finally, some believe that the observed accelerated expansion of the universe is an illusion due to the incorrect use of the homogeneous FLRW metric in a nonlinearly inhomogeneous universe, known as *backreaction*. We will leave the discussion of this dark riddle for some other time.

The substance central to this thesis is **dark matter** (DM). We will not discuss the evidence for its existence, since this is one of our primary assumptions, but we will mention the work of Zwicky (1933), who was one of the first to discover the necessity for an unseen source of gravity to explain the dynamics of observed luminous objects within the framework of General Relativity. Much further evidence exists, among which the previously discussed Cosmic Microwave Background anisotropy contributes strongly. All this is discussed in many

---

[11] References for much of this and other chapters are Bergström *&* Goobar (2006); Börner (2004); Dodelson (2003); Kolb *&* Turner (1994); Mukhanov (2005); Peacock (1998); Peebles (1993).

papers, reviews and books, we refer the reader to the extensive review of Bertone et al. (2005), for example. We discuss in some detail the thermodynamics of particle species of DM in the next chapter. Let us for now treat it in the simplest way possible, as made up of heavy particles at rest with respect to the coordinate grid and as absolutely non-interacting. This means that it is completely pressureless.

Baryons are often treated either as radiation or as dark matter in the cosmological context, but we will not concern ourselves with details about baryon physics at this stage either.

1.3.1 Evolution of energy density

The Friedmann eq. (1.20), acceleration eq. (1.21) and fluid eq. (1.22) can be solved if the total density, $\rho_{\text{tot}} = \sum_x \rho_x$ and pressure, $P_{\text{tot}} = \sum_x P_x$, are known[12]. Most simply, if a single species, x has a much larger density, ρ_x than all the others combined. For convenience, we introduce the following functions of the scale factor, a:

$$\begin{aligned} &\text{the Hubble parameter:} && H(a) = \frac{\dot{a}}{a} \\ &\text{the critical density for flatness, } k=0\text{:} && \rho_{\text{crit}}(a) = \frac{3H^2}{8\pi G} \\ &\text{the density parameter for species } x\text{:} && \Omega_x(a) = \frac{\rho_x(a)}{\rho_{\text{crit}}(a)} \quad . \end{aligned} \tag{1.33}$$

Having assumed the cosmological constant, Λ into the EM tensor in sec. 1.1.2, we can define its density parameters. In analogy we can define density parameters for the curvature, although they don't have a very physical meaning:

$$\rho_\Lambda = \frac{\Lambda}{8\pi G} \quad \& \quad \Omega_\Lambda(a) = \frac{\rho_\Lambda(a)}{\rho_{\text{crit}}(a)} = \frac{\Lambda}{3H^2} \tag{1.34}$$

$$\rho_{\text{k}}(a) = -\frac{3k}{8\pi G a^2} \quad \& \quad \Omega_{\text{k}}(a) = \frac{\rho_{\text{k}}(a)}{\rho_{\text{crit}}(a)} = -\frac{k}{H^2 a^2} \quad . \tag{1.35}$$

From now on, we assume a flat universe for simplicity and since the principles explored in this thesis are not deeply connected to the curvature of space. Thus we set $k = \rho_{\text{k}} = \Omega_{\text{k}} = 0$.

In the previous section we've shown that the equation of state for species x can be written down as $w_x = P_x/\rho_x$. We can rewrite the fluid (eq 1.22) as:

$$\dot{\rho}_x + 3H\rho_x(1 + w_x) = 0 \quad . \tag{1.36}$$

For **radiation**, $w_{\text{r}} = 1/3$ and we find the solution:

$$\boxed{\rho_{\text{r}}(a) = \rho_{\text{r},0}a^{-4}} \quad , \tag{1.37}$$

where $\rho_{x,0} = \rho_x(a = 1)$ is the density of species x today. For pressureless **matter** $w_{\text{m}} = 0$ and so:

$$\boxed{\rho_{\text{m}}(a) = \rho_{\text{m},0}a^{-3}} \quad . \tag{1.38}$$

---

[12] Note that ρ_x and P_x are not tensors. The index x merely implies a species of "matter". Secondly, beware that P_x is the pressure of species x, p^i is the 3-momentum and P^μ is the 4-momentum of a single particle.

Finally, the **cosmological constant** has the equation of state $\boxed{w_\Lambda = -1}$, which we can see from the following consideration, keeping in mind that it must remain a constant with time and therefore with a and so ρ_Λ must be constant too (eq. 1.34):

$$\rho_\Lambda(a) = \rho_{\Lambda,0} a^{-3(1+w_\Lambda)} = \rho_{\Lambda,0} \quad . \tag{1.39}$$

In the generalised case of dark energy, this equation of state parameter can be $w_{\mathrm{de}} \neq -1$.

1.3.2 The eras of evolution: radiation, matter and Λ domination

We wish to solve eq. 1.20 to understand how the scale factor evolves with time, t. If species x dominates the dynamics, $\rho_x \gg \rho_y$ (for all $y \neq x$) and so $\rho_{\mathrm{tot}}(a) \sim \rho_x(a)$. In such a case the Friedmann equation can be solved easily. We can find the eras of time, when each of the three species dominates[13]:

$$\begin{array}{rcl}
\textbf{Big Bang:} & & \Rightarrow \boxed{a_0 \sim 0} \\
\textbf{R.D.:} & \rho_{\mathrm{r}}(a) \gg \rho_{\mathrm{m}}(a) \iff \Omega_{\mathrm{r}}(a) \gg \Omega_{\mathrm{m}}(a) & \Rightarrow \boxed{a_{\mathrm{r.d.}} \ll \Omega_{\mathrm{r},0}/\Omega_{\mathrm{m},0}} \\
\textbf{M.D.:} & \rho_{\mathrm{m}}(a) \gg \rho_\Lambda \iff \Omega_{\mathrm{m}}(a) \gg \Omega_\Lambda & \Rightarrow \boxed{a_{\mathrm{m.d.}} \ll (\Omega_{\mathrm{m},0}/\Omega_\Lambda)^{1/3}} \\
\textbf{today:} & & \Rightarrow \boxed{a_{\mathrm{today}} \sim 1} \quad ,
\end{array} \tag{1.40}$$

where we have already assumed that $0 < \Omega_{\mathrm{r},0} < \Omega_{\mathrm{m},0} < \Omega_\Lambda$, which we know from observations that we will briefly discuss in sec. 2.2.1 (also Larson et al., 2011). Note also that the time, t_{eq} when $\Omega_{\mathrm{m}}(a_{\mathrm{eq}}) = \Omega_{\mathrm{r}}(a_{\mathrm{eq}})$ is often called the *time of equality.*

With this in mind we can finally return to the Friedmann equation (eq. 1.20) and by using eq. 1.33, rewrite it as:

$$\begin{aligned} H^2 &= \frac{8\pi G}{3} \sum_x \rho_x(a) \\ \Rightarrow 1 &= \sum_x \Omega_x(a) \qquad \text{as well as} \qquad (1.41) \\ \Rightarrow H^2 &= \frac{8\pi G}{3} \left(\rho_{\mathrm{r},0} a^{-4} + \rho_{\mathrm{m},0} a^{-3} + \rho_\Lambda \right) \end{aligned} \tag{1.42}$$

where the curvature parameter, $k = 0$ and $H_0 \equiv H(a = 1)$. Therefore eq. 1.20 can also be written as

$$\boxed{H^2 = H_0^2 \left(\Omega_{\mathrm{r},0} a^{-4} + \Omega_{\mathrm{m},0} a^{-3} + \Omega_\Lambda \right)} \quad , \tag{1.43}$$

where the present time Hubble parameter is often written as $H_0 = 100h\,\mathrm{km\ s^{-1}\,Mpc^{-1}}$ for historical reasons (e.g. Overbye, 1991). The dimensionless Hubble parameter is today known to have the value of around $h = 0.71$ (Komatsu et al., 2011).

---

[13] *Nota bene* that $\Omega_{x,0} = \rho_{x,0}/\rho_{\mathrm{crit},0} \neq \rho_{x,0}/\rho_{\mathrm{crit}}(a)$ and $\Omega_x(a) = \rho_x(a)/\rho_{\mathrm{crit}}(a) \neq \rho_x(a)/\rho_{\mathrm{crit},0}$!

This equation can be solved to obtain

$$\begin{aligned}
&\textbf{R.D.:} && \boxed{a_{r.d.} \approx t^{1/2}\left(H_0^2\Omega_{\mathrm{r},0}\right)^{1/4}} \\
&\textbf{M.D.:} && \boxed{a_{m.d.} \approx t^{2/3}\left(H_0^2\Omega_{\mathrm{m},0}\right)^{1/3}} \\
&\textbf{de Sitter space} \text{ or } \mathbf{\Lambda}\textbf{.D.:} && \boxed{a_{\Lambda.d.} \approx \exp\left\{t\sqrt{H_0^2\Omega_\Lambda}\right\}} \quad ,
\end{aligned} \tag{1.44}$$

having used that $a(t = 0) = 0$ in the integration. The fate of the universe can be deduced from these equations.

1.3.3 Thermodynamics

In the previous sections we have made the simplifying assumption that the only relevant thermodynamical properties of matter in calculating the dynamics of spacetime are *density* and *pressure*. This is indeed almost certainly a good assumption in many cases. For example, the large scale distribution of matter can for the most part be described in terms of the perfect fluid approximation, because we can neglect particle **free-streaming** and diffusion (Liddle *&* Lyth, 1993). Let us now find the relationship between density and pressure and justify the perfect fluid assumption.

The requirement for *local thermodynamic equilibrium* (LTE) in an expanding universe is that the interaction rate between the particles (often denoted by $\Gamma(t)$) must be much greater than the rate of the expansion of the universe, $H(t)$. For a relativistic ($m_x \ll T_{\mathrm{D}}$) or non-relativistic ($m_x \gg T_{\mathrm{D}}$) species that decouples from the *heat bath*[14] while still in equilibrium, the distributions function remains self-similar with expansion. This is not the case with semi-relativistic species for which $m_x \sim T_{\mathrm{D}}$. Fortunately not many cosmologically relevant species fall into the last category.

A perfect fluid

A perfect fluid fully characterised by $\rho(\boldsymbol{x}, t)$, $S(\boldsymbol{x}, t)$ and $\boldsymbol{V}(\boldsymbol{x}, t)$, its energy density distribution, its entropy per unit mass and its vector field of 3-velocities (see also ch. 6 of Mukhanov, 2005). Assuming that it is in *thermal equilibrium* gives the *equation of state* for the perfect fluid, which describes the relationship between these three quantities: $P = P(\rho, S)$. Taylor expanding the perturbed pressure to linear order,

$$P_0 + \delta P = P(\rho + \delta\rho, S + \delta S) \quad , \tag{1.45}$$

yields the familiar

$$\delta P = c_{\mathrm{s}}^2\delta\rho + \sigma\delta S \quad , \tag{1.46}$$

where clearly

$$c_{\mathrm{s}}^2 \equiv \left.\frac{\partial P}{\partial\rho}\right|_S \quad \text{and} \quad \sigma \equiv \left.\frac{\partial P}{\partial S}\right|_\rho \quad . \tag{1.47}$$

---

[14] The gas of species that are still interacting with each other.

The additional assumption that the matter in the universe can be described as an *adiabatic* perfect fluid, means that $\delta S = 0$, i.e. no perturbations in the total entropy. This results in that for a perfect fluid, to linear order, $w \approx c_{\mathrm{s}}^2$. The assumption of adiabaticity in an expanding volume is correct for a species in true thermal equilibrium, which can be shown by the consideration of the first and second laws of thermodynamics (see for example sec. 3.4 in Kolb *&* Turner, 1994).

Then, for the linear but **nonrelativistic** case, $P \ll \rho c^2$ and the speed of sound, $c_{\mathrm{s}} \ll c$ and effectively $\mathbf{w_{\mathrm{m}} \approx 0}$.

In everyday, Newtonian physics, the pressure, P, depends on the 3-velocity via the *Euler equation*, which describes movement of fluid in a gravitational potential (Mukhanov, 2005, p.267, eqn. 6.8) and the gravitational potential, ϕ, depends on ρ via the *Poisson equation*, which describes how mass sources the gravitational potential (Mukhanov, 2005, eqn. 6.10). Together with the *continuity equation*, which describes how matter flows and *conservation of entropy*, which describes the conservation of entropy if we neglect dissipation (Mukhanov, 2005, eqns. 6.3 and 6.9), these five equations form a complete set of equations describing a perfect fluid.

The Euler equation, the continuity equation and conservation of entropy all emerge from the conservation of the energy-momentum tensor, which is a consequence of intrinsic property called the *Bianchi identity* that emerges from the symmetries of the Riemann curvature tensor that we encountered in the previous sections. The Poisson equation is a combination of the $0-0$ and the integrated $0-i$ component of the perturbed Einstein field equations. Such perturbed equations will be described in the next chapter. The equation of state is the only equation here that does not directly emerge from Einstein's theory, but requires the assumption of the *ideal gas* (perfect fluid).

Phase space distribution

In order to see what happens in the relativistic case, we must extend our analysis to the phase space[15] distribution of particles of our perfect fluid. Generally, for a spatially homogeneous weakly-interacting fluid of particles with g internal *degrees of freedom*, we write down (Kolb *&* Turner, 1994, sec. 3.3):

$$\begin{aligned} \rho &= \frac{g}{(2\pi)^3}\int E(p_i) f_0(p_i)dp_i \\ P &= \frac{g}{(2\pi)^3}\int \frac{|p|^2}{3E} f_0(p_i)dp_i \quad , \end{aligned} \tag{1.48}$$

where $p^i = dx^i/ds$ is the physical momentum as defined in the previous section (eq 1.23), f_0 is the homogeneous one-particle phase space distribution function and $E = P^0$ is the energy of the particles of the fluid. As before, we can calculate the magnitude of the 4-momentum,

$$|P|^2 = P_\mu P^\mu = E^2 - a^2|p|^2 = m^2 \quad , \tag{1.49}$$

$|p|^2 = \delta_{ij}p^i p^j$ being the magnitude of the physical momentum and m being the mass of the particles making up the fluid and as always, the speed of light $c = 1$. Neglecting for the

---

[15] The phase space for a system of N particles is the 6N-dimensional space of positions and momenta of all the particles.

moment the expansion of the universe[16], $a = 1$, this yields the familiar expression:

$$E^2 = |p|^2 + m^2 \qquad . \tag{1.50}$$

In thermal equilibrium, the phase space function is given by either the *Fermi-Dirac* or *Bose-Einstein distribution*, depending on whether the particles are *fermions* or *bosons* respectively:

$$f_0(p_i) = \frac{1}{\exp\{(E-\mu)/T\} \pm 1} \qquad , \tag{1.51}$$

where T is the temperature of the gas of fermions $(+1)$ or bosons (-1) and μ is its chemical potential.

For a **relativistic** gas of either fermions or bosons not interacting chemically ($T \gg \mu$), inserting eq. (1.51) into eq. (1.48) yields the equation of state $\mathbf{w}_\mathrm{r} = \mathbf{1/3}$, since relativistic means that $T \gg m$, yielding $P = \rho/3$. Not spending too much time on the details let us also mention that from the above equations one finds that for a *non-degenerate*[17] relativistic species of matter, the energy density also found from multiplying the number density of particles by the average energy per particle, $\langle E \rangle$ is

$$\rho \propto n \langle E \rangle \propto g T^4 \qquad . \tag{1.52}$$

In fact, in a universe dominated by relativistic species, we can characterise the temperature by referring to the energy densty (or vice versa):

$$\rho_\mathrm{r} = \frac{\pi^2}{30} g_* T^4 \qquad , \tag{1.53}$$

where we have replaced the number of the degrees of freedom, g for different species by the summation over all the relativistic species, n to get the effective *number of relativistic degrees of freedom*:

$$g_*(T) = \sum_x^{\text{bosons}} g_x \left(\frac{T_x}{T}\right)^4 + \frac{7}{8} \sum_x^{\text{fermions}} g_x \left(\frac{T_x}{T}\right)^4 \qquad . \tag{1.54}$$

The factor of $7/8$ arises from simplifying eq. (1.48) for a relativistic fermion species. Note that this equation is different in characterising the relation between pressure and temperature if the contribution of non- and semi-relativistic species is significant.

We have already shown that for a nonrelativistic gas the equation of state is vanishing, but let us note here that the expressions in eq. (1.48) simplify the same way regardless of whether the gas is made up of bosons or fermions.

We will use these results in the sec. 1.3.1 and revisit the phase space distribution without assuming homogeneity in sec. 2.2.4.

1.3.4 Decouplings and the evolution of temperature

We have shown in sec. 1.3.3 the intuitive rule that temperature falls with density as the universe expands. Similarly, the rate for the any kind of interaction, $\Gamma_{\mathrm{int},x} \equiv n_x \langle \sigma_{\mathrm{int},x} |v_x| \rangle$,

---

[16] Alternatively, we can specify that we are stating our equations in this section in a comoving frame.

[17] A degenerate form of matter is the counterpart to the perfect fluid and it implies that all particles are in the lowest possible energy state.

which depends on the number density of the interacting particles, n, the interaction cross-section, σ and the particle speed, $|v|$, decreases with the expanding universe. This leads to three important thermodynamic events for any particle species (see also Kolb & Turner, 1994, ch. 3 and 5), assuming of course that it is completely stable, i.e. that it does not decay into other species:

Decoupling from the heat bath, when a species no longer is in local thermodynamic equilibrium. This means it no longer interacts with the other species in the heat bath and therefore does not receive the transference of entropy from other species. This means that its temperature is no longer related to the number of relativistic degrees of freedom, g_*, but rather redshifts as $T_x \propto 1/a$. Specifically, in the adiabatic early universe it can be shown that before decoupling, the entropy, $S = g_* T^3 a^3 = \text{const.}$, meaning that $aT \propto g_*^{-1/3}$ (T being the temperature of the heat bath). Once decoupled, by considering the equilibrium distribution we can show that:

$$T_x = \begin{cases} T_{\mathrm{D},x}(a_{\mathrm{D},x}/a) & \text{ultra-relativistic,} \quad E_\mathrm{k} \propto E \propto 1/a \\ T_{\mathrm{D},x}(a_{\mathrm{D},x}/a)^2 & \text{non-relativistic,} \quad E_\mathrm{k} \propto |p|^2 \propto 1/a^2 \end{cases} \quad . \tag{1.55}$$

The temperature, T_D at the time of decoupling, t_D therefore fully determines the temperature of the species in the future and depends entirely on the number of relativistic degrees of freedom and the scale factor at decoupling via:

$$a_\mathrm{D} T_{\mathrm{D},x} \propto \frac{1}{g_*^{1/3}(t_{\mathrm{D},x})} \quad . \tag{1.56}$$

Since g_* decreases with time as more and more species in equilibrium become nonrelativistic, an early decoupling means that the temperature of the species, T_x will be low. Such is the assumption in ΛCDM; cold dark matter is defined by its low temperature and hence early decoupling. On the other hand massive neutrinos are one of the last species to decouple from the photon-baryon plasma. For this reason they can be considered *hot dark matter* (HDM). Any species with properties between these two extremes is considered to be *warm dark matter* (WDM).

The phase space distribution function for a species that **decoupled while relativistic and in equilibrium** is given by eq. (1.51).

Freeze-out is characterised by the cessation of the processes that keep a matter species in thermal equilibrium with itself[18]. Similarly to the case of LTE, if a species is in equilibrium with itself when it becomes nonrelativistic, its abundance is exponentially suppressed. This reflects the fact that the species' abundance, Ω_x is determined by its time of freeze-out. The important factors in calculating the freeze-out time are the particle mass, the cross-section for annihilation in the case of a so called *cold relic*. However in the case of a *hot* or *warm relic*, these factors are irrelevant and the abundance can be calculated from the effective number of relativistic degrees of freedom at freeze-out, $g_{*,\mathrm{fo}}$, the particle mass for the species, m_x and the effective number of the degrees of freedom for the species, g_x (Kolb & Turner, 1994, eq. 5.31):

$$\Omega_x h^2 \approx 70 \left[\frac{g_x}{g_{*,\mathrm{fo}}}\right] \left(\frac{m_x}{\mathrm{keV}}\right) \quad . \tag{1.57}$$

---

[18] In other words, the species decouples from itself, but this process is not known as decoupling to avoid confusion.

We meet this equation again in sec. 2.3.3. Let us just note here that a $m_x \sim$ keV weakly interactive particle would match the measured abundance, if it froze out when $g_{*,\mathrm{fo}} \sim 500 g_x$.
In this thesis, we assume that we know this abundance to be as measured by the WMAP satellite (Dunkley et al., 2009), which we discuss a bit more in the next chapter (sec 2.2.1).

Becoming nonrelativistic means that the temperature of the species, T_x drops to $T_x \ll m_x$. A transfer of entropy that can heat up the heat bath occurs if a massive species becomes nonrelativistic while still in LTE and therefore its density becomes exponentially suppressed, $n \propto \exp(-m/T)$. This can be calculated from eq. (1.48) for nonrelativistic particles. We consider the effects of particles that become nonrelativistic later than regular CDM in sec. 2.3.3.

It is important to note that even though many simplifications can be made, in order to treat the process of decoupling and other non-equilibrium dynamics, one should use the full, covariant Boltzmann equation to describe the evolution of the phase space distribution function, $f(P^\mu, x^\mu)$:

$$\hat{L}[f] = C[f] \quad , \tag{1.58}$$

where $\hat{L}$ is the Liouville operator in the nonrelativistic case becomes:

$$\hat{L}_{\mathrm{nr}} = \frac{d}{dt} + \boldsymbol{v} \cdot \boldsymbol{\nabla}_x + \frac{\boldsymbol{F}}{m} \cdot \boldsymbol{\nabla}_c \quad , \tag{1.59}$$

and in the fully covariant, relativistic case:

$$\hat{L} = P^\mu \frac{\partial}{\partial x^\mu} - \Gamma^\mu{}_{\nu\kappa} P^\nu P^\kappa \frac{\partial}{\partial P^\mu} \quad , \tag{1.60}$$

where $\Gamma^\mu{}_{\nu\kappa}$ is now as previously the Christoffel symbol. We revisit the Boltzmann equation in sec. 2.2.4.

The matter distribution in our universe starts out almost completely uniform, but in the era of gravitation, gravitational instability amplifies initial tiny fluctuations into structure. This is the topic of the next two chapters.

CHAPTER 2

The Early, Linear Structure

In the previous chapter we considered the time-varying, spatially-flat, absolutely homogeneous and isotropic FLRW metric (eq 1.14) as a solution to the nonlinear Einstein field equations (eq 1.10). We found the equations for the dynamics of our spacetime (eq 1.44) by solving for the components of the spatially constant FLRW metric.

This is a relatively straightforward solution to the field equations, but it is far from most general. As in many systems of equations, the perturbative approach can be attempted to solve the field equations in the local case, where the components of the metric depend not only on time, but also vary with position. It is clear that such solutions are necessary in order to describe the real universe in which structure exists. In this chapter we will write down the result of using the simplest perturbative extension to the homogeneous FLRW metric. We will still make many assumptions to facilitate the calculations. In particularly, we will only consider the regime in which only the *first order perturbations* to the FLRW metric are considered. This is a reasonable assumption in some regimes, in particular at early times and on large scales. We will attempt to justify why in the following sections.

2.1 Perturbing the field equations

We have shown how the Einstein field equations can be solved fairly straightforwardly with a homogeneous and isotropic FLRW metric (eq 1.12) to describe the geometric LHS (eq 1.10), sourced by the perfect fluid EM tensor on the RHS (eq 1.17).

We now wish to drop the assumption that the field equations are constant in space and reintroduce spatial dependence of the EM and the Einstein tensors (eqns. 1.16 and 1.17). Finding solution in this case is very difficult and in fact has not yet been achieved without the use of approximating assumptions and numerical methods. The method we use in this chapter is *cosmological perturbation theory*, which makes small perturbations around the analytically obtained homogeneous solutions.

2.1.1 The perturbed FLRW metric

We start by generalising the metric:

$$\widetilde{g}_{\mu\nu} = g_{\mu\nu} + \delta g_{\mu\nu} \qquad , \tag{2.1}$$

where $g_{\mu\nu}$ is still the homogeneous metric given in eq. (1.14) and $\delta g_{\mu\nu}$ is the space-dependent perturbation, which at this point needs not be small yet. Let us then start by writing a general perturbed metric using the 3+1 *splitting* or *ADM splitting* (Alcubierre, 2008; Arnowitt et al., 1962):

$$ds^2 = N^2 dt^2 - \gamma_{ij}\left(dx^i - N^i dt\right)\left(dx^j - N^j dt\right) \qquad , \tag{2.2}$$

where $N^i(t, x^i)$ is the spatial *shift vector* and the $N(t, x^i)$ is the time *lapse function*.

We now make the explicit assumption that any perturbations in the metric are small, i.e. $\delta g_{\mu\nu} \ll g_{\mu\nu}$. As usual, the smallness of the perturbations ensures that the equations of motion, i.e. the field equations can be linearised and therefore utilised and interpreted fairly straightforwardly. Now we can state explicitly the most general form of a symmetric metric with only the *scalar perturbations* $\in \{\psi, \phi, b, h\}$[1]:

$$ds^2 = (1 + 2\psi)dt^2 - 2b_{,i}a dx^i dt - a^2\left[(1 - 2\phi)\delta_{ij} + 2h_{,ij})\right]dx^i dx^j \qquad . \tag{2.3}$$

Relating this to eq. (2.2) means that we set the lapse, $N = \bar{N}(1 + \psi)$, the shift, $N_i = -a^2 b_{,i}$ and the spatial metric, $\gamma_{ij} = a^2\left[(1 - 2\phi)\delta_{ij} + 2h_{,ij}\right]$, with $\bar{N} = 1$ for a proper time coordinate, t and $\bar{N} = a$ if we wish to start using conformal time, τ as we do later on.

We wish to be able to work with the perturbed metric components explicitly, however in order to do this, we need to first specify a coordinate system. This, seemingly trivial issue is in fact crucial in writing down our observables. Any choice of coordinates introduces a set of redundant degrees of freedom or *gauge*. We can see this by realising that the symmetric Einstein field equations in eq. (1.10) are a set of 10 algebraically independent equations and that the metric similarly has 10 independent components. This might mean that the Einstein field equations suffice to determine all 10 metric components. However, the Bianchi identities (eq 1.11) constrain a further 4 component field equations, leaving us with 4 redundant degrees of freedom, the gauge. These degrees of freedom are determined by a choice of 4 conditions defining the coordinate system. We refer the reader to Mukhanov (2005, sec. 7.1.2) and to Weinberg (1972, sec. 7.4) for a further cosmologically relevant explanation of gauge theory[2]. We simply state that in this thesis, for the reason of a simple connection to Newtonian gravity, we choose to give our equations in *conformal Newtonian gauge* (as also in Dodelson (2003) for example). This means that we choose our coordinates t and x^i such that $b = h = 0$, regaining a purely diagonal and therefore also obviously symmetric metric:

$$ds^2 = (1 + 2\psi)dt^2 - a^2(1 - 2\phi)\delta_{ij}dx^i dx^j \qquad . \tag{2.4}$$

In this gauge it is reasonable to refer to ϕ and ψ as gravitational potentials, which are of course dependent on all, t and x^i.

Let us redefine our time variable to make our equations a little simpler. We now start using *conformal time*, which re-defines the time interval to be $d\tau = a\ dt$ and the time-derivative to be $\partial_\tau = a^{-1}\partial_t$ and is denoted by a dash, e.g. $\partial_\tau a \equiv a'$. The Hubble parameter then becomes $H \equiv \dot{a}/a = \partial_\tau a$, we can define a new parameter $\mathcal{H} \equiv a'/a$ and we write the metric as:

$$ds^2 = a^2\left[(1 + 2\psi)d\tau^2 - (1 - 2\phi)\delta_{ij}dx^i dx^j\right] \qquad . \tag{2.5}$$

---

[1] For example, Mukhanov (2005) treats vector and tensor perturbations as well. Tensor perturbations give *gravitational waves*. Vector perturbations result from strange inflation theories and are often omitted. Note furthermore that the "scalar perturbations" only behave as scalars under spatial rotations and not under general coordinate transformations!

[2] This was also dealt with in some detail in my essay (Markovič, 2009), submitted as a part of my masters degree at Cambridge and therefore will not be discussed further here.

2.1.2 The perturbed perfect fluid: the EM tensor

In order to still conform to the Einstein field equations, clearly the EM tensor must also become position dependent. Analogously to the metric, we can write it down as the homogeneous and isotropic background EM tensor, plus a local perturbation:

$$\widetilde{T}^{\mu}_{\nu} = T^{\mu}_{\nu} + \delta T^{\mu}_{\nu} \quad , \tag{2.6}$$

where δT^{μ}_{ν} now evolves with time but also depends on the position. We can write down the temporal and spatial components of the local perturbation in a form that anticipates the insertion into the field equations, but remains general:

$$\begin{aligned} \delta T^{0}_{0} &= \delta\rho \\ \delta T^{0}_{i} &= -(\rho + P)v_i \\ \delta T^{i}{}_{j} &= -\delta^{i}{}_{j}\delta P + \Pi^{i}{}_{j} \quad , \end{aligned} \tag{2.7}$$

where we have split the spatial, ij component into a trace, $\delta^{i}{}_{j}\delta P$ and a traceless part, $\Pi^{i}{}_{j}$. We can also define a scalar stress variable, $\sigma = -[\partial_i\partial^j - \delta^{j}{}_{i}/3]\Pi^{i}{}_{j}/(\rho + P)$, as in Ma & Bertschinger (1995). It turns out that these perturbations can be interpreted in an intuitive manner: $\widetilde{\rho}(\tau, x^i) = \rho(\tau) + \delta\rho(\tau, x^i)$ is the space and time dependent perturbed density, δP is similarly the perturbation in the pressure and v^i is the coordinate fluid velocity. The $\Pi^{i}{}_{j}$ is an anisotropic shear perturbation. The density perturbation is a crucial quantity in this thesis and it is convenient to here define another related variable, the **fractional density perturbation** for a "matter" species, x: $\delta_x = \delta\rho_x/\rho_x$.

2.2 Linearised solutions

Having generalised the FLRW metric by making the assumptions that its newly introduced spatial dependence only generates scalar degrees of freedom and that the metric remains symmetric as well as choosing our gauge, we can now again attempt to solve the field equations (eq 1.10) for the metric components.

2.2.1 Small anisotropy in the Cosmic Microwave Background

It has been known for many decades, since the discovery in 1965 that the most exact *black-body radiation* known reaches us nearly perfectly isotropically from the entire sky (Dicke et al., 1965; Peebles, 1965; Penzias & Wilson, 1965; Silk, 1967). This black body radiation can be explained by the presence of an opaque fluid in the very early, "fireball" universe, distributed homogeneously and in local thermal equilibrium[3] with the radiation. Having expanded and cooled, the fluid would have decoupled and the universe would have become transparent to the radiation which would then have cooled drastically with the expansion of the universe until reaching a frequency distribution[4] corresponding to a black body with $T \sim 3$K. Such a history would imply that our universe must have been very nearly homogeneous at some point, justifying using the homogeneous FLRW solution from eq. (1.14) at least as a reasonable approximation.

---

[3] The condition for thermal equilibrium in an expanding universe is that the rate of the relevant interaction is greater than the *Hubble rate*, H (eq 1.33), i.e. the rate of the expansion of the universe.

[4] The mean number of photons with a certain frequency, f for a black body with temperature, T is given by the Planck distribution, where $\bar{n} \propto (\exp\{2\pi f/T\} - 1)^{-1}$.

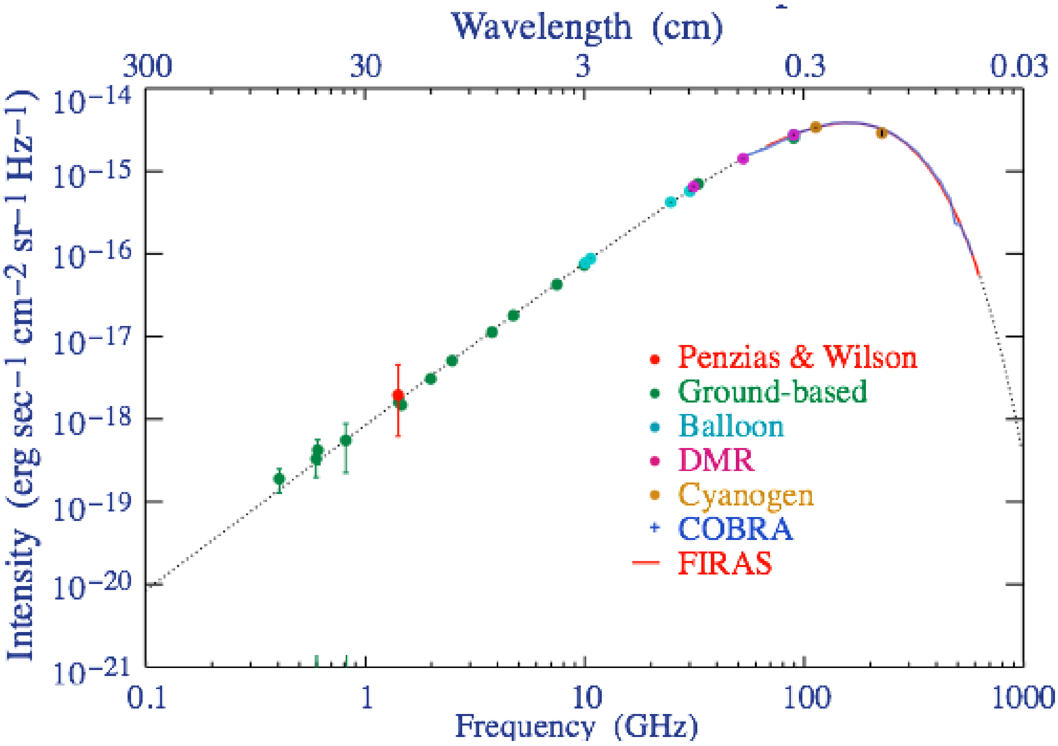

FIGURE 2.1: The black-body spectrum of the CMB on a logarithmic scale from the Lawrence Berkeley National Lab's COBE-FIRAS display. This is the most perfect black body curve found in nature and suggests that the early universe was in thermal equilibrium, whose temperature can be straightforwardly defined and calculated by taking into account the cosmological redshift (sec 1.2.2). Today it corresponds to a temperature of 2.728K.
FIGURE SOURCE: LBNL

Some decades later, new measurements were made[5]. NASA's COBE satellite first measured the entire black-body curve very precisely (see fig. (2.1) and Mather et al., 1991, 1994) and then for the first time discovered minuscule variations or **anisotropies** in temperature of this *background radiation* (Smoot et al., 1992, see also fig. 2.2). The DMR instrument on the COBE satellite looked at *microwave* frequencies, where the background radiation is strongest compared to the foreground emission from the gas in our Milky Way galaxy (Smoot et al., 1991), giving it the name *Cosmic Microwave Background* or CMB. NASA launched a new satellite about a decade later called WMAP, which measured CMB anisotropy even more precisely (Komatsu et al., 2011) and is still taking measurements today. In addition, in 2009, the European Space Agency launched the PLANCK satellite designed to repeat and improve these measurements (e.g. Ade et al., 2011).

Even though we will leave the discussion of deriving the precise properties of the density field from the observation of temperature anisotropies for another time, roughly, we can see, by considering the Stefan-Boltzmann law that the energy density of radiation $\rho_r \propto T^4$. Therefore we may conclude that the observations of the very small CMB anisotropy in the temperature support the idea that the universe is nearly homogeneous, with **small perturbations** in the density. And hence, it may be useful to solve our local Einstein field equations using

---

[5] See also Bergström & Goobar (2006, ch.11)

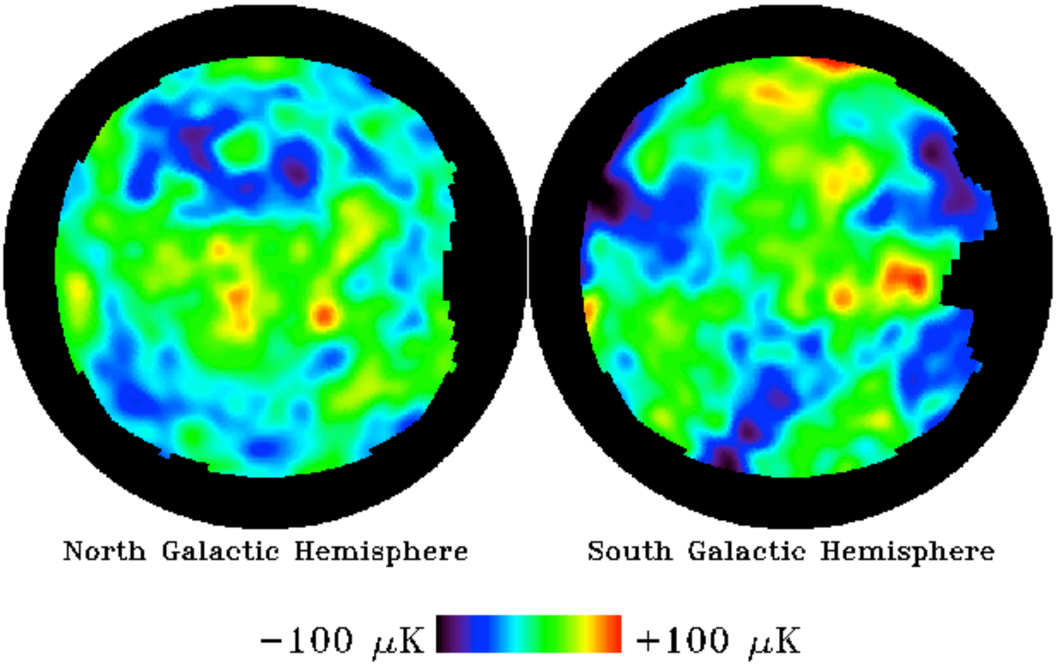

FIGURE 2.2: 4th year COBE-DMR map of the CMB anisotropy from NASA's COBE web page shows the tiny fluctuations in the 3 K background radiation. The fluctuations in temperature are at 10^{-5} level, as can be seen from the colour legend, seemingly justifying the treatment of the universe as nearly homogeneous.
FIGURE SOURCE: NASA

pertubation theory. The origin of these small perturbations is again far beyond the scope of this thesis, but we do refer the reader to the concept of *inflation* discussed in detail in many texts, for example in Mukhanov (2005) as well as Bergström & Goobar (2006, appendix E) as well as briefly mentioned again in sec. 2.3.

2.2.2 Linearised field equations

We assume that the perturbation quantities defined in equations (2.5) and (2.7) are much smaller than their background values in order to solve the Einstein field equations perturbatively (initially by Lifshitz, 1946). In particular, if the metric only has small perturbations, we can calculate the Einstein tensor to linear order, since higher orders in the metric perturbations will become negligible: $\widetilde{G}_{\alpha\beta} = G_{\alpha\beta} + \delta G_{\alpha\beta} + \dots$, where all the terms in $\delta G_{\alpha\beta}$ must be linear in the metric perturbation. Having similarly split up the EM tensor, we can now write down the general field equations for the perturbations only:

$$\delta G_{\alpha\beta} + \dots = 8\pi G \delta T_{\alpha\beta} \quad , \tag{2.8}$$

which written in the *linearised* form becomes:

$$\delta G_{\alpha\beta} = 8\pi G \delta T_{\alpha\beta} \quad , \tag{2.9}$$

which corresponds to equation (7.34) in Mukhanov (2005) and is the linear perturbation of eq. (1.10). We then simply write down the components of the covariant form of the local

Einstein tensor given in eq. (1.16):

$$\begin{aligned}
\delta G^0{}_0 &= \frac{2}{a^2}\nabla^2\phi - \frac{6}{a^2}\mathcal{H}\left(\phi' + \mathcal{H}\psi\right) \\
\delta G^0{}_i &= \frac{2}{a^2}\left(\phi' + \mathcal{H}\psi\right)_{,i} \\
\delta G^i{}_j(\text{pure diagonal}) &= -\frac{2}{a^2}\left[\phi'' + \mathcal{H}(2\phi+\psi)' + (2\mathcal{H}' + \mathcal{H}^2)\psi + \frac{1}{2}\nabla^2(\psi-\phi)\right]\delta^i{}_j \\
\delta G^i{}_j(\text{pure derivative}) &= \frac{1}{a^2}\delta^{ik}\left(\psi-\phi\right)_{,kj} \quad ,
\end{aligned} \tag{2.10}$$

where finding these equations is a matter of relatively simple but longwinded algebra that requires at every step to neglect the term that contain either of the perturbation variables at larger than first order (see for e.g. Challinor, 2009; Kodama & Sasaki, 1984; Lyth & Liddle, 2009; Mukhanov, 2005; Weinberg, 2008, etc.). Furthermore, we can easily see that $\phi = \psi$ in the case of the perfect fluid, which does not have any anisotropic stress, $\Pi^i{}_j = \sigma = 0$, by equating the pure derivative parts of the field equations only:

$$-\frac{1}{2}\delta^{ik}\left(\psi-\phi\right)_{,kj} = 8\pi G\Pi^i{}_j = 0 \quad . \tag{2.11}$$

We can now insert the first order perturbations to the Einstein tensor (eq 2.10) as well as those to the EM tensor (eq 2.7) into the first order field equations (eq 2.9) and substitute $\psi = \phi$ (eq 2.11). Furthermore, we can re-write the density perturbation as the fractional perturbation multiplying the background density, $\delta\rho = \rho\delta$. Finally, we can write down the three separate components of the first order field equations.

Combining the 00 and the $0i$ components of eq. (2.10), gives us the equivalent of what we know as the **Poisson equation** in regular, *Newtonian gravity*. Note that the velocity, v where $v_i = v_{,i} = \partial_i v$ and we have performed an integral over space assuming the perturbations decay at infinity (c.f. to eq. (8.35) in Lyth & Liddle, 2009):

$$\boxed{\nabla^2\phi = 4\pi G\rho(\delta - 3\mathcal{H}(1+w)v)} \quad . \tag{2.12}$$

In order to simplify the ij component, we refer to sec. 1.3.3 and consider that for an *adiabatic* perfect fluid, there are no entropy perturbations, $\delta S = 0$ and so $\delta P = c_\mathrm{s}^2\delta\rho$, where c_s is the speed of sound. Substituting this into the ij component of the linear-order perturbed field equations and using eq. (2.12) to replace the $\rho\delta$, we can write down the ij component of the linearised field equations as:

$$\phi'' + 3\phi'\mathcal{H}(1+c_\mathrm{s}^2) + (2\mathcal{H}' + \mathcal{H}^2(1+3c_\mathrm{s}^2) - c_\mathrm{s}^2\nabla^2)\phi = 0 \quad , \tag{2.13}$$

an **equation of motion for the gravitational potential**, ϕ.

2.2.3 Linearised conservation equation

In the previous section we derived the dynamical equation governing the evolution of the gravitational field as well as the equation describing how the perturbation in the energy density of the “matter” in the universe sources the gravitational potential. We derived these from the first order perturbed Einstein field equations. These form a redundant set of equations together with the *Bianchi identities*, which result in the conservation equations for the Einstein and the EM tensors eq. (1.11).

We first take the $\nu = 0$ component of the EM conservation, $T^{\mu}_{\nu;\mu} = 0$ and find that the zeroth order terms, meaning that they contain only the background variables, return the **continuity equation** (eq 1.22) as we would expect (e.g. Ma & Bertschinger, 1995). The first order terms on the other hand give:

$$\boxed{\delta' + (1+w)\left(\partial_i v^i - 3\phi'\right) + 3\mathcal{H}\left(c_{\rm s}^2 - w\right)\delta = 0} \quad , \tag{2.14}$$

where we could insert the divergence of the spatial velocity[6], $\theta = \partial_i v^i = \partial^i v_i$, the equation of state, $w = P/\rho$ and the speed of sound, $c_{\rm s}^2 = \delta P/\delta\rho$. In fact, we can write the speed of sound as $c_{\rm s}^2 = dP/d\rho = w + \rho dw/d\rho$. Therefore, for a constant equation of state, $c_{\rm s}^2 - w = 0$.

Now turning our attention to the $\nu = i$ component of the conservation equation, we similarly find that:

$$v_i' + \mathcal{H}(1-3w)v_i + \frac{w'}{1+w}v_i + \frac{c_{\rm s}^2}{1+w}\partial_i\delta + \partial_i\phi = 0 \quad , \tag{2.15}$$

for no anisotropic stress, where the second term represents the slowing due to cosmic expansion (Kodama & Sasaki, 1984).

2.2.4 The full phase-space treatment: the Boltzmann equation

We have so far used the EM tensor for a perfect fluid simply and straightforwardly. This is applicable for a limited range of fluids. One must use the full energy-momentum phase space distribution function in order to describe other fluids, which need more than only their density and pressure to be described.

In this section we reexamine the perturbed densities in the early universe. We throw away the assumptions that all matter is non-relativistic and non-interacting. In essence, this section is a brief review of the perturbed Boltzmann equation of the early thermal universe before recombination and follows closely sections 5 and 8 in the work of Ma & Bertschinger (1995).

We can describe the evolution of the perturbations in the *cold dark matter* as well as the baryon density fields in the early universe by a simple non-relativistic fluid treatment (as in sec. 2.2). However, the relativistic photons and neutrinos can only be described accurately by the full relativistic treatment of their distribution function in phase space. In addition, in the simple treatment of perturbations in sec. 2.2, we only take into account non-interacting fluids. Taking into account the momentum transfer due to interactions, we must add an extra term into the equations describing the evolution of the perturbations. Most importantly, photons couple to the baryonic fluid via Thompson scattering before recombination, at which time the un-ionised particles stop interacting with the photons.

In order to describe a relativistic fluid in a perturbed spacetime, as pointed out in sec. 1.3.4 it is insufficient to describe it with the perfect fluid formalism, instead one must consider the full phase space of 3 spatial coordinates and their 3 corresponding momenta. The **Boltzmann equation** (eq 2.18) is a differential equation that describes the evolution of this phase space

---

[6] The following is equivalent since it is clear from eq. 1.14 that $g_{ij}g^{ik} = a^2\delta_{ij}a^{-2}\delta^{ik} = \delta^k_{\ j}$.

distribution function, $f\left(x^i, P_j, \tau\right)$ with time. The components of the energy-momentum tensor for **relativistic species** depend on the phase space distribution in the following manner:

$$T_{\mu\nu} = \int \frac{dP_j}{\sqrt{-g}} \frac{P_\mu P_\nu}{P^0} f\left(x^i, P_j, \tau\right) \quad , \tag{2.16}$$

where as before, x^i are the spatial coordinates, P_j its Hamiltonian conjugate, $\tau = x^0$ is the conformal time, P_μ is the full 4-momentum and $f(x^\mu, P_\nu)$ is the full phase space distribution (noting also that $|P| = P^\mu P_\mu = 0$ or m^2, the squared particle mass), which can be decomposed into a zeroth-order and perturbed term:

$$f\left(x^i, P_j, \tau\right) = f_0(q)\left[1 + \Psi(x^i, q, n_j, \tau)\right] \quad , \tag{2.17}$$

and where we have decomposed the momentum $P_i = ap_i(1-\phi) = q_i(1-\phi)$ and $q_i = qn_i$, with n_i being the component of an orthogonal, normalised direction vector. The Boltzmann equation then gives the evolution of this phase space distribution and can be written in terms of the here-relevant variables as:

$$\frac{df}{d\tau} = \frac{\partial f}{\partial \tau} + \frac{dx^i}{d\tau}\frac{\partial f}{\partial x^i} + \frac{dq}{d\tau}\frac{\partial f}{\partial q} + \frac{dn^i}{d\tau}\frac{\partial f}{\partial n^i} = \left(\frac{\partial f}{\partial \tau}\right)_{\text{coll}} \quad , \tag{2.18}$$

where the right-hand-side depends only on collisional terms and vanishes for dark matter and neutrinos.

We leave out the algebra, which is described in detail in Ma *&* Bertschinger (1995) from equation (36) onwards, and skip right to the resulting **linearised** differential equations describing the evolution of the individual matter and radiation species with significant densities before recombination.

We wish to make a comparison in the *Newtonian gauge* between the species, by writing down the scalar perturbations, δ_x (overdensity), θ_x (divergence of velocity, $\partial_i v_x^i$), δP_x (overpressure) and σ_x (anisotropic stress), to the energy-momentum tensor of each species in Fourier space (where k is the wavenumber). Note that as in sec. 2.1, ϕ and ψ are the scalar metric perturbations. From now on we also work in Fourier space, where a divergence, $\partial_i \to -ik_i$ and the Laplacian $\partial_i\partial^i \to -k^2$, k being the *wavenumber*.

Then for **cold dark matter**, a pressureless, perfect fluid:

$$\begin{aligned} \delta'_{\text{cdm}} &= -\theta_{\text{cdm}} + 3\phi' \quad \text{and} \\ \theta'_{\text{cdm}} &= -\mathcal{H}\theta_{\text{cdm}} + k^2\psi \quad , \end{aligned} \tag{2.19}$$

with other perturbations being zero. These are exactly (2.14) & ∂^i(2.15) in Fourier space, with the equations of state, $w = 0$ and the speed of sound, $c_s^2 = 0$.

For the **massless neutrinos** the collisionless Boltzman equation is used to find:

$$\begin{aligned} F'_{\nu 0} = \delta'_\nu &= -\frac{4}{3}\theta_\nu + 4\phi' \quad , \\ \frac{3}{4}kF'_{\nu 1} = \theta'_\nu &= k^2\left(\frac{1}{4}\delta_\nu - \sigma_\nu\right) + k^2\psi \quad \text{and} \\ F'_{\nu l} &= \frac{k}{2l+1}\left[lF_{\nu(l-1)} - (l+1)F_{\nu(l+1)}\right] \quad \text{for } l \geq 2 \quad , \end{aligned} \tag{2.20}$$

where the $F_{\nu l}(\boldsymbol{k}, \tau)$ are the coefficients of the Legendre expansion of the Fourier transformed neutrino phase space function, $F_\nu(\boldsymbol{k}, \hat{\boldsymbol{n}}, \tau)$, and $F_{\nu 2} = 2\sigma_\nu$. The explicit momentum-dependence happens to vanish, because for masseless particles, the momentum equals the total energy, $q = \epsilon$ (in natural units, where $c = 1$). In addition, unlike in the equations above, the stress, σ does not vanish. This means these equations do not directly correspond to (2.14) & ∂^i(2.15) in Fourier space. We would need to include a non-zero $\Pi^i{}_j$ into our algebra as they have in Ma & Bertschinger (1995) to find the exact correspondence.

Then in the case of collisionless, **massive neutrinos**, the perturbation to the phase space function introduced in eq. (2.17) is expanded in terms of Legendre polynomials and so:

$$\begin{aligned} \delta P_{\mathrm{h}} \text{ and } \delta\rho_{\mathrm{h}} \leftrightarrow \qquad \Psi'_{\mathrm{h}0} &= -\frac{qk}{\epsilon}\Psi_{\mathrm{h}1} - \phi'\frac{d\ln f_0}{d\ln q} \qquad , \\ \theta_{\mathrm{h}} \leftrightarrow \qquad \Psi'_{\mathrm{h}1} &= \frac{qk}{3\epsilon}\left(\Psi_{\mathrm{h}0} - 2\Psi_{\mathrm{h}2}\right) - \frac{\epsilon k}{3q}\psi\frac{d\ln f_0}{d\ln q} \qquad \text{and} \\ \sigma_{\mathrm{h}} \leftrightarrow \qquad \Psi'_{\mathrm{h}l} &= \frac{qk}{(2l+1)\epsilon}\left[l\Psi_{\mathrm{h}(l-1)} - (l+1)\Psi_{\mathrm{h}(l+1)}\right] \qquad \text{for } l \geq 2, \end{aligned} \tag{2.21}$$

where we label massive neutrinos with a subscript of ‘h’, because they represent **hot dark matter** (HDM). In order to relate these perturbative quantities to the perturbations in density, pressure etc. indicated above, we must integrate over the comoving momentum, q, as in equations (55) of Ma & Bertschinger (1995). If we define a new integrand variable for integrating over the perturbation to the phase space function from eq. (2.17) for the sake of clarity:

$$dQ_l = q^2 dq f_0(q)\Psi_l \qquad , \tag{2.22}$$

and considering that the comoving energy, $\epsilon = \sqrt{q^2 + m^2a^2}$, we find that generally:

$$\begin{aligned} \delta &= \frac{4\pi}{\rho}a^{-4}\int \epsilon \; dQ_0 \\ \delta P &= \frac{4\pi}{3}a^{-4}\int \frac{q^2}{\epsilon} \; dQ_0 \\ \theta &= \frac{4\pi k}{(\rho+P)}a^{-4}\int q \; dQ_1 \\ \sigma &= \frac{8\pi}{3(\rho+P)}a^{-4}\int \frac{q^2}{\epsilon} \; dQ_2 \qquad . \end{aligned} \tag{2.23}$$

Let us take note here of the two extremes: the cold, presureless, non-relativistic dark matter and the hot, relativistic massive neutrinos. The treatment of anything in between, what we call **warm dark matter**, must be treated to how relativistic it is in the era and regime of interest as well as how long the particle stays relativistic. We discuss this in detail below, in sec. 2.3.3.

The three species discussed here, cold dark matter, massless and massive neutrinos, couple together only via ϕ and ψ. We forego describing in detail the evolution of perturbations in the **baryonic** and **photonic** density fields as this is not within the scope of this thesis. But we do note that each of their perturbation evolution equations receives an additional term, which depends on the perturbation in the energy-momentum tensor of the other species. This comes from the constraint that when coupled, the combined momentum of photos and baryons must be conserved. So, even though baryons are very non-relativistic after neutrino decoupling, they get a transfer of momentum from the relativistic photons. We can calculate the adiabatic sound speed for baryons as

$$c^2_{\mathrm{s,b}} = \frac{\partial P_{\mathrm{b}}}{\partial \rho_{\mathrm{b}}} = \frac{P'_{\mathrm{b}}}{\rho'_{\mathrm{b}}} \qquad . \tag{2.24}$$

In addition, the photons receive two sets of perturbation equations, one for either polarisation state. The two sets differ only in the additional term due to Thompson scattering. Note that before recombination the photons and baryons act together like a single fluid. In order to calculate the evolution of their density perturbations the so-called "tight-coupling approximation" can be used (e.g. Ma & Bertschinger, 1995).

The above equations that describe the evolution of perturbations in EM tensors of the different species can be simplified and solved analytically for the times before the so-called "horizon entry" of the individual, independent k-modes. However once $k\tau \gtrsim \pi$, the Fourier mode corresponding to k can only be calculated taking into account the full perturbation equations, because it "comes into causal contact". The full equations can then only be solved numerically, especially if we want to realistically sum over all of the relevant species: dark matter, massive neutrinos, photons and baryons. We discuss the relevant regimes in the following sections.

2.2.5 Evolution of perturbations

Even though generally, Newtonian gauge is more intuitive in many contexts when discussing large scale structure in the universe, it is very often more convenient to work in the *synchronous gauge*. In the synchronous gauge, the particles of regular cold dark matter are the tracers of metric perturbations and so the velocity, $v = 0$.

It is now that we unfortunately must plunge into the synchronous gauge for the treacherous reason of convenience. In this gauge, the linear perturbed metric from eq. (2.2) becomes:

$$ds^2 = dt^2 - a^2\left[\delta_{ij} + 2h_{ij})\right]dx^i dx^j \quad , \tag{2.25}$$

if $\bar{N} = 1$ for proper time, $N_i = 0$ and $\gamma_{ij} = a^2[\delta_{ij} + 2h_{ij}]$ and the perturbations need not only be scalar, but must be small. Or comparing to eq. (2.3), $\phi = b = 0$, $\phi = -(h - h_{\text{scalar}})/6$ and $h_{,ij} = h_{\text{scalar}}/2$. Here we have performed a standard scalar-vector-tensor (SVT) decomposition for a general tensor, A_{ij}. If D_i is a general derivative in a curved spacetime:

$$A^i{}_j = \underbrace{\tfrac{1}{3}\delta^i{}_j A}_{\text{trace part}} + \underbrace{\left(D^i D_j + \tfrac{1}{3}\delta^i{}_j\Delta\right) A^{\text{scal}}}_{\text{anisotropic scalar part}} + \underbrace{D^i A^{\text{vect}}_j + D_j A^i_{\text{vect}}}_{\text{vector part}} + \underbrace{A^{\text{T}}{}_j{}^i}_{\text{irreducible tensor}} \quad , \tag{2.26}$$

with conditions that $D_i A^i_{\text{vect}} = 0$ and the final, "transverse" term is trace free and $D_i A^{\text{T}}{}_j{}^i = 0$ as well. And in conformal time, we get:

$$ds^2 = a^2\left[d\tau^2 - \left[\delta_{ij} + 2h_{ij})\right]dx^i dx^j\right] \quad . \tag{2.27}$$

Solving the perturbed momentum conservation equation gives the synchronous gauge equivalent to eq. (2.19), which is extremely convenient, because it relates the trace metric perturbation directly to the perturbation in the CDM density: $\delta_{\text{cdm}} = -h/2$.

Let us now re-write the general equations for the evolution of perturbations eq. (2.14) and eq. (2.15) in the **synchronous gauge** variables (see also eqns. (29) in Ma & Bertschinger, 1995) for a multicomponent perfect fluid with a constant equation of state, w:

$$\begin{aligned} \delta' + (1+w)\left(\partial_i v^i + \frac{h'}{2}\right) &= 0 \\ v_i' + \mathcal{H}(1-3w)v_i + \frac{w}{1+w}\partial_i\delta &= 0 \quad , \end{aligned} \tag{2.28}$$

where $\delta = \sum_x \delta_x$ and $v = \sum_x v_x$, each component of the fluid denoted by x.

In eq. (1.40) we defined the eras of radiation, matter and Λ domination. In 1.3 generally, we calculated how the background density, ρ_x of each of these components evolves with the scale factor, a and how the scale factor evolves with time. Assuming we are far away in time from the transitions between these eras, we can say that the density of the dominating species equals the total density. We have also hinted towards the evidence that the early universe was radiation dominated. This radiation domination is measured to have ended at a redshift (see 1.29) of approximately $z_{\rm eq} \approx 3200$ (Komatsu et al., 2011). One can integrate eq. (1.43) from a short time after $a(t=0)=0$ to $a(t_{\rm eq}) = 1/(1+z_{\rm eq})$ to find that radiation dominates for around 100.000 years from the time of the initial singularity.

2.3 Features of the linear power spectrum

The solution to the origin of structure was found in the 1980s, when firstly Starobinskiĭ (1979) developed the theory of the quantum fluctuations in the primordial scalar field and then secondly, Guth (1981) realised that the flatness, monopole and horizon problems are resolved by an early de-Sitter-like phase of extremely rapid expansion of space called *inflation*. Many pedagogical texts show that for a single scalar field driving this early inflation, we expect to see nearly perfectly scale invariant curvature perturbations with a Gaussian probability function (Challinor, 2009; Mukhanov, 2005; Mukhanov et al., 1992; Weinberg, 2008, are just a few examples). As in for example Markovič (2009), we should define a gauge invariant curvature variable in terms of the conformal Newtonian gauge variables ϕ and v:

$$\zeta = \phi + \mathcal{H} v \qquad , \tag{2.29}$$

where ϕ and $\mathcal{H}$ are defined in eq. (2.5) as the metric perturbation (and the Newtonian gravitational potenital) and the conformal time Hubble parameter encoding the speed of expansion. The fluid velocity, v is defined in the context of eq. (2.12). Let us mention here that eq. (2.12) has a special form if we choose a different "comoving" gauge, where as in the synchronous gauge, the peculiar velocities are null, $v = 0$. This results in a Poisson equation that matches in its form the Poisson equation from simple Newtonian physics:

$$\nabla^2 \phi = 4\pi G \rho \delta_{\rm como} \qquad . \tag{2.30}$$

It is possible to show that in the case of *adiabaticity* and no anisotropic stress, $\zeta' = 0$, on scales larger than the Hubble horizon[7], in other words the gauge-invariant curvature is constant. Setting $v = 0$ in our special gauge as above gives $\zeta \propto \phi$.

The physical (dimensionless) density power spectrum for this variable can be written as

$$\Delta^2_\zeta(k) = \Delta^2_\zeta(k_0) \left(\frac{k}{k_0}\right)^{n_s(k_0)-1} \propto \Delta^2_\phi \qquad , \tag{2.31}$$

where the scalar spectral index $n_s - 1 \equiv \frac{d \ln P^2_\zeta}{d \ln k}$ and k_0 is a pivot scale. Therefore for a perfectly scale-invariant or *fractal* spectrum, $n_s = 1$. This **spectral index** has indeed been measured

---

[7] At the end of inflation most scales relevant today are outside the Hubble horizon of inflation.

to be very close to, but distinctly different than one (e.g. Larson et al., 2011). And very impressively emerges from the theory of inflation (see e.g. Dodelson, 2003, p.184).

Note that the power spectrum is defined[8] as the Fourier space two-point correlator,

$$\left\langle \phi(\tau,\boldsymbol{k})\phi(\tau,\tilde{\boldsymbol{k}})^* \right\rangle = \frac{2\pi^2}{k^3}\Delta_\phi(\tau,k)\delta(\boldsymbol{k}-\tilde{\boldsymbol{k}}) \propto k^{-3} \quad , \tag{2.32}$$

since $\Delta_\phi \propto$ const. Now comparing the above to eq. (2.12), we can see that in Fourier space, $\nabla^2\phi \propto \delta$ gives $-k^2\phi \propto \delta$. This means that the two-point correlator is

$$k^4\left\langle \phi(\tau,\boldsymbol{k})\phi(\tau,\tilde{\boldsymbol{k}})^* \right\rangle \propto \left\langle \delta(\tau,\boldsymbol{k})\delta(\tau,\tilde{\boldsymbol{k}})^* \right\rangle = \frac{2\pi^2}{k^3}\Delta_\delta(\tau,k)\delta(\boldsymbol{k}-\tilde{\boldsymbol{k}}) \propto k \quad , \tag{2.33}$$

So the scale dependence of the power spectrum of energy density perturbations can be written down with reference above:

$$\therefore \qquad \Delta_\delta(\tau,k) \equiv \frac{k^3 P(\tau,k)}{2\pi^2} \propto k^4 \quad . \tag{2.34}$$

2.3.1 The transfer function from radiation domination

In order to find the linear matter power spectrum that has evolved through radiation domination and has therefore been suppressed on scales that have *entered the Hubble horizon* in practice, one may use the fitting function from equation (7) in Ma (1996), which is based on the functional form of Bardeen (1985), but taking into account the effects of baryonic oscillation that prevent collapse on small scales before recombination. The coefficients $\alpha_1 = 2.34, \alpha_2 = 3.89, \alpha_3 = 16.1, \alpha_4 = 5.46$, and $\alpha_5 = 6.71$ from Bardeen (1985) are used. Alternatively one can use $\alpha_1 = 2.205, \alpha_2 = 4.05, \alpha_3 = 18.3, \alpha_4 = 8.725$, and $\alpha_5 = 8.0$ and $\Gamma = \Omega_m h$. Error comparing to numerical simulations using these is smaller than 1% for $k < 40\,h\mathrm{Mpc}^{-1}$. Then the transfer function is:

$$T_\mathrm{r}(q) = \left(\frac{\ln(1+\alpha_1 q)}{\alpha_1 q}\right)\frac{1}{\left[1+\alpha_2 q+(\alpha_3 q)^2+(\alpha_4 q)^3+(\alpha_5 q)^4\right]^{1/4}} \tag{2.35}$$

where

$$q = \frac{k}{\Gamma h} \qquad \text{and} \qquad \Gamma \;=\; e^{-2\Omega_{b,0}h}\Omega_{m,0}h \tag{2.36}$$

with wavenumbers going from $k = 10^{-4} \rightarrow 10^4\,h\mathrm{Mpc}^{-1}$. In paper Ma (1996) this is multiplied by $\sqrt{a}$, which is here taken into account with the **growth factor**. In this case it is important to note that $T_\mathrm{r}(q) \rightarrow 1$ as $k \rightarrow 0$. Also in eq. (2.36) we are dividing k/h, however we omit the $1/h$ for the case where the unit of k is $h\mathrm{Mpc}^{-1}$.

Then as discussed in sec. 2.3,

$$P_\delta^\mathrm{initial}(k) = Ak^{n_\mathrm{s}} \qquad \text{and} \qquad P_\delta(k) = P_\delta^\mathrm{initial}(k)T_\mathrm{r}^2(t,k), \tag{2.37}$$

(note that A here is only a normalisation constant, which differs from the below by $A = A_\mathrm{s}/k_\mathrm{pivot}^{n_\mathrm{s}}$ for $\alpha = 0$).

---

[8] This definition is based on statistical homogeneity and isotropy (see e.g. Challinor, 2009).

It is possible to include the running, α, of the scalar spectral index, n_s, and so the primordial (initial) matter power spectrum becomes:

$$P_\delta^{\mathrm{initial}}(k) = A_\mathrm{s}\left(\frac{k}{k_{\mathrm{pivot}}}\right)^{n_\mathrm{s}+\frac{\alpha}{2}\ln\left(\frac{k}{k_{\mathrm{pivot}}}\right)} \qquad \text{now with} \qquad A_\mathrm{s} = P_{\mathrm{cdm}}^{\mathrm{initial}}(k_{\mathrm{pivot}}). \tag{2.38}$$

with commonly assumed values $k_{\mathrm{pivot}} = 0.05$ and $A_\mathrm{s} = 3 \times 10^6 k_{\mathrm{pivot}}$. In this thesis however, we set $\alpha = 0$.

2.3.2 Growth factor in the matter dominated era

The present-day, linear-theory power spectrum is found by multiplying the primordial matter power spectrum found in eq. (2.37) by the growth factor squared, $D_+^2(z)$, found with the full differential equation of the evolution of matter perturbations in the matter era:

$$\delta_\mathrm{m}'' + \mathcal{H}(\tau)\delta_\mathrm{m}' - 4\pi G a^2 \rho_\mathrm{m}(\tau)\delta_\mathrm{m} = 0 \quad , \tag{2.39}$$

which can be derived from the Poisson equation combined with eq. (2.13), the evolution of the metric perturbation, assuming that the comoving frame moves with matter and that the pressure is negligible in the matter dominated era. We have wrote down this equation again in the Newtonian gauge in order to be compatible with the literature. The solution to this equation, $\delta_m(\tau)$ is normalised to equal one today. Equivalently, this equation can be derived by linearising the perturbed Newtonian equations for the evolution of the density field, namely the Poisson, continuity and Euler equations.

Now we have the linear matter power spectrum at any redshift. In order to have a picture of what the matter distribution looks like today (and at low redshift in general), we need to account for effects of non-linear structures as well. This is especially significant on small scales (where the effects of free-streaming of WDM leave their signature) and it unfortunately causes a significant loss of information. We will attempt this calculation in the next chapter.

2.3.3 Hot and *warm dark matter* effects

Neutrinos decouple when the temperature of the primordial soup (or heat bath), $T \sim 1\,\mathrm{MeV}$ and $a \sim 10^{-10}$ and become non-relativistic when $T_\mathrm{h} \sim m_\mathrm{h}/3k_\mathrm{B}$[9]. Dark matter decouples and becomes non-relativistic much earlier in both the cold and **warm dark matter** (WDM) cases. If warm dark matter has a simple thermal history, analogous to neutrinos, but with a larger particle mass, we can calculate its *free-streaming*. Such a dark matter particle is called a *thermal relic*, because it decouples out of equilibrium as has been discussed in sec. 1.3.4.

The Jeans length[10] can be calculated for a perfect fluid and denotes the limit on which the gravitational effect balance out the thermal effects. For collisionless fluids like the dark matter and neutrino fluids, we define the analogous free-streaming length, which tells how far the fast-moving particles can travel within the gravitational time-scale i.e. in the time of

---

[9] As a quick reference, the Boltzmann constant, $k_\mathrm{B} = 8.617 \times 10^{-5}\,\mathrm{eV\ K}^{-1}$.

[10] See Bond & Szalay (1983) for a discussion of Jeans lengths for collisionless particles.

free-fall:

$$\begin{aligned} k_{\rm fs}(a) &= \sqrt{4\pi G\bar{\rho}}\,\frac{a}{v_{x,\rm median}} \\ &= \sqrt{\frac{3}{2a}}\,H_0\frac{1}{v_{x,\rm median}} \\ \text{(relativistic)} &= \sqrt{\frac{3}{2a}}\,H_0 \\ \text{(non-relativistic)} &= \sqrt{\frac{3}{2a}}\,H_0\frac{am_x}{3k_{\rm B}T_{0,x}} \quad , \end{aligned} \tag{2.40}$$

where $v_x = 1$, when the particles are relativistic. When they go non-relativistic (i.e. when $3k_{\rm B}T_{0,x} \lesssim m_x$),

$$v_x = \frac{3k_{\rm B}T_{0,x}}{am_x} \tag{2.41}$$

and then $k_{\rm fs} \to \infty$ as $a \to 1$ and $T \to 0$, which is the case for cold dark matter very early on, and therefore, the effects of free-streaming are pushed to very very large k, i.e. very very small scales. This means that the damping of the overdensity field becomes insignificant!

The most basic model of WDM particles is to say that they are thermal relics. This means that they were in equilibrium at some point. When their temperature and density dropped, they went out of equilibrium (e.g. Bond & Szalay, 1983). This means DM particles decoupled from each other.

Theoretically there would have been another kind of decoupling. This would have been when DM particles and baryons were in an extremely dense environment and so there would have been a significant interaction rate between them. We know very little about this regime, because we would have to know the mass and interaction cross-section of DM particles, but we don't even know the nature (and even existence) of the interaction between DM particles and other types of matter.

However, it's most likely that these two decouplings happened at the same time, because any self-interaction of DM is likely to involve the weak, strong or electromagnetic force, which means this self-interaction would necessarily involve baryons. Were this not the case, it may be that the interaction between baryons and DM particles is weaker than the interaction among DM particles. In this case the decoupling from baryons would happen at an earlier time than decoupling of DM out of equilibrium.

The last important scale feature in the linear matter power spectrum is the suppression by dark matter free-streaming. In the WDM model the scale of suppression is called the free-streaming scale, $k_{\rm fs}$ and corresponds to the mode that enters the horizon at the time when WDM partcles become non-relativistic, $t_{\rm rel}$. For CDM on the other hand, this happens very early and so $k_{\rm fs} \gg 1\,h^{-1}$Mpc and it's cosmological effects can be neglected. A species can become non-relativistic while still in thermal equilibrium or after it decouples (Bode et al., 2001; Bond & Szalay, 1983; White et al., 1987). If it is after, we say that DM particles decouple while non-relativistic. This is what we assume in this thesis because exploring many different particle models is out of our scope.

From Bond & Szalay (1983), eqn. (1), we get the temperature of WDM relative to that of the photons:

$$T_{\rm wdm} = \left(\frac{3.9}{g_*}\right)^{\frac{1}{3}} T_\gamma \quad \Rightarrow \quad g_* = 3.9\left(\frac{T_\gamma}{T_{\rm wdm}}\right)^3 \tag{2.42}$$

$$\Omega_{\rm wdm} = 1.1h^{-2}\left(\frac{g_{\rm wdm}}{1.5}\right)\left(\frac{100}{g_*}\right)\left(\frac{m_{\rm wdm}}{1\,{\rm keV}}\right) \tag{2.43}$$

$$= 1.1\left(\frac{100}{3.9}\right)h^{-2}\left(\frac{g_{\rm wdm}}{1.5}\right)\left(\frac{T_{\rm wdm}}{T_\gamma}\right)^3\left(\frac{m_{\rm wdm}}{1\,{\rm keV}}\right) \quad , \tag{2.44}$$

where g_* is the number of all relativistic degrees of freedom at **WDM** decoupling, T_γ is the present day photon temperature and $T_{\rm wdm}$ is the temperature of WDM. This matches the results from sec. 1.3.4. We can calculate the degrees of freedom:

$$g_{\rm wdm} = \begin{cases} N_{\rm wdm} & \text{bosons} \\ \frac{3}{4}N_{\rm wdm} & \text{fermions} \end{cases} \quad , \tag{2.45}$$

where $N_{\rm wdm}$ are the number of spin degrees of freedom . Then determining $\Omega_{\rm dm} = \Omega_{\rm wdm}$ gives a direct relationship between $T_{\rm wdm}$ and $m_{\rm wdm}$. Otherwise must introduce a new parameter $f_{\rm wdm} = \Omega_{\rm wdm}/\Omega_{\rm dm}$, the fraction of warm dark matter. This parameter becomes relevant when we start to consider *mixed dark matter* models.

In addition we can calculate the *velocity dispersion* of WDM particles relative to that of the neutrinos (Bond et al., 1980):

$$\sqrt{\langle v^2\rangle_\nu} = 6\,{\rm km\ s^{-1}}\left(\frac{30\,{\rm eV}}{m_\nu}\right)(1+z) \quad , \tag{2.46}$$

Rescaling for warm dark matter, if it has decoupled while relativistic:

$$\sqrt{\langle v^2\rangle_{\rm wdm}} = \sqrt{\langle v^2\rangle_\nu}\left(\frac{T_{\rm wdm}}{m_{\rm wdm}}\right)\left(\frac{m_\nu}{T_\nu}\right) \quad . \tag{2.47}$$

If particles decouple while non-relativistic, $\sqrt{\langle v^2\rangle_{\rm wdm}} \lesssim$ cm s^{-1}, so the damping is completely insignificant.

Power spectrum suppression from free-streaming

In the case of warm dark matter, the initial matter power spectrum emerging from radiation domination is modified by an additional transfer function due to free streaming. Viel et al. (2005) found this fitting function, but it can be calculated very accurately with a numerical Boltzmann equation solver code, like for example `CMBFAST` (Seljak & Zaldarriaga, 1996), `CAMB` (Lewis et al., 2000) or `CLASS` (Blas et al., 2011). For now we use the fitting function with $\nu = 1.12$ like in Viel et al. (2005) (the alternative is $\nu = 1.2$ like in Bode et al. (2001)). Then the scale break parameter is:

$$\alpha = 0.049\left(\frac{m_{\rm wdm}}{1\,{\rm keV}}\right)^{-1.11}\left(\frac{\Omega_{\rm wdm}}{0.25}\right)^{0.11}\left(\frac{h}{0.7}\right)^{1.22} \tag{2.48}$$

which is used in calculating the linear matter power spectrum by multiplying with the following warm transfer function:

$$T_{\rm wdm}(k) = \left(1+(\alpha k)^{2\nu}\right)^{-5/\nu} \quad \text{and so} \quad P_{\rm wdm}(k) = P_{\rm cdm}(k)T^2_{\rm wdm}(k) \tag{2.49}$$

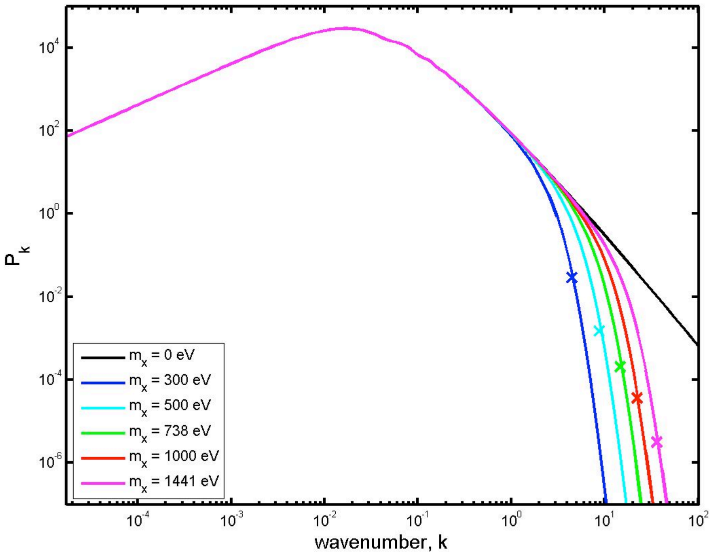

Figure 2.3: The linear matter power spectra for five different WDM models and standard CDM. The particle masses, $m_{\rm wdm} \in \{0.3, 0.5, 0.7, 1.0, 1.4\}\,$keV are color coded with blue, cyan, green, red and magenta respectively. The crosses correspond to the free-streaming wavenumber, $k_{\rm fs}$, for each model of WDM. The wiggles at $k \sim 0.1$ are due to baryonic acoustic oscillations and the peak at $k \sim 0.01$ corresponds to radiation-matter equality. on the left hand side of this peak, the slope corresponds to the fractal primordial power spectrum from inflation, where $P_\delta(k) \propto k$.

(see Boyanovsky et al. (2008) for a calculation of the transfer function for a general initial thermal distribution of DM particles - cold WIMP dark matter, thermal fermionic or bosonic dark matter). The linear power spectrum, $P_{\rm wdm}(k)$, must then be normalised to ensure the value σ_8^2 at $k = 1/8\,h{\rm Mpc}^{-1}$ (see also Bardeen, 1985). Finally we now can plot the linear matter power spectra in fig. (2.3). The lightest WDM particle mass shown (250 eV) causes the linear theory matter power spectrum to fall dramatically at a wavenumber significantly above 1 $h{\rm Mpc}^{-1}$. The matter power spectrum of WDM starts to turn off well above the free-streaming scale, which changes the slope of the power spectrum to fall much more steeply than $n_{\rm eff} = \log P(k)/\log k = -3$, which is the slope for standard, bottom-up structure formation (Knebe et al., 2003; White & Frenk, 1991).

In fact the above seemingly artificial scale break, α relates to the free-streaming length of thermal relic warm dark matter particles (Zentner & Bullock, 2003):

$$\lambda_{\rm fs} \simeq 0.11 \left[\frac{\Omega_{\rm wdm} h^2}{0.15}\right]^{1/3} \left[\frac{m_{\rm wdm}}{\rm keV}\right]^{-4/3} {\rm Mpc} \quad , \tag{2.50}$$

which of course is related to the free-streaming scale:

$$k_{\rm fs} = 5\,{\rm Mpc} \left(\frac{m_{\rm wdm}}{\rm keV}\right) \left(\frac{T_\nu}{T_{\rm wdm}}\right) \quad , \tag{2.51}$$

which is plotted in fig. (2.3) and around which the significant suppression of the power in the linear matter power spectrum begins.

Now that we are familiar with the effects of WDM on the linear matter density field we must discuss the standard model of structure formation. In the matter dominated era, the density contrast grows and eventually reaches unity. From this point on, standard perturbation theory is no longer appropriate and we must employ approximation methods as exact solutions to the Einstein field equations no longer exist. We discuss this in the next chapter.

CHAPTER 3

The Present-day Structure

Being present day astronomers Klypin et al. (1999) noticed a discrepancy in the observed numbers of the smallest galaxies, assumed to reside within dark matter haloes with masses $M_{\text{dwarf}} \leq 10^9 M_\odot$ and what they expected these numbers to be from running their numerical simulations of structure formation (see also 3.2). The proposed that the numerical models used to run the simulations might be modified to account for this discrepancy, which has become known as the *dwarf galaxy problem* or *missing satellite problem*. To an extent this has been the case, since the N-body codes have improved significantly in the past two decades (e.g. Benitez-Llambay et al., 2012). In addition, modern surveys have found new faint objects (see this review of the problem Bullock, 2010, and references within). The gap in the numbers of small objects has therefore been closing from above an below.

One could therefore perhaps feel at ease that the issue will solve itself with better numerical prescriptions for the complex baryonic processes (see e.g. Brooks et al., 2012), if it weren't for several other issues. The density profiles and concentrations of individual haloes (Donato et al., 2009) as well as the properties of voids (Tikhonov et al., 2009) don't seem to match what one would expect from pure ΛCDM theory in that the theory again predicts too much power. It is unlikely that baryonic processes are responsible for the lack of power in voids, as the density there is too low for baryonic pressure of any kind to influence the total gravitational potentials.

An elegant solution would be to introduce a simple ΛWDM model with one additional parameter, which would explain all of these discrepancies at once. Because of its free-streaming, WDM is capable to dampen the density field on small scales without any changes to the large scale behaviour of structure or to the dynamical evolution of spacetime. For this reason we wish to now consider how to calculate nonlinear corrections to predict the statistical properties of cosmological structure as would be observed today. This is not a straightforward task, but nonetheless, in the following chapters, we attempt to develop a prescription valid also in ΛWDM models that may be used one day to account for the discrepancies in the small scales of ΛCDM, by comparison with galaxy and weak lensing surveys.

The theories of the origin, contents and dynamics of the universe we follow today are able to paint a relatively accurate analytical picture of the universe between shortly after the Big Bang until the end of linearity. At those times the universe is well described as filled with more-or-less homogeneous distribution of matter and radiation. However, as anyone can clearly observe, the place and time we live in could hardly seem further from this description. When we observe the sky we see planets, stars, galaxies, arranged into galaxy clusters, superclusters, filaments and sheets. And only on the largest scales, if we recall the far-sighted Hubble giant, has the universe not changed much and remains describable by mere perturbations in the density. Unfortunately, astronomers only exist today; at a time when a perturbative description can no longer be used to describe the distribution of matter on, in fact, most scales relevant to astronomy.

In the previous chapter (ch 2), we've discussed how to describe the universe up until around the time of matter-radiation equality. Up until this time, the radiation dominates the contents of the universe and dictates the expansion of the background metric. This in turn determines the evolution of the amplitudes of the perturbations in the density of the matter components (δ_i). So far, we have been able to describe the universe by considering its homogeneous contents with linear perturbations in the density added on top. However, as the matter-radiation equality approaches at:

$$1 \equiv \frac{\bar{\rho}_{\mathrm{m},0} a_{\mathrm{eq}}^3}{\bar{\rho}_{\mathrm{r},0} a_{\mathrm{eq}}^4} \qquad \Rightarrow \qquad a_{\mathrm{eq}} = \frac{\bar{\rho}_{\mathrm{m},0}}{\bar{\rho}_{\mathrm{r},0}} = \frac{1}{1+z_{\mathrm{eq}}} \qquad , \tag{3.1}$$

which follows from the background evolution equation or Friedmann Equation, eq. (1.20), the linear approximation becomes less and less appropriate.

3.1 The halo model

The halo model is a way to account for nonlinear structure growth. It is based on the spherical collapse model, where the overdensities of the matter density field collapse as spherically symmetric objects. In the most rudimentary form, the halo model assumes that all matter can be found within dark matter *haloes*, which merge into larger and larger haloes with time, stopping only around the present time, when further nonlinear collapse is halted by the domination of Dark Energy and the re-start of accelerated expansion.

In order to describe non-linear structure with the halo model, we first need to find some of the parameters derived from spherical collapse, which determine the density contrast needed for collapse. These can be found with fitting functions collected in Henry (2000), where

$$\delta_c(\Omega_{\mathrm{m},0}, z) = \frac{3(12\pi)^{2/3}}{20}\left[1 - 0.0123\log(1+x^3)\right] \qquad \text{with} \qquad x \equiv \frac{\left(\Omega_{\mathrm{m},0}^{-1} - 1\right)^{1/3}}{1+z} \tag{3.2}$$

is the linear overdensity needed for the collapse of a spherical perturbation at redshift z. Note that this is not the same $\delta_c(c)$, which equals the square brackets in eq. (3.27), and is a function of the halo concentration parameter, $c(M, z)$ from eq. (3.19). The density contrast of collapsed objects is:

$$\Delta(\Omega_{\mathrm{m},0}, z) = 18\pi(1 + 0.4093x^{2.71572}) \qquad , \tag{3.3}$$

being the ratio of the average density of a halo to the background density **at the virialization redshift**. Therefore the average halo density $\bar{\rho}_{\mathrm{h}}(z) = \Delta(z)\rho_{\mathrm{m}}(z)$, assuming we observe the halo at approximately the virialization redshift.

Today, for the WMAP7 value of $\Omega_{\mathrm{m},0} = 0.266$, we get $\delta_{\mathrm{c}}(z = 0) \approx 1.659$ and $\Delta(z = 0) \approx 115$. Note here that this does not change the results much in comparison with the closed model ($\Omega_{\mathrm{m},0} = 1$), where $\delta_{\mathrm{c}}(1, z) \approx 1.686$ and $\Delta(1, z) \approx 177.7$.
However, the value used for $\Delta(z)$ really only depends on the convention used in the simulations that yielded the mass functions! See for example figure (5) in White (2002)[1] or Hu & Kravtsov (2003), which indicated that taking $\Delta = 180$ seems to match the simulations Sheth-Tormen the best. Therefore if using such theoretical mass functions it seems consistent with convention to use this last value for the density contrast.

Root-mean-square fluctuation

A further parameter we should consider is the '*variance* of the smoothed matter density field, $\sigma(R)$. It is a function of **comoving** length, R, which is defined by the size of the smoothing function, in this case a top-hat window function:

$$W(x) = \frac{3(\sin(x) - x\cos(x))}{x^3} \qquad . \tag{3.4}$$

Then the rms fluctuation of a Gaussian field described by it's power spectrum P(k), calculated in eq. (2.37), is:

$$\sigma^2(R) = \int P(k, z = 0)\, |W(Rk)|^2 \frac{k^3}{2\pi} d\ln k \qquad . \tag{3.5}$$

In order to associate particular halos with particular values of $\sigma(R)$, we need to connect the size of the window function, R, to the halo mass, M. For this we should realise that R is the size of the comoving region (i.e. the region at present times), which contains the amount of matter accounting fully for the mass of the associated halo. A comoving region will always contain the same of matter as it expands with the dilution of the density.

$$R(M) = \left(\frac{3M}{4\pi\rho_{\mathrm{m},0}}\right)^{\frac{1}{3}} \qquad \text{with} \qquad \rho_{\mathrm{m},0} = \Omega_{\mathrm{m},0}\, \rho_{\mathrm{crit},0} \qquad . \tag{3.6}$$

Since we used the present-day matter power spectrum in eq. (3.5), we need to multiply $\sigma(R)$ by the growth factor (sec 2.3.2) in order to account for its dependence on redshift. So, $\sigma(R, z) = \sigma(R)D^+(z)$. Furthermore there should be no need to normalise this to $\sigma(R = 8\, h\mathrm{Mpc}^{-1}) = \sigma_8$, since the power spectrum is normalised already.

Mass functions

Unfortunately there exist several naming conventions for mass functions in literature, so let us first clear up our definitions: $\left|\frac{dn(<M)}{dM}\right| dM = n(M)dM$.

We use the Sheth & Tormen (1999) semi-analytic equations as an improvement to the Press & Schechter (1974) formalism to find the mass functions.

There are several different papers that contain the Sheth-Tormen equation. Unfortunately all their conventions differ slightly, so it is difficult to check for consistencies. The equation used is from Vale & Ostriker (2004):

$$n(M)dM = A\left(1 + \frac{1}{\nu^{2q}}\right)\sqrt{\frac{2}{\pi}}\frac{\rho_{\mathrm{m},0}}{M}\frac{d\nu}{dM}e^{-\nu^2/2}dM \qquad \text{with} \qquad \nu = \sqrt{a}\,\frac{\delta_{\mathrm{c}}}{D^+(z)\sigma(M)}, \tag{3.7}$$

---

[1] As suggested by Masahiro Takada online: `http://cosmocoffee.info/viewtopic.php?t=367&postdays=0&postorder=asc&highlight=virial+radius&start=15`.

where A is not the same as in the matter power spectrum calculation and is taken to be $A = 0.353$ as in Jenkins et al. (2001). Also, $a = 0.73$ and $q = 0.175$. $D^+(z)$ above is the linear growth factor found in sec. 2.3.2 and for $\sigma(M)$ is found with eq. (3.5). Also note that one needs to calculate:

$$\frac{d\nu}{dM} = -\frac{\nu}{M}\frac{d\ln\sigma}{d\ln M} \quad . \tag{3.8}$$

Alternatively one may use Takada & Jain (2003), where

$$n(M)dM = \frac{\rho_{\mathrm{m},0}}{M} A\left[1+(a\nu)^{-p}\right]\sqrt{(a\nu)}\,e^{-a\nu/2}\frac{d\nu}{\nu} \qquad \text{with} \qquad \nu = \left(\frac{\delta_{\mathrm{c}}(z)}{D^+(z)\sigma(M)}\right)^2 \tag{3.9}$$

and $p = 0.3$, $a = 0.707$ and $A \approx 0.129$, which comes from the normalisation of the mass function $\int_0^\infty d\nu f(\nu) = 1$, where

$$\nu f(\nu) \equiv n(M,z)\frac{M^2}{\rho_{\mathrm{m},0}}\frac{dlnM}{dln\nu} \qquad \Leftrightarrow \qquad n(M)dM = \nu f(\nu)\frac{d\nu}{\nu}\frac{\rho_{\mathrm{m},0}}{M} \quad , \tag{3.10}$$

is the relation given in the original paper, Sheth & Tormen (1999), together with the following version of the relation:

$$\nu f(\nu) = A\left(1+\nu'^{-p}\right)\left(\frac{\nu'}{2}\right)^{1/2}\frac{e^{-\nu'/2}}{\sqrt{\pi}} \quad , \tag{3.11}$$

where, for example, in Seljak (2000) the factor of $\sqrt{2\pi}$ gets absorbed into the constant A. Also, here, ν is as above and $\nu' = a\nu$, $a = 0.707$, $p = 0.3$ (these are the Sheth-Tormen fitting parameters). Also note that only in eq. (3.7) we have stated the fitting parameters from Jenkins et al. (2001). After equation eq. (3.9) we have stated the original parameters as in Sheth & Tormen (1999).

An interesting question may be whether one should normalise the mass function (as is recommended in Seljak (2000)):

$$\frac{1}{\rho_{\mathrm{m},0}}\int\frac{dn}{dM}MdM = \int f(\nu)d\nu = 1 \quad . \tag{3.12}$$

If yes, here we must normalise the mass function to the present-day matter density, since the mass function is defined per unit *comoving* density. However, since it is not accurate to assume that all matter is found within halos (today there should be $> 50\%$ of mass within halos, but $< 100\%$), it is better to avoid normalisation of the mass functions. In fact, since the size of halos is determined somewhat arbitrarily, in most cases normalisation of mass functions would be incorrect. We discuss this further in the second part of this thesis.

Bias

From Takada & Jain (2003) we can calculate the halo bias:

$$b(M) = 1 + \frac{a\nu - 1}{\delta_{\mathrm{c}}} + \frac{2p}{\delta_{\mathrm{c}}\left(1+(a\nu)^p\right)} \qquad \text{with} \qquad \nu = \left(\frac{\delta_{\mathrm{c}}(z)}{D^+(z)\sigma(M)}\right)^2, \tag{3.13}$$

which must be normalised according to Seljak (2000) as $\int b(\nu)f(\nu)d\nu = 1$. Note that the convention for ν here is the same as in eq. (3.25) above.

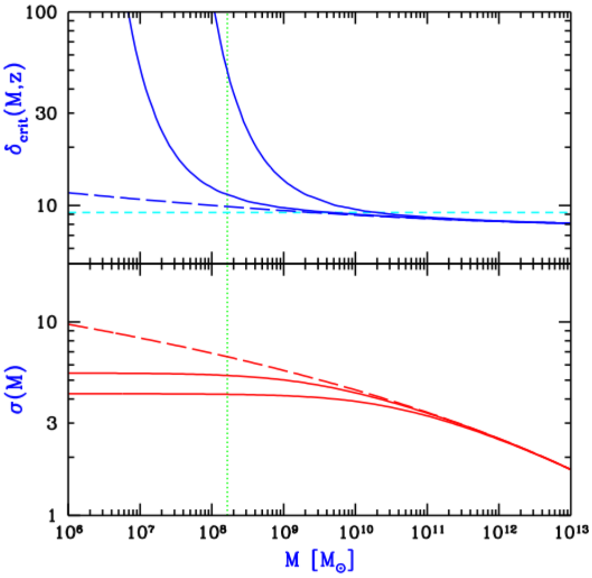

FIGURE 3.1: The overdensity required for the collapse of a halo, δ_c (eq 3.2) and the root-mean-square fluctuation at the scale of the radius of a spherical volume containing the mass, M, $\sigma(M)$ (eq 3.5) against mass in solar masses, $M_\odot$.
FIGURE SOURCE: Barkana et al. (2001).

Non-linear mass scale

The non-linear mass scale is defined to be the maximum mass that is undergoing non-linear collapse at a given redshift. Then have from Seljak (2000) for example:

$$\nu(M_*) = \left(\frac{\delta_c(z)}{D^+(z)\sigma(M_*)}\right)^2 = 1 \quad . \tag{3.14}$$

Distances and comoving volume

The equations for cosmological distances are from Hogg (1999) and sec. 1.2.3. Firstly one needs the Hubble distance, $d_H = c[\,\mathrm{km\ s^{-1}}]/H_0[\,\mathrm{km\ s^{-1}\ Mpc^{-1}}]$, where square brackets indicate the units. Then to find the line-of-sight comoving distance, which in the flat case equals the transverse comoving distance, d_M and the comoving angular diameter distance :

$$d = d_H \int_0^z \frac{dz'}{E(z')} = d_M \tag{3.15}$$

where the function $E(z)$ is defined as:

$$E(z) \equiv \sqrt{\Omega_{m,0}(1+z)^3 + \Omega_{k,0}(1+z)^2 + \Omega_{de,0}} \quad , \tag{3.16}$$

for the case, where $w = -1$. From this we calculate the angular diameter distance:

$$d_A = \frac{d_M}{(1+z)} \quad . \tag{3.17}$$

Furthermore, we shall need the differential comoving volume to multiply the mass functions, which are defined per unit comoving volume:

$$\frac{dV}{d\Omega\, dz} = d_{\mathrm{H}} \frac{(1+z)^2 d_{\mathrm{A}}^2}{E(z)} \quad . \tag{3.18}$$

Here $d\Omega$ denotes the increment in the solid angle.

Concentration parameter

Seljak (2000) parametrise the concentration parameter dependence on the halo mass as:

$$c(M) = c_0 \left(\frac{M}{M_*}\right)^{\beta} \quad , \tag{3.19}$$

where to combine with Sheth-Tormen mass functions, they set $c_0 = 10$ and $\beta = -0.2$ and M_* is calculated in eq. (3.14). Note however that they set $\Delta = 200$ to be the density contrast defining the span of halos, whereas we use the function for $\Delta(z)$ from Henry (2000), or as it turns out to be best, $\Delta = 180$ (see beginning of this chapter). Furthermore Seljak (2000) warns that: "both PS and ST assume that each mass element belongs to only one halo, counting only the isolated halos. This is certainly a valid description on large scales, where the total halo mass determines the white noise amplitude of the power spectrum. On small scales the clumpiness caused by subhaloes within the halos may become important. Recent numerical simulations have in fact shown that most of the small halos that merge into larger ones are not immediately destroyed, but stay around for some time until they are finally merged on the dynamical friction time scale. In such a case a given mass particle can be part of more than one halo at any given time. Because on very small scales the correlation function is dominated by the small halos it may make a difference whether the mass is smoothly distributed within the halos or some fraction of it is in the subhaloes. However, the contribution to the total mass of the halo coming from the subhaloes is below 10%. Recently, the mass function for subhaloes from high resolution simulations was determined and it was shown that it is an order of magnitude below the one for isolated halos."

We use a modified redshift-dependent concentration parameter as in Cooray et al. (2000):

$$c(M,z) = a(z) \left(\frac{M}{M_*(z)}\right)^{b(z)} \quad , \tag{3.20}$$

where $a(z) = 10.3(1+z)^{-0.3}$ and $b(z) = 0.24(1+z)^{-0.3}$, reproducing the final power spectrum to within 20% for wavenumbers $0.0001 < k < 500$ Mpc^{-1} for redshifts, $z < 1$.

Virial radius

The virial radius defining the halo sizes:

$$r_v(M,z) = \left(\frac{3M}{4\pi\Delta(z)\rho_m(z)}\right)^{1/3} \tag{3.21}$$

and converted into an angle on the sky by dividing with the comoving distance to the halo: $\theta_v(M,z) = r_v(M,z)/d(z)$. Note that we use $\Delta(z) = \Delta = 180$!

NFW halo profile

The NFW density profile is:

$$\rho(r) = \frac{\rho_s}{\frac{r}{r_s}\left(1 + \frac{r^2}{r_s^2}\right)} \qquad \text{with} \qquad r_s(M,z) = \frac{r_v(M,z)}{c(M,z)} \tag{3.22}$$

and

$$\rho_s(M,z) = \frac{\Delta(z)\rho_m(z)}{3}\frac{c(M,z)^3}{\left[\ln(1+c(M,z)) - \frac{c(M,z)}{1+c(M,z)}\right]} \quad , \tag{3.23}$$

where $\Delta(z)$ is calculated using eq. (2.39). The parameter r_s determines where the NFW halo density profile changes from a power law. The above must correspond to a halo mass:

$$M = \frac{4\pi\rho_s r_v^3}{c^3}\left[\ln(1+c(M,z)) - \frac{c(M,z)}{1+c(M,z)}\right] = \frac{4\pi r_v^3}{3}\Delta(z)\rho_m(z) \quad . \tag{3.24}$$

3.1.1 The halo model nonlinear power spectrum

We use the Sheth-Tormen (Sheth & Tormen, 1999) mass function (see also Seljak, 2000; Takada & Jain, 2003)):

$$n(M)dM = \frac{\rho_{\mathrm{m},0}}{M}A\left[1+(a\nu)^{-p}\right]\sqrt{(a\nu)}\,e^{-a\nu/2}\frac{d\nu}{\nu} \qquad \text{with} \qquad \nu = \left(\frac{\delta_c(z)}{D^+(z)\sigma(M)}\right)^2 , \tag{3.25}$$

where $A = 0.353$ as in Jenkins et al. (2001). Also, $a = 0.73$ and $p = 0.175$. $D^+(z)$ above is the linear growth factor and $\sigma(M)$ is root-mean-square fluctuation in a sphere of volume containing a mass M in a smooth universe, calculated from the linear power spectrum. δ_c is the critical threshold for a linear density fluctuation to collapse to form a halo (see eq. 3.2), calculated from spherical collapse.

From Takada & Jain (2003) the bias consistent with the Sheth-Tormen mass functions:

$$b(M) = 1 + \frac{a\nu - 1}{\delta_{\mathrm{c}}} + \frac{2p}{\delta_{\mathrm{c}}\left(1+(a\nu)^p\right)} \qquad \text{with} \qquad \nu = \left(\frac{\delta_{\mathrm{c}}(z)}{D^+(z)\sigma(M)}\right)^2 , \tag{3.26}$$

which must be normalised according to Seljak (2000).

The non-linear mass scale, $M_*(z)$ is defined to be the maximum mass that is undergoing non-linear collapse at a given redshift. As mentioned above, we require the threshold for the linear density perturbations to collapse and form a halo. This was given by Henry (2000) above. The density contrast of collapsed objects to the background mass density is taken to be $\Delta(\Omega_{\mathrm{m},0}, z) = 180$. The halo density profile is taken to be the Navarro-Frenk-White (NFW, Navarro et al., 1997) profile and halo mass is defined as:

$$M = \frac{4\pi r_{\mathrm{v}}^3}{3}180\rho_{\mathrm{m}}(z) \quad . \tag{3.27}$$

The NFW profile, like other ingredients of the halo model is calculated from ΛCDM models. Other halo profiles have been explored by e.g. Alam et al. (2002). The halo profile is a function of the halo concentration parameter, c(M,z).

In order to calculate the full power spectrum characterising the statistics of the density field (see also app. A), one can then use the equations given for example in equations (45) and (49) of Smith et al. (2003) (but also Cooray et al., 2000; Seljak, 2000, etc.):

$$P_{\mathrm{nl}}^{\mathrm{P}}(k,z) = \frac{1}{(2\pi)^3}\int dM\frac{dn}{dM}\left[\frac{\tilde{\rho}(k,M,z)}{\rho_{\mathrm{m},0}}\right]^2 \tag{3.28}$$

$$P_{\mathrm{nl}}^{\mathrm{C}}(k,z) = P_{\mathrm{lin}}(k,z)\left[\int dM\frac{dn}{dM}b(M,z)\frac{\tilde{\rho}(k,M,z)}{\rho_{\mathrm{m},0}}\right]^2 \quad , \tag{3.29}$$

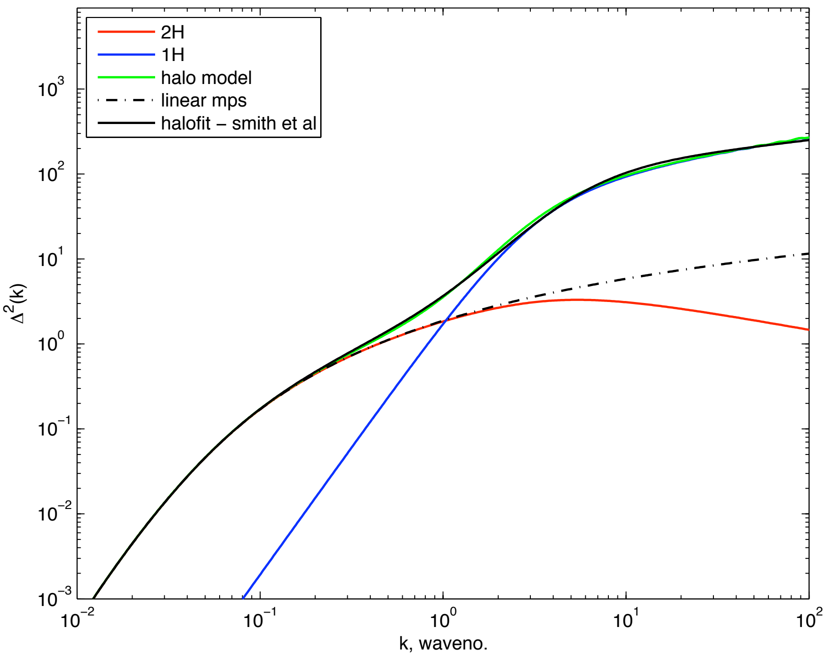

Figure 3.2: Dimensionless matter power spectra using the two different methods; the halofit method by Smith et al. (2003) and the full halo model, z = 0.0.

where $\tilde{\rho}(k, M, z)$ is the 3D Fourier transform of the NFW halo density profile. Note that to get the full non-linear power spectrum we must add the 1-halo and 2-halo contributions: $P_{\rm nl}(k, z) = P_{\rm nl}^{\rm P}(k, z) + P_{\rm nl}^{\rm C}(k, z)$. This is plotted in fig. 3.2.

3.1.2 The `halofit` formula

The non-linear matter density power spectrum in its dimensionless form

$$\frac{d\sigma^2}{d\ln k} \equiv \Delta_{\rm nl}^2(k) = \frac{k^3 P_{\rm nl}(k)}{2\pi^2} \qquad , \tag{3.30}$$

can be calculated using the fitting function found by Smith et al. (2003), which improves on the previous fit by Peacock & Dodds (1996). It is a fit to N-body simulations based on the halo model and so, the power spectrum is decomposed into the "quasilinear" and "halo" terms:

$$\Delta_{\rm nl}^2(k) = \Delta_{\rm Q}^2(k) + \Delta_{\rm H}^2(k) \qquad , \tag{3.31}$$

where the general fitting functions in terms of the variable $y \equiv \frac{k}{k_\sigma}$ and the function $f(y) = \frac{y}{4} + \frac{y^2}{8}$ are:

$$\Delta_{\rm Q}^2(k) = \Delta_{\rm lin}^2(k) \left[\frac{(1 + \Delta_{\rm lin}^2(k))^{\beta_n}}{1 + \alpha_n \Delta_{\rm lin}^2(k)} \right] e^{-f(y)} \tag{3.32}$$

and

$$\Delta_{\rm H}^2(k) = \frac{1}{1 + \mu_n y^{-1} + \nu_n y^{-2}} \left[\frac{a_n y^{3 f_1(\Omega)}}{1 + b_n y^{f_2(\Omega)} + [c_n f_3(\Omega) y]^{3-\gamma_n}} \right] \qquad . \tag{3.33}$$

The fitting coefficients are:

$$\alpha_n = 1.3884 + 0.3700n - 0.1452n^2 \tag{3.34}$$
$$\beta_n = 0.8291 + 0.9854n + 0.3401n^2 \tag{3.35}$$
$$\gamma_n = 0.8649 + 0.2989n - 0.1631C \tag{3.36}$$
$$\log_{10}\mu_n = -3.5442 + 0.1908n \tag{3.37}$$
$$\log_{10}\nu_n = 0.9589 + 1.2857n \tag{3.38}$$

as well as

$$\log_{10} a_n = 1.4861 + 1.8369n + 1.6762n^2 + 0.7940n^3 + 0.1670n^4 - 0.6206C \tag{3.39}$$
$$\log_{10} b_n = 0.9463 + 0.9466n + 0.3084n^2 - 0.9400C \tag{3.40}$$
$$\log_{10} c_n = -0.2807 + 0.6669n + 0.3214n^2 - 0.0793C \tag{3.41}$$

and for a flat universe with $\Omega_\mathrm{m} + \Omega_\Lambda = 1$,

$$f_1(\Omega_\mathrm{m}) = \Omega_\mathrm{m}^{-0.0307} \quad , \quad f_2(\Omega_\mathrm{m}) = \Omega_\mathrm{m}^{-0.1423} \quad \text{and} \quad f_1(\Omega_\mathrm{m}) = \Omega_\mathrm{m}^{0.0725} \quad . \tag{3.42}$$

The parameters of the spectrum are calculated in terms of the Gaussian-filtered spectral variance,

$$\sigma_\mathrm{G}^2(R) \equiv \int \Delta_\mathrm{lin}^2(k) e^{-k^2R^2} d\ln k \tag{3.43}$$

are the following: k_σ is defined by $\sigma_\mathrm{G}(k_\sigma^{-1}) \equiv 1$, n in the above equations is the effective spectral index calculated from the slope of the power spectrum and C is the second derivative and is the spectral curvature

$$n_\mathrm{eff} \equiv -3 - \left.\frac{d\ln\sigma_\mathrm{G}^2(R)}{d\ln R}\right|_{\sigma_\mathrm{G}(R)=1} \quad \& \quad C \equiv - \left.\frac{d^2\ln\sigma_\mathrm{G}^2(R)}{d\ln R^2}\right|_{\sigma_\mathrm{G}(R)=1} \quad , \tag{3.44}$$

and $\Delta_\mathrm{lin}^2(k)$ is the dimensionless linear matter power spectrum.

3.2 Numerical methods

In the above sec. 3.1, we have seen an attempt of describing the evolution of density perturbations in the universe. In order to solve eq. (2.9) we have however had to make some severe simplifying assumptions. These assumptions have restricted us to only the simplest systems, treating a density perturbation as a single, highly symmetrical object that collapses. In order to be able to not only find better descriptions of the collapse of individual objects, but to also to truly understand their clustering, we need to do better.

Therefore, we must be able to calculate the evolution of the linear power spectrum through the non-linear regime. We still can make some simplifying assumptions: we know that collapsing matter is non-relativistic ($\rho \gg P$) and we know that collapse is only possible on sub-horizon scales ($k \gg aH$). This means that in ΛCDM, we can stick to the non-relativistic, Newtonian perturbation equations and so, the collisionless Boltzmann equation (eq 2.18):

$$\frac{df}{dt} = \frac{\partial f}{\partial t} + \boldsymbol{v}\frac{\partial f}{\partial \boldsymbol{x}} - \frac{\partial \Phi}{\partial \boldsymbol{r}}\frac{\partial f}{\partial \boldsymbol{v}} \tag{3.45}$$

and the non-relativistic version of the Poisson equation, which becomes the below, since in this regime, our coordinates are comoving with the fluid and hence the velocity term from eq. (2.12) vanishes:

$$\nabla^2\Phi(\boldsymbol{r},t) = 4\pi G \int f(\boldsymbol{r},\boldsymbol{v},t)d\boldsymbol{v} \tag{3.46}$$

should be solved (Springel et al., 2001). It is difficult to achieve this simply with *finite difference methods*, so Monte Carlo like N-body simulations are employed to integrate the Boltzmann equations of N particles populating the phase space, using the *method of characteristics*[2].

The dynamics of any group of collisionless particles interacting only through gravity can be described by the following *Hamiltonian*, $H(\boldsymbol{p}_1...\boldsymbol{p}_N, \boldsymbol{x}_1...\boldsymbol{x}_N, t)$:

$$H = \sum_i^N \frac{\boldsymbol{p}_i^2}{2m_i a^2(t)} + \frac{1}{2}\sum_{ij}^N \frac{m_i m_j \varphi(\boldsymbol{x}_i - \boldsymbol{x}_j)}{a(t)} \quad , \tag{3.47}$$

where the Newtonian potential is a sum over the discretised potentials, φ:

$$\phi(\boldsymbol{x}) = \sum_i^N m_i \varphi(\boldsymbol{x} - \boldsymbol{x}_i) \quad . \tag{3.48}$$

Here, the $\boldsymbol{x}_i$ are position vectors and $\boldsymbol{p}_i = a^2(t) m_i \boldsymbol{v}_i$ are the canonical momenta, $\boldsymbol{v}_i$ being the peculiar velocity of the individual particle i and we have switched back from conformal time, τ to cosmic time t for convenience.

A *periodic boundary condition* means that our cosmological box is surrounded by identical cosmological boxes for the sake of calculating forces on particles coming from beyond the simulation box. Assuming such a boundary condition in a box with a side L enables us to rewrite the Poisson equation in a discreet form as:

$$\nabla^2\varphi = 4\pi G \left(-\frac{1}{L^3} + \sum_{\boldsymbol{n}} \tilde{\delta}(\boldsymbol{x} - \boldsymbol{n}L) \right) \quad , \tag{3.49}$$

where the sum goes over all direction, $\boldsymbol{n}$ and $\tilde{\delta}$ is the “density” field of a single simulation particle, i.e. a delta-function, convolved with a particular *softening kernel*, characterised by a comoving length, ϵ.

3.2.1 The N-body code: `GADGET-2`

We want to in particular consider the descendant of the widely used `GADGET` code (Springel et al., 2001), called `GADGET-2` (Springel, 2005). In fact for simplicity and relevance to the topics covered in this thesis, we only consider the `GADGET-2` N-body code for DM-only simulations and for now ignore its capability to model baryonic physics through smoothed particle hydrodynamics (SPH).

---

[2] The method of characteristics is a way of solving partial differential equations by reducing them to a set of ordinary differential equations and integrating from a set of initial conditions. In other words the partial differential equations are solved by integration along *characteristic curves*, in this case the characteristic curves of the collisionless Boltzmann equation.

`GADGET` is a Lagrangian code, meaning that it does not calculate physical parameters, like pressure and density and their evolution at points on a mesh, but rather it assigns values of mass and force to individual particles that are then able to move through the comoving volume as well as generally through phase-space. In other words, Lagrangian codes discretise the mass rather than space and work with fluid particles. This has been chosen, because `GADGET` was written purposefully for the simulation of structure formation, where highly nonlinear inhomogeneities are relevant in most regimes and so it is highly advantageous that in Lagrangian codes, the resolution automatically increases with density. On the other hand, Eulerian, mesh-based approaches are significantly faster for near-homogeneous conditions and are often very useful especially when it comes to hydrodynamical calculations, for which the adaptive mesh refinement technique has been developed relatively recently (Bryan *&* Norman, 1997).

The main classification of `GADGET` is that it is a TreePM code, which means that it is a mixture of the two main approaches to summing the forces on the particles. The first approach is the hierarchical **tree algorithm**, the second is the **particle-mesh**.

The "tree" grouping algorithm is used in `GADGET`over alternatives, because it requires less internal memory storage and because its geometric properties mean that it can be used as a range-searching tool. Finally, it corresponds well with the space filling *Peano-Hilbert curve* used for splitting up the simulation, so it can run on many computer cores in parallel (*parallelisation*).

On the other hand, the particle-mesh method is a very fast scheme, but suffers from resolution issues for scales smaller than a mesh cell. Unlike the particle-mesh, the tree approach does not have an intrinsic resolution limit, but can be significantly slower. One possible improvement on the resolution of particle-mesh codes is adaptive refinement. However in the case of `GADGET`, the tree algorithm is utilised on small scales and the particle-mesh approach is applies on larger scales in order to achieve optimal synergy between the two methods.

The power of the tree-algorithm is to simplify the calculation of the potential field when the gravitational force acts over long distances (Appel, 1985). The tree is constructed with the BH algorithm (Barnes *&* Hut, 1986), in which the field of N *simulation particles* is divided in to nodes and sub-nodes, called branches and leaves. The "root" node is the entire simulation box and it is successively divided into eights until there is either one or no particles in the sub-node cube (see fig. 3.3). This tree is then used to sum over remote groups of particles, so that their gravitational force can be approximated as that coming from a single body at their centre of mass at the lowest order. This reduces the number of computations of force for N simulation particles to be $\sim \mathcal{O}(N \log N)$ as opposed to N^2 in direct force summation. Accuracy can be increased by including higher *multipole moments* of the gravitational potential field, however at some point it becomes more reasonable to consider the separate sub-nodes. In `GADGET-2`, after discarding the empty nodes, each node of this *oct-tree* either contains only one particle or is a progenitor to further nodes (or *siblings*), in which case the monopole moments of the gravitational potential field due to all the node's particles are calculated and stored.

The gravitational force is computed on a particle by *walking the tree*, which means for each particle the influences of the entire box are taken into account by decomposing it into nodes and finally expanding in multipoles of the gravitational potential as described above. In particular, a condition is defined for when further nodes must be opened as opposed to when the node is far enough to proceed with multipole expansion. This condition depends

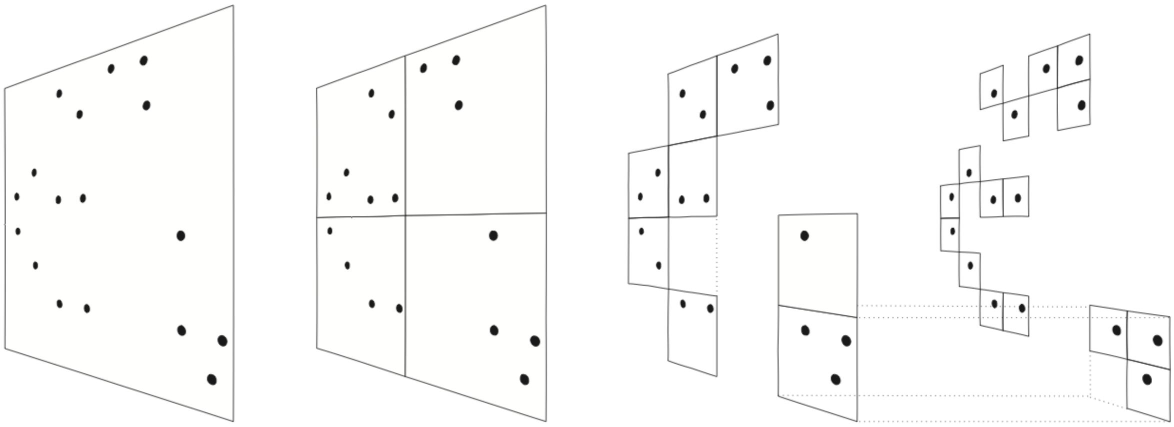

FIGURE 3.3: The tree-algorithm of Barnes & Hut (1986) in two dimensions. The root node on the left is subdivided into quarters until each sub-node contains either one or no particles. The nodes containing no particles are discarded.
FIGURE SOURCE: Springel et al. (2001)

on a user-defined *opening angle*, θ and is[3]

$$r > \frac{l}{\theta} \quad , \tag{3.50}$$

where r is the distance from the particle in question to the centre of the node and l is the length of the side of the node. If this criterion if fulfilled, the tree walk is terminated and multipole expansion follows. If not, the walk is continued by *opening* the node and its siblings. Both force computation inaccuracy and speed increase for larger values of the opening angle, θ. Therefore regulating this parameter regulates the efficiency of the code and yields the errors on the force calculations.

`GADGET-2` in fact uses a relative node-opening criterion, which adjusts to the dynamical state of the siimulation, where

$$\theta = \sqrt{\alpha \frac{|\boldsymbol{a}|r^2}{GM}} \quad , \tag{3.51}$$

where $|\boldsymbol{a}|$ is the acceleration in the last timestep of the simulation α is an adjustable *tolerance parameter* and M is the total mass contained in the node.

As mentioned above, `GADGET` is a TreePM code (Bagla & Ray, 2003), meaning that it splits the potential field and hence the force calculation in Fourier space into a long-range, $\tilde{\phi}^{\text{long}}(\boldsymbol{k})$ and short-range, $\tilde{\phi}^{\text{short}}(\boldsymbol{k})$, term (as seen in fig. 3.4). The Fourer transform of eq. (3.48) can then be written as,

$$\begin{aligned} \tilde{\phi}(\boldsymbol{k}) &= \tilde{\phi}^{\text{long}}(\boldsymbol{k}) + \tilde{\phi}^{\text{short}}(\boldsymbol{k}) \qquad \text{where} \\ \tilde{\phi}^{\text{long}}(\boldsymbol{k}) &= \tilde{\phi}(\boldsymbol{k}) \exp\{-\boldsymbol{k}^2 r_{\text{s}}^2\} \\ &\text{and} \\ \phi^{\text{short}}(\boldsymbol{x}) &= -G \sum_i \frac{m_i}{r_i} \text{erfc}\left(\frac{r_i}{2r_{\text{s}}}\right) \quad , \end{aligned} \tag{3.52}$$

---

[3] θ used to mean the divergence of the fluid velocity in the previous chapters, but is here in no way connected to that.

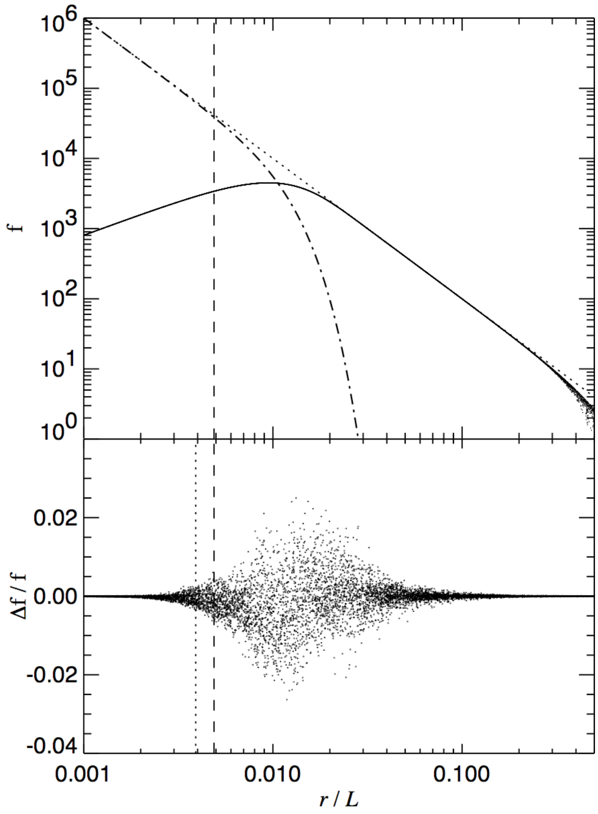

FIGURE 3.4: This figure plots the summed force (in the upper panel) and the error on the force (lower panel) against the distance between the particle and the node as a fraction of the box size. The split between the long- and short-range force is denoted by a vertical dashed line at r_s and the vertical doted line in the bottom panel denotes the mesh scale. In the upper panel on small scales, the dot-dashed line uses the tree set up and on large scales the solid line is calculated using the particle-mesh approach.
FIGURE SOURCE: Springel (2005)

where $r_i = \min(|\boldsymbol{x} - \boldsymbol{r}_i - \boldsymbol{n}L|)$ ensuring that only the closes version of each source of the same gravitational potential is counted in the periodic set up. The cumulative error function in this equation governs the transition into the short-range regime and the sum utilises the above described tree algorithm in real space. Note also that the split-scale, $r_\mathrm{s} \ll L$.

Time evolution of the simulation

The Hamiltonian for an N-body problem can usually be separated into a kinetic and a potential part: $H = H_\mathrm{k} + H_\mathrm{p}$. The time evolution of these separate terms can be computed exactly and can be described in terms of the *drift* and *kick* operators, where:

$$\textit{drift} \quad D_t(\Delta t) \quad : \quad \begin{cases} \boldsymbol{x}_i & \rightarrow \quad \boldsymbol{x}_i + \frac{\boldsymbol{p}_i}{m_i} \int_t^{t+\Delta t} a^{-2} dt \\ \boldsymbol{p}_i & \rightarrow \quad \boldsymbol{p}_i \end{cases} \tag{3.53}$$

$$\textit{kick} \quad K_t(\Delta t) \quad : \quad \begin{cases} \boldsymbol{x}_i & \rightarrow \quad \boldsymbol{x}_i \\ \boldsymbol{p}_i & \rightarrow \quad \boldsymbol{p}_i - \sum_j m_i m_j \frac{\partial \phi(\boldsymbol{x}_{ij})}{\partial \boldsymbol{x}_i} \int_t^{t+\Delta t} a^{-2} dt \end{cases} . \tag{3.54}$$

Now one can apply this operator splitting to approximate the total time evolution operator with either the drift-kick-drift (DKD) or kick-drift-kick (KDK) **leapfrog integrator**:

$$U(\Delta t) = \begin{cases} D(\Delta t/2) K(\Delta t) D(\Delta t/2) & \text{DKD} \\ K(\Delta t/2) D(\Delta t) K(\Delta t/2) & \text{KDK} \end{cases} . \tag{3.55}$$

Because in cosmological simulations the needed precision in the time integral varies depending on the density field, which has a very large dynamical range, it is useful to selectively apply

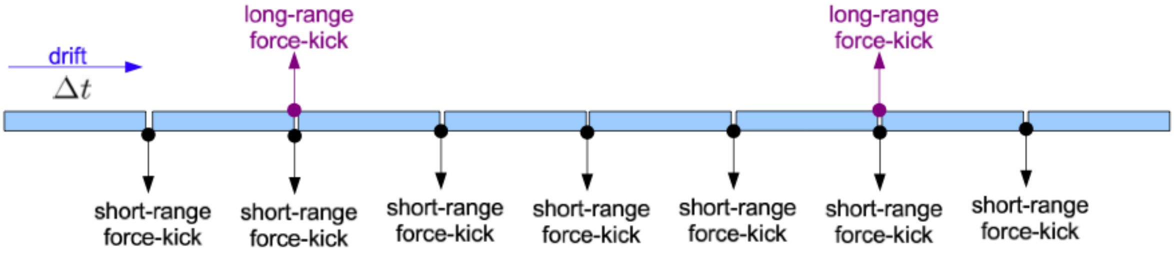

FIGURE 3.5: The leapfrog scheme of time stepping with short- and long- range *kicks*, and *drifts* to the point of the synchronisation.
FIGURE SOURCE: Springel (2005)

time steps of different lengths to different sets of particles in the simulation. This can be done with either individual time steps, which may induce a large overhead in memory or with adaptive time steps, which depend on the local density. Such time steps of course need to be synchronised every so often, which can be done most efficiently, if the time steps are discretised in a power of 2 hierarchy (see also fig. 3.5). Note also that the KDK leapfrog integration scheme turns out to be more numerically stable over several time steps.

Parallelisation of the code

It is beyond the scope of this thesis to discuss the details of parallelisation of computer programs, but it may be interesting to consider it in passing. The `GADGET-2` code is a *massively parallel code*, meaning that it treats the individual central processing units (CPU) of the multi-core computer as separate computers and assigns them all parts of the simulation volume to evolve, whilst trying to minimise the necessary amount of communication between the cores. This means that an appropriate domain-decomposition scheme must be used.

In the case of `GADGET-2`, the fractal, space-filling *Peano-Hilbert curve* is used to map the 3-dimensional simulation volume onto a 1-dimensional curve in order to insure any force error to be independent of the number of CPU (see fig. 3.6). Importantly and interestingly, any points that lie close to each other in the 1D curve are also located close to each other in the original 3D volume. Moreover, the Peano-Hilbert decomposition is very closely related to the BH oct-tree described above in that dividing the BH node into eight sub-nodes usefully yields the same particle grouping as dividing the Peano-Hilbert curve into eight equal lengths. Note also that the division of the volume needs not consist of equal parts, all the benefits of using this fractal curve are still applicable.

Performance

Finally be would like to briefly discuss the performance demands of this code in particular the CPU-time needed for cosmological simulation and the amount of memory consumed. The amount of RAM important to consider in the context deciding how many particles to use in the simulations. We refer to tab. (3.1) for two examples of needed CPU times.

It is also important to note that each dark matter particle in the simulation is described by 20 variable, which means for single precision, we use 20×4 bytes $= 80$ bytes per particle. In addition there are 12 variables per node and 4 additional variables for a secondary data

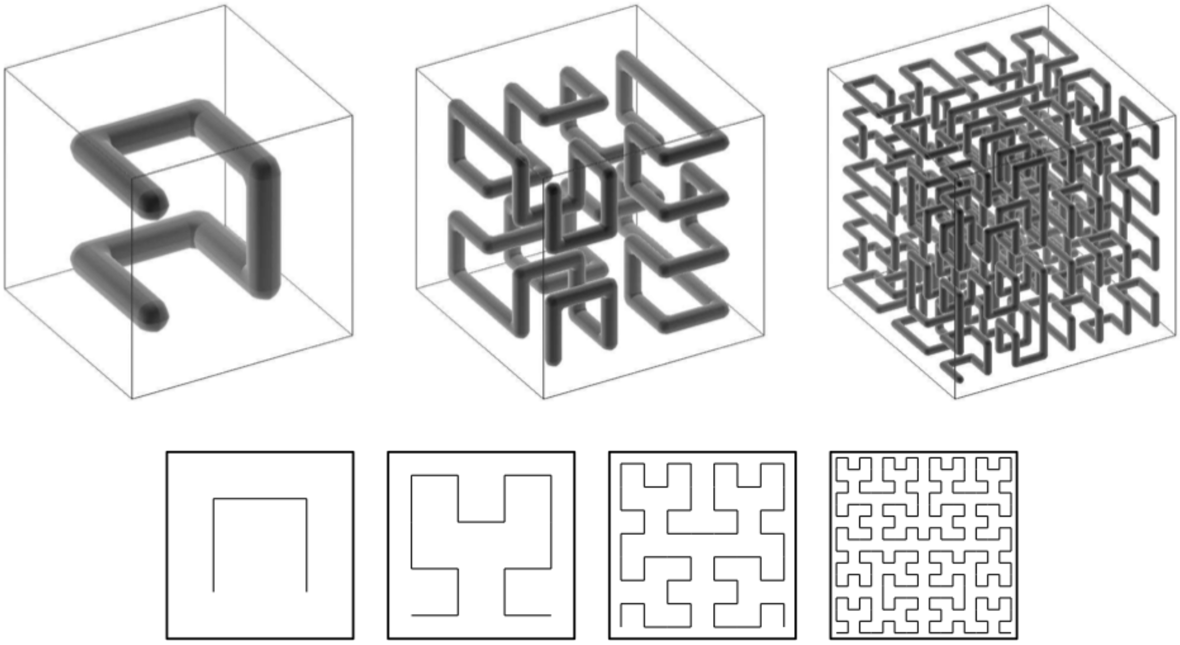

FIGURE 3.6: The fractal space-filling Peano-Hilbert curve is used for domain decomposition for the purpose of the parallelisation of the `GADGET-2` code. In the top panel is the 3D, in the bottom panel is the 2D curve.
FIGURE SOURCE: Springel (2005)

Boxsize (256^3 parts.)	256 h^{-1}Mpc	64 h^{-1}Mpc
timesteps	2648	5794
time	60600 s	173700 s
tree walk	52.8 %	41.0 %
tree construction	4.5 %	6.4 %
tree walk communication	0.9 %	1.6 %
work-load imbalance	6.7 %	14.4 %
domain decomposition	13.0 %	15.2 %
PM force	4.4 %	4.9 %
particle and tree drifts	5.3 %	4.9 %
kicks and timestepping	1.4 %	1.1 %
peano and ordering	8.0 %	7.8 %
other	2.9 %	2.6 %

TABLE 3.1: A table showing the CPU-time consumption for two example cosmological simulations running down to present time (z=0). TABLE SOURCE: Springel (2005)

structure. Typically 0.65 nodes per particle are needed, which means we add 42 bytes to the memory needed for each particle. In addition 4 variables per mesh-cell are needed for the PM part, needing up to 16 bytes per mesh-cell.

3.2.2 Hydrodynamics

It is significantly more complicated to describe the evolution of the density field of baryonic matter. This is because the assumption of the collisionless Boltzmann equation is no longer valid. The dynamics of the baryonic gas are modeled in `Gadget` with *smoothed particle hydrodynamics* (SPH). This is a common approach used by many Lagrangian codes (codes that model the density field as a fluid of discrete particles), because compared with mesh-based codes, they are better suited for the high dynamic range required by cosmological simulations.

The continuous quantities in the discretised simulation are then found by interpolation. A continuous function $f(\boldsymbol{r})$ is approximated by using a *smoothing kernel*, W (or window function):

$$\tilde{f}_h(\boldsymbol{r}) = \int f(\boldsymbol{r'}) W(\boldsymbol{r} - \boldsymbol{r'}, h) d^3 r' \quad , \tag{3.56}$$

with the smoothing length, h determining the width of the kernel, W. Besides being normailsed of course, the condition should hold that $W \to \delta_\mathrm{D}$, the Dirac delta, as $h \to 0$. To calculate the interpolated continuous density then, for example, we sum as:

$$\rho(\boldsymbol{r}) = \sum_n m_n W(\boldsymbol{r} - \boldsymbol{r}_n, h) \quad . \tag{3.57}$$

The simplest, usual form of the kernel is a cubic spline function, which is made to only depend on $|\boldsymbol{r} - \boldsymbol{r}'|$ i.e. a *radial kernel.*

In order to model the hydrodynamics one needs to use the perfect fluid Lagrangian to obtain the Euler equation and the first law of thermodynamics to describe the evolution of entropy. So far this all seems very familiar and is indeed related to what is done in purely dark matter simulations. The difference and complication can for example be seen in the Euler equation in Lagrangian form:

$$\frac{d\boldsymbol{v}}{dt} = -\frac{\nabla P}{\rho} + \boldsymbol{F} \quad , \tag{3.58}$$

where $\boldsymbol{F}$ entails gravitational, but also magnetic forces for example and where the first term indicates that the fluid is accelerated by pressure gradients, which is not the case in pure dark matter simulations.

This is an enormous topic and is far beyond the scope of this humble thesis, but if one wished to discuss it in more detail, we recommend for example the pedagogical review of Rosswog (2009). However, we should, for the sake of the coming discussion in ch. 6 briefly explain here that on top of including additional forces and pressure effect into the dynamical simulations, other physical processes may have to be included, depending on the system modeled.

For example, when considering the formation of cosmological structures, radiative cooling and heating as well as certain feedback processes can become extremely relevant, especially on the smallest scales in cosmological structure. This is the case so much so, that through gravitational effect, these processes can influence even the distribution of the dominant dark matter. A useful example of such processes may be that implemented by Viel et al. (2004), which models the radiative cooling by Hydrogen and Helium in the intergalactic medium (IGM) as well as a basic star formation mechanism. The star formation mechanism simply converts the gas particles whose temperatures are sufficiently low and whose densities are sufficiently high into collisionless stars. The cooling prescription follows that of Katz et al. (1996).

It has also recently been reported by the authors of the `OWLS` simulations (Semboloni et al., 2011; van Daalen et al., 2011, etc.) that the effects of baryonic processes, in particular the feedback from *active galactic nuclei* (AGN) can become dominant on scales that are significant to cosmology. This is certainly important issue to consider in the future.

3.3 Gravitational lensing by cosmological structures: cosmic shear

We have mentioned above that the presence of matter causes the spacetime to be curved. This means that the geodesic, i.e. light paths are not longer straight lines, causing a lens-like effect when looking at distant images of galaxies. This gravitational *lensing* lends itself to an interesting possibility of mapping out the 3D field of otherwise invisible dark matter density field, without relying much on an assumed relationship between the distribution of visible and dark matter in the universe. In particular, the very *weak gravitational lensing* induced in the background distribution of distant galaxy images is known as *cosmic shear* and is only detectable statistically. For this reason we wish to describe in this section how to theoretically calculate the weak lensing angular power spectrum, given a 3D dark matter power spectrum found in the previous sections (see also Bartelmann & Schneider, 2001). We are particularly interested in the future weak lensing survey Euclid (Amendola et al., 2012; Refregier et al., 2010). In fact we would like to consider how to find weak lensing power spectra from theory for when in several years the data becomes available. This is also useful for making predictions for constraints and measurements, which is what we do in the following chapters in this thesis.

3.3.1 Lensing by a single object

Let us first consider the contribution to cosmic lensing from a single object by looking at its projected density profile.

Critical surface density

At the distance to the centre of the lens halo, projected on the 2D sky-sphere and converted to an angle, θ, the lensing convergence, $\kappa(\theta)$ is obtained via the density profile of halos (NFW in this case), projected onto the sky-sphere, divided by the critical surface density, $\Sigma_{\rm crit}$:

$$\Sigma_{\rm crit} = \frac{c^2}{4\pi G}\frac{d_{\rm s}}{d_{\rm l} d_{\rm ls}}\frac{1}{(1+z_{\rm l})} \qquad , \tag{3.59}$$

where c here is the speed of light, the subscript l denotes a quantity related to the lensing halo and s to the source galaxy and the distances are comoving angular distances, which as mentioned above (fig 3.1), are equal to line-of-sight comoving distances in flat space.

2D projection of the NFW profile

In order to calculate the projected mass density $\Sigma(r_\perp)$ one needs to integrate $\rho(r)$ (see eq. 3.22) over the line of sight i.e. along the component of the radial vector, perpendicular to the line of sight. In order to do this integral, rewrite r as a dimensionless variable $x = \frac{r}{r_{\rm s}}$ & $dr = r_{\rm s} dx$ and decompose it into a perpendicular $x_\perp = \frac{r_\perp}{r_{\rm s}}$ and a parallel component $x_\parallel = \frac{r_\parallel}{r_{\rm s}}$:

$$\Sigma(x_\perp) = \int_{\rm halo} \rho\left(\sqrt{x_\perp^2 + x_\parallel^2}\right) dx_\parallel = \rho_{\rm s} r_{\rm s} \int_{\rm halo} \frac{dx_\parallel}{\sqrt{x_\perp^2 + x_\parallel^2}\left(1+\sqrt{x_\perp^2 + x_\parallel^2}\right)^2} \tag{3.60}$$

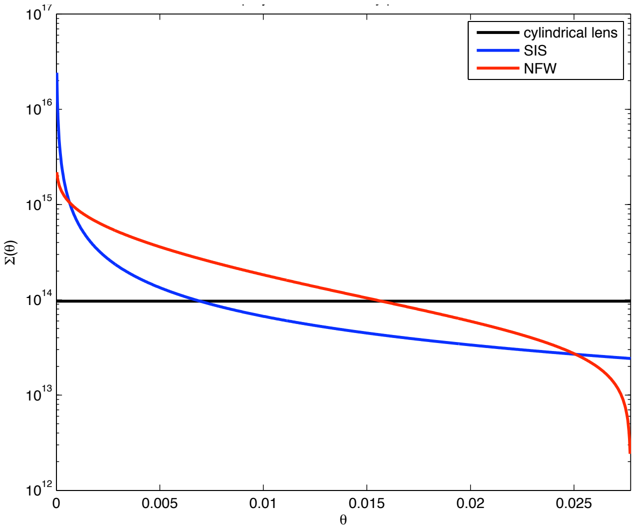

FIGURE 3.7: The projected density of three different halo density profile models, truncated at the virial radius and projected along the line-of-sight (see eq. 3.61).

Integrating over the entire halo means truncating the integral at the virial radius. We do the integral directly, with the limit becoming $x_{\|}^{\text{limit}} = \sqrt{c^2 - x_{\perp}^2}$, since $r_{\|}^{\text{limit}} = \sqrt{r_v^2 - r_{\perp}^2}$ and $c = r_v/r_s$. Then the solution is (as in Takada & Jain (2003)):

$$\Sigma(x_{\perp}) = 2\rho_{\mathrm{s}} r_{\mathrm{s}} \times \left\{ \begin{array}{ll} -\frac{\sqrt{c^2-x_{\perp}^2}}{(1+c)(1-x_{\perp}^2)} + \frac{1}{(1-x_{\perp}^2)^{3/2}} \text{arccosh}\left(\frac{x_{\perp}^2+c}{x_{\perp}(1+c)}\right) & (\text{if } x_{\perp} < 1) \\ \frac{(c+2)\sqrt{c-1}}{3(c+1)^{3/2}} & (\text{if } x_{\perp} = 1) \\ \frac{\sqrt{c^2-x_{\perp}^2}}{(1+c)(x_{\perp}^2-1)} - \frac{1}{(x_{\perp}^2-1)^{3/2}} \arccos\left(\frac{x_{\perp}^2+c}{x_{\perp}(1+c)}\right) & (\text{if } c > x_{\perp} > 1) \end{array} \right\} , \tag{3.61}$$

which we plot in fig. (3.7) along two simpler density profile models. Finally we find $\kappa(\theta)$:

$$\kappa(\theta, M, z_{\mathrm{l}}) = \frac{\Sigma\left(c\theta/\theta_{\mathrm{v}}\right)}{\Sigma_{\text{crit}}(z_{\mathrm{l}}, z_{\mathrm{s}})} \quad , \tag{3.62}$$

where z_{l} is the redshift of the lensing halo and z_{s} is the redshift of the source galaxies. Furthermore, $\theta = r_{\perp}/d_{\mathrm{l}}$ and note that c here is the concentration parameter.

2D Fourier transform of the NFW density profile

The solution to the $x_{\perp} = 0$ case is undefined since the integral diverges at the lower limit of $x_{\|} = 0$ & $x_{\perp} = 0$. As we can safely assume that the infinite density at the centre of a halo would be unphysical, we can assume it is somehow smoothened. Fortunately the entire 3D integral of the NFW density converges as we integrate over $\sim \rho(r) r^2 dr$. So in the integral over $\theta = x_{\perp} r_{\mathrm{s}}/d$ for the Fourier transformation of $\kappa(\theta)$ converges at 0:

$$\tilde{\kappa}(l) = 2\pi \int_0^{\theta_{\mathrm{v}}} \kappa(\theta) J_0\left(\left(\frac{1}{2} + l\right)\theta\right) \theta d\theta \tag{3.63}$$

The J_0 is the two-dimensional Bessel function of order 0. This is integrated numerically using the trapezium rule with 500 steps in θ, between $\theta = 0 \rightarrow \theta_{\rm v}$, the angular virial radius from eq. (3.21), which has been deemed to be accurate enough[4].

3.3.2 The weak lensing power spectrum

The power spectrum is made up of 2 terms, the 1-halo (or Poisson) term and the 2-halo (or correlations) term:

$$C_\kappa^{\rm P}(l) = \int_0^{z_{\rm s}} dz \frac{d^2V}{dzd\Omega} \int_{M_{\rm min}}^{M_{\rm max}} dM \frac{dn(M,z)}{dM} \left[\tilde{\kappa}(l,M,z)\right]^2 \tag{3.64}$$

and

$$C_\kappa^{\rm C}(l) = \int_0^{z_s} dz \frac{d^2V}{dzd\Omega} P\left(\frac{l}{d}, z\right) \left[\int_{M_{\rm min}}^{M_{\rm max}} dM \frac{dn(M,z)}{dM} b(M,z)\tilde{\kappa}(l,M,z)\right]^2 \quad , \tag{3.65}$$

where in order to project the matter power spectrum to 2D, the small angle (Limber, 1953; LoVerde & Afshordi, 2008) approximation has been made. .

Tomography

In this thesis we consider how to measure the WDM particle mass using observations of cosmic shear power spectra. From an observer's point of view, the image of each galaxy in the Universe is distorted by gravitational lensing effects of all intervening matter. Therefore the cosmic shear power spectra are closely related to the matter power spectrum integrated over redshift. Future surveys are expected to use broadband photometry to estimate the redshifts of the observed galaxies. This should allow shear power spectra to be calculated at a range of different redshifts, and also allow cross power spectra between redshifts (see Csabai et al., 2003, for a review).

The above sections assume all sources at the same redshift for simplicity, however we can expand the calculations to have a source redshift distribution and divide the source galaxies into redshift determined tomographic bins. We consider a cosmic shear survey which has a number of galaxies per unit redshift

$$n(z) = z^\alpha e^{-(z/z_0)^\beta} \quad , \tag{3.66}$$

(Smail et al. (1994)) where $\alpha = 2$, $\beta = 1.5$ and $z_0 = z_{\rm m}/1.412$, where $z_{\rm m} = 0.9$ is the median redshift of the survey. For example, this is reasonable for a EUCLID-like survey (Amara & Refregier (2007)). We assume a photometric redshift uncertainty of $\delta(1+z) = 0.05(1+z)$ and take top-hat photometric redshift bins containing equal numbers of galaxies (as in Amara & Refregier (2007)). We use 35 galaxies per square arcminute and take $f_{\rm sky}$, the fraction of the sky covered by the survey, to be a half. We assume there are no catastrophic outliers. We calculate power spectra at 20 spherical harmonic multipoles in the range $20 < \ell < 20000$ (roughly $0.0065 < k < 6.5$ at redshift 0.9, or down to scales of order 1 arcminute).

The lensing power spectra are given by

$$C_{ij}(l) = \int_0^{\chi_{\rm H}} d\chi_1 W_i(\chi_1) W_j(\chi_1) \chi_1^{-2} P_{\rm nl}\left(k = \frac{l}{\chi_1}, \chi_1\right) \quad , \tag{3.67}$$

---

[4] See app. B for a detailed calculation.

where $\chi_\mathrm{l}(z_\mathrm{l})$ is the comoving distance to the lens at redshift z_l and W_i is the lensing weight in the tomographic bin i:

$$W_i(z_\mathrm{l}) = \rho_{\mathrm{m},0} \int_{z_\mathrm{l}}^{z_\mathrm{max}} \left[\frac{n_i(z_\mathrm{s})}{\Sigma_\mathrm{crit}(z_\mathrm{l}, z_\mathrm{s})} \right] dz_\mathrm{s} \qquad , \tag{3.68}$$

where

$$\Sigma_\mathrm{crit}(z_\mathrm{l}, z_\mathrm{s}) = \frac{c^2}{4\pi G} \frac{\chi_\mathrm{s}}{\chi_\mathrm{ls}\chi_\mathrm{l}} \frac{1}{(1+z_\mathrm{l})} \qquad , \tag{3.69}$$

and the subscripts s, l and ls denote the distance to the source, the distance to the lens and the distance between the lens and source respectively.

In the halo model one can simplify the above equation using some approximations (e.g. Cooray & Hu, 2001) in the halo model non-linear matter power spectrum so that the lensing power spectra are made up of one-halo and two-halo terms,

$$C_{ij}(l) = C_{ij}^\mathrm{P}(l) + C_{ij}^\mathrm{C}(l) \qquad . \tag{3.70}$$

which are given by

$$\begin{aligned} C_{ij}^\mathrm{P}(l) &= \int_0^{z_\mathrm{max}} dz \frac{d^2V}{dz d\Omega} \int_{M_\mathrm{min}}^{M_\mathrm{max}} dM \frac{dn(M,z)}{dM} \tilde{\kappa}_i(l,M,z) \tilde{\kappa}_j(l,M,z) \\ C_{ij}^\mathrm{C}(l) &= \int_0^{z_\mathrm{max}} dz \frac{d^2V}{dz d\Omega} P\left(\frac{l}{\chi}, z\right) T_i(l,z) T_j(l,z) \\ T_i(l,z) &= \int_{M_\mathrm{min}}^{M_\mathrm{max}} \frac{dn(M,z)}{dM} b(M,z) \tilde{\kappa}_i(l,M,z) dM \qquad , \end{aligned} \tag{3.71}$$

(Cooray et al., 2000): where $\tilde{\kappa}_i(l, M, z)$ is the 2-dimensional Fourier transform of the lensing convergence for which one needs to integrate the NFW halo density profile (Navarro et al., 1997), truncating the integral at R_{180}, the spherical radius, where the density contrast, $\Delta = 180$. We use the analytic results given in Takada & Jain (2003). The lensing convergence signal in redshift bin i is found by the following equation:

$$\kappa_i(\theta, M, z_\mathrm{l}) = \int_{z_\mathrm{l}}^{z_\mathrm{max}} n_i(z_\mathrm{s}) \kappa(\theta, M, z_\mathrm{l}, z_\mathrm{s}) dz_\mathrm{s} \qquad . \tag{3.72}$$

In Takada & Jain (2004) we get the lensing weight to be:

$$W_i(\chi_l) = \frac{3}{2}\Omega_{m,0} H_0^2 \frac{\chi_l}{a_l} \int_{\chi_i}^{\chi_{i+1}} d\chi_s \frac{n(z_s)}{\bar{n}_i} \frac{dz_s}{d\chi_s} \frac{\chi_{ls}}{\chi_s} \qquad \text{for} \qquad \chi_l \leq \chi_{i+1} \quad \text{and} \quad \chi_l \leq \chi_s \qquad , \tag{3.73}$$

where the χ are comoving distances. Alternatively we can write:

$$W_i(\chi_l) = \frac{3}{2}\Omega_{m,0} H_0^2 \frac{\chi_l}{a_l} \int_0^{z_{max}} n_i(z_s) \frac{\chi_{ls}}{\chi_s} dz_s \qquad . \tag{3.74}$$

Then to calculate the cosmic shear (approximately - see Takada & Jain (2004)):

$$\kappa_i(\theta) = \int_0^{\chi_\mathrm{H}} d\chi W_i(\chi) \delta(\chi, \chi\theta) \qquad , \tag{3.75}$$

where δ is the matter density perturbation, and define the angular power spectrum:

$$\langle \tilde{\kappa}_i(\boldsymbol{l})\tilde{\kappa}_j(\boldsymbol{l'})\rangle \equiv 4\pi^2 \delta_{\mathrm{Dirac}}(\boldsymbol{l}-\boldsymbol{l'})C_{ij}(l) \qquad . \tag{3.76}$$

Finally we can find:

$$C_{ij}(l) = \int_0^{\chi_H} d\chi W_i(\chi)W_j(\chi)\chi^{-2}P_{\mathrm{nl}}\left(k=\frac{l}{\chi},\chi\right) \qquad , \tag{3.77}$$

where $P_{\mathrm{nl}}(k,\chi)$ is the 3D non-inear matter density power spectrum found in sec. 3.1.2 or sec. 3.1.1 at redshift corresponding to χ and the Limber (flat sky/small angle) approximation is used to project the 3D power spectrum wavenumbers, k onto multipoles of angular scales, l.

CHAPTER 4

Testing *Warm Dark Matter* with Cosmic Weak Lensing

This chapter corresponds closely to
Markovic, Bridle, Slosar & Weller,
Constraining Warm Dark Matter with Cosmic Shear Power Spectra,
published in 2011 in the Journal of Cosmology and Astroparticle Physics,
January issue, paper 022 (Markovič et al., 2011).

We are familiar with the effects on the linearly perturbed density field that are caused by the *free-streaming* of dark matter particles in the early universe, we have discussed it in ch. 2. We have described the statistical properties of the perturbed density field in terms of the *power spectrum*. The power spectrum of matter in a universe, where the dark matter particles had large thermal velocities at early times, becomes suppressed on small scales through this free-streaming (sec 2.3.3).

This chapter examines the methods to calculate the power spectrum of a perturbed density field after the perturbations have began nonlinear collapse in the matter *dominated era*, which we encountered in ch. 3, now in a new context. The measurements of Viel et al. (2008), who inferred a lower limit on the mass of the thermalised dark matter particle by examining the small scale power of the linear power spectrum, using Lyα forest data, can be enhanced by looking at the non-linear power spectrum.

We discuss in this chapter, the possibility of using the the statistical properties of the field of distortions due to gravitational lensing - the weak lensing power spectrum, which we discussed in sec. 3.3, to find the traces of the free-streaming of *warm dark matter*. In order to make predictions on how well future weak lensing surveys will be able to exclude or measure the mass of the thermalised dark matter particle, we however must extensively examine the methods employed in calculating the non-linear correction to our early universe power spectrum!

At first, in sec. 4.1, we use the established approaches for calculating non-linear corrections to the matter power spectrum and apply them to the warm-dark-matter-suppressed linear power spectrum. We begin by describing in more detail the "evaporation" of the seeds for low mass halos through free-streaming and write down an approximate halo mass limit. We do not try to develop a new model for non-linear WDM structure yet, we make an attempt of this later, in chapters 5 & 6. For now, we implement the halo model as described in sec. 3.1 into the WDM scenario and extrapolate the fitting formulae to CDM simulations in order to describe non-linear WDM structure. In sec. 4.2 we calculate the weak lensing power spectrum for CDM and different models of WDM. Predictions for a Euclid-like survey and the potential of such a survey to constrain the WDM particle mass are reported in sec. 4.3, where it is also examined why the standard statistical methods employed in basic forecasting are inappropriate for the parameter $m_{\rm wdm}$ and an attempt is made at developing an alternative.

We take a flat ΛCDM or ΛWDM Universe throughout, with parameter values of WMAP7 (Larson et al., 2011): the dimensionless Hubble expansion rate parameter, $h = 0.71$, the present day baryon density in units of the critical density, $\Omega_{\rm b} = 0.045$, the present day dark matter density in units of the critical density, $\Omega_{\rm m} = 0.27$, the cosmological constant energy density in units of the critical density, $\Omega_\Lambda = 0.73$ (all defined in eq. 1.33), the scalar primordial power spectrum slope, $n_{\rm s} = 0.96$ (defined in eq. 2.31), and the present day linear theory root-mean-square density fluctuation in $8\,h^{-1}$Mpc spheres, $\sigma_8 = 0.80$ (defined in eq. 3.5).

4.1 Non-linear corrections to the suppressed power spectrum

The measurements of the Lyα forest data, they have the advantage of not having to understand much of the complicated structure formation, but they have the disadvantage of probing the universe far away, meaning that small scales are not easily resolved and may be troubled by foreground effects and noise (e.g. Lee, 2012; Viel et al., 2009). In order to avoid being restricted to only the largest scales of the power spectrum one needs to look at the universe close by. Close objects that are relatively can obviously be more easily resolved, but due to the finiteness of the speed of light, they appear in a more advanced stage of evolution. For this reason, the structure we see relatively close to the Milky Way has become non-linear. Therefore, it is essential to understand non-linearity in order to examine the small scales of cosmological structure!

In order to supplement the Lyα constraints on the thermalised dark matter particle mass, we must look at the cosmological data of objects seen as they are close to the present time. An example of such a probe is gravitational lensing (see sec. 3.3), being also the only probe that does not rely on making assumptions about the coupling between dark and luminous objects.

4.1.1 Halo model with *warm dark matter*

As introduced in sec. 3.1, the halo model assumes that the Universe is made up of halos with positions sampled from the linear theory matter distribution. As a result, there are two main contributions to the non-linear matter power spectrum. Firstly, the two-halo term, which dominates on large scales, encodes the correlation between different haloes and is equal to the linear matter power spectrum on large scales. Secondly, the one-halo term refers to the correlations within a halo and therefore depends on the density profile of the halo. Both terms depend on the number of halos as a function of halo mass, which can be found to a reasonable approximation using analytic arguments or more usually measured from numerical simulations and modified according to the underlying matter power spectrum and in the context of weak lensing. For reasons of simplicity we retain the assumption of spherical collapse in our halo model calculations.

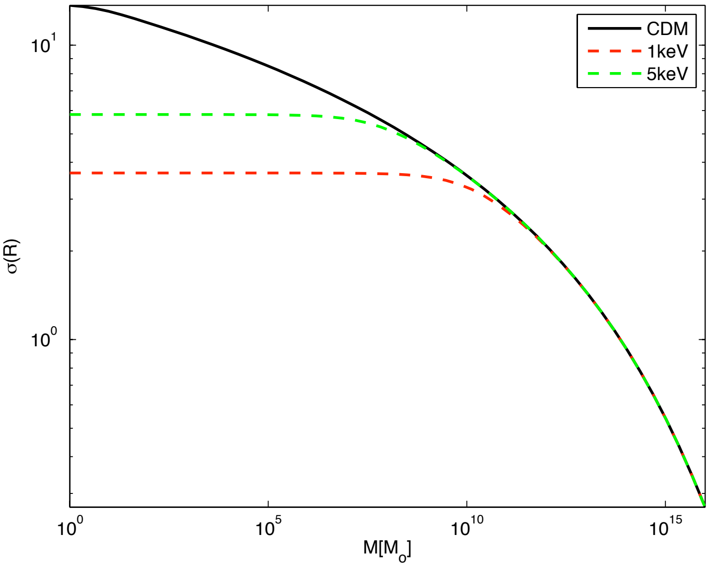

FIGURE 4.1: The root-mean-square density fluctuation for CDM (top, solid line), 1 keV WDM (bottom, dashed) and 5 keV (middle, dashed). The $\sigma(M)$ flattens off for the smallest halo masses in the WDM model, as one would expect for any smoothed field.

We extend the halo model to WDM scenarios by modifying the ingredients. We use the WDM linear power spectrum described in sec. 2.3.3 to calculate a new mass function using the Sheth *&* Tormen (1999) prescription (eq 3.11). We make the conservative assumption that the halo profiles are unchanged relative to CDM (see also app. B). It is in the one-halo term of the power spectrum that the effects of free-streaming of WDM are seen most strongly. This is because of the difference in the root-mean-square fluctuation, $\sigma(R)$, which becomes suppressed at small R in a WDM Universe (see eq. 3.5 and fig. 4.1).

We choose not to normalise the mass functions because the result of free-streaming is the suppression of the formation of small structures, not by accreting the excess matter onto larger haloes, but rather by resulting in a larger uncollapsed background matter density (see fig. 4.4). In contrast, we do normalise the halo bias by requiring

$$\frac{1}{\rho_{\mathrm{m},0}}\int b(M)\frac{dn}{dM}MdM = 1 \qquad . \tag{4.1}$$

This ensures that our model reproduces the linear predictions in the limit of $k \to 0$. We re-examine the justification for this normalisation in the next chapter (5).

We explore the effect of WDM on the mass functions in fig. 4.3. As expected, the number density for the smallest haloes is reduced in the case of WDM. This is shown most visibly in the lower panel of fig. 4.3 which shows the fractional suppression on a linear scale. This is useful for comparison to the general assumption of the absence of haloes below the *free-streaming halo mass*, defined as (Avila-Reese et al., 2001):

$$M_{\mathrm{fs}} = \frac{4\pi}{3}\left(\frac{\lambda_{\mathrm{fs}}}{2}\right)^3 \rho_{\mathrm{m}}(z) \qquad , \tag{4.2}$$

where $\rho_{\mathrm{m}}(z)$ is the background matter density at redshift z and λ_{fs} is the free-streaming length defined in eq. 2.50. The quantity of the free-streaming mass is somewhat arbitrary, since it does not really correspond to a physical halo, since it does not include the density contrast parameter, Δ from eq. (3.3) (as it does in Sommer-Larsen *&* Dolgov, 2001). In fig. 4.5, we plot the eight-times free-streaming mass against the WDM particle mass, m_{wdm} as well as the **half-mode mass** (see also later fig. 5.1).

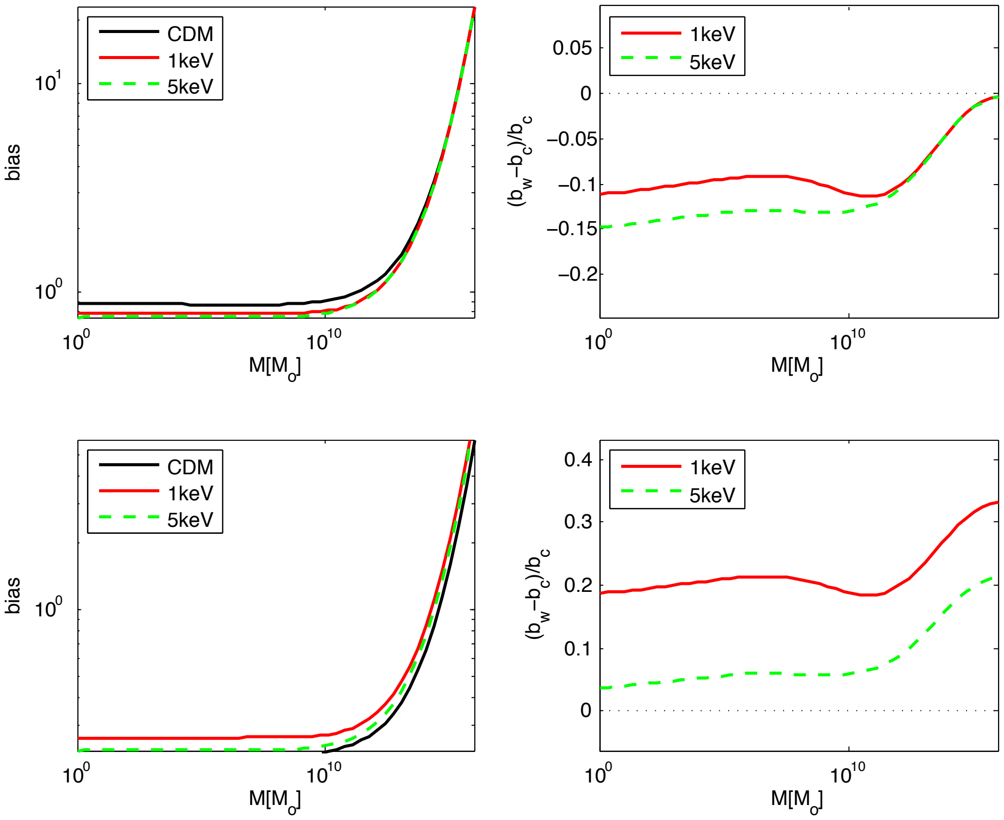

FIGURE 4.2: In the left panels of the above figure we plot the unnormalised (top) and normalised (bottom) halo bias in two different WDM and the CDM scenarios. On the right we plot the fractional difference of the WDM to the CDM bias for 2 different WDM particles. Notice the boost in WDM bias introduced by normalisation. This issue has been re-examined with respect to simulations by Dunstan et al. (2011); Schneider et al. (2012)

The crosses in fig. (4.3) make a comparison to an N-body simulation of Zavala et al. (2009). This comparison indicates that the Sheth-Tormen mass functions underestimate the strength of this suppression. Indeed, comparing the simulated mass function for the 1 keV particle to the Sheth-Tormen version, we find a very large discrepancy around the free-streaming mass and below.

The simulated mass function seems to decline much more steeply than the Sheth-Tormen. This suggests that we underestimate the effect of WDM on the mass functions. This demonstrates the need for modifications to the halo model, which we attempt in ch. 5 and further WDM N-body simulations described in ch. 6. Note that we have removed the first three points in the simulated mass function in the figure for the lowest three halo mass bins. This is because these are too affected by Poisson noise (Zavala et al., 2009). On the other hand, there could be unforeseen resolution effects coming from the simulations. However this is unlikely, since there are usually spurious haloes *created* in WDM simulations, which increases the mass function, as seen in fig. 4.3 for masses $M \lesssim 10^9 \, M_\odot$. Nonetheless this should be examined in future WDM simulations.

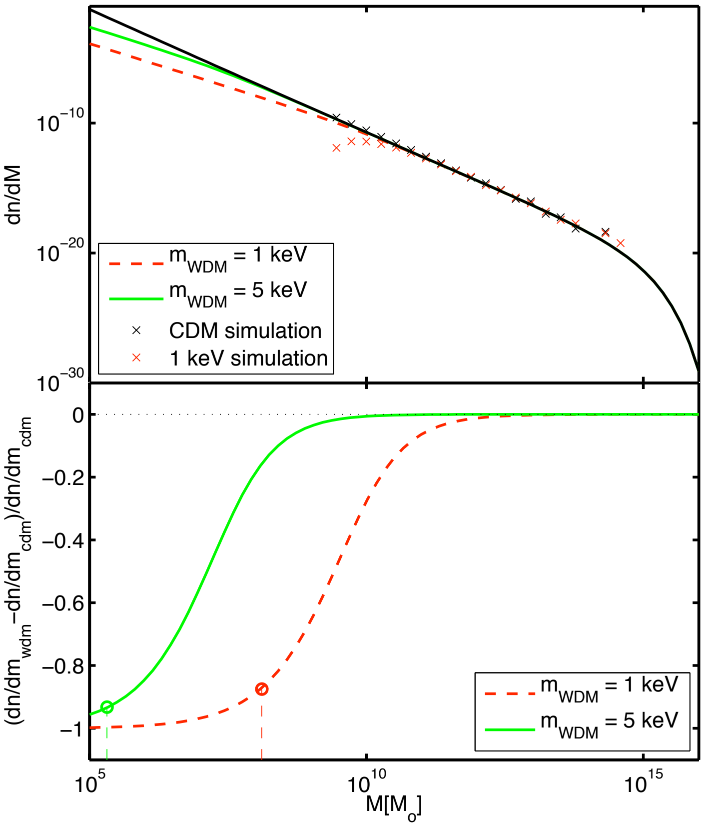

FIGURE 4.3: The top figure shows Sheth-Tormen mass functions suppressed by free-streaming of WDM particles for two different *warm dark matter* scenarios: 1 keV particles (dashed red line), 5 keV particles (solid green line) and CDM (solid black line).

The bottom figure shows the fractional difference between the WDM and CDM mass functions for the 2 different warm scenarios. The circles mark the halo mass on the x-axis that corresponds to the free-streaming radius of each WDM particle (or the free-streaming mass). Data points from the simulation by Zavala et al. (2009) are marked with crosses on the upper panel: the red crosses correspond to the same WDM scenario as the red dashed line (only data points above the limiting mass of the simulation are shown). The sudden increase in the WDM mass function for masses below $10^9\,M_\odot$ has been removed as it is only a result of spurious halo formation in simulations due to the finite size of the particles. The bump at $M \sim 2\times 10^{14}\,M_\odot$ is probably also a numeric artifact of forcing the presence of a large structure in the simulation volume.

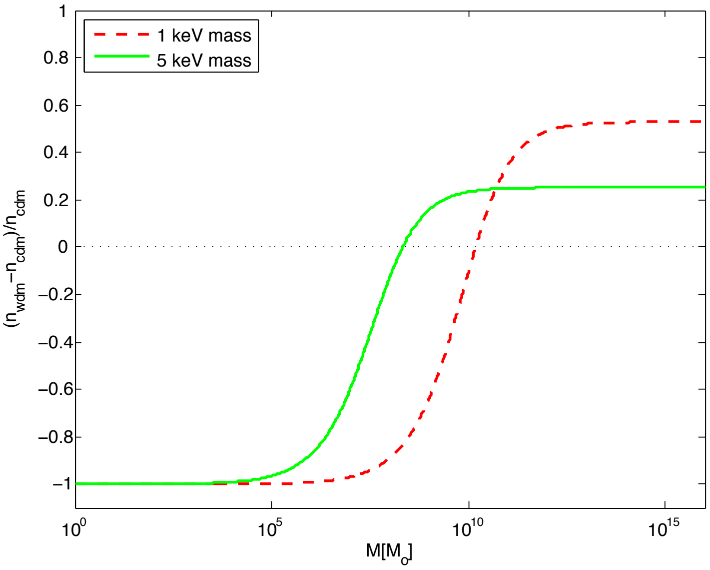

FIGURE 4.4: The two WDM lines reaching above the dotted zero line demonstrates the artificial boost in structure that is introduced by forced normalisation of the WDM mass functions. This is because WDM removes power on small scales, which means small halos are prevented from collapsing. Therefore requiring all matter within haloes forces more matter into large halos. This is unphysical since WDM free-streaming causes there to be more diffused, uncollapsed matter.

4.1.2 `Halofit` with *warm dark matter*

In the ΛCDM model, the non-linear evolution of the matter power spectrum can be calculated from the primordial linear matter power spectrum, using the **HALOFIT** formula of Smith et al. (2003), described in sec. 3.1.2. This method is a fitting function based on the halo model

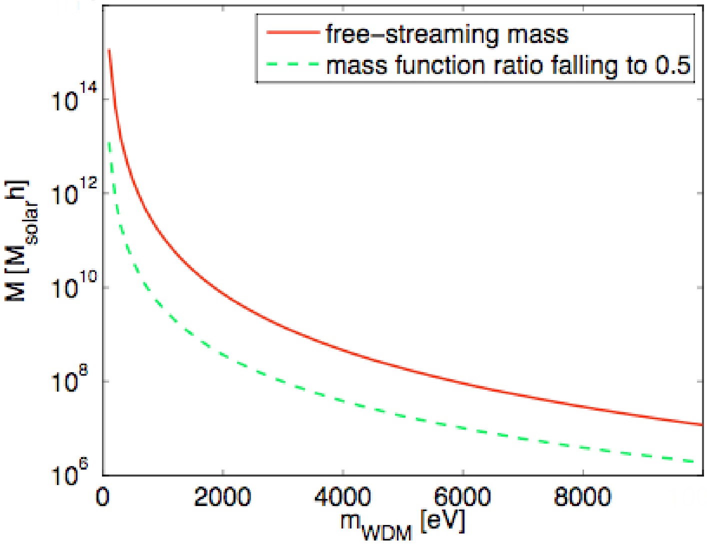

Figure 4.5: This figure compares the halo mass that corresponds to the mass function ratio between WDM and CDM mass functions falling to a half, called the **half-mode mass** and the eight-times free-streaming halo mass for WDM particles with masses $m_{\rm wdm}$.

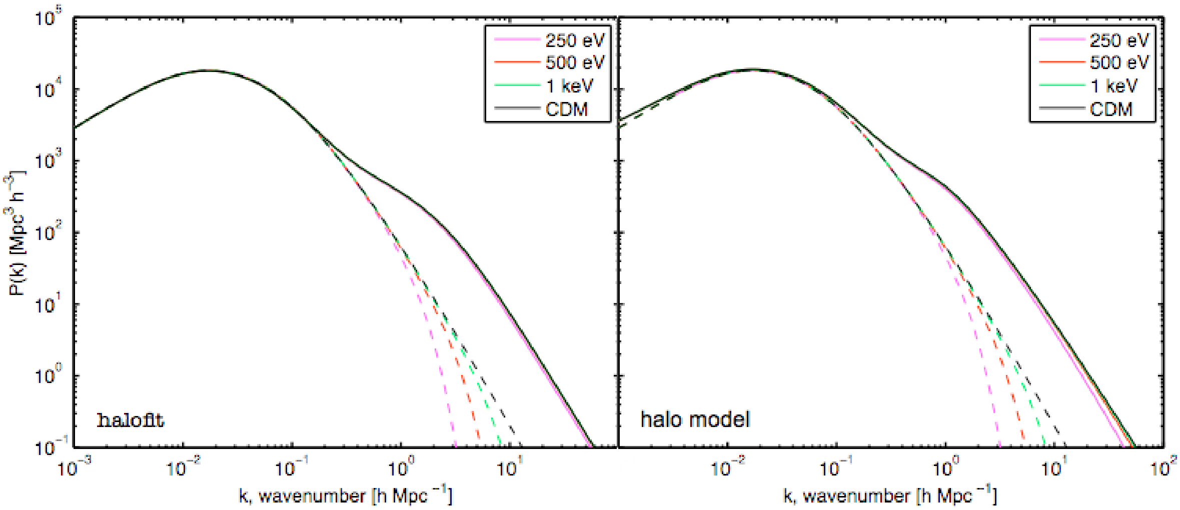

Figure 4.6: Matter power spectra today ($z = 0$), suppressed by free-streaming of WDM particles. The dashed lines are the linear power spectra corresponding to, from left to right in each panel, 250 eV, 500 eV, 1 keV *warm dark matter* and cold dark matter. The dashed lines are the same in both plots and represent the linear power spectra. The solid lines are the corresponding non-linear power spectra. The non-linear power spectrum in the left panel uses the halo model and that in the right panel was calculated using the HALOFIT formula. The slight excess of power on large scales in the halo model most likely comes from neglecting the effect of 'halo exclusion' (Smith et al., 2011).

that reproduces very accurately the results of many CDM numerical simulations. It is more accurate and more general than the fitting function from Peacock & Dodds (1996). For now, until ch. 6, we make the large extrapolation of assuming that the HALOFIT method is valid for WDM. In fig. 4.6 we compare non-linear matter power spectra calculated using this method to power spectra calculated using the halo model approach described in the sec. 4.1.1 above.

Non-linear evolution of the matter power spectrum washes out the difference between

WDM and CDM on small scales, which is apparent when comparing the linear spectra to the non-linear spectra in either panel of fig. 4.6. This is likely to be due to the collapse of structures, which significantly boosts the power on small scales and more than compensates for any missing structure (Boehm et al., 2005). This same process correlates the power at different wavenumbers in the power spectrum simply due to the collapse of the physical dimensions of objects. Furthermore this seems to also be a result of smooth accretion onto the already formed haloes (Benson et al., 2012).

The information about cosmological parameters contained in the matter power spectrum is encoded in its shape. If the matter power spectrum is modified (e.g. by non-linear growth) then some of the information contained in the shape may no longer be available. In particular on small scales there is very little power to begin with, so when power at different wavenumbers becomes correlated from non-linear growth, it becomes increasingly difficult to recover the power from pure linear growth. For any mildly noisy observation therefore the information originally encoded in the small scales would be much harder to recover after the power has cascaded down, i.e. information about WDM free-streaming in the non-linear matter power spectrum would have been lost. This information may however be recovered by examining these objects individually, most conveniently in real space.

4.2 Shear power spectra with *warm dark matter*

We use these approaches to calculating the non-linear matter power spectrum to calculate the weak lensing shear power spectra, cross-correlating 10 bins in redshift (see eq. 3.3.2). We first use the WDM linear theory matter power spectrum within the full halo model analysis, and calculate the resulting shear power spectrum, shown by the dashed line in fig. (4.7) for the case of a 1 keV WDM particle mass, for the autocorrelation of the 5^{th} redshift bin with itself.

As expected, the shear power spectrum amplitude is reduced on medium to small scales due to the lack of contributions to the one-halo term from smaller halos. On mid-range scales the two-halo term is very slightly greater than the CDM power spectrum due to the renormalisation of the halo bias given in eq. (4.1). The mass function is decreased on small scales by WDM and therefore the bias must increase on all scales to satisfy the bias normalisation constraint (illustrated in fig. 4.2). For the matter power spectrum this exactly preserves the large scale power. However, the lensing two-halo term weights the halos by their lensing effect ($\tilde{\kappa}$ in eq. 3.71), which is largest for high mass halos, where the mass function was unchanged but the bias is larger. Consequently, as expected, the lensing power spectrum is increased on larger scales. Note that we consider bias in the WDM model further in the next chapter, but refer the reader to the more recent work on the WDM halo (Benson et al., 2012; Schneider et al., 2012).

We then use the linear theory WDM function within `HALOFIT` to calculate the non-linear matter power spectrum, which we insert into the lensing power spectrum integrals. This is shown by the black solid line in fig. (4.8). The effect is similar to that from the halo method but the deviation from CDM is about half the size.

In using these two different methods we have attempted to somewhat span the range of possibilities given the theoretical uncertainties of the standard, CDM-based non-linear models. They all agree surprisingly well, to within a factor of two. To be conservative, we use the `HALOFIT` method from now on, unless otherwise stated, because it gives results in lesser WDM

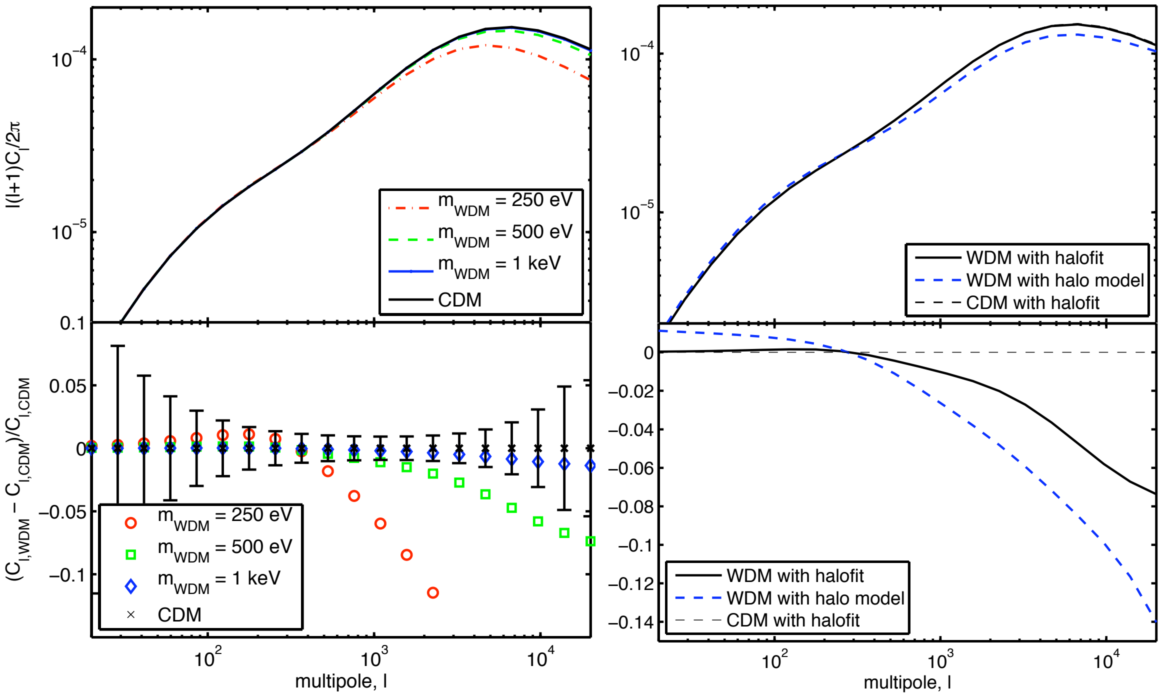

Figure 4.7: In the upper panels we plot the weak lensing auto-correlation power spectra for tomographic redshift bin 5, for WDM and CDM. The lower panels show the fractional differences between WDM and CDM spectra.

On the left side: we show the shear power spectra for CDM (solid black) and three different WDM particle masses: 250 eV, 500 eV and 1 keV denoted with the dashed (red), dot-dashed (green) and solid (blue) lines respectively. The effect of the 1 keV particle is not visible on this plot and the blue line overlaps with the black. These were found using the `HALOFIT` nonlinear corrections. In the lower panel we plot fractional differences between the WDM and CDM power spectra. The (red) circles, the (green) squares and the (blue) diamonds represent the 250 eV, 500 eV and 1 keV particles respectively. Furthermore, here we plot the error bars for a Euclid-like survey in 20 multipole bins. Note that these error bars are correlated and in order to find errors one must use the entire correlation matrix as we do in sec. 4.3.

On the right side: the WDM model plotted here is for 1 keV particles for illustration. The thick solid (black) and the thick dashed (blue) lines were found using the WDM linear theory matter power spectrum with the non-linear contribution calculated with the `HALOFIT` method and the halo model respectively. The thin dashed line was found using `HALOFIT` with CDM in upper and lower right panels. However it cannot be seen in the panel above, because it is only different from the thick (black) line by 1%. Note that the excess of power in the halo model on large scales is due to the normalisation of the halo bias and is unphysical.

effects in the power spectrum. We have also checked our results against a simple cut-off in the lower limit of mass integral of equations 3.64 and 3.65. We plot in fig. 4.8 the resulting fractional differences in the shear bin-5 autocorrelation power spectra similar to those in the lower right panel of fig. 4.7.

For illustration we show the `HALOFIT` results for three different WDM particle masses in the left hand panel of fig. 4.7. As expected, the suppression of the shear power spectrum is strongest and reaches the largest scales for the lowest DM particle masses. This reflects the scarcity of low mass lenses in the WDM Universe. The effect of WDM on the shear power

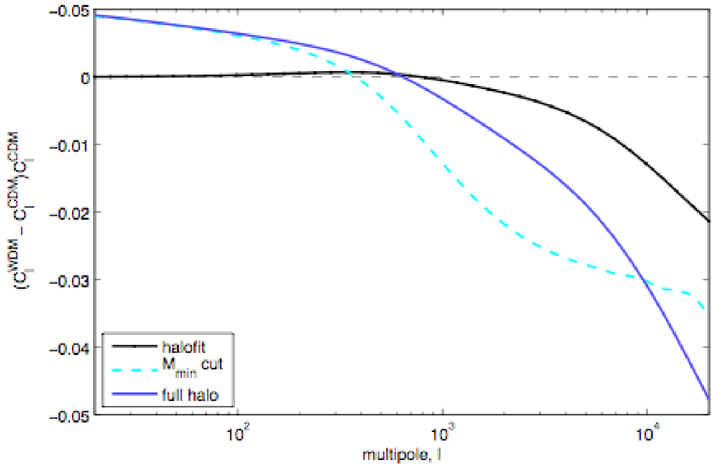

FIGURE 4.8: We plot fractional differences between WDM and CDM spectra, as above, but here they are all for a 1 keV WDM using three different approaches. The black line is using the **HALOFIT** non-linear power spectrum; the solid dark blue line is the full halo model approach using the WDM transfer function and finally the dashed cyan line is the halo model again but this time with the mass integral in eqs. 3.64 and 3.65 simply cut below the free-streaming mass. Note that the increase on large scales in the halo model lines is due to a renormalization bias. Here we can see how the effect of damping of small scales by free-streaming of WDM manifests itself using different methods of calculating non-linear large scale structure. Note also that the **HALOFIT** method gives the least effect. Also note that the black solid line (with dots) is the same as the red solid line in the upper panel of the same figure).

spectrum is more prominent than that on the non-linear matter power spectrum at redshift zero (fig 4.6). WDM has a greater effect on the linear theory matter power spectrum than the non-linear matter power spectrum and, therefore, has a greater effect on the non-linear matter power spectrum at higher redshifts, where there is less nonlinearity. Since the shear power spectrum is an integral of the matter power spectrum over redshift, WDM has a greater effect on the shear power spectrum, which probes higher redshifts. We also see that the effect of halving the WDM particle mass is to more than double the suppression compared to the CDM power spectrum i.e. the change in the deviation from CDM is nonlinear in the inverse particle mass. We return to this in the following sections.

We compare the lensing power spectra in fig. 4.7 to predicted statistical uncertainties on 20 logarithmically spaced bins in ℓ for this redshift bin. Here and in the following section, we assume a EUCLID-like survey with 35 galaxies per square arcminute covering half the sky with shear measurement error on each galaxy of $\sigma_\gamma = 0.35/\sqrt{2}$ (Refregier et al., 2010). The comparison is only indicative, since there are strong correlations between ℓ bins on small scales and between the 90 different redshift cross power-spectra (not shown). However, we already see that very high WDM particle masses around 250 eV will be easily ruled out.

4.3 Forecasting constraints on *warm dark matter*

In this section we forecast constraints on the WDM particle mass for a EUCLID-like weak lensing survey, using a Fisher matrix (FM) analysis (see for e.g. Dodelson, 2003). We vary four other cosmological parameters in the cosmic shear analysis and compare constraints between the `HALOFIT` and halo model approaches. We then combine the `HALOFIT` results with forecast constraints from the CMB (sec 2.2.1).

We use CDM as our fiducial model and place limits on the inverse WDM particle mass so that our fiducial model has a parameter value of zero, corresponding to an effectively infinite WDM particle mass (in practice we use $m_{\rm wdm} = 100\,{\rm MeV}$). We vary the following additional parameters: the total matter density today, $\Omega_{\rm m}$, the primordial perturbation spectral index, $n_{\rm s}$, the primordial spectral amplitude, $A_{\rm s}$ and the matter power spectrum shape parameter, $\Gamma = e^{-2\Omega_{\rm b}h}\Omega_m h$. We use $A_{\rm s}$ instead of σ_8 to normalise the matter power spectrum for convenience when combining with the CMB (sec 2.2.1) constraints. For the CDM linear theory matter power spectrum we use a fitting formula for the matter power spectrum from Ma (1996), which uses the shape parameter Γ. Cosmic shear alone is very insensitive to $\Omega_{\rm b}$ and h individually.

The Fisher matrix for cosmic shear is given as:

$$F_{\alpha,\beta} = \sum_{l} \sum_{(i,j),(m,n)} \frac{\partial C_{ij}(l)}{\partial \phi_\alpha} \left[{\rm Cov}[C_{ij}(l), C_{mn}(l)]\right]^{-1} \frac{\partial C_{mn}(l)}{\partial \phi_\beta} \quad , \tag{4.3}$$

where C_{ij} is the shear power spectrum of bin i correlated with bin j, ϕ_α are the parameters over which we marginalise and ${\rm Cov}(C_{ij}(l), C_{mn}(l))$ is the covariance matrix of bins i, j, m and n. We use equation (14) in Takada & Jain (2004) to find the elements of the covariance matrix, after adding the shot noise term coming from the shear error, σ_γ:

$$\bar{C}_{ij}(l) = C_{ij}(l) + \delta_{ij}\frac{\sigma_\gamma^2}{\bar{n}_i} \quad , \tag{4.4}$$

where $\bar{n}_i$ is the average number density of galaxies in redshift bin i.

The FM analysis assumes that the first non-vanishing order of the Tayor expansion of the log-likelihood is quadratic. However taking CDM as the fiducial model, this is not the case for $m_{\rm wdm}^{-1}$ (or $m_{\rm wdm}$) as a parameter. Therefore the standard FM approach breaks down. As a result, the error found from FM analysis depends on the fiducial model chosen, errors are asymmetric around the fiducial value, and it turns out that the power spectra are completely insensitive to the inverse WDM particle mass at small values of $m_{\rm wdm}^{-1}$. Therefore it is not possible to use a very small step size in this parameter when calculating the derivative of the power spectrum in the Fisher matrix analysis. We discuss how we deal with this below, in sec. 4.3.1. Briefly, we tune the step size in the inverse WDM particle mass to equal the 1σ error bar on this parameter.

We show the resulting parameter constraints on $m_{\rm wdm}$, $\Omega_{\rm m}$ and $n_{\rm s}$ in fig. 4.9, marginalised over the power spectrum amplitude and shape. The `HALOFIT` results are shown by the solid contours and the halo model by the dashed curves. The agreement between the uncertainties on each parameter is good, with the halo model giving slightly tighter constraints, as expected from the lensing power spectra shown in fig. 4.7. The degeneracy direction between $m_{\rm wdm}^{-1}$ and $\Omega_{\rm m}$ is slightly different between the two methods. We have verified that on fixing all other cosmological parameters the degeneracy direction is extremely similar for the two methods, so the difference arises from the interplay between changing the WDM mass simultaneously with other parameters including the large scale amplitude parameter $A_{\rm s}$. The degeneracy direction between $m_{\rm wdm}^{-1}$ and $n_{\rm s}$ is as expected: increasing $m_{\rm wdm}^{-1}$ causes a decrease in power on small scales, which can be partially compensated by increasing the power spectrum index $n_{\rm s}$.

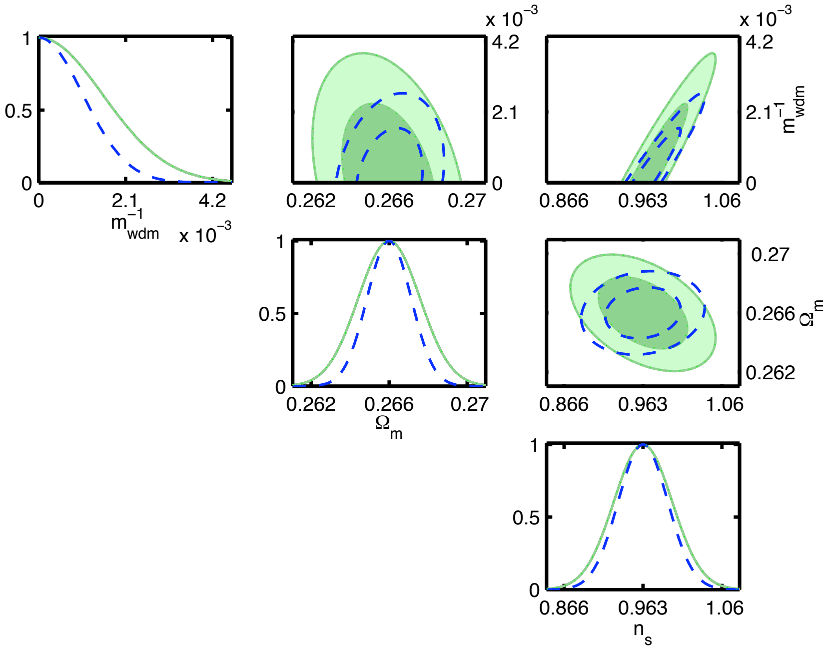

FIGURE 4.9: 68 and 95 % confidence *likelihood contours* for both the halo model (blue dashed) and the HALOFIT (green solid) approaches, marginalised over the power spectrum amplitude parameter A_s and shape parameter Γ. The units on $m_{\rm wdm}^{-1}$ are eV^{-1}.

The marginalised errors that result from this analysis can be found in tab. 4.1, using a one-tailed confidence limit for $m_{\rm wdm}^{-1}$. We find approximately 30% smaller errors when using the halo model, compared to the `HALOFIT` method.

As mentioned above, we use the FM forecast for the PLANCK CMB experiment (à la also Colombo et al., 2009; Hamann et al., 2008) and include it into our analysis to predict combined constraints from both EUCLID and PLANCK. We derive the cosmological constraints from PLANCK following the description by the *Dark Energy Task Force* (DETF Albrecht et al., 2006). A more detailed discussion can be found in Rassat et al. (2008). For this prediction we consider only the 143 GHz channel data. This channel has a beam with the full-width-half-maximum of $\theta_{\rm fwhm} = 7.1'$ and is sensitive to anisotropies in the temperature of $T = 2.2\mu K/K$ and in polarization of $P = 4.2\mu K/K$. We take $f_{\rm sky} = 0.80$ as the sky fraction in order to account for having to exclude parts of the sky due to galactic foregrounds (noise from the Milky Way). We only consider the multipoles in the CMB power spectrum that are larger than $l_{\rm min} = 30$ in order to avoid problems with polarization foregrounds. In other words, we exclude the small scales from the CMB power spectrum. It is for this reason that we assume that WDM effects in the CMB power spectrum are negligible and set a flat CMB prior on the $m_{\rm wdm}$. In other words, the FM components relating our WDM parameter are set to zero. This is based on the assumption that the scales affected by WDM with $m_{\rm wdm} \gtrsim 100$ eV are far away from the scales considered. Therefore, while PLANCK adds quite strong constraints on the other cosmological parameters, especially on the curvature, the Planck FM does not add any constraints on $m_{\rm wdm}^{-1}$ and only contributes to breaking degeneracies

As described in the DETF report (Albrecht et al., 2006), we choose the parameter set to be: $\omega_{\rm m} = h^2\Omega_{\rm m}$, $\theta_{\rm s}$, $\ln A_{\rm s}$, $\omega_{\rm b} = h^2\Omega_{\rm b}$, $n_{\rm s}$, τ, where $\theta_{\rm s}$ is the angular size of the sound horizon

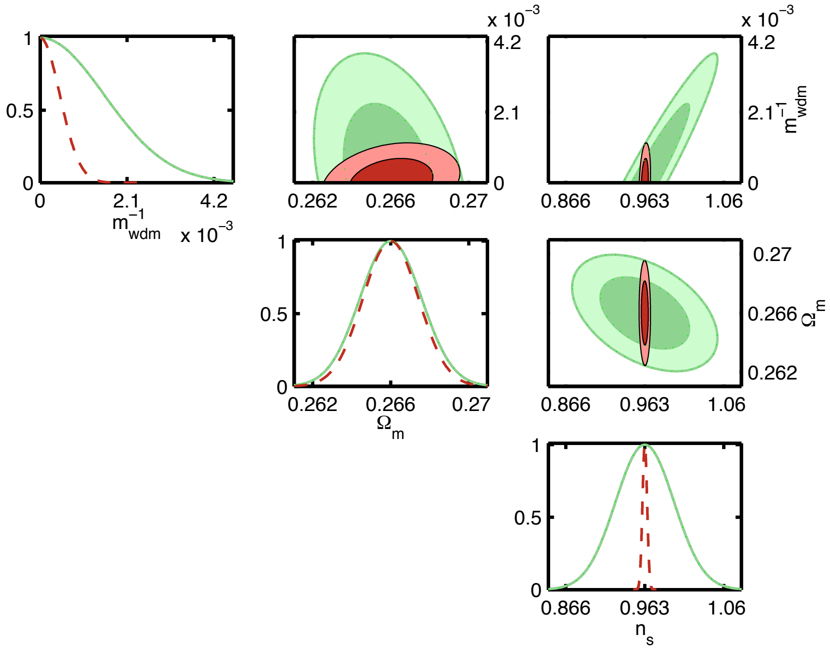

Figure 4.10: 68 and 95 % confidence *likelihood contours* for the `HALOFIT` approach using cosmic shear (thick green solid) and cosmic shear combined with Planck forecasts (red dashed line and thin black solid contours shaded red). The units on $m_{\rm wdm}^{-1}$ are $\rm eV^{-1}$.

at last scattering, $\ln A_{\rm s}$ is the logarithm of the primordial amplitude of scalar perturbations and τ is the optical depth to reionisation. After marginalization over the optical depth and the physical baryon density, ω_b we then calculate the Planck CMB Fisher matrix in the parameters: Γ, $A_{\rm s}$, $n_{\rm s}$, $\Omega_{\rm m}$ by using the appropriate *Jacobian matrix* of partial derivatives for the needed parameter transformation (Eisenstein et al., 1998; Rassat et al., 2008).

The parameter constraints are shown in fig. 4.10 for the `HALOFIT` method. We see that the very tight constraint on $n_{\rm s}$ from the CMB breaks the degeneracy between $n_{\rm s}$ and $m_{\rm wdm}$ from cosmic shear alone, to produce a tighter constraint on $m_{\rm wdm}$. The single parameter marginalised results for `HALOFIT` and the halo model methods are shown in tab. 4.1.

	Fiducial value	*Halo model*	`HALOFIT`	
		Shear only	Shear only	Shear + Planck
$m_{\rm wdm}$	CDM	> 935 eV	> 645 eV	> 2500 eV
$m_{\rm wdm}^{-1}\ [eV^{-1}]$	$10^{-8} (\approx 0)$	$+0.00107$	$+0.00155$	$+0.00040$
$\Omega_{\rm m}$	0.27	± 0.0011	± 0.0016	± 0.0012
$n_{\rm s}$	0.96	± 0.031	± 0.035	± 0.002
$A_{\rm s}\ [h^{-3} Mpc^3]$	1.3×10^5	$\pm 0.119 \times 10^5$	$\pm 0.183 \times 10^5$	$\pm 0.005 \times 10^5$
Γ	0.18	± 0.0090	± 0.0123	± 0.0005

Table 4.1: Table of 68% confidence limits for a flat ΛWDM cosmology marginalised over 4 other parameters in each case. The errors on the inverse particle mass, $m_{\rm wdm}^{-1}$, are single tailed limits described in sec. 4.3.1.

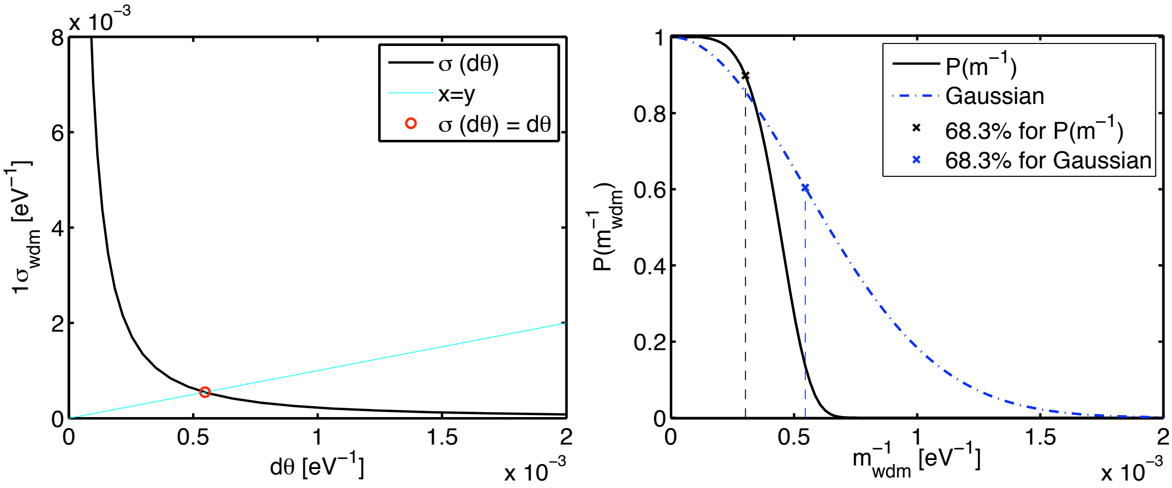

FIGURE 4.11: Left: The 1σ error calculated from FM (solid black line), but with different differentiation step sizes, $d\theta$, used to calculate the gradient of the cosmic shear power spectra with respect to the parameter $\theta = m_{\rm wdm}^{-1}$. The red circle marks the point when the differentiation step size equals the 1σ error on the inverse DM particle mass. We fix all other parameters. Right: The 1-dimensional probability $P(m_{\rm wdm}^{-1})$ is plotted with a solid black curve. The dot-dashed (blue) curve is the Gaussian probability distribution corresponding to the FM error obtained when using a step size equal to the 1σ error. The vertical dashed lines correspond to the 68.3% of the probability. The red circle on the left corresponds to the vertical dashed blue line on the left.

4.3.1 Step sizes in the Fisher matrix

We first perform a simple likelihood analysis, only varying $m_{\rm wdm}^{-1}$, assuming all other parameters are fixed. We use this to illustrate our proposed method and assess how well it works in one dimension, where we can compare with the truth.

As discussed in the main text, we choose to use the inverse WDM particle mass as the free parameter in our FM analysis because it has a non-infinite value for our fiducial model, CDM. However as $m_{\rm wdm}^{-1}$ tends to zero the lensing power spectra become completely insensitive to the exact value, which makes it impossible to perform a traditional numerical FM calculation in which the step sizes used in calculating the derivatives are very small. This is illustrated in the left hand panel of fig. (4.11) for the simple case where all other parameters are kept fixed.

Clearly the choice of step size has a big effect on the result. We propose to use a step size such that it is equal to the error bar, as illustrated by the intersection of the dark (black) and light (cyan) lines in the left hand panel of the figure, shown by the (red) circle. Due to the convex nature of the function this cannot be done by iteration but instead is most simply done by making the figure we show. This can equally well be carried out in multi-dimensional space as in one dimension by working with the one-dimensional marginalised error bar.

By working briefly in one dimension we can compare our result to the truth obtained by plotting the full likelihood as a function of $m_{\rm wdm}^{-1}$. This is shown in the right hand panel of fig. 4.11. The solid line shows the exact likelihood and the dot-dashed line illustrates the FM error obtained by setting the step size equal to the 1σ error bar. The crosses and vertical lines show the 68% one-tailed upper limits from each curve. We see that the exact 68% upper limit is within a factor of two of the FM limit using our proposal. Our proposal gives a more conservative result. We can also see from the difference in shape between the solid and dot-dashed lines quite how non-Gaussian the exact probability distribution is. We proceed by using this method in multi-dimensional parameter space.

4.4 Summary & discussion

So far, we have made the first estimate of constraints on the WDM particle mass from cosmic shear power spectra. We compared approaches to estimating the impact of *warm dark matter* on cosmic lensing. We found the `HALOFIT` approach of Smith et al. (2003) more conservative than the halo model. We comment on the difference below. We also find that the effects on the mass functions (fig 4.3) reach on mass scales significantly larger than the “free-streaming” mass. We have made forecasts for parameter constraints from a EUCLID-like cosmic shear survey combined with PLANCK and found that if the true cosmological model were CDM, we could place a limit of $m_{\mathrm{wdm}} > 2.5\,\mathrm{keV}$ at 68% confidence.

Our calculations are conservative in several ways. Firstly, we use a transfer function to relate the CDM linear theory matter power spectrum to the WDM linear theory power spectrum, from which we calculate the Sheth-Tormen mass function. We showed a comparison with a mass function from simulations which suggest a much bigger suppression of the number of lower mass halos. To improve our constraints it would be necessary to have a fitting formula to simulations giving the mass function as a function of WDM particle mass, extending to smaller masses than most cosmological CDM simulations. A better physical model for the non-linear collapse of WDM structures might be developed on the basis of such work. This has recently been attempted by other authors like Benson et al. (2012); Schneider et al. (2012) on the basis on the formulation described in ch. 5. In addition, the new WDM models for the mass functions must be physical enough to translate into the `HALOFIT` method and explain the decrease in signal due to WDM in the non-linear power spectrum (Vanderveld et al., 2012). Furthermore, we assumed that the NFW profile is unaffected by the dark matter particle mass, whereas at the very least we expect the central core to be smoothed out. We assume that the effect of this on cosmic shear power spectra is subdominant to the decrease in the number of small halos. To overcome this limitation we would need to use a replacement for the NFW which gives the density profile as a function of WDM particle mass and halo mass. We discuss this somewhat in app. B.

However, our calculations are optimistic, in that we use mass functions and mass profiles obtained from simulations containing no **baryons** (Semboloni et al., 2011; van Daalen et al., 2011). To perform this measurement on real data it would be necessary to use results from simulations using baryons. These are in only the preliminary stages of development at the present time, and there is considerable uncertainty on the prescriptions used as well as on many free parameters that need to enter the calculations. The effect of baryons is to change the predicted cosmic shear power spectra, and to introduce uncertainty in the predictions. We assume for the purpose of this prediction that these problems will be solved by the time we will be analysing a EUCLID-like survey. We hope that studies like these will provide extra motivation to improve the quality of simulations using baryons, which we discuss further in Chapter 8 with reference to the work of van Daalen et al. (2011) and Semboloni et al. (2011) and the OWLS hydrodynamical simulations (Schaye et al., 2010) of large scale structure.

We also assume spherical collapse, which is less realistic in describing non-linear structure than ellipsoidal collapse, which has additional halo mass dependence in the collapse threshold. In other words, a further source of suppression of small scales is the decreased amount of collapse for small haloes, which tend to have higher ellipticity.

Additionally, we normalise the halo bias in order to recover the linear matter power spectrum on very large scales. In fact, the correct approach would be to add a third term to the halo model, which would account for the uncollapsed matter. It would be necessary to specify the power spectrum and correlation of this uncollapsed matter. We develop this in ch. 5. For now, we have chosen to normalise the mass-function weighted bias, following convention in CDM halo model calculations. However, the effect of WDM is to decrease the number of low mass halos and therefore the bias is increased on all scales to meet the normalisation condition. This causes an increase in power on mid-range scales.
This may be the reason why the correlations between Ω_{m} and m_{wdm}^{-1} are inconsistent between the halo model and **HALOFIT** (see fig. 4.9). However, these issues only affect the halo model calculations and do not influence our final constraint from the **HALOFIT** method. The halo model for WDM is discussed in great detail in ch. 5.

It is well known that FMs are an approximate method for forecasting uncertainties on parameters. The formal derivation of the FM states that it gives a *lower limit* on the parameter errors. If the predicted data points are non-linearly related to the parameters, then we can expect likelihood contours in parameter space to be *banana shaped*, which is not captured within the FM errors. Even when considering a single parameter the FM approximation breaks down due to the *flatness of the log-likelihood*, giving a gradient of zero at the fiducial value of $m_{\mathrm{wdm}}^{-1} = 0$.
We find this to be a significant problem for the WDM particle mass. Small changes in WDM particle mass around our fiducial CDM model make negligible changes in the cosmic shear power spectra which makes it impossible to sensibly use a derivative taken with small step sizes in the FM. We use CDM as our fiducial model in order to be able to compare our result to other methods (Lyα, X-ray). We solve the above problem by using a larger step size, but the FM method must eventually be replaced by a full Markov-Chain Monte Carlo exploration of parameter space, which we discuss in ch. 8.

We have assumed that the CMB is insensitive to WDM when we calculated joint constraints with PLANCK, because the effects of WDM are only important on the smallest scales. We have further assumed that only primary CMB anisotropies from PLANCK are used for constraining cosmology. However, gravitational lensing of the CMB itself can be used to reconstruct single-bin lensing indtomography information on the lensing potential (e.g. see Lewis *&* Challinor, 2006). This would enhance the constraints on WDM further, but is not tackled in this thesis.

Our cosmic shear calculations rest on a linear theory WDM power spectrum fitting formula which assumes dark matter particles are light and thermalised, like for example a light gravitino. This fitting formula can be straight-forwardly re-expressed for sterile neutrinos and our lower limit on the thermalised WDM particle can be converted to a lower bound on the sterile neutrino mass. For our final result using **HALOFIT** plus PLANCK forecasts the limit is $m_{\mathrm{wdm}} > 2.5\,\mathrm{keV}$ which can be translated to $m_{\mathrm{s}\nu} > 15.5\,\mathrm{keV}$. If dark matter is made of sterile neutrinos created using the simplest mechanisms then constraints from cosmic shear can be compared to those from X-ray observations to test the consistency of the model. If cosmic shear were to place the upper limit we derive, then it would be inconsistent with current X-ray lower limits and would rule out the simple sterile neutrinos as WDM candidates.

Our forecast constraints for future cosmic shear studies are similar to the upper limits already being obtained from observations of the Lyα forest. The main advantage of using cosmic shear is that it does not rely on hydro-dynamical simulations of the intergalactic medium. However the Lyα observations are at higher redshift (around $z \sim 3$) than the cosmic shear (which roughly probes mass at $z \lesssim 1$). This is advantageous because the matter fluctuations are more in the linear regime and there is less reliance on simulations of non-linear theory. Also the linear theory matter power spectrum is much more sensitive to the WDM particle mass. A deeper cosmic shear survey would gain from this effect.

Cosmic shear power spectra are just one way to probe dark matter structure using gravitational lensing. However, higher order shear statistics such as the bispectrum are more sensitive to small scale clustering than cosmic shear and therefore would be expected to be more powerful in constraining the dark matter mass. Furthermore, higher order distortions of galaxies, such as flexion, also probe smaller scales and would be a better test. Bacon et al. (2009) find that galaxy-galaxy flexion is sensitive to structure of around 10^9 solar masses. The methodology described in this paper could in the future be extended to make predictions for these statistics.

CHAPTER 5

An Improved Halo Model for *Warm Dark Matter*

This chapter corresponds closely to
Smith & Markovic,
Testing the Warm Dark Matter Paradigm with Large-scale Structures,
published in 2011 in the Physical Review D,
volume 84, issue 6, paper id. 063507 (Smith & Markovič, 2011).

In the previous chapter we discussed the possibility of testing the ΛWDM cosmology using cosmic weak lensing as a probe for the small-scale-suppressed distribution of dark matter. We used the halo model of cosmological structure to calculate the non-linear corrections to the suppressed linear matter power spectrum. We then calculated them with the `halofit` and some discrepancies were found.

Besides the discrepancies between `halofit` approach and the halo model, we discovered that it was difficult to determine how the halo bias and the halo mass function should be normalised. We suggested that dividing the matter field into a smooth and a clumped component might clarify this problem. We also found that the mass function derived from the suppressed linear matter power spectrum according to the Sheth & Tormen (1999) formalism seemed to yield far too many haloes smaller than the free-streaming length of *warm dark matter*, when comparing to N-body simulations of Zavala et al. (2008). We furthermore pointed out that using standard NFW (Navarro et al., 1997) profiles did not reflect the true shapes of profiles of *warm dark matter* haloes.

In this chapter, we describe an attempt at modifying the halo model ingredients that we are familiar with from sec. 3.1 to better fit the assumptions we make about structure formation in the *warm dark matter* scenario. The formalism was developed by Dr. Robert Smith and was then employed in finding the non-linear corrections, weak lensing power spectra and Fisher matrices (FM) for the Euclid survey.

The splitting of the matter over-density field into a clumped, structure-like and a smooth, linear-like component is described in terms of correlation functions in sec. 5.1.1. In sec. 5.1 the calculations of the halo mass function, bias and density profiles are re-examined and modified according to some assumptions about the formation of haloes in the *warm dark*

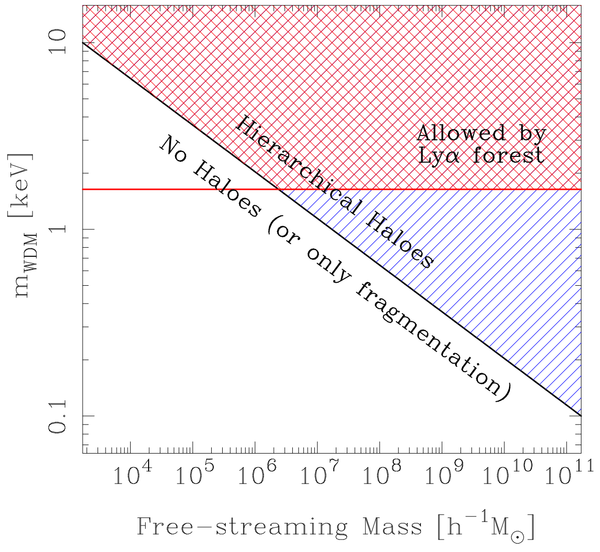

Figure 5.1: Free-streaming mass ($M_{\rm fs}$) as a function of the mass of the WDM particle mass. The formation of haloes below the black line is suppressed, because the overdensity field is smoothed by WDM on the corresponding scales. Haloes in this region may possibly form through fragmentation. The cross-hatched red region shows the allowed region from the Lyα forest (Boyarsky et al., 2009), where the correspondence between the thermal relic WDM mass and the sterile neutrino mass can be found as in for example Viel et al. (2004).
Figure source: Smith & Markovič (2011)

matter universe. In section 5.2 the resulting power spectra of matter and weak lensing statistics are presented. Finally, in sec. 5.2.1 the FMs for the Euclid survey are calculated.

5.1 A modified halo model

It became clear in the previous chapter (ch. 4) that the halo model developed in the context of ΛCDM has some deficiencies in the ΛWDM model. For this reason we reexamine its ingredients: the mass function, the bias and the halo density profile in the new context. In fig. 5.1 we show the present constraint on the WDM particle mass in fig. 5.1.

5.1.1 Statistics of the divided matter field

If we describe the inhomogeneous density distribution of matter in the universe with the position dependent function $\rho(\boldsymbol{x})$, we can then attempt to split it up into a smoothly distributed component, $\rho_{\rm s}(\boldsymbol{x})$ and a component that is made up of many individual object - haloes, with particular density profiles $\rho_{\rm h}(r, M)$. These density profiles depend on the mass of the halo M and since we assume these profiles to be spherically symmetrical, the distance from the halo centre, $r = |\boldsymbol{x} - \boldsymbol{x}_0|$. We can then sum over the individual objects to get the total density of the clumped component, $\rho_{\rm c}(\boldsymbol{x})$, and write the total density distribution in the universe as:

$$\rho(\boldsymbol{x}) = \rho_{\rm s}(\boldsymbol{x}) + \sum_{i=1}^{N} M_i\, u_{\rm h}(|\boldsymbol{x} - \boldsymbol{x}_{0,i}|, M_i) \quad , \tag{5.1}$$

where $u_{\rm h}(r, M) = \rho_{\rm h}(r, M)/M$ is the density profile normalised to the halo mass.

Averaging over the universe, we can define a background density, $\bar{\rho}$, which can also be split into a smooth and a clumped component:

$$\langle\rho(\boldsymbol{x})\rangle = \langle\rho_{\rm s}(\boldsymbol{x})\rangle + \langle\rho_{\rm c}(\boldsymbol{x})\rangle = \bar{\rho} = \bar{\rho}_{\rm s} + \bar{\rho}_{\rm c} \quad . \tag{5.2}$$

where we can define the fraction of matter contained within haloes as $f = \bar{\rho}_{\rm c}/\bar{\rho}$ and therefore also $(1 - f) = \bar{\rho}_{\rm s}/\bar{\rho}$. In order to calculate the fraction of matter contained within haloes, we integrate over the differential mass function, $dn(M)/dM$ (eq 3.1) and cut the integral at a lower cut-off mass scale, which we already briefly discussed in ch. 4. This is reasonable because for now, we assume that no haloes exist with masses smaller than this cut-off, M_{cut}, which we equate to the "free-streaming halo mass", M_{fs} - the mass of a halo with radius $r_{\text{fs}}/2$, a half of the free-streaming scale of *warm dark matter* particles (sec 2.3.3). Now we can re-write the fraction of matter contained within haloes as:

$$f = \frac{1}{\bar{\rho}} \int_{M_{\text{cut}}}^{\infty} dM M \frac{dn(M)}{dM} \quad . \tag{5.3}$$

We wish to calculate the statistics of clustering in the form of the non-linear matter power spectrum, so we first start with the two-point correlation function of the matter density field, which we split into the two components:

$$\begin{aligned} \langle \rho(\boldsymbol{x})\rho(\boldsymbol{x}+\boldsymbol{r}) \rangle &= \langle [\rho_{\text{s}}(\boldsymbol{x}) + \rho_{\text{c}}(\boldsymbol{x})] \, [\rho_{\text{s}}(\boldsymbol{x}+\boldsymbol{r}) + \rho_{\text{c}}(\boldsymbol{x}+\boldsymbol{r})] \rangle \\ &= \langle \rho_{\text{s}}(\boldsymbol{x})\rho_{\text{s}}(\boldsymbol{x}+\boldsymbol{r}) \rangle + \langle \rho_{\text{c}}(\boldsymbol{x})\rho_{\text{c}}(\boldsymbol{x}+\boldsymbol{r}) \rangle + 2 \, \langle \rho_{\text{c}}(\boldsymbol{x})\rho_{\text{s}}(\boldsymbol{x}+\boldsymbol{r}) \rangle \quad , \end{aligned} \tag{5.4}$$

where we've set $\langle \rho_{\text{s}}(\boldsymbol{x})\rho_{\text{c}}(\boldsymbol{x}+\boldsymbol{r}) \rangle = \langle \rho_{\text{c}}(\boldsymbol{x})\rho_{\text{s}}(\boldsymbol{x}+\boldsymbol{r}) \rangle$, because we assume statistical homogeneity and isotropy in the standard cosmological model, meaning that the correlations in density between different points in the universe only depend on the distance between these points.

Now define, as it is common (see also eq. 2.7), the perturbation to the density field for either component, $\delta_i(\boldsymbol{x})$, where $i \in \{\text{s}, \text{c}\}$, by the equation:

$$\rho_i(\boldsymbol{x}) \equiv \bar{\rho}_i \, (1 + \delta_i(\boldsymbol{x})) \quad , \tag{5.5}$$

and rewrite equation 5.4, noting that by this definition, $\langle \delta(\boldsymbol{x}) \rangle = 0$:

$$\begin{aligned} \langle \rho(\boldsymbol{x})\rho(\boldsymbol{x}+\boldsymbol{r}) \rangle &= \bar{\rho}^2 \, (1 + \langle \delta(\boldsymbol{x})\delta(\boldsymbol{x}+\boldsymbol{r}) \rangle) \\ &= \bar{\rho}^2 \, (1 + \xi(r)) \\ &= \bar{\rho}_{\text{s}}^2 \, (1 + \xi_{\text{ss}}(r)) + \bar{\rho}_{\text{c}}^2 \, (1 + \ \xi_{\text{cc}}(r)) + 2\bar{\rho}_{\text{c}}\bar{\rho}_{\text{s}} \, (1 + \xi_{\text{cs}}(r)) \quad , \end{aligned} \tag{5.6}$$

where we've replaced in the definition of a correlation function as:

$$\xi_{ij}(|\boldsymbol{r}|) \equiv \xi_{ij}(r) \equiv \langle \delta_i(\boldsymbol{x})\delta_j(\boldsymbol{x}+\boldsymbol{r}) \rangle \quad . \tag{5.7}$$

Note also that the total perturbation is

$$\delta(\boldsymbol{x}) = \frac{\rho(\boldsymbol{x}) - \bar{\rho}}{\bar{\rho}} = \frac{\bar{\rho}_{\text{s}}\delta_{\text{s}}(\boldsymbol{x}) + \bar{\rho}_{\text{c}}\delta_{\text{c}}(\boldsymbol{x})}{\bar{\rho}} = (1-f)\delta_s(\boldsymbol{x}) + f\delta_{\text{c}}(\boldsymbol{x}) \quad . \tag{5.8}$$

Using the definition of the fraction of clumped matter, we can now rearrange equation 5.6 to obtain:

$$\begin{aligned} 1 + \xi(r) &= (1-f)^2(1 + \xi_{\text{ss}}(r)) + f^2(1 + \xi_{\text{cc}}(r)) + 2f(1-f)(1 + \xi_{\text{sc}}(r)) \\ &= 1 + (1-f)^2\xi_{\text{ss}}(r) + f^2\xi_{\text{cc}}(r) + 2f(1-f)\xi_{\text{sc}}(r) \quad , \end{aligned} \tag{5.9}$$

finally arriving to:

$$\xi(r) = (1-f)^2\xi_{\text{ss}}(r) + 2f(1-f)\xi_{\text{sc}}(r) + f^2\xi_{\text{cc}}(r) \quad . \tag{5.10}$$

So the total correlation function of the over-density field is just a sum of the correlation functions and the cross-correlation of the smooth and clumped fields, all weighed by the fraction of matter contained within haloes, f.

The halo-halo correlation function

In order to calculate the clump-clump, or “halo-halo” correlations, we need to return to the standard halo model, already much discussed (sec 3.1). We split up the correlation function into the over-density correlation within a single halo - the *1-halo* or *Poisson* term, $\xi_{\rm cc}^{\rm P}$ and the correlation between different haloes - the *2-halo* term, $\xi_{\rm cc}^{\rm C}$:

$$\xi_{\rm cc} = \xi_{\rm cc}^{\rm P} + \xi_{\rm cc}^{\rm C} \quad , \tag{5.11}$$

where the halo model gives these terms as (see also app. A):

$$\begin{aligned} \xi_{\rm cc}^{\rm P}(r) &= \frac{1}{\bar{\rho}_{\rm c}^2}\int_{M_{\rm cut}}^{\infty} dM M^2 \frac{dn(M)}{dM}\int {\rm d}^3\boldsymbol{x}_0\, u_{\rm h}(|\boldsymbol{x}_1-\boldsymbol{x}_0|,M)u_{\rm h}(|\boldsymbol{x}_2-\boldsymbol{x}_0|,M) \qquad (5.12)\\ \xi_{\rm cc}^{\rm C}(r) &= \frac{1}{\bar{\rho}_{\rm c}^2}\prod_{i=1,2}\left[\int_{M_{\rm cut}}^{\infty} dM_i M_i \frac{dn(M_i)}{dM_i}\int {\rm d}^3\boldsymbol{x}_{0,i}\, u_{\rm h}(|\boldsymbol{x}_i-\boldsymbol{x}_{0,i}|,M_i)\right]\xi_{\rm cc}^{\rm cent}(r_0,M_1,M_2)\ , \end{aligned}$$

$u_{\rm h}(|\boldsymbol{x}|,M)$ being the normalised halo density and $dn(M)/dM$ the mass function as above and now $r = |\boldsymbol{x}_1-\boldsymbol{x}_2|$. Here, $\xi_{\rm cc}^{\rm cent}(r_0,M_1,M_2)$ is the correlation function of the field of halo centres and is a function of the halo masses and $r_0 = |\boldsymbol{x}_{1,0}-\boldsymbol{x}_{2,0}|$. Assuming that the background density field dictates the position of haloes via a *“local” deterministic bias*, the correlation function of halo centres can be written as in (Fry & Gaztanaga, 1993; Mo & White, 1996; Smith et al., 2007):

$$\begin{aligned} \xi_{{\rm cc},R}^{\rm cent}(r,M_1,M_2) &= \langle\delta_R(\boldsymbol{x})\delta_R(\boldsymbol{x}+\boldsymbol{r})\rangle\, b_1(M_1)b_1(M_2) + \\ &+ \frac{1}{6}\left\langle\delta_R(\boldsymbol{x})\delta_R^3(\boldsymbol{x}+\boldsymbol{r})\right\rangle\Big[b_1(M_1)b_3(M_2)\ + b_3(M_1)b_1(M_2)\Big] + \\ &+ \left\langle\delta_R^2(\boldsymbol{x})\delta_R^2(\boldsymbol{x}+\boldsymbol{r})\right\rangle\frac{b_2(M_1)b_2(M_2)}{4} + \ldots , \end{aligned} \tag{5.13}$$

where we have smoothed the density field over the length R and so $\delta_R(\boldsymbol{x})$ is the smoothed overdensity distribution and where the non-linear bias parameters b_i are defined through the above assumed relationship between the underlying dark matter density and the positions of haloes via:

$$\delta_{{\rm c},R}(\boldsymbol{x},M) = \sum_i \frac{b_i(M)}{i!}\left[\delta_R(\boldsymbol{x})\right]^i \quad . \tag{5.14}$$

Assuming only the first order significant in equation 5.13:

$$\xi_{{\rm cc},R}^{\rm cent}(r,M_1,M_2) \approx \xi_R(r)b_1(M_1)b_1(M_2) \quad , \tag{5.15}$$

we can replace the correlation function of halo centres back into eq. 5.12 to finally obtain the *2-halo* term:

$$\xi_{\rm cc}^{\rm C}(r) \approx \frac{1}{\bar{\rho}_{\rm c}^2}\prod_{i=1,2}\left[\int_{M_{\rm cut}}^{\infty} dM_i M_i \frac{dn(M_i)}{dM_i} b_1(M_i)\int {\rm d}^3\boldsymbol{x}_{i,0}\, u_{\rm h}(|\boldsymbol{x}_i-\boldsymbol{x}_{0,i}|,M)\right]\xi_R(r_0)\ . \tag{5.16}$$

(compare this also to app. A).

In order to further increase the accuracy of this description of the statistic of the density field, we should take into account that the smooth component density should go to zero where the haloes are located. This is left for further work. Additionally, the halo exclusion principle (Smith et al., 2011, 2007; Takada & Jain, 2004) would ensure that we don’t doubly count the correlations into the *2-halo* term, where the correlation distance, r is smaller than the sum of the two halo radii, since if this were the case, there would not be two but only one halo. In this case, the correlation should add to the *Poisson* term.

The smooth-smooth correlation function

Now in finding the smooth-smooth correlation function, we again assume the smooth density field is related to the underlying total dark matter field via a local deterministic bias and so we write again, as in equation 5.14:

$$\delta_{\mathrm{s},R}(\boldsymbol{x}) = \sum_i \frac{b_{\mathrm{s},i}}{i!} \left[\delta_R(\boldsymbol{x})\right]^i \quad . \tag{5.17}$$

We again make an approximation to relate the total smoothed correlation function to the correlation function of the smooth component, neglecting non-linear terms, $\mathcal{O}(b_{\mathrm{s},2}, b_{\mathrm{s},3}, \dots)$:

$$\xi_{\mathrm{ss},R}(r) \approx b_{\mathrm{s},1}^2 \, \xi_R(r) \quad . \tag{5.18}$$

The smooth-halo cross-correlaton

Finally and equivalently, we find the smooth-clumped cross-correlation function, neglecting terms of higher order, $\mathcal{O}(b_2, b_{\mathrm{s},2} \dots)$:

$$\xi_{\mathrm{sc}}(r) \approx \frac{1}{\bar{\rho}_{\mathrm{c}}} \int_{M_{\mathrm{cut}}}^{\infty} dM M \frac{dn(M)}{dM} b_1(M) \int \mathrm{d}^3\boldsymbol{x}_0 \, u(|\boldsymbol{x}_1 - \boldsymbol{x}_0|, M) \, b_{\mathrm{s},1} \, \xi_R(|\boldsymbol{x}_2 - \boldsymbol{x}_0|) \quad . \tag{5.19}$$

Bias of the smooth, linear-like matter field

Having an idea of how to calculate the first halo bias using the Sheth & Tormen (1999) perscription in eq. 3.13, we now need to find the bias factors for the smooth component. If mass is to be conserved, knowing this halo bias, we can immediately derive the bias of the smooth component. In other words, fully knowing how the underlying total dark matter distribution determines the distribution of haloes, we can fully understand the density distribution of the smooth component without much further effort.

Therefore we first determine the bias of the clumped component, by mass-integrating over eq. (5.14):

$$\int_{M_{\mathrm{cut}}}^{\infty} dM M \frac{dn(M)}{dM} \, \delta_{\mathrm{c},R}(\boldsymbol{x}, M) = \int_{M_{\mathrm{cut}}}^{\infty} dM M \frac{dn(M)}{dM} \sum_i \frac{b_i(M)}{i!} \left[\delta_R(\boldsymbol{x})\right]^i \quad , \tag{5.20}$$

where M and R are related as always, through the mass-radius relationship for haloes (eq 3.21). But we also know, from our definition of $f = \bar{\rho}_{\mathrm{c}}/\bar{\rho}$ and equation 5.3, that mass-integrating the mass function alone down to a cut-off mass-scale gives us the amount of matter contained within haloes, therefore:

$$\begin{aligned} \rho_{\mathrm{c}}(\boldsymbol{x}) &= \bar{\rho}_{\mathrm{c}} \left[1 + \delta_{\mathrm{c}}(\boldsymbol{x})\right] \\ &= \int_{M_{\mathrm{cut}}}^{\infty} dM M \frac{dn(M)}{dM} \left[1 + \delta_{\mathrm{c}}(\boldsymbol{x}, M)\right] \quad . \end{aligned} \tag{5.21}$$

Then we can re-write eq. (5.20) and arrive at an expression for $\delta_{\mathrm{c}}(\boldsymbol{x})$:

$$\delta_{\mathrm{c}}(\boldsymbol{x}) = \frac{1}{\bar{\rho}_{\mathrm{c}}} \int_{M_{\mathrm{cut}}}^{\infty} dM M \frac{dn(M)}{dM} \sum_i \frac{b_i(M)}{i!} \left[\delta_R(\boldsymbol{x})\right]^i \quad , \tag{5.22}$$

defining a new, mass-weighed effective bias for the clumped component as:

$$b_i^{\text{eff}} = \frac{\int_{M_{\text{cut}}} dMM \frac{dn(M)}{dM} b_i(M)}{\int_{M_{\text{cut}}} dMM \frac{dn(M)}{dM}} \quad , \tag{5.23}$$

we get a concise expression for the clumped density perturbation:

$$\delta_{\text{c}}(\boldsymbol{x}) = \sum_i \frac{b_i^{\text{eff}}}{i!} \left[\delta_R(\boldsymbol{x})\right]^i \quad . \tag{5.24}$$

We can now use this equation together with eq. (5.17), which defines the bias parameters of the smooth component, insert them into eq. (5.8) and find that:

$$\begin{aligned}
\delta(\boldsymbol{x}) &= (1-f)\delta_{s,R}(\boldsymbol{x}) + f\delta_{\text{c}}(\boldsymbol{x}) \\
&= (1-f)\sum_i \frac{b_{\text{s},i}}{i!}\left[\delta_R(\boldsymbol{x})\right]^i + f\sum_i \frac{b_i^{\text{eff}}}{i!}\left[\delta_R(\boldsymbol{x})\right]^i \\
&= \sum_i \left[(1-f)b_{\text{s},i} + f b_i^{\text{eff}}\right] \frac{\left[\delta_R(\boldsymbol{x})\right]^i}{i!} \quad .
\end{aligned} \tag{5.25}$$

From this, two conditions emerge naturally. Firstly,

$$1 = (1-f)b_{\text{s},1} + f b_1^{\text{eff}} \quad , \tag{5.26}$$

$$\Rightarrow b_{\text{s},1} = \frac{1 - f b_1^{\text{eff}}}{1-f} \quad . \tag{5.27}$$

Secondly, a linearly biased smooth component implies the dissapearance of all non-linear bias coefficients:

$$\int_{M_{\text{cut}}} dMM \frac{dn(M)}{dM} b_i(M) = 0 \quad \text{with} \quad i \neq 1 \quad . \tag{5.28}$$

However, if, as in the local model, the smooth component *is* non-linearly biased, the condition is less strict:

$$(1-f)b_{\text{s},i} + f b_i^{\text{eff}} = 0 \quad \text{with} \quad i \neq 1 \quad , \tag{5.29}$$

$$\Rightarrow b_{\text{s},i} = -\frac{f b_{\text{c},i}^{\text{eff}}}{1-f} \quad \text{with} \quad i \neq 1 \quad . \tag{5.30}$$

The total power spectrum

Now to obtain power spectra, we must Fourier transform and so the weighted contributions from the 3 separate correlation combinations, as in eq. (5.10) become:

$$P(k) = (1-f)^2 P_{\text{ss}}(k) + 2(1-f)f P_{\text{sc}}(k) + f^2 P_{\text{cc}}(k) \quad . \tag{5.31}$$

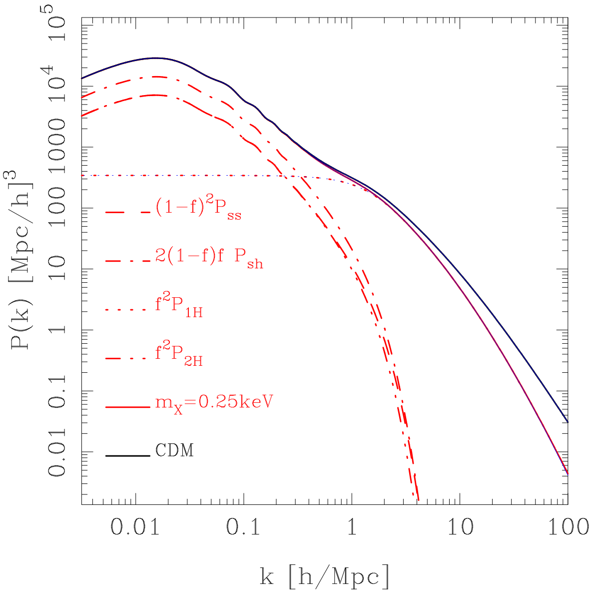

FIGURE 5.2: The nonlinear matter power spectrum calculated using the modified halo model with $m_{\rm wdm} = 0.25\,$keV (red & blue lines) and the CDM model (black lines). The solid black and red lines denote the total CDM and total WDM power spectra. For the WDM case, the dashed, dot-dash, dotted and triple dot-dashed lines denote, $P_{\rm ss}$, $P_{\rm sc}$, $P_{\rm P}$, and $P_{\rm C}$, respectively. The solid blue line is calculated for the WDM model, but also taking into account the relic velocities (as also discussed in app. B).
FIGURE SOURCE: Smith & Markovič (2011)

Fourier transforming our 3 approximate correlation functions from equations (5.11), (5.18) and (5.19):

$$\begin{aligned}
P_{\rm ss}(k) &= b_{\rm s,1}^2 P_R(k) \quad , \\
P_{\rm sc}(k) &= \frac{b_{\rm s,1}P_R(k)}{\bar{\rho}_{\rm c}} \int_{M_{\rm cut}}^{\infty} dM M b_1(M) \frac{dn(M)}{dM} \tilde{u}(k,M) \\
P_{\rm cc}(k) &= \frac{P_R(k)}{\bar{\rho}_{\rm c}^2} \left[\int_{M_{\rm cut}}^{\infty} dM M b_1(M) \frac{dn(M)}{dM} \tilde{u}(k,M) \right]^2 \\
&\qquad + \frac{1}{\bar{\rho}_{\rm c}^2} \int_{M_{\rm cut}}^{\infty} dM \frac{dn(M)}{dM} M^2 \tilde{u}^2(k,M) \quad , \qquad (5.32)
\end{aligned}$$

where $\tilde{u}(k, M)$ is the Fourier-transformed, mass-normalised halo density profile and where we may approximate the smoothed non-linear power spectrum, $P_R(k)$ with the WDM suppressed linear power spectrum (eq 2.49). The two terms in the expression for $P_{\rm cc}$ corresppond to the standard two- and one-halo i.e. Poisson and Clustering terms. We plot the final power spectrum in fig. (5.2) together with the individual components. Note however, that in this plot the mass function has been modified too as is described below in sec. 5.1.2.

5.1.2 Modified halo model ingredients

We now consider the modification to the mass functions and the halo bias. The halo density profiles are briefly discussed in app. B.

Mass functions

As discovered in ch. 4, there seems to be an excess in the number of low mass haloes obtained if the standard Sheth-Tormen approach is used for WDM compared to simulations (Polisensky & Ricotti, 2010; Zavala et al., 2009). Moreover, considering that the initial density field becomes strongly smoothed on small scales by WDM free-steaming (sec 2.3.3), it may be argued that small haloes should not form on their own and may perhaps only be able to exist within much larger haloes (Bode et al., 2001; Wang & White, 2007). This comes from considering *peak theory* of structure formation (Mo & White, 1996; Press & Schechter, 1974; Sheth & Tormen, 1999). Namely, if peaks corresponding to short wavenumbers in Fourier space become suppressed in amplitude, they should only end up as haloes if they are initially in a high density environment, meaning that they overlap with peaks corresponding to large Fourier wavenumbers, which still can have large amplitudes.

For this reason we wish to introduce an arguably *ad-hoc* modification to the mass functions, which suppressed the number of the very smallest haloes to zero. For this reason, we multiply the calculated Sheth-Tormen mass functions, dn/dM, from our WDM-suppressed linear matter power spectra by a smoothed step function that depends on the halo mass rescaled by the *free-streaming halo mass*, $M_{\rm fs}$ as defined in eq. (4.2):

$$\frac{d\tilde{n}_{\rm wdm}}{d\log M} = \frac{1}{2}\left\{1 + {\rm erf}\left[\frac{\log_{10}(M/M_{\rm fs})}{\sigma_{\log M}}\right]\right\}\frac{dn_{\rm wdm}}{d\log M} \quad , \tag{5.33}$$

where we have chosen the smoothing parameter for the step function $\sigma_{\rm logM} = 0.5$. Were we to chose this smoothing parameter to equal zero, our smooth step function would become the Heaviside step function. The free-streaming mass on the other hand decides the halo mass at which the suppression is applied. For CDM, $M_{\rm fs} \to 0$ and so, $d\tilde{n} \to dn$, since ${\rm erf}(x) \to 1$ for $x \to \infty$.

We plot the resulting mass functions in fig. (5.3) in comparison with the original Sheth-Tormen version. We do this for several different WDM particle masses. We also plot the ratio of the WDM functions to the CDM functions with respect to the rescaled halo mass, $M/M_{\rm fs}$. This step results in suppressing the number of haloes slightly also for haloes with masses in the range of about $M_{\rm fs} - 100M_{\rm fs}$.

More recently (Schneider et al., 2012) examined this model in comparison to N-body simulations (discussed generally in sec. 3.2). Figure 5.4 shows their result, plotting the ratio of the WDM and CDM mass functions. They rescaled the halo masses with respect to the so-called "half-mode mass", $M_{\rm hm} \approx 2.7 \times 10^3 M_{\rm fs}$[1], rather than the free-streaming mass as above. They find the simple fitting formula:

$$\frac{d\tilde{n}_{\rm wdm}}{dn_{\rm wdm}} = \left(1 + \frac{M}{M_{\rm hm}}\right)^{-\alpha} \quad , \tag{5.34}$$

to match their simulation results well without the need to apply an artificial step function. The single fitting parameter, $\alpha = 0.6$ was able to match the simulations with less than 5% root-mean-square error. Dunstan et al. (2011) find very similar results.

Halo bias

We make no further modifications to the halo bias here apart from defining new bias variables relating to the clumped and smooth density field components (sec 5.1.2). A more recent result from Schneider et al. (2012), who ran WDM simulations and with a halo finder measured the mass functions, is that the bias prescription from Sheth & Tormen (1999) holds relatively well for WDM (plotted in the previous chapter in fig. 4.2). This may come across as surprising

---

[1] The half-mode mass is defined to be the mass corresponding to he scale where the WDM linear transfer function (eq 2.49) drops to a value of 0.5.

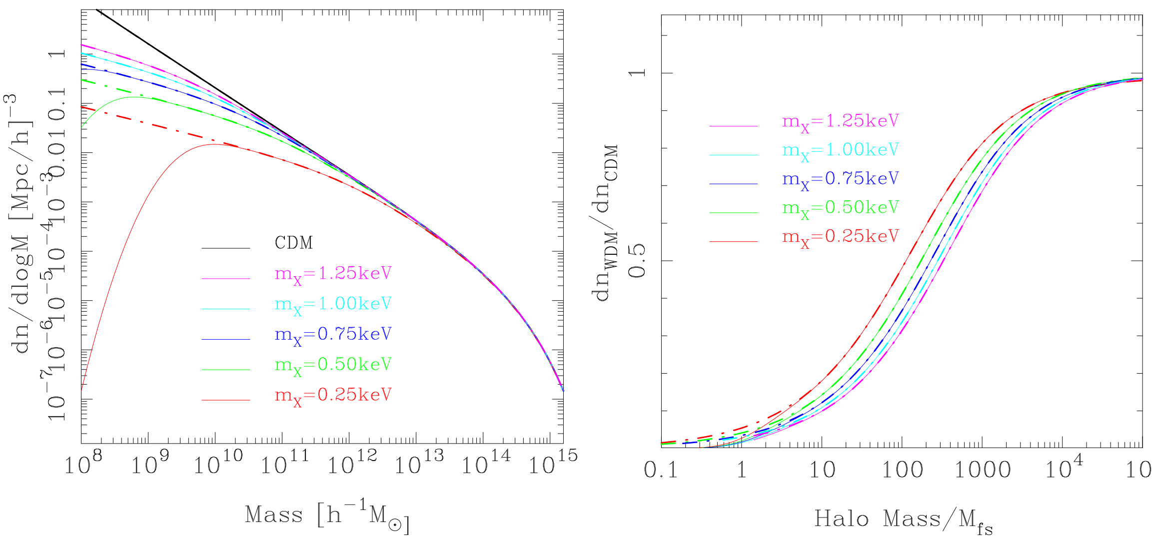

FIGURE 5.3: In the left panel we plot the halo mass functions calculated from the WDM suppresed linear matter power spectra for 5 different WDM (colorful lines) and one CDM model (black line). The dot-dashed lines correspond to standard Sheth-Tormen mass functions eq. 3.1. The solid lines on the other hand are the mass functions with an additional suppression to diminish the number of low mass haloes following eq. (5.33). We use the step-smoothing parameter to be $\sigma_{\log M} = 0.5$.
On the right side we plot the ratios between the WDM and CDM mass functions for both approaches. We lot them against the rescaled halo mass in units of the WDM free-streaming mass-scale $M_{\rm fs}$.
FIGURE SOURCE: Smith & Markovič (2011)

at first, since one would expect that by smoothing out the small scales and hence preventing the smallest haloes from forming unless located near the larger peaks would result in a larger bias for the small haloes. This is since the bias describes the dependence of the local number density of haloes of a certain mass depends on the total local density. However, the reason why Schneider et al. (2012) saw only slight differences in the bias between WDM and CDM models is presumably because their cosmological simulations did not reach scales small enough to probe the relevant halo masses. It should be noted here, that they indeed seem to see an increase in the halo bias at $M \sim 10^{11}\,M_\odot$ for the $m_{\rm wdm} = 0.25\,$keV, however this seems to largely be a result of **spurious halo formation** in WDM N-body simulations.

Concentration parameter

We have defined the concentration parameter in eq. (3.20). It describes how concentrated a halo is at its core. The concentration parameter enters into the definition of the NFW (Navarro et al., 1997) density via the *scale radius*, $r_{\rm s}$ in eq. (3.22). We examine the density profiles in app. B, but do not discuss them in detail here, since the changes in the profiles induced by WDM free-streaming do not impact the resulting nonlinear matter power spectrum significantly. We do however note the recent result from Schneider et al. (2012), which seems to indicate that the profiles of low-mass haloes become much less concentrated, i.e., less cuspy, in the WDM case. This can be seen in their plot, here fig. 5.5.

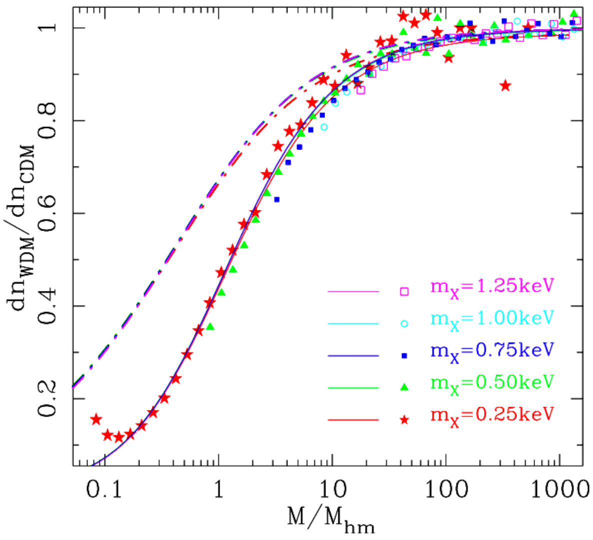

Figure 5.4: Mass function ratios comparing WDM and CDM halo mass distribution are shown here for 5 different thermal relic WDM particle masses (different colors). The halo masses are rescaled with respect to the *half-mode mass*. The dot-dashed lines are the theoretically calculated mass functions using the Sheth-Tormen formalism starting from a WDM-suppressed linear matter power spectrum as described in sec. 4.1.1. The star, triangle, filled square, circle and empty square shaped points are the results from N-body simulations. For this *finder code* has to be run on the simulation results by the paper authors. The solid lines correspond to the universal fit from eq. (5.34). It can be seen here that the shape of the suppression of the mass functions is independent of the WDM model. The WDM dependence comes in only via the halo mass rescaling, which is to be expected, because the rescaling is calculated from the behaviour of the mass function.
Figure source: Schneider et al. (2012)

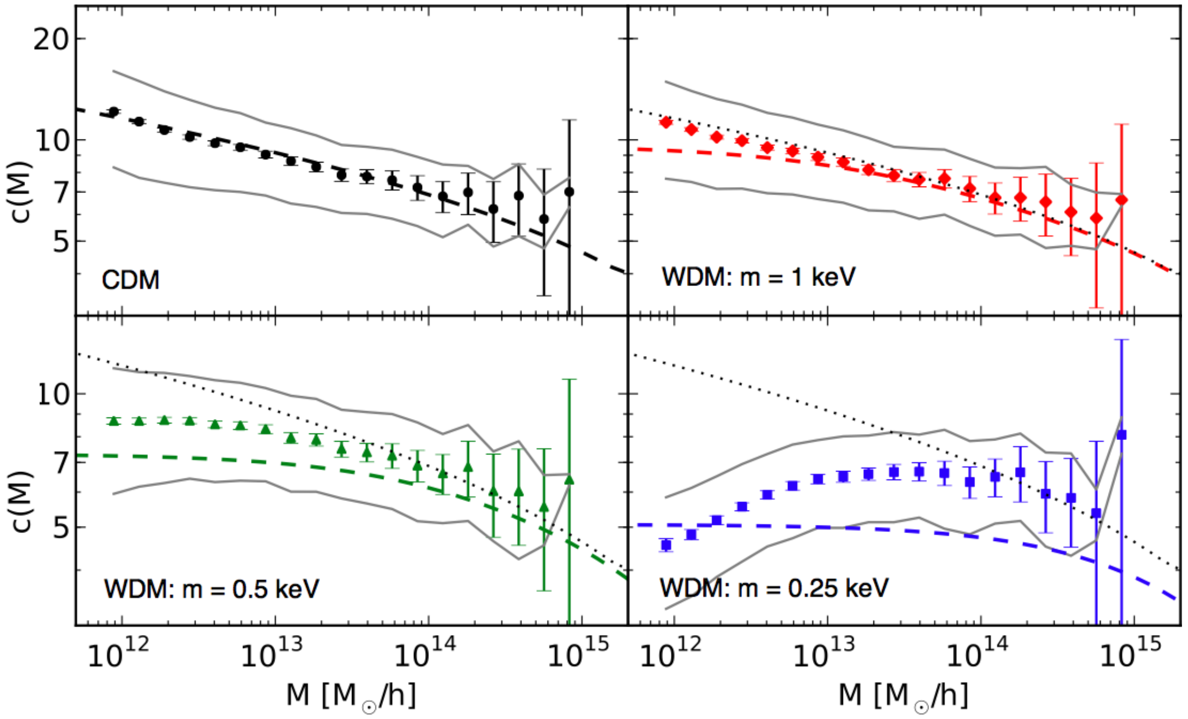

Figure 5.5: Here plotted are the mass-dependent concentration parameters (eq 3.20) from the study of Schneider et al. (2012). The different panels show different WDM and CDM models. The dots with error bars are the results from their cosmological simulations. The grey lines show the spread in the concentration parameters of the individual haloes from the simulation. The dashed lines are the fits they found using the model of Bullock et al. (2001) and the dotted lines in the WDM panels correspond with the theoretical predictions from pure CDM and match the dashed line of the upper left panel. We can see that the concentration seems to be suppressed for low-mass haloes in the WDM models.
Figure source: Schneider et al. (2012)

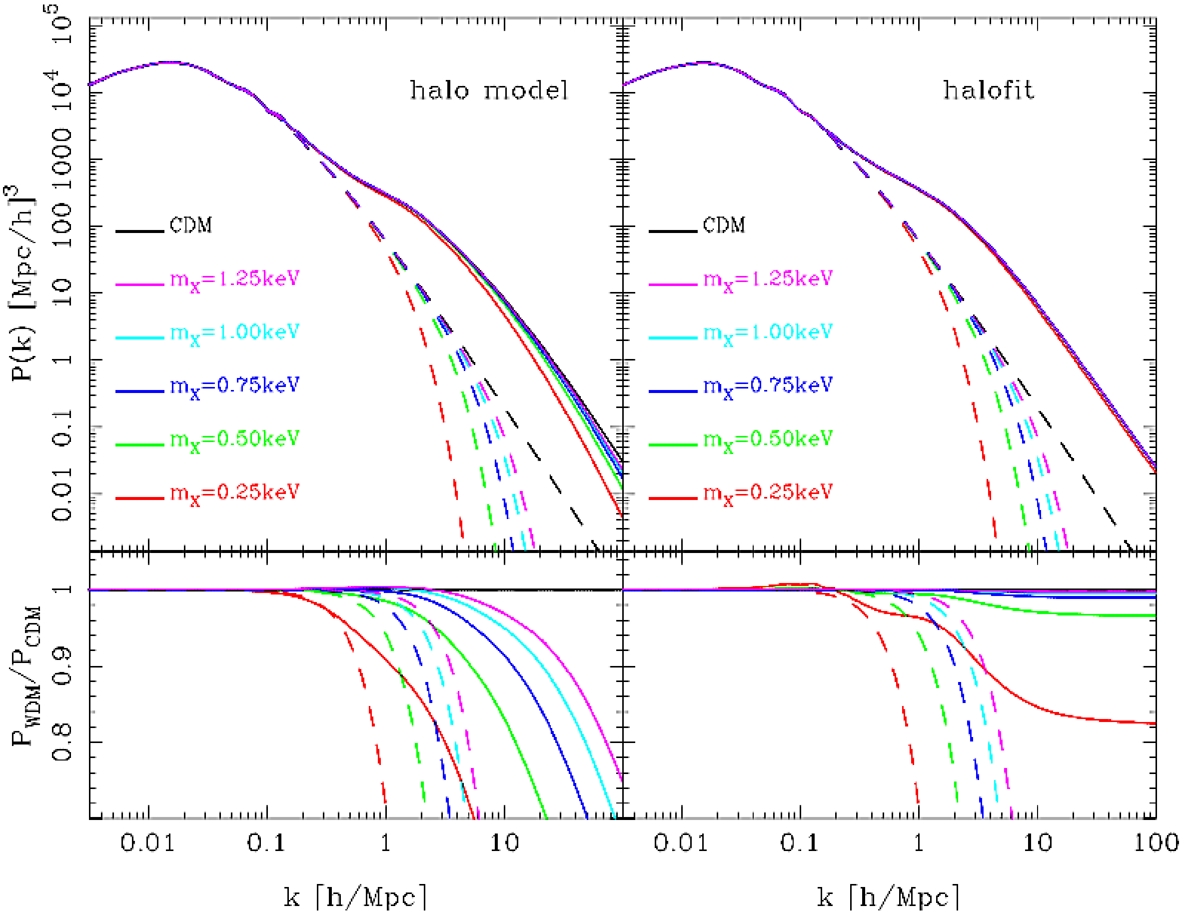

FIGURE 5.6: In the upper panels are plotted nonlinear (solid) as well as linear (dashed) **matter power spectra** for different WDM models, where the particle masses for a thermal relic, $m_{\rm wdm} \in \{0.25, 0.5, 0.75, 1.0, 1.25\}\,$keV. In the lower panels are the ratios between the WDM and CDM power spectra.
On the left panels are the power spectra calculated assuming the new, modified halo model described in this chapter. On the right panels are the power spectra plotted using the `HALOFIT` prescription, as in ch. 4 for comparison.
FIGURE SOURCE: Smith & Markovič (2011)

5.2 Forecasts for non-linear measurements

We have plotted the nonlinear power spectrum for the $m_{\rm wdm} = 0.25\,$keV case already in fig. (5.2). In this figure we have seen the power spectra for the separate components of the cosmological density field: the smooth component, $P_{\rm ss}(k)$; the clumped clustering component, $P^{\rm C}_{\rm cc}$; the clumped Poisson component, $P^{\rm P}_{\rm cc}$ and the cross-component, $P_{\rm sc}(k)$.

We now plot only the weighted sum of these components, i.e. the total nonlinear matter power spectrum for different WDM as well as the CDM model in fig. (5.6). We also plot the ratio of the WDM and CDM nonlinear power. We plot these alongside the analogous linear matter power spectra and see that through nonlinear collapse power is regenerated. This matches our conclusions from the previous chapter. We also compare this new modified halo model to the HALOFIT approach already used in a similar way in sec. 4.1.2. We can see that the general trend is similar, but in the halo model the suppression of the power spectrum is significantly stronger. For example, in the most extreme model, where $m_{\rm wdm} = 0.25\,$keV, the suppression at the wavenumber, $k \sim 10\,h$Mpc^{-1} is greater than 30%. On the other hand, in the HALOFIT, the suppression in this same model saturates already at scales $k \sim 10\,h$Mpc^{-1} to a maximum of $\sim 18\%$.

5.2.1 Weak lensing power spectra

As in the previous chapter, we again use the methods described in sec. 3.3 together with the nonlinear power spectra obtained with our new modified halo model to calculate the weak lensing power spectra with multipoles up to $l = 5000$. We show these power spectra and as before, the ratios comparing the convergence[2] power spectra of WDM to those of CDM in fig. 5.7. In addition we again use HALOFIT to find the lensing power spectra and plot them alongside those found using the new halo model. We see that the effects of WDM are much stronger in the halo model calculation as would be expected from the nonlinear matter power spectrum results plotted in fig. (5.6). Note that as in the previous chapter we assume our lensing survey to be Euclid-like, but here, for simplicity, we take all source galaxies to be found in a single redshift plane at $z_{\rm s} = 1$. This simplifies the calculations, but slightly diminished the constraining power. We take full account of lensing tomography in the next section in that we again find the full covariance matrix for 10 tomographic redshift bins.

Finally, we repeat the forecast for the proposed Euclid (Refregier et al., 2010) survey. Because Euclid will include an extensive photometric, as well as a spectroscopic redshift survey, it will be able to map out the distribution of galaxies in three dimensions. For this reason we now, as in the previous chapter, extend our analysis into the redshift dimension by assuming an *extended source distribution* function in eq. 3.74, $G(z)$, of the same form as in the previous chapter and in (Markovič et al., 2011). As in ch. 4, we divide it into 10 separate redshift bins. Our covariance matrix gives covariances between different redshift bins and has the form of Takada & Jain (2004):

$$\mathrm{Cov}\left[C^{\rm obs}_{l,ij}, C^{\rm obs}_{l',op}\right] = \frac{\delta^K_{l,l'}}{N(l_m,l_n)f_{\rm sky}}\left[C^{\rm obs}_{l,io}C^{\rm obs}_{l,jp} + C^{\rm obs}_{l,ip}C^{\rm obs}_{l,jo}\right] \quad , \tag{5.35}$$

ignoring the contribution from higher order spectra and with $C^{\rm obs}_{l,ij} = C_{l,ij} + \delta_{ij}\frac{\sigma^2_\gamma}{\bar{n}_i}$.

Assuming Gaussian errors we then estimate the curvature of the 5-dimensional likelihood function around its maximum. Hence we find the errors as well as 2-dimensional likelihood contours in fig. 5.8, centred on our fiducial model. We vary the following set of five parameters: the inverse WDM particle mass, $m^{-1}_{\rm wdm}$, the total matter density today, $\Omega_{\rm m}$, the primordial perturbation spectral index, $n_{\rm s}$, the primordial spectral amplitude, $A_{\rm s}$ and the matter power spectrum shape parameter, $\Gamma = e^{-2\Omega_{\rm b}h}\Omega_{\rm m}h$.

We choose $m^{-1}_{\rm wdm}$ as a parameter in order to avoid setting the fiducial model at infinity. However, redefining this variable does not avoid the strong variation of error on $m_{\rm wdm}$ with the chosen fiducial model. Furthermore, and most problematically for such an analysis, the likelihood function is flat with respect to the variation of this parameter around the maximum

---

[2] As discussed in sec. 3.3, the magnitude of the weak lensing **shear** and the lensing **convergence** are equal. Therefore the power spectrum of convergence equals that of cosmic shear.

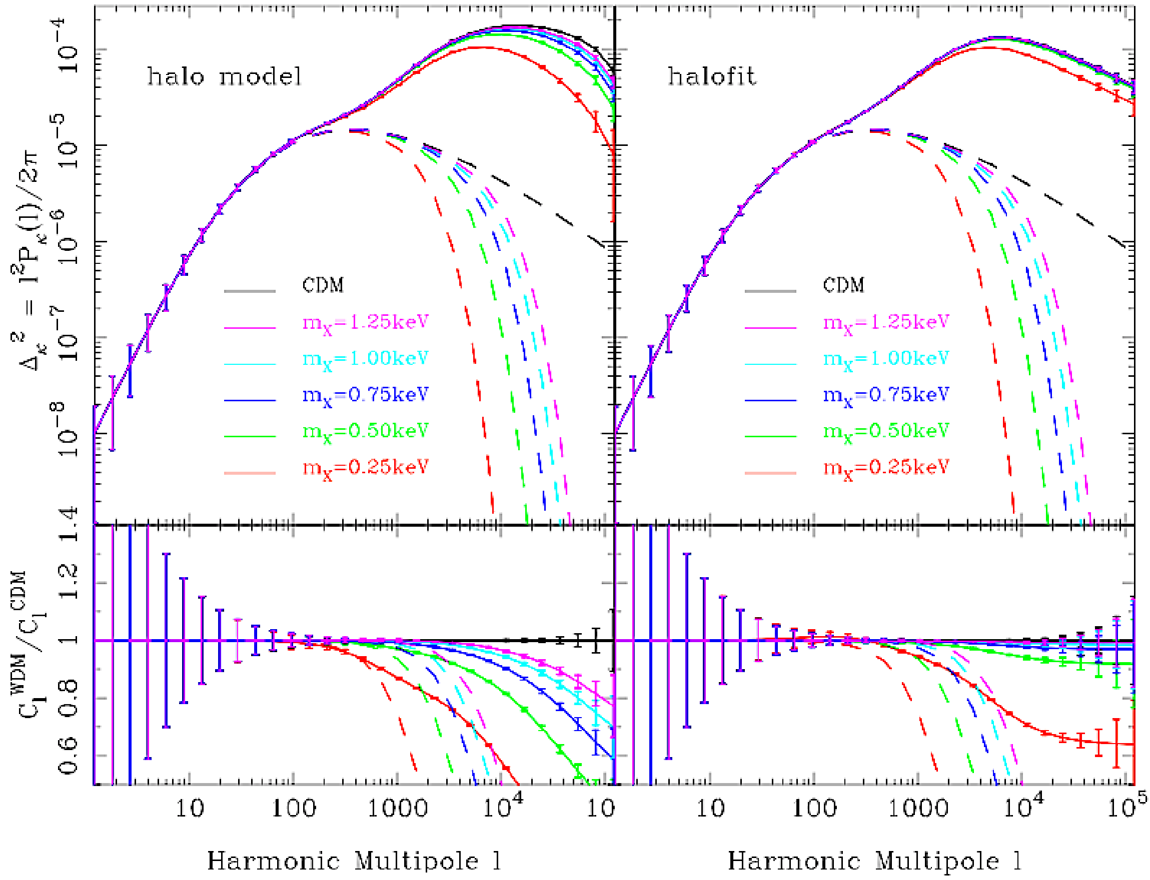

FIGURE 5.7: In the upper panels are plotted the weak lensing power spectra using full nonlinear (solid) as well as linear (dashed) **matter power spectra** for different WDM models, where the particle masses for a thermal relic, $m_{\rm wdm} \in \{0.25, 0.5, 0.75, 1.0, 1.25\}$ keV. Note that all source galaxies are assumed to be found in a slice at $z_]s = 1$. In the lower panels are the ratios between the WDM and CDM lensing power spectra.
On the left panels are the power spectra calculated assuming the new, modified halo model described in this chapter. On the right panels are the power spectra plotted using the `HALOFIT` prescription, as in ch. 4 for comparison.
FIGURE SOURCE: Smith & Markovič (2011)

likelihood point. For this reason, we fit half a Gaussian curve on top of this likelihood function and find single tailed errors as in ch. 4 and in Markovič et al. (2011).

In order to compare our results to those obtained with the standard halo model of the previous chapter, we again apply PLANCK priors to our lensing forecast. We use the PLANCK FM for the fiducial parameter set prescribed by Albrecht et al. (2006). We marginalise over the optical depth and the baryon density and perform a parameter transformation as in Eisenstein et al. (1998); Rassat et al. (2008). As before, we assume to have only the 143 GHz channel CMB data. Furthermore we make the assumption that WDM with particle masses of the order of a keV does not leave an observable signature in the CMB data and hence set the corresponding entries in the PLANCK FM to zero.

We then forecast a minimum limit on the WDM particle mass in the CDM scenario from

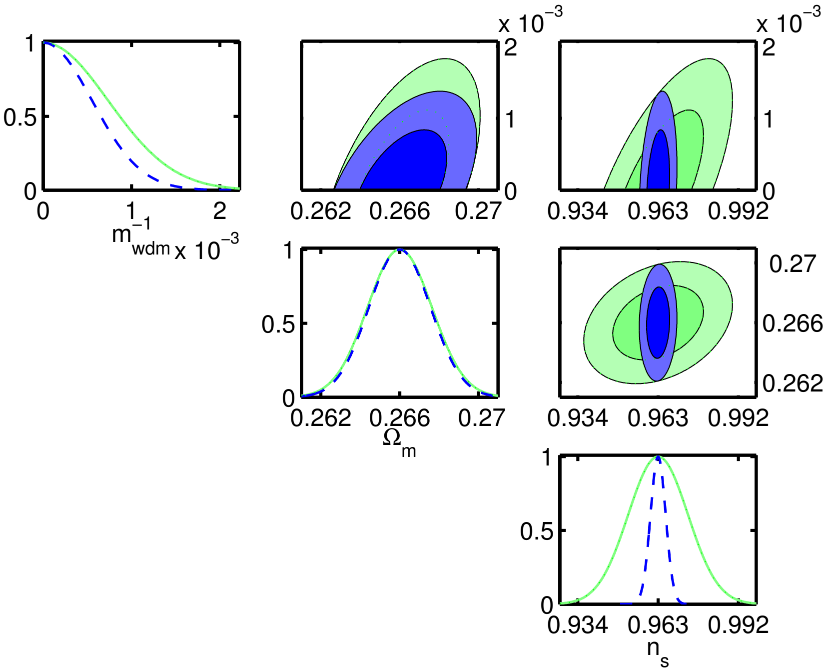

Figure 5.8: We plot 65% and 95% likelihood contours for the Euclid (green) survey as well as Euclid combined with Planck (blue) for three parameters $m_{\rm wdm}^{-1}$, $\Omega_{\rm m}$ and $n_{\rm s}$, while marginalising over two additional parameters: $A_{\rm s}$ and Γ. Our fiducial model is ΛCDM. Also, $l_{\rm max} = 5000$.

Euclid as $m_{\rm wdm}^{\rm min} = 1.4$ keV and from combining Euclid and Planck data, $m_{\rm wdm}^{\rm min} = 1.8$ keV. Note that this limit is somewhat less restrictive than the limit found in the previous chapter. This is because in this analysis we use only multipoles up to $l_{\rm max} = 5000$, which at the median redshift of the Euclid survey, $z_{\rm m} = 0.9$, corresponds to approximately $k_{\rm max} = 1.6$. We exclude scales smaller than this in order to avoid the range where baryonic effects may be significant.

5.3 Summary & discussion

In this chapter we have reexamined the phenomenological halo model in the context of WDM. We discovered in the previous chapter, ch. 4 that because WDM free-streaming prevents the formation of small haloes it seems that not all matter in the universe can be assumed to be contained within collapsed structures. For this reason we have tried to develop a new approach in this chapter, in which we have split the dark matter density field into two separate components, the *smooth* and the *clumped* density field. We have developed the formalism for calculating the two-point clustering statistic for such a divided field in sec. 5.1.2. We have shown that in this model, the nonlinear matter power spectrum is made up of four terms: the smooth field autocorrelation term, $P_{\rm ss}(k)$

In the process of deriving the new power spectrum, we have defined a new local deterministic bias variablee, $b_{\rm s}$, which relates the smooth background density field to the total nonlinear density field. We have assumed the standard peak-background split formulation for $b(M)$, still being the first order nonlinear bias parameter familiar from the classical halo model formalism. We have found that the smooth field was anti-biased with respect to the total density field. This may reasonably be expected since, as we have mentioned, small haloes can still form int he WDM, but only in high density environments, which would result in a stronger biasing of small haloes but an anti bias to the non-collapsed component.

We have suppressed the mass function with a step function in an *ad hoc* manner, to find a function more fitting to the assumption that small haloes are nearly erased from the clumped density field. We have also discussed some more recent N-body simulations by other authors, who modified our mass function and found a fit to their simulations. They did this by rescaling the halo mass with respect to the **half mode mass**, which depends on the WDM model. This half-mode halo mass is larger for models where the dark matter is colder, since it is proportional to the **free-streaming** mass, which can be calculated from the WDM free-streaming length discussed in sec. 2.3.3. We have found surprisingly that there exists significant suppression in the number of haloes with masses also slightly above the so-called "free-streaming" mass. Perhaps this is not so surprising when considering the stochastic nature of the initial density field and structure formation.

We have briefly discussed the concentration parameter, $c(M)$ as the most significant effect for the nonlinear matter power spectrum. We will briefly discuss the WDM influence on the shapes of halo profiles in app. B, but an in-depth discussion of this topic is out of the scope of this thesis. Note however that density profiles of haloes is an extremely important part of this field of research (e.g. Avila-Reese et al., 2001; Colin et al., 2000; Maccio et al., 2012; Vinas et al., 2012).

We then calculated the full nonlinear matter power spectra for five different WDM particle masses, $m_{\rm wdm} \in \{0.25, 0.5, 0.75, 1.0, 1.25\}$ keV with the new halo model approach and compared them to the CDM power spectrum as well as to the previously found HALOFIT approach. We found that the halo model, modified or not, predict that WDM has larger effects on cosmic nonlinear structure than the HALOFIT approach, which admittedly was developed on the basis of CDM-only simulations. In particular the nonlinear power spectra become suppressed by about 10% on scales $k \sim 1\,h\text{Mpc}^{-1}$ for a WDM particle with mass $m_{\rm wdm} = 0.25$ keV. If the WDM particle has a greater mass, e.g. $m_{\rm wdm} = 1.0$ keV the suppression is much less, in this case the suppression is $\gtrsim 10\%$ only on scales $k \gtrsim 20\,h\text{Mpc}^{-1}$.

We finally computed the impact of a set of WDM particle masses on the expected convergence power spectrum from a future weak lensing survey. We also calculated the expected errors, assuming that each spherical harmonic is an independent Gaussian variable. We found that, if our halo model is correct, then it would be possible to differentiate between different WDM candidates with a systematics free, full-sky, weak lensing survey like Euclid (Refregier et al., 2010) or LSST (Ivezic et al., 2008). Using FM we found a prediction of the limit on the WDM particle mass for the Euclid survey to be 1.4 keV and when combining Euclid and Planck FM, the prediction improved to 1.8 keV. This is similar to our results in the previous chapter, but less constraining, because we chose $l_{\rm max} = 5000$ unlike in ch. 4, where we took $l_{\rm max} = 20000$ in order to avoid regimes strongly impacted by baryonic physics.

CHAPTER 6

N-body Simulations of ***Warm Dark Matter*** Large Scale Structure

This chapter corresponds closely to
Viel, Markovič, Baldi & Weller,
The nonlinear Mater Power Spectrum in Warm Dark Matter Cosmologies,
published in 2012 in the Monthly Notices of the Royal Astronomical Society,
volume 421, issue 1, pp. 50-62 (Viel et al., 2012).

In the previous chapters we have discussed the nonlinear structure in the warm dark matter scenario. We have attempted to construct approaches to calculating the nonlinear corrections to the small-scale suppressed linear matter power spectrum. We have done this in ch. 4 first by a brute force calculation of the `HALOFIT` prescription (Smith et al., 2003) and by using the standard halo model (Cooray *&* Sheth, 2002, and references within). Then we attempted to modify the halo model to better account for what we expect from large scale structure formation in the WDM model in ch. 5. In this chapter we run cosmological N-body simulations (see 3.2), where we have set up the initial conditions to reflect the small-scale suppressed power spectra calculated in ch. 2. We also consider briefly the effects of remnant thermal velocities of the dark matter particles in our WDM models. We show the results of convergence studies, where we have run several simulations with the same values of cosmological parameters, i.e. with the same cosmology, but with different volumes and particle numbers in order to attempt to account for effects coming from too low a resolution. We finally also briefly considered the effect of baryonic cooling on the underlying dark matter distribution (see also 3.2.2). We only discuss this briefly, because it is a very complex and extensive subject that is out of the scope of this thesis. We find a fitting function to the simulation results for the nonlinear corrections to the WDM suppressed linear matter power spectrum. We repeat our FM analysis and forecasts for a Euclid-like survey, similarly to ch. 4and ch. 5. We compare all the approaches: the classic `HALOFIT`, the new halo model from ch. 5 and the fit to simulations.

6.1 The set-up

We use the TreePM N-body code `GADGET-2` described in sec. 3.2 to run mostly pure dark matter simulations. For a few runs we also added baryonic particles into our simulations for which `GADGET-2` uses the SPH (Lagrangian) approach (Springel, 2005). In our runs we vary the sizes of our cosmological volumes to account for any large scale errors and more importantly to test the effects of resolution. The issue of spurious halo formation on small scales has been a long standing one and we want to make sure we are not plagued by such effects. The gravitational softening is set to be $1/40th$ of the mean linear inter-particle separation and is kept fixed in comoving units.

The PM grid, which guides the force calculations on the largest scales in the simulations was chosen to have the size of the box side divided by the number of particles. In the majority of the simulations the number of particles is 512^3. In the resolution testing simulations this is of course not the case and the number varies as we report below. Our initial conditions are set up the have the small scales suppressed by WDM particles with particle masses of $m_{\rm wdm} \sim 1\,$keV. The free-streaming scale below which the power spectrum becomes exponentially suppressed are of the order of $k \sim 1\,h$Mpc^{-1}. We use N-body simulations to try to understand this suppression in these highly nonlinear scales.

The initial conditions can in practice be generated as in Viel et al. (2005), which means suppressing the linear matter power spectrum by the WDM transfer function encountered already in ch. 2, but repeated here for the sake of analogy:

$$\begin{aligned} T^2_{\rm wdm}(k) &\equiv P_{\rm wdm}(k)/P_{\rm cdm}(k) = (1 + (\alpha\, k)^{2\nu})^{-5/\nu} \\ \alpha(m_{\rm wdm}) &= 0.049 \left(\frac{1\,\rm keV}{m_{\rm wdm}}\right)^{1.11} \left(\frac{\Omega_{\rm wdm}}{0.25}\right)^{0.11} \left(\frac{h}{0.7}\right)^{1.22} \quad , \end{aligned} \tag{6.1}$$

with $\nu = 1.12$. Also note that α has units of h^{-1}Mpc (e.g. Hansen et al., 2002). This fit is an approximation used often in order to avoid the strange behaviour of the transfer functions calculated with Boltzmann codes (as also in ch. 7). We use the `P-GenIC_WDM` code (related to `N-GenIC`) to generated the initial conditions ICs for the simulation. `P-GenIC` was written by Springel et al. (2001) and modified by Viel et al. (2005) to account for the suppression in the linear matter power spectrum due to WDM. The initial conditions are generated on a mesh and match the required input files for `Gadget-2`.

Assuming WDM to be thermal relic fermions, their relic velocities have a Fermi-Dirac distribution (eq 1.51), which can be added to the proper velocities calculated from the gravitational potentials from linear theory. The velocities for some of the WDM models we use can be found to be: $v_{\rm th} \in \{27.9, 11.5, 4.4, 1.7, 0.7\}$ km s^{-1} for $m_{\rm wdm} \in \{0.25, 0.5, 1, 2, 4\}$ keV, respectively. For comparison, the typical rms velocity in a ΛCDM run is $v_{\rm g} \sim 30$ km s^{-1}, so it is significantly larger than any thermal velocities of WDM particles in the models that are still allowed by for example the Lyα forest ($m_{\rm wdm} \gtrsim 2\,$keV).

6.2 The nonlinear power spectrum from simulations

We run several simulations, which we list in tab. (6.1) that vary in their volume and WDM model mainly, but we also run one simulation that includes baryonic cooling. In fig. (6.1) we show slices from two of the simulations, which are projections of 2.5 Mpc-thick slices through the 25^3 Mpc^3 simulation volume for the CDM and the 1 keV WDM model. In this simulation

side of simulation box $[h\mathrm{Mpc}^{-1}]$	$m_{\mathrm{wdm}}[\mathrm{keV}]$	softening $[h^{-1}\mathrm{kpc}]$
12.5	–	0.62
12.5	1	0.62
25^{a}	–	1.25
25	1	1.25
50	–	2.5
50	1	2.5
100	–	5
100	1	5
25	0.25	1.25
25	0.5	1.25
$25^{a,b}$	1	1.25
25	2	1.25
25	4	1.25
12.5	1	0.625
6.25	1	0.33

Table 6.1: This table contains a summary of all the simulation runs relevant to this chapter. The lengths of the side of the cosmological box and the softening length are reported in units comoving distance. The particle-mesh (PM) grid is chosen to be equal to $\mathrm{N}_{\mathrm{DM}}^{1/3}$ with $\mathrm{N}_{\mathrm{DM}} = 512^3$. The subscript ($b$) denotes the simulation in which baryonic particles were included with some rudimentary cooling prescriptions. Because such simulations are very computationally demanding they have been run at a lower resolution of $N_{\mathrm{DM}} = 384^3$.
Table source: Viel et al. (2012)

run, we set the number of simulation particles to $N = 512^2$ and the cosmological box side to $L = 25\,\mathrm{Mpc}$, which gives simulations particles the masses of $8.7 \times 10^6\, M_{\odot} h^{-1}$, which is assumed to be sufficiently below the free-streaming mass (eq 4.2).

We analyse the output of our simulations using the code `P-Power` by Springel et al. (2001), which uses the particle-mesh with the *cloud-in-cell* (CIC) algorithm to assign simulation particles onto the Cartesian grid (e.g. Viel et al., 2010)). This approach is of course in Fourier space, where the local density on the grid from the CIC mass assignment is Fourier transformed using the Fastest Fourier Transform in the West (FFTW, Frigo, 1999). FFTW relates the mass density in the simulation volume in real space to the mass density in Fourier space and then finds the two point correlation to get the power spectrum.

To begin with we plot the percentage differences between WDM and CDM nonlinear power spectra found using the above approach together with the so-called *folding method* (Colombi et al., 2008; Jenkins et al., 1998) from our simulation results. In fig. (6.2) we compare simulation results with varying resolution. In order to be able to work with a constant working memory requirement, we do not vary the particle number and keep it constant at $N = 512^3$. In order to vary the resolution, we vary the simulated cosmological volume between $100^3 - 25^3\,\mathrm{Mpc}^3$. We run one simulation with less particles, where $N = 384^2$ and the side of the simulation box, $L = 25\,\mathrm{Mpc}$.

The shot-noise power due to the finiteness of our simulation particles is subtracted from all the power spectrum estimates made. The shot-noise power becomes comparable to the real, physical power at $z = 0$ at $k \sim 150\, h\mathrm{Mpc}^{-1}$ for the simulation box side of $L = 100\,\mathrm{Mpc}$. For the simulation with $L = 25\,\mathrm{Mpc}$ in the WDM model with $m_{\mathrm{wdm}} = 1\,\mathrm{keV}$ the matter power is always larger than the shot-noise power for $z < 10$ and for $k < 20\, h\mathrm{Mpc}^{-1}$.

It was checked in Viel et al. (2012) that increasing the Particle-Mesh grid by a factor three impacts the matter power spectrum on scales, $k < 100\ h\mathrm{Mpc}^{-1}$ negligibly. In this work a higher resolution simulation was run by increasing the number of particles in a box with $L = 25\,\mathrm{Mpc}$ to $N = 640^3$ and yielded a less than 1% difference on scales, $k < 100\,\mathrm{Mpc}$. This is an indicator that spurious halo formation plagues the nonlinear matter power spectrum on

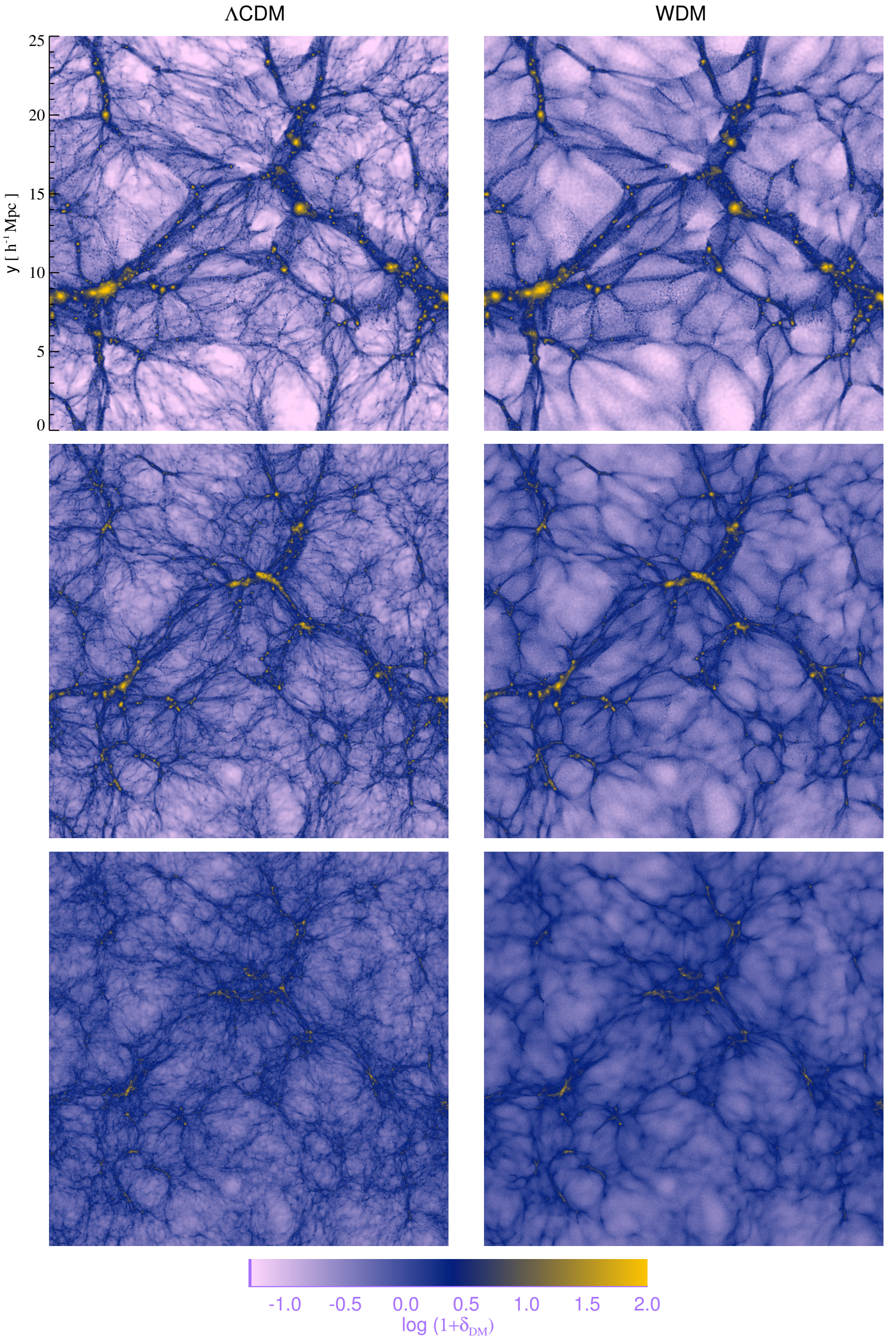

Figure 6.1: Here are plotted 2.5 Mpc-thick slices of the simulation at redshifts $z \in \{0, 2, 5\}$ from top to bottom for ΛCDM (left) and $m_{\mathrm{wdm}} = 1\,\mathrm{keV}$ ΛWDM (right). In the present day slice on top, the clustering is indistinguishable on scales $k < 10$ Mpc, but at $z = 2, 5$ the WDM model is smoothed by WDM free-streaming, which results in a suppression in the power spectrum of about 5% and 25% (respectively) at $k \sim 10\,h\mathrm{Mpc}^{-1}$.
Figure source: Viel et al. (2012)

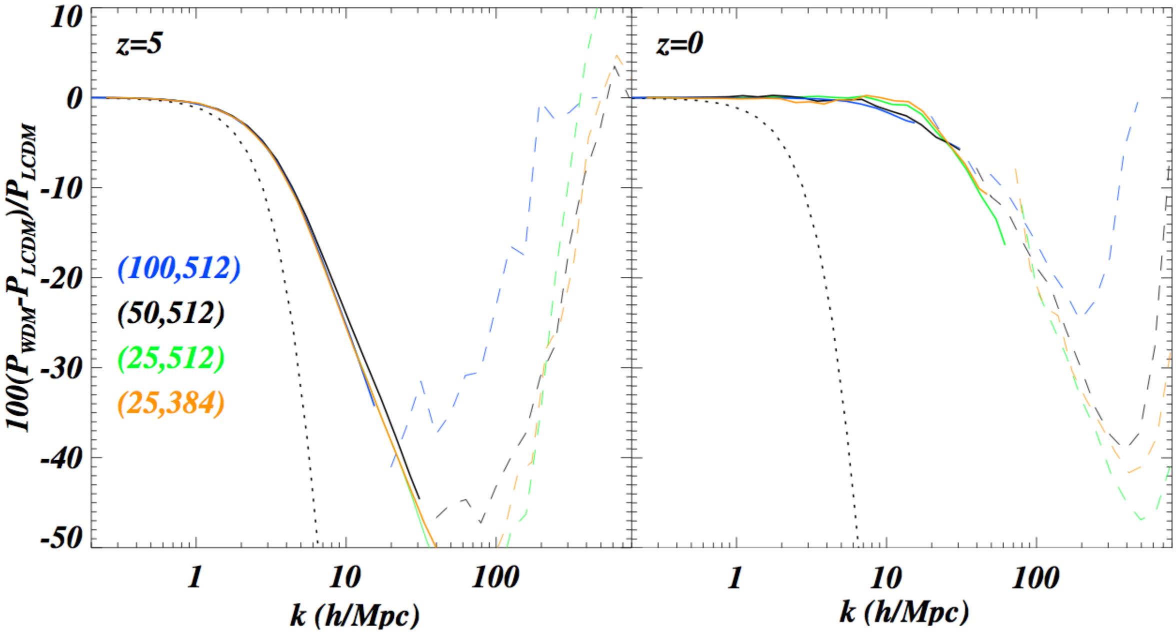

Figure 6.2: Percentage difference between WDM and CDM nonlinear power spectra from the simulations, all with $m_{\rm wdm} = 1$ keV. The blue, black, and green curves correspond to simulation box sides or $L \in \{100, 50, 25\}\,h^{-1}$Mpc respectively. These were all run with the same number of particles, $N_{\rm DM} = 512^3$. On the other hand, the orange curve is the $L = 25\,h^{-1}$Mpc run with $N_{\rm DM} = 384^3$. The continuous lines represent the large scale estimate of the power, while the dashed ones describe the small scale power obtained with the *folding method* (this is not used in our analysis). The dotted line is the suppression to the linear matter power spectrum from eq. (6.1).
Figure source: Viel et al. (2012)

relevant scales minimally.

6.2.1 The fitting formula

In analogy to the linear fitting formula in eq. (6.1), which defines a scale-break, α, we find the following fitting function to the results of our dark-matter only simulations:

$$\begin{aligned} T^2_{\rm nl}(k) &\equiv P_{\rm wdm}(k)/P_{\rm cdm}(k) = (1 + (\alpha\, k)^{\nu l})^{-s/\nu} \\ \alpha(m_{\rm wdm}, z) &= 0.0476 \left(\frac{1\,{\rm keV}}{m_{\rm wdm}}\right)^{1.85} \left(\frac{1+z}{2}\right)^{1.3} \quad , \end{aligned} \tag{6.2}$$

where $\nu = 3$, $l = 0.6$ and $s = 0.4$ are the fitting parameters. This function can and is applied by first calculating the nonlinear matter power spectrum using ΛCDM parameter values in the `HALOFIT` and then multiplying with the square of the WDM “transfer function”.

We show the percentage differences between nonlinear power spectra from the simulations with ΛWDM parameters and those with the simple ΛCDM model in fig. 6.3. We show this at two different redshifts to note the decrease in the suppression due to initial WDM free-streaming with time. The suppression is far stronger at $z = 5$, where it rather close to that obtained when comparing the effects on the linear matter power spectrum At $z = 0$ the

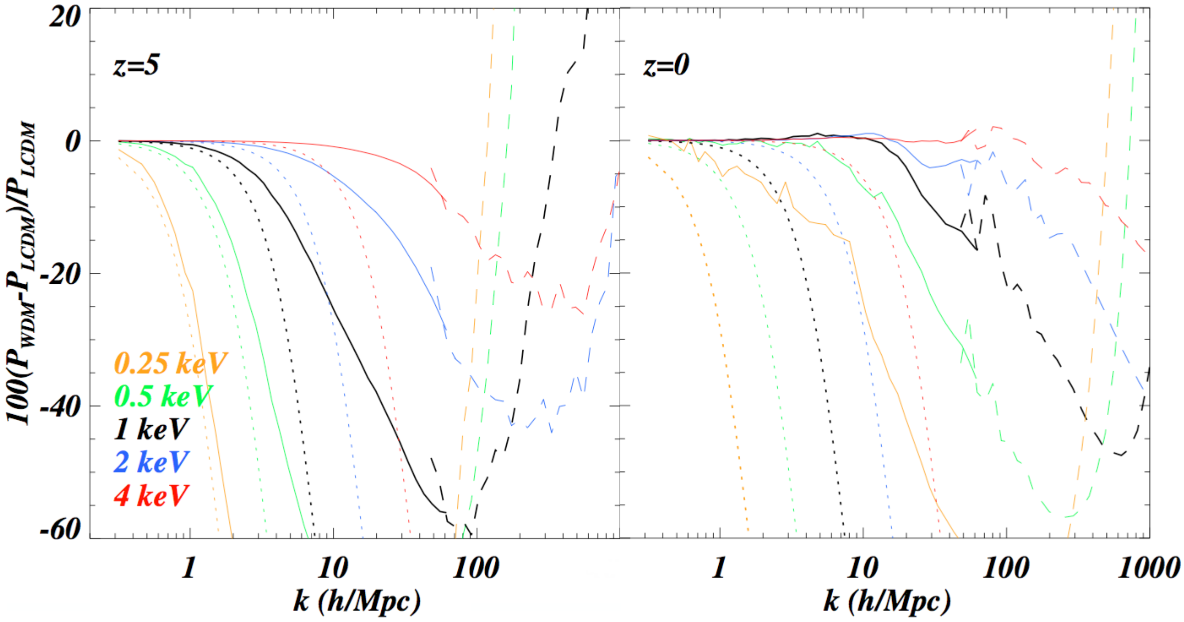

FIGURE 6.3: Percentage difference between WDM and CDM nonlinear power spectra. The orange, green, black, blue and red curves are the runs with to $m_{\rm wdm} \in \{0.25, 0.5, 1, 2, 4\}$ keV, respectively. The continuous lines represent the large scale estimate of the power, while the dashed ones describe the small scale power obtained with the *folding method*. The dotted lines represent the linear suppression (z-independent) from eq. (6.1).
FIGURE SOURCE: Viel et al. (2012)

suppression only remains significant for the extreme WDM models, which have been ruled out by Lyα forest data (e.g. Seljak et al., 2006; Viel et al., 2005).

6.2.2 Comparison with `halofit` and WDM halo model

It is necessary to have a robust model of nonlinear structure in order to take full advantage of future weak lensing data. For this reason we compare the nonlinear matter power spectra extracted from our simulations with previously derived nonlinear models. The halo model of nonlinear structure is based on the assumption that large scale structure is made up of individual objects occupying peaks in the matter overdensity field (Cooray & Sheth, 2002; Press & Schechter, 1974; Seljak, 2000). The most important elements of this model, the mass function, the halo bias (Press & Schechter, 1974) and the halo density profile (Navarro et al., 1997) are based on the assumptions that all dark matter in the universe is found in haloes and that there is no observable suppression of small scale overdensities from early-times free-streaming of dark matter particles or late-times thermal velocities.

These are characteristic properties of CDM, but do not apply to WDM. For this reason we considered a modified halo model by applying a specific prescription to the nonlinear contribution, in addition to suppressing the initial density field, modeled by applying a transfer function from eq. (6.1) to the linear matter power spectrum. Such prescription consists of: *i*) treating the dark matter density field as made up of two components: a smooth, linear component and a nonlinear component, both with power at all scales; *ii*) introducing a cut-off mass scale, below which no haloes are found; *iii*) suppressing the mass function also above the cut-off scale and *iv*) suppressing the centres of halo density profiles by convolving them with a Gaussian function, whose width depended on the WDM relic thermal velocity.

Here, we do not attempt to explore each of these elements with simulations individually, but rather compare the final matter power spectra found from simulations with those from the WDM halo model of ch. 5.

Secondly, Smith et al. (2003) compared the standard CDM halo model to CDM simulations of large scale structure formation and developed an analytical fit to the nonlinear corrections of the matter power spectrum, known as `HALOFIT`. We apply these corrections to a linear matter power suppressed by the Viel et al. (2005) WDM transfer function (eq 6.1).

We show the results of these comparisons in fig. 6.4. As before, we plot the percent differences between the WDM and CDM matter power spectra obtained from our simulations of WDM only. We show this for particle masses of $m_{\rm wdm}$=1 keV (left panels) and $m_{\rm wdm} = 0.5\,$keV (right panels) at redshifts $z = 1$ (top row) and $z = 0.5$ (bottom row). We find that the WDM halo model is closest to simulations at redshift 1 for 1 keV WDM, but that it over-estimates the suppression effect at redshift 0.5 for 0.5 keV WDM by about 5 percent on scales $k > 1$. On scales $k < 1\,h\mathrm{Mpc}^{-1}$ however, the `HALOFIT` nonlinear correction describes the simulations better than the halo model, even though on smaller scales it severely underestimates the suppression effect, which becomes worse at lower redshifts. A further small modification of the WDM halo model will improve its correspondence to the simulations and allow one to use it at small scales.

As has been shown by many authors (e.g. Casarini et al., 2011; Semboloni et al., 2011; van Daalen et al., 2011), baryons, making up 17% of the total matter density, affect the distribution of dark matter on small scales significantly. Delving into detail about this topic (sec 3.2.2) is beyond the scope of this thesis, but we do briefly discuss one simulation run by Viel et al. (2012), which includes a prescription for radiative cooling and heating. In this simulation all the cooling comes from hydrogen and helium (Katz et al., 1996, as in). Metal cooling is omitted for simplicity. Secondly, the feedback from supernovae and AGN is also omitted in this particular run. The prescription for modeling the cooling and the star fromation criterion are described in more detail in Viel et al. (2004) and is called “quick Lyα”, since it can be used well for quantitative description of the Lyα forest.

We plot in fig. (6.5), the resulting percentage difference between a 1 keV WDM and CDM nonlinear matter power spectrum, where both come from simulations that include cooling and heating processes from the ultraviolet background and a simple star formation criterion mentioned above. This simulation was stopped at $z = 1.2$ due to limited computational resources and is therefore plotted at this redshift. It can be seen on fig. (6.5) that the inclusion of baryonic processes can have a very significant effect on the suppression signal from WDM. It seems likely that some baryonic processes become more efficient in a collapsing overdensity field that has been smoothed. Because the baryonic processes affect the power on small scales, this can erase the suppression from WDM, which is relevant on similar scales Gao *&* Theuns (see also 2007) .

6.3 Weak lensing power spectra using the N-body fit

Following chapters 4 and 5, we examine the effect of the fitting function in eq. (6.2) on the weak lensing power spectrum (sec. 3.3).

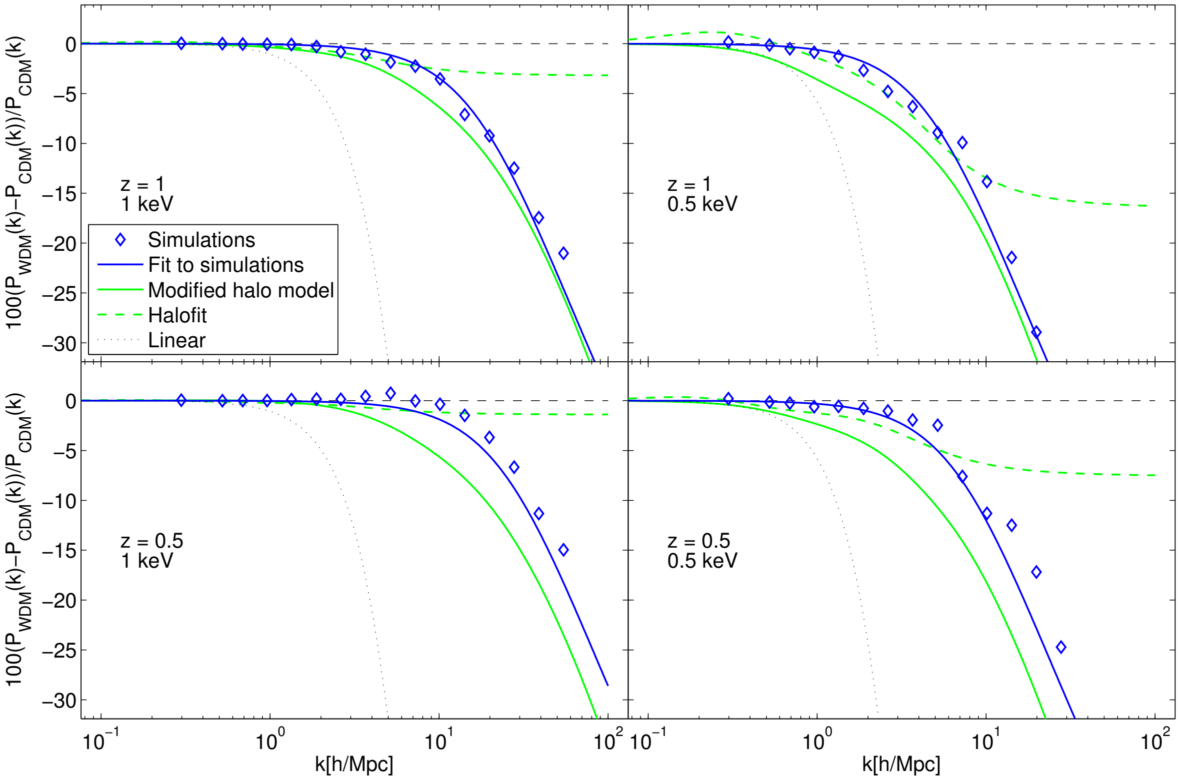

Figure 6.4: The comparison of different nonlinear models at redshifts 1.0 (top panels) and 0.5 (bottom panels) for WDM particles with masses 1 keV (left panels) and 0.5 keV (right panels). The blue diamonds represent the fractional differences calculated from DM-only simulations. The blue solid lines are the corresponding analytical fits from eq. (6.2). The green solid lines are calculated using the modified halo model, whereas the green dashed line is the standard HALOFIT. The dotted line is the effect as seen in the linear matter power spectrum.

We use **HALOFIT** (Smith et al., 2003) to calculate nonlinear corrections to the approximate linear matter power spectrum (Ma, 1996). We then apply eq. (6.2) to approximate the WDM effects and find the weak lensing power spectrum (e.g. Takada & Jain, 2004):

$$C_{ij}(l) = \int_0^{\chi_\mathrm{H}} d\chi_\mathrm{l} W_i(\chi_\mathrm{l}) W_j(\chi_\mathrm{l}) \chi_\mathrm{l}^{-2} P_\mathrm{nl}\left(k = \frac{l}{\chi_\mathrm{l}}, \chi_\mathrm{l}\right) , \tag{6.3}$$

where $\chi_\mathrm{l}(z_\mathrm{l})$ is the comoving distance to the lens at redshift z_l and W_i is the lensing weight in the tomographic bin i:

$$W_i(z_\mathrm{l}) = \frac{4\pi G}{a_\mathrm{l}(z_\mathrm{l}) c^2} \rho_{\mathrm{m},0} \chi_\mathrm{l} \int_{z_\mathrm{l}}^{z_\mathrm{max}} n_i(z_\mathrm{s}) \frac{\chi_\mathrm{ls}(z_\mathrm{s}, z_\mathrm{l})}{\chi_\mathrm{s}(z_\mathrm{s})} dz_\mathrm{s} \quad , \tag{6.4}$$

where we assume a flat universe and $a_\mathrm{l}(z_\mathrm{l})$ is the scale factor at the redshift of the lens, $\rho_{\mathrm{m},0}$ is the matter energy density today and $n_i(z_\mathrm{s})$ is the normalised redshift distribution of sources in the i^th tomographic bin. We bin the multipoles into 20 bins.

In order to asses detectability of WDM by future weak lensing surveys, we calculate predicted error bars on the weak lensing power spectrum using the covariance matrix formalism (Takada & Jain, 2004) and assuming errors for a future realistic weak lensing survey as in

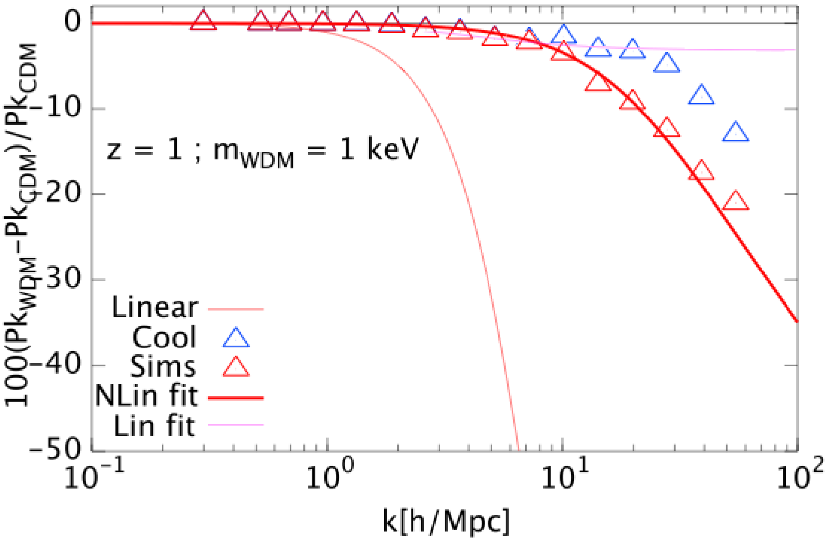

FIGURE 6.5: Here we plot the percentage differences between the WDM and CDM power spectra. We have included the power spectra runs that include baryonic cooling due to H and He (blue). The prescription used for the cooling processes is called “quick Lyα”.

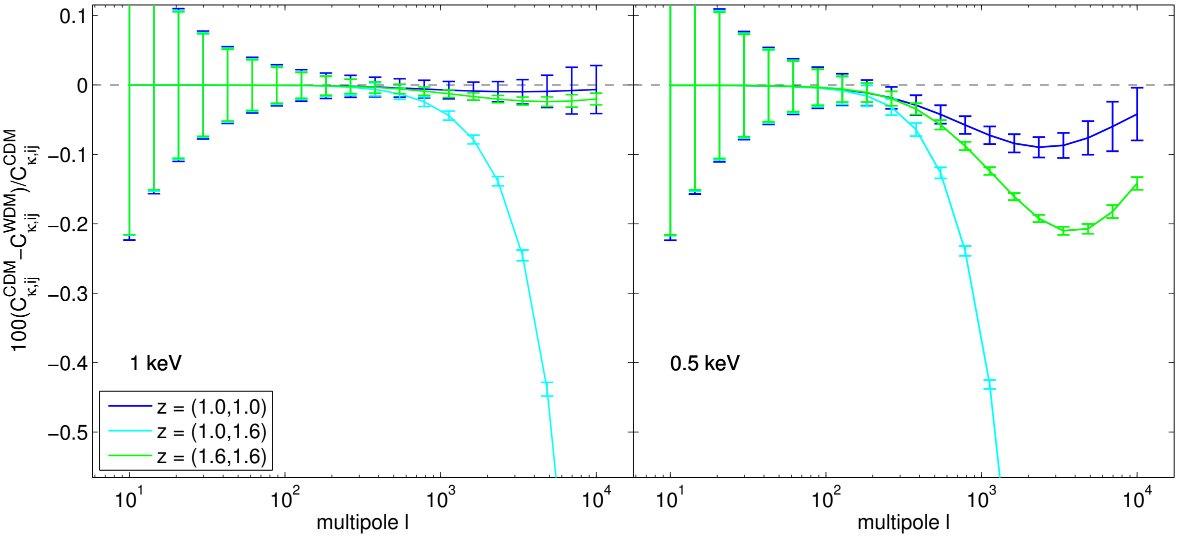

FIGURE 6.6: The percentage WDM effect in auto- and cross-correlation power spectra of redshift bins at approximately $z = 1$ and $z = 1.6$, respectively. All the lines are calculated from nonlinear matter power spectra modified for WDM by the fitting function in eq. (6.2) for WDM particle masses of 1 keV (left panel) and 0.5 keV (right panel). In addition we plot predicted error bars for a future weak lensing survey, dividing the multipoles into 20 redshift bins. Note that the error bars on auto and cross power spectra of different bins are correlated and therefore in order to fully characterise the detectable differences between the WDM (solid lines) and CDM (dashed black line at 0) models, one must know the entire covariance matrix for a survey. Note secondly that the auto power spectra of redshift bins at $z = 1$ and $z = 1.6$ have an upturn around $l \sim 10^3$. This is due to the dominance of shot noise on those scales. This upturn is not present in the cross power spectrum, because through cross correlation this noise due to intrinsic galaxy ellipticities is eliminated.

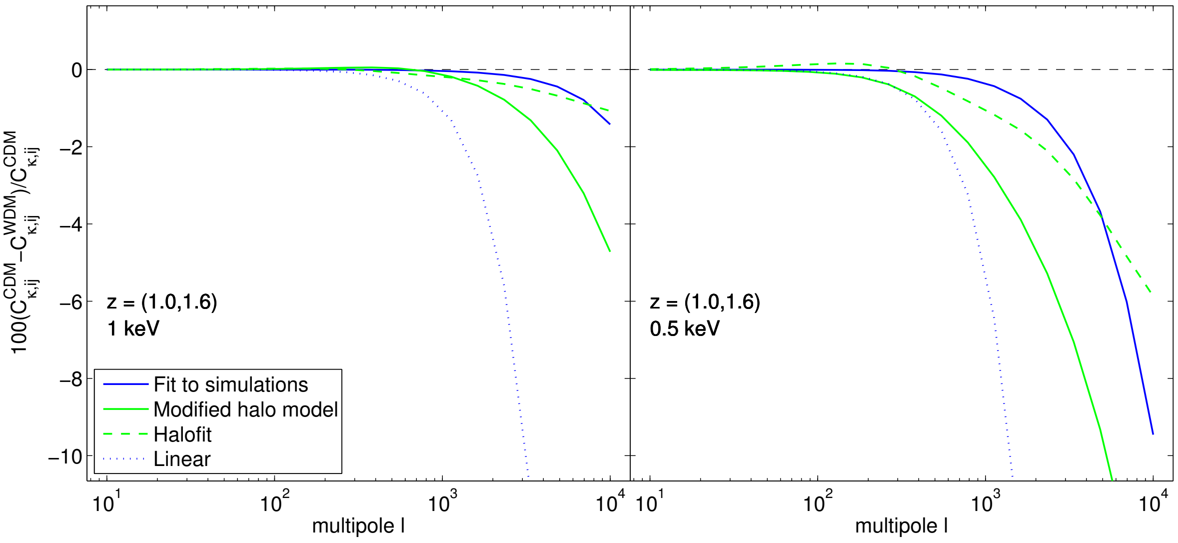

FIGURE 6.7: The comparison of the impact of using different models of nonlinear power spectra from fig. 6.4 on the weak lensing power spectrum. As above, the blue line is the fractional difference in percent between weak lensing power spectra calculated using the fitting function found in this chapter (eq 6.2). The green solid line is the weak lensing power spectrum calculated using the halo model modified for WDM. The dashed green line is the same using standard `HALOFIT`. The dotted line is calculated by omitting all nonlinear corrections. It is evident that excluding such corrections causes a significant overestimation of the WDM effect. All the lines in this plot are calculated from cross power spectra of the 5th and 8th tomographic bins (corresponding to $z = 1.6$ and $z = 1$, respectively) for WDM particle masses of $m_{\rm wdm} = 1\,{\rm keV}$ (left panel) and $m_{\rm wdm} = 0.5\,{\rm keV}$ (right panel).

chapters 4 and 5, this time with 8 redshift bins in the range $z = 0.5 - 2.0$. We plot the resulting percentage differences between WDM and CDM weak lensing power spectra in fig. (6.6). It is important to note that the error bars in the figure do not fully characterise the sensitivity of the power spectra, since there are additional correlations between the error bars of different bin combinations. Additionally, there are correlations in the error bars on large l (small scales) due to nonlinearities. Further statistical tests using the entire covariance matrix must be used in order to fully account for the above correlations. For this plot we choose only the 5th and 8th redshift bins, whose source galaxy distributions have the mean at $z \sim 1.0$ and 1.6 respectively. These bins are chosen because they represent a range with the maximal WDM effect as well as lensing signal. Note that the upturn around $l \sim 10^3$ in the auto-correlation power spectra of bins 5 and 8 is due to the dominance of shot noise on those scales. This noise is due to intrinsic galaxy ellipticities and can be eliminated by cross-correlating different redshift bins, as can also be seen in fig. (6.6) (see also Takada & Jain, 2004).

We additionally consider the above models of nonlinear WDM structure to calculate the weak lensing power spectra in order to explore the significance of using the correct model. We again plot percentage differences between WDM and CDM weak lensing power spectra in fig. (6.7). We show only curves representing the cross correlation power spectrum of redshift bins at $z = 1$ and $z = 1.6$ for consistency with fig. (6.6). We again examine WDM models with particle masses of $m_{\rm wdm} = 1\,{\rm keV}$ (left panel) and $m_{\rm wdm} = 0.5\,{\rm keV}$ (right panel). We also calculate the weak lensing power spectra without nonlinear corrections to the matter power spectrum and note that this severely over-estimates the effect of WDM suppression. In the lensing calculation, the `HALOFIT` nonlinear corrections applied to the WDM suppressed linear matter power spectrum seem to perform better in describing the results of our WDM simulations than than the WDM halo model. This is most likely due to the fact that the range of wavenumbers that are better described by the `HALOFIT` corrections, namely $k < 1\,h\mathrm{Mpc}^{-1}$ are significantly more relevant to the weak lensing power spectrum than the smaller scales where `HALOFIT` strongly deviates from the simulation results.

In the right panel of fig. (6.6) we plot the effects of the 0.5 keV particle and since the black dashed line lies far outside the error bars this is a strong indication that such a particle can be ruled out (or detected) by a future weak lensing survey. This is consistent with the previous chapters. In the left panel of fig. (6.6) we plot the effects of a 1 keV WDM particle: in this case it is more difficult to distinguish from CDM (black dashed line), but the strongly affected cross power spectra are still significantly different from their expected values in ΛCDM.

In a recent paper, Semboloni et al. (2011) have explored the effect that AGN feedback has in terms of matter power and weak lensing power spectra finding that there is a suppression of about 30% at $k = 10\,h\mathrm{Mpc}^{-1}$ when this feedback mechanism is included. Although they did not investigate WDM models this finding is important, since it shows that this effect could be much larger than the corresponding WDM induced suppression and comparable at $z = 0$ to the $m_{\mathrm{wdm}} = 0.25\,\mathrm{keV}$ case. It is clear that future weak lensing surveys aiming at measuring the matter power at these scales should carefully consider AGN effects since they could be degenerate with cosmological parameters such as the mass of the WDM particle.

6.4 Summary & discussion

We have shown in this chapter the results of several cosmological N-body simulations. These simulations were run using the publicly available N-body code `GADGET-2` by Springel (2005). We have run simulations for several different WDM models as well as the standard, WMAP7 ΛCDM model. We have in addition run resolution studies to show that our results are not plagued by the effects of Poisson *shot noise* or *spurious halo formation*. Finally, we report on a simulation that included baryonic matter with a so-called "quick Lyα" prescription for radiative cooling and heating. We find that baryonic physics becomes important on scales similar to those, which are most affected by the suppression of the density field by WDM free-streaming. We also give a useful fitting function in eq. (6.2), which can be used to calculate nonlinear power spectra in the ΛWDM cosmology by first finding those for ΛCDM and then simply multiplying them with the square of the so-called WDM "transfer function".

We make a comparison with the methods discussed in the previous chapters and calculate weak lensing power spectra in order to try to gauge the detectability of the suppression found in our simulations. We find that the nonlinear corrections to the matter power spectrum in the WDM scenario obtained from `HALOFIT` correspond better to the results of the WDM only simulation at scales $k < 10\,h\mathrm{Mpc}^{-1}$, if compared to the nonlinear corrections of the halo model from Smith *&* Markovič (2011). Because these scales are most relevant for weak lensing power spectra, using `HALOFIT` yields a better correspondence to the weak lensing power spectra calculated using our fitting function. However, on scales $k > 10\,h\mathrm{Mpc}^{-1}$, the halo model performs slightly better in that it better describes the shape of the suppression in the power spectrum, even if it does overestimate the effect. For this reason we believe that a further modification to the halo model may be needed, especially for weak lensing power spectra calculations. Such modifications have recently been suggested by others, for example Schneider et al. (2012). As already discussed in ch. 5, they have found a fitting function for the mass functions, using the results of their own WDM simulations.

An important issue not dealt with in the scope of this thesis is the problem of *discreteness effects*. In particular spurious halo formation tends to plague simulations with small scale smoothing. This is not considered crucial in simulations using CDM only, but is becoming important in the present time when the computational capabilities are enabling us to run high resolution cosmological WDM simulations. This issue arises as a purely numerical artefact and is completely nonphysical. It is possible to check for the importance of these effects by varying the size of the initial grid, as is briefly done in Viel et al. (2012). An extensive discussion of discreteness effects in WDM simulations is Wang & White (2007) (they are also considered by others, e.g. Bode et al., 2001; Pfitzner et al., 1997).

The present state-of-the-art technology is just becoming strong enough to be able to probe non-standard models of dark matter. Warm dark matter has been explored here with Lagrangian N-body simulations of the formation of cosmological large scale structure. Warm dark matter is arguably the simplest extension of CDM, because only one parameter, namely the dark matter particle mass, $m_{\rm wdm}$ must be added to the parameter space of ΛCDM. Further extensions might be to consider mixed dark matter models in which some fraction of the dark matter, $f_{\rm wdm}$ is warm or hot and the rest is made up of a standard cold thermal relic. In this case, we would be adding 2 additional parameters. We are able to explore this scenario with existing numerical codes, like GADGET, but this has not been done within the scope of this thesis for the reason of limited resources and time.

Another extension of the CDM model would be to consider *decaying dark matter* or perhaps *interacting dark matter*. Of course the decay of dark matter cannot occur until very recently so as not to contradict the constraints from the CMB or large scale structure observations that nearly seem to match the CDM model. The interacting like decaying dark matter on the other hand are constrained to only have a very small interaction rate by direct detection as well as X-ray observation (e.g Boyarsky et al., 2006). Such scenarios, which involve more than gravitational interactions for the dark matter component would require modifications to the existing numerical codes. Prescriptions would need to be added to include such new interactions perhaps with based on the prescriptions used for adding baryonic particles into these simulations, which we have briefly encountered above. Another extension to ΛCDM examines the interaction between dark matter and dark energy. The modification to the GADGET N-body code to account for such exotic interactions has for example been developed by Baldi et al. (2010).

A final interesting extension would be the very realistic mixed dark matter model in which we add massive neutrinos to standard CDM or perhaps even WDM. The N-body simulations using ΛCDM together with massive neutrinos have been explored much more extensively than the WDM case (Bird et al., 2012, and references therein), because it is clear that massive neutrinos exist. Furthermore, with present surveys we can constrain and in the future perhaps even measure the sum of the neutrino masses (Audren et al., 2012; Seljak et al., 2006; Thomas et al., 2010; Xia et al., 2012; Zhao et al., 2012). This brings us to the topic of the next chapter.

CHAPTER 7

The Degeneracy of *Warm Dark Matter* and Massive Neutrinos

This chapter corresponds to
Markovic, Abdalla, Kilbinger, Weller & Lahav,
Testing Warm Dark Matter and Neutrinos with the SDSS Galaxy Distribution,
(in preparation).

So far we have discussed models in which all dark matter is made up of thermal relic particles with keV masses. In other words, all dark matter is *warm*. However a more realistic picture would be to take into account a component of the dark matter density we know exists - **massive neutrinos**. Massive neutrinos have sub-eV masses. In fact most recent constraints from cosmology put the sum of the 3 neutrino masses of the electron, τ and μ neutrinos to be somewhere $M_\nu < 0.5\,\mathrm{eV}$ (e.g. Audren et al., 2012; Bird et al., 2012; Seljak et al., 2006; Thomas et al., 2010; Viel et al., 2010; Xia et al., 2012; Zhao et al., 2012). For this reason we classify neutrinos as **HDM** (sec 1.3.3). In fact such a **mixed dark matter** model can contain many different species, with different temperatures, interactions or decay mechanisms. However such additional properties of the dark matter density field necessarily introduce further parameters into the model. Until such addition of parameters is justified by a physical theory, let us take the next simplest case from what we have discussed now and examine the combined effect of WDM and massive neutrino free-streaming in the initial density field on the formation of cosmological structure.

In particular, since the detectability of the WDM signature is still uncertain and since detecting the neutrino mass is within the possibility of upcoming data, we wish to ensure that there will be no degeneracy between the two parameters: the sum of neutrino masses, M_ν and the WDM particle mass, m_{wdm}.

In this brief chapter we make a simple calculation to compare the suppression of the power spectra due to massive neutrinos to that of WDM. We wish to eventually repeat the analysis of Thomas et al. (2010), but include m_{wdm} as a parameter. They utilise the galaxy clustering data from the Sloan Digital Sky Survey (SDSS) MegaZ Luminous Red Galaxies (LRG) sample of Data-Release-7 (DR7) (Abazajian et al., 2009; Thomas et al., 2011) and combine it with the WMAP 5-year data (Dunkley et al., 2009). They use the `CosmoMC` package (Lewis

& Bridle, 2002) to explore the parameter space.

7.1 The linear regime suppression in $\nu\Lambda$WDM

We use the Class Boltzmann solver code (Lesgourgues, 2011) to find the transfer functions that account for the suppression of the primordial power spectra. These transfer functions account for the suppression of the primordial scale-free power spectra due to early universe effect. Of course the most dominant suppression effect is that from the decay of the comoving matter overdensities during radiation domination. But the effects we are interested in here are due to the free-streaming of non-cold relics like the thermal WDM particle and massive neutrinos making up a small fraction of the total energy density as HDM. We have discussed these effects in sec. 2.2.4, where we have made a brief overview of the Boltzmann equations.

The Class code is similar to the previous Camb or CmbFast by Lewis et al. (2000); Seljak & Zaldarriaga (1996) respectively. The main and very convenient option, new in Class is that it allows the inclusion of non-cold dark matter relics, which we utilise here. For a detailed comparison of the Class and Camb codes for the ΛCDM case, see the papers associated with the newer code, Class Lesgourgues (2011, etc.).

Unlike in the previous chapters where we have calculated our linear matter power spectra using fitting functions (described in ch. 2)), here we choose to calculate the power spectra by solving the full Boltzmann equations. We do this for two reasons. Firstly, the fitting function of Viel et al. (2005) does not explicitly account for the presence of standard active massive neutrinos. It is important to accurately account for the separate effects of WDM and massive neutrino free-streaming, because we wish to characterise their similarities and any possible overlap. Secondly, in the previous chapters we used the fitting function for the linear WDM transfer function $T_{\rm wdm}(k)$ from Viel et al. (2005), because using Camb or CmbFast resulted in some seemingly numerical artefacts on small scales that resulted in a power spectrum that was not differentiable with respect to the wavenumber, k. These artefacts are still present in the results from Class, but this is no longer a problem, because we use Class's own nonlinear correction program (see the next section), which seems to deal with this issue.

We plot the resulting linear matter power spectra for the models: ΛCDM, $\nu\Lambda$CDM, ΛWDM and $\nu\Lambda$WDM, in the left panel of fig. (7.1). The model used for WDM is that where the particle mass is $m_{\rm wdm} = 1\,$keV, for neutrinos we use such parameter values as to get the energy density fraction for neutrinos to be $\Omega_\nu = 0.025$. This density fraction corresponds to the sum of neutrino masses of $M_\nu \approx 2.3h^2\,$eV (Bird et al., 2012). The mentioned artefacts can be seen at scales of $k \sim 5\,h$Mpc^{-1}. In this figure, the solid lines are the power spectra in both ΛWDM models - one with and one with no massive neutrinos. The dotted lines are models with regular CDM. What we note in this plot is that the suppression of the linear scales is much stronger when considering WDM, but it reaches much larger scales (smaller k) if the free-streaming of massive neutrinos is accounted for. Including both, massive neutrinos and WDM results in a twice suppressed power. The two suppression occur at two different scales with two different amplitudes. The reason why the suppression is so much stronger in the ΛWDM model is because in this case *all* of DM is warm, whereas in the $\nu\Lambda$CDM case, only a tiny fraction of dark matter is mase up of massive neutrinos. The idea of massive neutrinos making up a significant part of dark matter density was rejected long ago for this reason, as the suppression would be too strong for these large scales. If neutrinos dominated the matter energy density, there would be virtually no power in the power spectrum on scales

$k > 0.1\,h\mathrm{Mpc}^{-1}$ and therefore we would observe no structures in the universe. Note that the wiggles at $k \sim 0.1\,h\mathrm{Mpc}^{-1}$ in fig. (7.1) are due to *Baryonic Acoustic Oscillations* and seem to not be much influenced by WDM, but loose power when including massive neutrinos with the "continuous" power spectrum.

7.2 Nonlinear corrections in $\nu\Lambda$WDM

Ultimately we wish to compare our models with data. As noted many times in the previous chapters, the most relevant data for measuring WDM are on the small scales. This means that we must map out object and structures at low redshifts (nearby), meaning that the overdensity field that we probe and must be able to describe theoretically has become nonlinear long ago. As before, we therefore wish to make nonlinear corrections to our linear matter power spectra described in the previous section. In the future we wish to consider the modified halo model that matches our WDM N-body simulations from ch. 6. For now we use what is given by the `CLASS` code: the `HALOFIT` formula (sec 3.1.2).

7.2.1 The `halofit` prescription

We use the `HALOFIT` prescription as is given in the `CLASS` code. There exists a correction to the pure, basic ΛCDM `HALOFIT`, which takes $f_\nu = \Omega_\nu/\Omega_\mathrm{m}$, the fraction of the cosmic matter density made of neutrinos, as a parameter. This correction is based on the N-body simulations run by Bird et al. (2012) and means adding an additional neutrino-mass-dependent term to the `HALOFIT` dimenstionless power spectrum in eq. (3.31). Bird et al. (2012) ran simulations using a modified version of the `GADGET` code (Viel et al., 2010). They then added some terms to the original `HALOFIT` prescription by fitting the additional parameters to the results of their simulations. Note that we have had to make a minimal modification to the `CLASS` function that calculates the nonlinear corrections, because it originally assumed the only possible non-cold dark matter was massive neutrinos. This caused an issue with the above-described additional terms, but it was relatively easily corrected.

We plot the resulting power spectra in the right panel of fig. (7.1). The color scheme matches that on the left, where we plotted the linear matter power spectra described in the previous section. It is immediately obvious that as before, the nonlinear correction erases a lot of the suppression from the linear regime. As we have discussed in the previous chapters, this is likely to be a consequence of smooth accretion and general correlation of the small scale modes by gravitational collapse. On the other hand, the suppression due to neutrinos doesn't seem to be much affected by this. The reason is that whereas the scale of suppression due to WDM is smaller, the scale of the suppression due to neutrinos is *larger* than the nonlinear scale, i.e. $k_\mathrm{wdm} > k_\mathrm{nl} > k_\nu$.

We have made these calculations in anticipation of later working with the halo model in order to make theoretical predictions for galaxy clustering. We discuss this in the next and final section.

7.3 Outlook

Less discussed in this thesis has been the topic of actually measuring the distribution of dark matter structure in our universe. This is not out main topic, but it is a future goal. For this

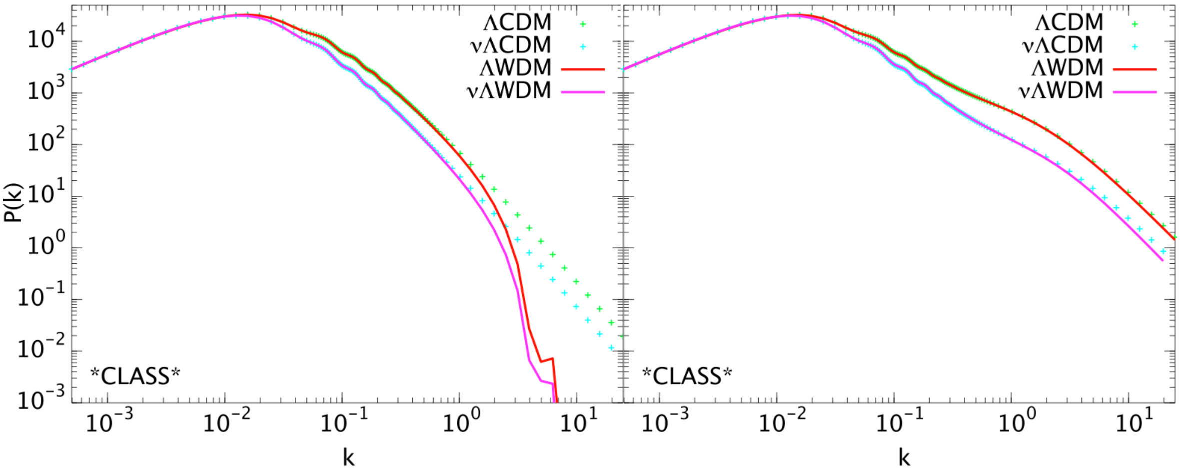

FIGURE 7.1: We plot the power spectra showing the suppression due to the free-streaming of massive neutrinos as well as WDM thermal relic particles in the early universe. We use $m_{\mathrm{wdm}} = 1\,\mathrm{keV}$ and $\Omega_\nu = 0.025$ for illustration.
In the left panel we plot the linear matter power spectra. The dotted lines are the CDM models and the solid lines correspond to WDM. In each of the two sets of lines, the line with less power has been suppressed by the free-streaming of neutrinos. We note some further details in the plot below fig. 7.2, where they appear more clearly.
Note also that on very small scales in the WDM suppressed functions become jagged. We suspect this is a numerical artefact. We have checked and such "wiggles" appear in results obtained with several Boltzmann-solver codes: CLASS, CAMB and CMBFAST.

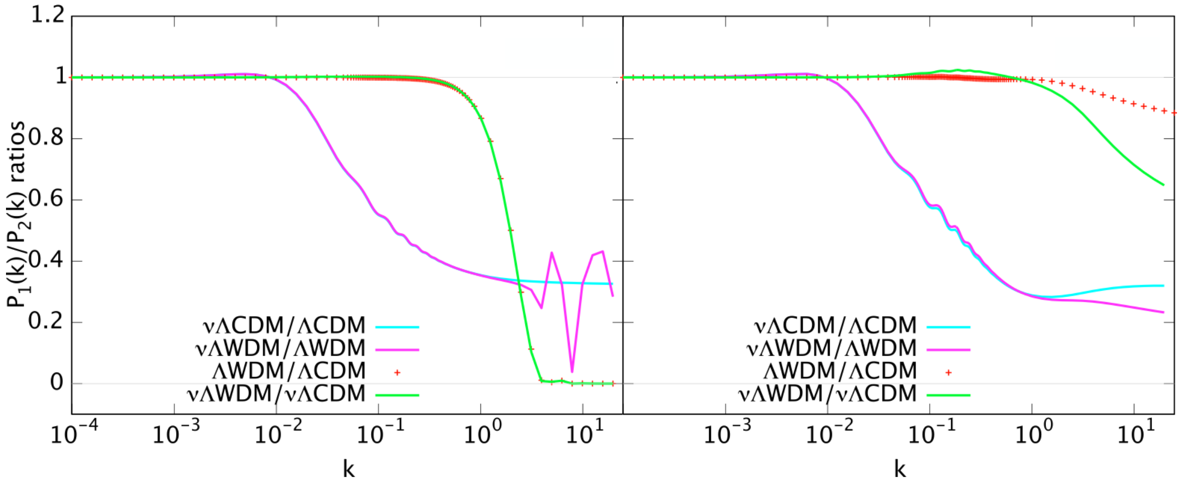

FIGURE 7.2: We plot the ratios of matter power spectra suppressed on small scales by the free-streaming of non-cold dark matter species. We find ratios of the expected ΛWDM, νΛCDM,νΛWDM or the standard ΛCDM power spectra. The the blue and magenta lines are the scenarios that highlight the suppression due to massive neutrinos, the green and dotted red highlight the suppression due to WDM.
In the left panel we plot only ratios of linear, on the right we plot only spectra. The linear spectra were calculates using the CLASS Boltzmann solver. For nonlinear corrections we used the HALOFIT prescription within CLASS. The used nonlinear prescription includes a correction for the presence of massive neutrinos (à la Bird et al., 2012).

reason we now briefly describe one measurement that will be done. This measurement relies on mapping out the 3-dimensional clustering of galaxies. While this relies on knowing how the distribution of galaxies traces the dark matter density field, it is the most straightforward way to make a map of the 3D universe.

7.3.1 Galaxy clustering data

The SDSS Data-Release-7 (Abazajian et al., 2009) is the latest and final set of data from this survey that finds the *photometric redshifts* of distant galaxies. Because the redshift is effectively a measurement of the distance of a galaxy (sec 1.2.2), it enables us to reconstruct their 3D distribution, when combined with their positions on the 2D sky. Acquiring redshifts photometrically means measuring galaxy spectra within only 5 wavelength bands and is therefore less accurate that getting full unbinned spectra. The advantage however lies in the statistics, because it is much more time efficient, the galaxy catalogue, MEGAZ-LRG DR7, contains ≈ 1.5 million galaxies. The redshifts are calculated by comparing the magnitudes of the galaxies in the 5 wavelength bands. Because of the large number of target objects, Thomas et al. (2011) use an Artificial Neural Network code (`ANNz` by Collister & Lahav, 2004) for redshift calculation. Of course, the relationship between distance and redshift is not direct due to individual peculiar velocities of galaxies, the redshift space distribution of galaxies is distorted. This effect is accounted for when trying to construct the matching cosmological model - it is known as *redshift space distortions.*

In order to compare these data to theory, power spectra must be constructed from the galaxy number density field. This is done by projecting the 3D distribution of galaxies onto 2D spherical surfaces. In order to retain the information coming from the direction parallel to the line of sight (i.e. the redshift direction), galaxies with similar redshifts are binned and therefore the galaxy distribution in projected to several spherical shells, increasing in size. The 2D distribution is decomposed into spherical harmonics to construct an angular power spectrum, C_l, analogous to the one we encountered in sec. 3.3. This angular power spectrum can be straightforwardly calculated from the theoretical power spectrum of galaxies by making the *small angle approximation.* This can then be connected to the underlying matter power spectrum via a *galaxy bias*, b_{g}:

$$P_{\mathrm{g}}(k) = b^2 P(k) \qquad . \tag{7.1}$$

For more details on these calculations, one can follow the work of Thomas et al. (2011), whose resulting angular power spectrum we plot in fig. (7.3). Note that unlike power spectra plotted in the previous chapters, in this figure, only the y-axis is logarithmic. This figure also shows that the angular power spectrum can be measured very precisely using galaxy distribution surveys. The resulting best fit to the data points is plotted with a solid line and corresponds to a $\nu\Lambda$CDM cosmology with a sum of neutrino masses, $m_\nu \leq 0.28\,\mathrm{eV}$. Of course the figure only plots 4 redshift bins, but the calculation of Thomas et al. (2011) includes the entire covariance matrix. In order to obtain the above tight constraint on the sum of neutrino masses, the MEGAZ covariance matrix is combined with several other data sets. These datasets are relatively independent of the galaxy distribution data. They are: supernovae distances from the SUPERNOVA LEGACY SURVEY (Astier et al., 2006), baryonic acoustic oscillations from SDSS and 2DF (Percival et al., 2007) and the Hubble parameter measurement by the HUBBLE SPACE TELESCOPE (Riess et al., 2009).

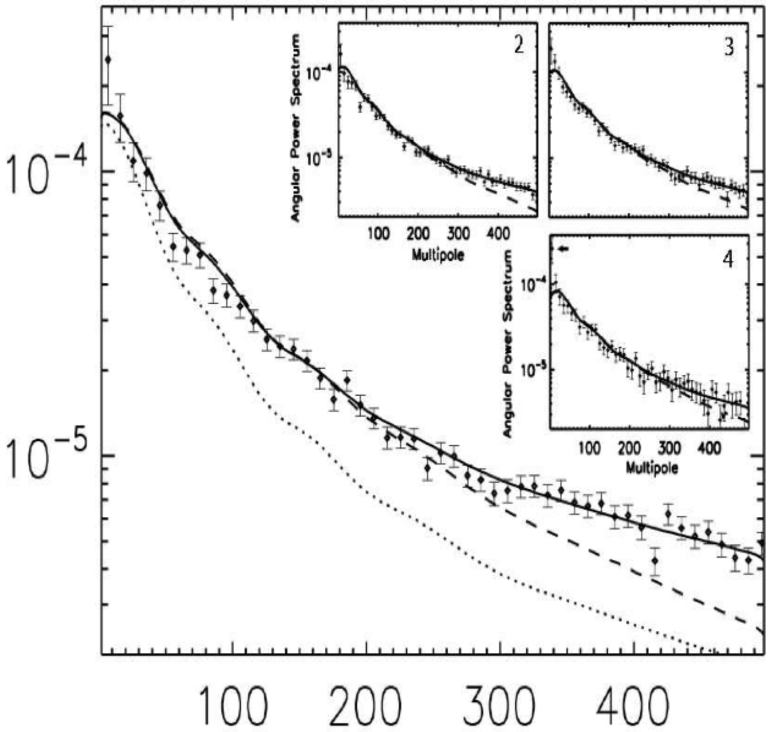

FIGURE 7.3: This figure shows the angular power spectra for four redshift bins, $z \in 0.45, 0.50, 0.55, 0.60$ (panels $1-4$ respectively) from the MEGAZ-LRG DR7 photometric redshift catalogue of the SDSS. The dots and error bars come from the data and the solid lines are the best fitting theoretical power spectra. In addition, the dashed lines are the purely linear corresponding power spectra plotted to explicitly highlight the nonlinear effects. Finally the dotted line in the main panel is the power spectrum calculated from theory with all but one cosmological parameters kept the same. The cosmological parameter altered is the sum of neutrino masses, which is set to $M_\nu = 1\,\mathrm{eV}$. The result of these data set an upper limit on the sum of neutrino masses of $M_\nu \leq 0.28\,\mathrm{eV}$ (at the 95% confidence limit). This limit comes from the combination of several types of datasets, namely CMB, supernovae, baryonic acoustic oscillations, the Hubble parameter with the MEGAZ sample.
FIGURE SOURCE: Thomas et al. (2010)

7.3.2 The halo model and galaxies

We wish to repeat and update the above described analysis to include the WDM parameter in order to check for degeneracies using the full covariance matrix of the SDSS MEGAZ catalogue. Moreover, it would be interesting to use first try the above analysis using the `HALOFIT` with the massive neutrino correction of Bird et al. (2012) and ultimately use the full halo model, which should also be corrected for WDM free-streaming as indicated in ch. 5 as well as in Dunstan et al. (2011) (but also Benson et al., 2012; Lovell et al., 2012; Schneider et al., 2012).

Unlike in the previous sections, where we used a custom written code, here, for the comparison to the MEGAZ catalogue power spectrum, the publicly available `NICAEA` can be used Kilbinger et al. (2009). However if one wishes to include WDM corrections, custom modifications to the code must be made once again. The advantages of using `NICAEA` are that it includes prescriptions for Halo Occupation Distributions (HOD). The simplest HOD is that of Hamana et al. (2004), where the number of galaxies in a halo of mass M is given by the following relation:

$$N_{\rm g}(M) = \begin{cases} \left(\frac{M}{M_1}\right)^{\alpha} & M > M_{\rm min} \\ 0 & M < M_{\rm min} \end{cases} \quad , \tag{7.2}$$

where M_1, α and $M_{\rm min}$ are free, nuisance parameters. We hope that such modifications will add to the accuracy of the comparison between data and theory.

Massive neutrinos are very light thermal relic particles that free-streamed in the early universe. This means that their effects on the primordial density field can be understood analogously to those of a keV thermal relic. The major differences between their free streaming effect are manifest in the scales and amplitudes of their suppression of the matter power spectrum. Because the effects of neutrinos reach larger scales, they remain observable even in the present day nonlinear distribution of matter. On the other hand, WDM became non-relativistic much earlier in cosmic time and therefore its free-streaming did not influence very large scales. However, because it potentially makes up a much larger fraction of the density, its free streaming could have suppressed the overdensity field to zero. Such effect are potentially still measurable at low redshifts and should be accounted for when using similar properties of the power spectrum to constrain other cosmological parameters. It is important to be careful especially when measuring the neutrino masses, but it is possible that we will be able to confidently separate the two effects in the future.

CHAPTER 8

Conclusions

Cosmology today is an impressive science, which provides a deep understanding of the nature of our universe. However, having answered so many questions over the past few decades it has also discovered so many curious properties, which have still to be explained. The presence of Dark Matter and Dark Energy is justified by their power in explaining the gravitational effects unaccounted for by considering only the matter we can see. Their true nature yet remains a mystery. The cosmological model containing these two components alongside regular matter is known as ΛCDM (sec 1.3). This thesis has dealt with a proposed type of dark matter called *warm dark matter*. The property of warmness does not entirely specify its particle physics properties, but it does narrow down to a small range of possibilities. Its advantage in particular is its potential to explain the small scale discrepancies between observation and ΛCDM (ch 3).

The most concerning conflict with astronomical data of the ΛCDM model exists at the smallest cosmological scales in the distribution of structure in the universe. A possible reason for this issue may lay in the assumption that baryonic matter (luminous and dark) through its physical processes cannot significantly affect the Dark Matter overdensity field. If it can do so, it could erase power in the small scale dark matter overdensity field through feedback processes (van Daalen et al., 2011, and references therein). A further possibility would be warm dark matter, which can smooth the initial dark matter density field on small scales. An accurate description of small scales of cosmological structures is essential to utilise the full precision of future data for the extraction of the true cosmological model.

Both, warm dark matter and neutrinos affects the structures in our universe by suppressing their formation. This is a result of both types of particles being relativistic for long enough to erase the perturbations in the cosmological energy density in a potentially observable way. This suppression is important on a range of scales that depends on the properties of the particles (sec 1.3.3). Neutrinos make up a very small fraction of the total energy density and stay relativistic until the present day due to their small, sub-eV masses. This means that they affect the structure in our universe only mildly, but to relatively large scales. On the other hand, warm dark matter consists, in its simplest form, of relatively heavy, keV particles, which become non-relativistic relatively early, but make up all of dark matter, therefore about 25% of the total energy density. This means that warm dark matter suppresses the formation of small structure very strongly, but only up to relatively small scales, which are at present times described as very non-linear perturbations to the average background density (ch 3).

This thesis has investigated the difficulties in modeling the highly non-linear structure by modifying existing models (ch 5) as well as running N-body numerical simulations (ch 6). We have made forecasts for future large scale structure surveys, in particular for the EUCLID weak lensing survey (ch 4). This was done in order to investigate how the free-streaming of warm dark matter, which smoothes out the sub-0.1 Mpc scales in the linear density field impacts the present day nonlinear density field. In other words, it is very difficult to describe the present day, nonlinear density field analytically. This is not only because the full nonlinear Einstein field equations have not yet been solved (ch 1), but because even the approximation used in the linear regime (first order perturbation theory) no longer applies. This is the case already in the standard ΛCDM model. However, many successful approaches have been developed over the past several decades (ch 3), many of which have not been discussed in this thesis, because they become too inaccurate on the scales of interest, i.e. on the scales where warm dark matter can account for the small scale issues of ΛCDM.

The three approaches in this thesis to calculating the nonlinear power spectrum, which describes the statistics of the present-day density field, have been the *halo model*, the related **HALOFIT** prescription and the full numerical solving of the Newtonian dynamics - N-body simulations. We have attempted to modify the first two in such a way as to be compatible with the third.

The halo model modifications we made in ch. 5 were not calibrated here against N-body simulations and so they slightly overestimated the suppression in the nonlinear power spectrum in the ΛWDM scenario. This was done subsequently by other authors, who have suggested a useful prescription for the halo mass function in the WDM scenario (Schneider et al., 2012). The new "warm" halo model can be useful for a comparison with future galaxy surveys, where in order to compare the galaxy distribution measured from observations, one must populate the theoretical dark matter density field with galaxies. This is done with a rather physical motivation by constructing the density field from dark matter haloes, which act as hosts to galaxies. The prescription for this is known as the *halo occupation distribution*. We wish to use this in the near future to compare the ΛWDM model to the galaxy clustering data of the *Sloan Digital Sky Survey* MEGAZ catalogue of luminous red galaxies (ch 7).

Our modification to the **HALOFIT** was in the form of an additional WDM transfer function, which we fit to the results of our N-body simulations (ch 6). We ran these simulations using a non-modified version of the **GADGET-2** code (Springel, 2005). To include the effects of WDM, we created initial conditions for the simulation, whose statistics were described by a suppressed linear matter power spectrum (sec 2.3.3). We then ran the unmodified **GADGET-2** code, since by the time of gravitational collapse, the WDM particles have lost most of their thermal energy due to the expansion of the universe. Their velocities have become low enough to be negligible for the purposes of finding the matter power spectrum on scales larger than the very centres of our haloes. The fitting function resulting from our simulations is useful for calculating theoretical WDM power spectra in order to compare them to data of cosmic structure.

We have made forecasts for the EUCLID weak lensing survey and found that WDM particles with masses of the order of $m_{\rm wdm} \sim$ keV have a large enough impact on the nonlinear density field via the initial conditions they create, to be detectable. It would be interesting furthermore to go away from the power spectrum approach and use the properties of individual haloes to constrain the properties of dark matter particles. Or vice versa, to show explicitly with respect to the abovementioned surveys like, PLANCK, SDSS and EUCLID, but also other types of observations that WDM does indeed solve the small scale issues of ΛCDM fully.

Finally, we have touched upon the subject of baryonic physics, modeled by hydrodynamical simulations (sec 3.2.2). We ran one simulation that included some baryonic cooling as well as star formation, which has indicated that such effects affect the nonlinear matter power spectrum (via gravitational coupling) similarly and on similar scales to WDM. Even though such numerical prescriptions are yet uncertain, it is clear that before a measurement or constraint on the WDM mass is made, one must be familiar with the effects of baryonic physics. A potential solution to this important degeneracy may be the examination of the evolution of these effects. Whereas the WDM suppression increases with increasing redshift, the effect of baryons may have an entirely different signature in redshift. This would be interesting to model using numerical methods, but it would be a large undertaking as it would require extensive computational resources.

The small scales of cosmological structures are shaped by several different physical processes. Their exact effects are difficult to predict and the field of cosmology concerned with them is relatively young. Besides baryonic effects a warm dark matter would impact the small scales by changing the initial conditions. The presence of such dark matter could elegantly explain some of the conflicts with data that arise when assuming that all dark matter is cold. Because the upcoming cosmological surveys will be capable of impressive precision, they will be able to map out the 3D dark matter density field to a resolution achieved never before. This will give us a chance to test the WDM model by applying the nonlinear prescriptions developed in this thesis.

APPENDIX A

Correlation function of haloes

Beginning from Appendix A of Takada & Bridle (2007), we try to write down the correlation function assuming the entire density field in the universe, $\rho(\boldsymbol{x})$ is fully made up of virialised objects (unlike in eq. 5.1) with mass-normalized halo density profile $u_{\rm h}(|\boldsymbol{r}|, M)$, $\boldsymbol{r} = |\boldsymbol{x} - \boldsymbol{x}_0|$ begin the distance from the halo centre at $\boldsymbol{x}_0$, which is enough assuming a spherically symmetric halo:

$$\rho(\boldsymbol{x}) = \sum_{i=1}^{N} M_i \, u_{\rm h}(|\boldsymbol{x} - \boldsymbol{x}_{0,i}|, M_i) \quad . \tag{A.1}$$

From eq. (5.6), we already know that

$$\langle \rho(\boldsymbol{x})\rho(\boldsymbol{x}+\boldsymbol{r})\rangle = \bar{\rho}^2 \left(1 + \langle \delta(\boldsymbol{x})\delta(\boldsymbol{x}+\boldsymbol{r})\rangle\right) \quad . \tag{A.2}$$

Rewriting and re-expressing this, we can write the correlation function:

$$\begin{aligned} \xi(r) &= \langle \delta(\boldsymbol{x})\delta(\boldsymbol{x}+\boldsymbol{r})\rangle \\ &= \frac{\langle \rho(\boldsymbol{x})\rho(\boldsymbol{x}+\boldsymbol{r})\rangle - \bar{\rho}^2}{\bar{\rho}^2} \quad . \end{aligned} \tag{A.3}$$

For now, let's try to work out the first term, $\langle \rho(\boldsymbol{x})\rho(\boldsymbol{x}+\boldsymbol{r})\rangle$, using eq. A.1:

$$\begin{aligned} \langle \rho(\boldsymbol{x})\rho(\boldsymbol{x}+\boldsymbol{r})\rangle &= \left\langle \sum_{i=1}^{N} M_i \, u_{\rm h}(|\boldsymbol{x} - \boldsymbol{x}_{0,i}|, M_i) \sum_{j=1}^{N} M_j \, u_{\rm h}(|\boldsymbol{x} + \boldsymbol{r} - \boldsymbol{x}_{0,j}|, M_j) \right\rangle \\ &= \left\langle \sum_{i=1}^{N} M_i^2 \, u_{\rm h}(|\boldsymbol{x} - \boldsymbol{x}_{0,i}|, M_i) u_{\rm h}(|\boldsymbol{x} + \boldsymbol{r} - \boldsymbol{x}_{0,i}|, M_i) \right\rangle \quad + \\ &+ \left\langle \sum_{i \neq j}^{N} M_i M_j \, u_{\rm h}(|\boldsymbol{x} - \boldsymbol{x}_{0,i}|, M_i) u_{\rm h}(|\boldsymbol{x} + \boldsymbol{r} - \boldsymbol{x}_{0,j}|, M_j) \right\rangle \quad , \end{aligned} \tag{A.4}$$

where we have now split the sums into 2 terms, which will become: the Poisson, or *1-halo* term ($i = j$) and the Clustering or *2-halo* term ($i \neq j$), obviously, since we are summing over haloes.

In the next step we insert some random *Dirac delta*, $\delta_{\rm D}(x)$ functions:

$$\begin{aligned}
\langle\rho(\boldsymbol{x})\rho(\boldsymbol{x}+\boldsymbol{r})\rangle &= \\
&\Bigg\langle \int dM d^3\boldsymbol{y} \sum_{i=1}^{N} \delta_{\rm D}(M-M_i)\delta_{\rm D}(\boldsymbol{y}-\boldsymbol{x}_{0,i}) \\
&\quad\times\quad M^2 u_{\rm h}(|\boldsymbol{x}-\boldsymbol{y}|,M)u_{\rm h}(|\boldsymbol{x}+\boldsymbol{r}-\boldsymbol{y}|,M)\Bigg\rangle \quad + \\
&+\Bigg\langle \int dM_1 dM_2\, d^3\boldsymbol{y}_1 d^3\boldsymbol{y}_2 \sum_{i\neq j}^{N} \delta_{\rm D}(M_1-M_i)\delta_{\rm D}(M_2-M_j)\delta_{\rm D}(\boldsymbol{y}_1-\boldsymbol{x}_{0,i})\delta_{\rm D}(\boldsymbol{y}_2-\boldsymbol{x}_{0,j}) \\
&\quad\times\quad M_1 M_2\, u_{\rm h}(|\boldsymbol{x}-\boldsymbol{y}_1|,M_1)u_{\rm h}(|\boldsymbol{x}+\boldsymbol{r}-\boldsymbol{y}_2|,M_2)\Bigg\rangle \quad ,
\end{aligned} \tag{A.5}$$

and realising that the angular brackets imply an ensemble average over $\boldsymbol{x}_{0,i}$ and M_i, we can write:

$$\begin{aligned}
\langle\rho(\boldsymbol{x})\rho(\boldsymbol{x}+\boldsymbol{r})\rangle &= \\
&\int dM d^3\boldsymbol{y} \left\langle \sum_{i=1}^{N} \delta_{\rm D}(M-M_i)\delta_{\rm D}(\boldsymbol{y}-\boldsymbol{x}_{0,i}) \right\rangle \\
&\quad\times\quad M^2 u_{\rm h}(|\boldsymbol{x}-\boldsymbol{y}|,M)u_{\rm h}(|\boldsymbol{x}+\boldsymbol{r}-\boldsymbol{y}|,M) \quad + \\
&+\int dM_1 dM_2\, d^3\boldsymbol{y}_1 d^3\boldsymbol{y}_2 \left\langle \sum_{i\neq j}^{N} \delta_{\rm D}(M_1-M_i)\delta_{\rm D}(M_2-M_j)\delta_{\rm D}(\boldsymbol{y}_1-\boldsymbol{x}_{0,i})\delta_{\rm D}(\boldsymbol{y}_2-\boldsymbol{x}_{0,j}) \right\rangle \\
&\quad\times\quad M_1 M_2\, u_{\rm h}(|\boldsymbol{x}-\boldsymbol{y}_1|,M_1)u_{\rm h}(|\boldsymbol{x}+\boldsymbol{r}-\boldsymbol{y}_2|,M_2) \quad ,
\end{aligned} \tag{A.6}$$

and applying the *Ergodic principle* (e.g. Weinberg, 2008, in the appendix), the mass function is just defined as a volume average:

$$n(M) = \left\langle \sum_{i=1}^{N} \delta_{\rm D}(M-M_i)\delta_{\rm D}(\boldsymbol{y}-\boldsymbol{x}_{0,i}) \right\rangle \underbrace{\left(\int d^3\boldsymbol{y}\, u_{\rm h}\right)}_{=1} \quad . \tag{A.7}$$

Then, using eq. (A.1) and making similar replacements as above, we get similarly to eq. (5.3):

$$\begin{aligned}
\bar{\rho} &= \langle\rho(\boldsymbol{x})\rangle \\
&= \left\langle \sum_{i=1}^{N} M_i\, u_{\rm h}(|\boldsymbol{x}-\boldsymbol{x}_{0,i}|,M_i) \right\rangle \\
&= \int dM d^3\boldsymbol{y} \left\langle \sum_{i=1}^{N} \delta_{\rm D}(M-M_i)\delta_{\rm D}(\boldsymbol{y}-\boldsymbol{x}_{0,i}) \right\rangle M\, u_{\rm h}(|\boldsymbol{x}-\boldsymbol{y}|,M) \\
&= \int dM\, M n(M)
\end{aligned} \tag{A.8}$$

$$\begin{aligned}
\Rightarrow \bar{\rho}^2 &= \int dM_1 dM_2\, d^3\boldsymbol{y}_1 d^3\boldsymbol{y}_2 \\
&\times\quad \left\langle \sum_{i=1}^{N} \delta_{\rm D}(M_1-M_i)\delta_{\rm D}(\boldsymbol{y}_1-\boldsymbol{x}_{0,i}) \right\rangle \left\langle \sum_{j=1}^{N} \delta_{\rm D}(M_2-M_j)\delta_{\rm D}(\boldsymbol{y}_2-\boldsymbol{x}_{0,j}) \right\rangle \\
&\times\quad M_1 M_2\, u_{\rm h}(|\boldsymbol{x}-\boldsymbol{y}_1|,M_1)u_{\rm h}(|\boldsymbol{x}+\boldsymbol{r}-\boldsymbol{y}_2|,M_2) \quad .
\end{aligned} \tag{A.9}$$

Now let us insert our result from equations (A.9) and (A.6) back into eq. (A.11):

$$\begin{aligned}
\bar{\rho}^2\,\xi(r) &= \langle \rho(\boldsymbol{x})\rho(\boldsymbol{x}+\boldsymbol{r})\rangle - \bar{\rho}^2 \\
&= \int dM d^3\boldsymbol{y} \left\langle \sum_{i=1}^{N} \delta_{\mathrm{D}}(M-M_i)\delta_{\mathrm{D}}(\boldsymbol{y}-\boldsymbol{x}_{0,i}) \right\rangle \\
&\times \quad M^2 u_{\mathrm{h}}(|\boldsymbol{x}-\boldsymbol{y}|, M) u_{\mathrm{h}}(|\boldsymbol{x}+\boldsymbol{r}-\boldsymbol{y}|, M) \quad + \\
&+ \int dM_1 dM_2\, d^3\boldsymbol{y}_1 d^3\boldsymbol{y}_2 \\
&\times \quad \left\langle \sum_{i\neq j}^{N} \delta_{\mathrm{D}}(M_1-M_i)\delta_{\mathrm{D}}(M_2-M_j)\delta_{\mathrm{D}}(\boldsymbol{y}_1-\boldsymbol{x}_{0,i})\delta_{\mathrm{D}}(\boldsymbol{y}_2-\boldsymbol{x}_{0,j}) \right\rangle \\
&\times \quad M_1 M_2\, u_{\mathrm{h}}(|\boldsymbol{x}-\boldsymbol{y}_1|, M_1) u_{\mathrm{h}}(|\boldsymbol{x}+\boldsymbol{r}-\boldsymbol{y}_2|, M_2) \quad + \\
&- \int dM_1 dM_2\, d^3\boldsymbol{y}_1 d^3\boldsymbol{y}_2 \\
&\times \quad \left\langle \sum_{i=1}^{N} \delta_{\mathrm{D}}(M_1-M_i)\delta_{\mathrm{D}}(\boldsymbol{y}_1-\boldsymbol{x}_{0,i}) \right\rangle \left\langle \sum_{j=1}^{N} \delta_{\mathrm{D}}(M_2-M_j)\delta_{\mathrm{D}}(\boldsymbol{y}_2-\boldsymbol{x}_{0,j}) \right\rangle \\
&\times \quad M_1 M_2\, u_{\mathrm{h}}(|\boldsymbol{x}-\boldsymbol{y}_1|, M_1) u_{\mathrm{h}}(|\boldsymbol{x}+\boldsymbol{r}-\boldsymbol{y}_2|, M_2) \quad , \qquad \text{(A.10)}
\end{aligned}$$

put the last two terms together,

$$\begin{aligned}
\bar{\rho}^2\,\xi(r) &= \int dM d^3\boldsymbol{y}\, n(M) M^2 u_{\mathrm{h}}(|\boldsymbol{x}_1-\boldsymbol{y}|, M) u_{\mathrm{h}}(|\boldsymbol{x}_2-\boldsymbol{y}|, M) \quad + \\
&+ \prod_{i=1,2} \left[\int dM_i\, M_i n(M_i)\, d^3\boldsymbol{y}_i\, u_{\mathrm{h}}(|\boldsymbol{x}_i-\boldsymbol{y}_i|, M_i) \right] \xi^{\mathrm{cent}}(r_0, M_1, M_2) \qquad \text{(A.11)}
\end{aligned}$$

where we've taken $\boldsymbol{x}=\boldsymbol{x}_1$, $\boldsymbol{r}=\boldsymbol{x}_2-\boldsymbol{x}_1$, $r_0=|\boldsymbol{y_1}-\boldsymbol{y_2}|$ and

$$\begin{aligned}
\xi^{\mathrm{cent}}(r_0, M_1, M_2) n(M_1) n(M_2) \quad &\equiv \\
&\left\langle \sum_{i\neq j}^{N} \delta_{\mathrm{D}}(M_1-M_i)\delta_{\mathrm{D}}(M_2-M_j)\delta_{\mathrm{D}}(\boldsymbol{y}_1-\boldsymbol{x}_{0,i})\delta_{\mathrm{D}}(\boldsymbol{y}_2-\boldsymbol{x}_{0,j}) \right\rangle \quad + \\
- \quad &\left\langle \sum_{i=1}^{N} \delta_{\mathrm{D}}(M_1-M_i)\delta_{\mathrm{D}}(\boldsymbol{y}_1-\boldsymbol{x}_{0,i}) \right\rangle \left\langle \sum_{j=1}^{N} \delta_{\mathrm{D}}(M_2-M_j)\delta_{\mathrm{D}}(\boldsymbol{y}_2-\boldsymbol{x}_{0,j}) \right\rangle \quad , \qquad \text{(A.12)}
\end{aligned}$$

is the correlation function of halo centres. This equaiton makes sense, because ξ^{cent} is the "exces probability" (see also eq. (25) of Smith et al., 2007).

Note that setting $\boldsymbol{y}=\boldsymbol{x}_0$ and $M_{\mathrm{cut}}=0$ in eq. (A.11), one recovers eq. (5.11).

APPENDIX B

Density profile of halos

The halo density profile is taken to be the Navarro-Frenk-White (NFW) profile with r_s being the scale radius defined as the ration of the virial radius and the halo concentration parameter: $r_s = \frac{r_v}{c}$ and ρ_s is the scale density, which $\rho_s = \delta_c \rho_m$, where $\delta_c = (200/3)c^3 \left[\log(1+c) - c/(1+c)\right]^{-1}$.

$$\rho(r) = \frac{\rho_s}{\left(\frac{r}{r_s}\right)\left(1 + \frac{r}{r_s}\right)^2} \tag{B.1}$$

The NFW profile, like other ingredients of the halo model is calculated from ΛCDM models. . In order to asses the effect of this deviation from ΛCDM on the non-linear matter power spectrum the parameters used to calculate the concentration parameter, $c(M, z)$, have been readjusted. A further issue is the dependence of the critical overdensity δ_{crit} (n.b. $\delta_{crit} \neq \delta_c$) on halo mass (Barkana et al., 2001). Furthermore have $\Delta = 200$ giving the virial radius, where halos are truncated.

In order to calculate the projected mass density $\Sigma(r_\perp)$ one needs to integrate $\rho(r)$ over the line of sight i.e. along the component of the radial vector, perpendicular to the line of sight. In order to do this integral, rewrite r as a dimensionless variable $x = \frac{r}{r_s}$ & $dr = r_s dx$ and decompose it into a perpendicular $r_\perp$ and a parallel component $r_\parallel$:

$$\Sigma(r_\perp) = \int_{halo} \rho(r_\perp, r_\parallel) dr_\parallel = \rho_s \int_{halo} \frac{dr_\parallel}{\left(\frac{\sqrt{r_\perp^2 + r_\parallel^2}}{r_s}\right)\left(1 + \frac{\sqrt{r_\perp^2 + r_\parallel^2}}{r_s}\right)^2} \tag{B.2}$$

$$\Sigma(x_\perp) = \rho_s r_s \int_{halo} \frac{dx_\parallel}{\sqrt{x_\perp^2 + x_\parallel^2}\left(1 + \sqrt{x_\perp^2 + x_\parallel^2}\right)^2} \tag{B.3}$$

Projected 2D halo density profile - integrated over the line of sight to infinity

In order to solve the integral, substitute $x_{\parallel} = x\sin\theta = x_{\perp}\tan\theta$ & $dx_{\parallel} = x_{\perp}\sec^2\theta d\theta$. Consequently:

$$x = \sqrt{x_{\perp}^2 + x_{\parallel}^2} = x_{\perp}\sqrt{1+\tan^2\theta} = \frac{x_{\perp}}{\cos\theta} \tag{B.4}$$

and so, the integral becomes:

$$\Sigma(x_{\perp}) = \rho_s r_s \int_{halo} \frac{x_{\perp}\sec^2\theta d\theta}{\left(\frac{x_{\perp}}{\cos\theta}\right)\left(1+\frac{x_{\perp}}{\cos\theta}\right)^2} = \rho_s r_s \int_{halo} \frac{\cos\theta d\theta}{(\cos\theta + x_{\perp})^2} \tag{B.5}$$

Now, in order to integrate over the entire profile, here we set the limits to go from $r_{\parallel} = \infty$ to $r_{\parallel} = -\infty$, but since the halo profile is symmetric around $r = 0$, we can multiply the integral by 2 and set it to go from $r_{\parallel} = 0 \rightarrow +\infty$. For the variable θ this corresponds to $\theta = 0 \rightarrow \pi/2$:

$$\begin{aligned}
\Sigma(x_{\perp}) &= 2\rho_s r_s \int_0^{\pi/2} \frac{\cos\theta d\theta}{(\cos\theta + x_{\perp})^2} && \text{(B.6)}\\
&= \frac{2\rho_s r_s}{x_{\perp}^2 - 1}\left[\frac{2}{\sqrt{1-x_{\perp}^2}}\operatorname{arctanh}\left(\frac{(x_{\perp}-1)\tan\left(\frac{\theta}{2}\right)}{\sqrt{1-x_{\perp}^2}}\right) + \frac{x_{\perp}\sin\theta}{x_{\perp}+\cos\theta}\right]_{\theta=0}^{\theta=\pi/2} && \text{(B.7)}\\
&= \frac{2\rho_s r_s}{x_{\perp}^2 - 1}\left[1 + \frac{2}{\sqrt{1-x_{\perp}}}\operatorname{arctanh}\left(-\frac{\sqrt{1-x_{\perp}}}{\sqrt{1+x_{\perp}}}\right)\right] && \text{(B.8)}\\
&= \frac{2\rho_s r_s}{x_{\perp}^2 - 1}\left[1 - \frac{2}{\sqrt{1-x_{\perp}}}\operatorname{arctanh}\left(\frac{\sqrt{1-x_{\perp}}}{\sqrt{1+x_{\perp}}}\right)\right] && \text{(B.9)}
\end{aligned}$$

This solution only works for $x_{\perp} \neq 1$. We need to solve the integral separately for $x_{\perp} = 1$:

$$\Sigma(x_{\perp} = 1) = 2\rho_s r_s \int_0^{\pi/2} \frac{\cos\theta d\theta}{(\cos\theta + 1)^2} = \frac{2\rho_s r_s}{3} \tag{B.10}$$

Furthermore, in order to avoind complex numbers, we can simplify the above solution in the case $x_{\perp} > 1$, using the known result that

$$\begin{aligned}
\Sigma(x_{\perp} > 1) &= \frac{2\rho_s r_s}{x_{\perp}^2 - 1}\left[1 - \frac{2}{\mathrm{i}\sqrt{x_{\perp}-1}}\operatorname{arctanh}\left(\frac{\mathrm{i}\sqrt{x_{\perp}-1}}{\sqrt{x_{\perp}+1}}\right)\right] && \text{(B.11)}\\
&= \frac{2\rho_s r_s}{x_{\perp}^2 - 1}\left[1 - \frac{2\mathrm{i}}{\mathrm{i}\sqrt{x_{\perp}-1}}\arctan\left(\frac{\sqrt{x_{\perp}-1}}{\sqrt{x_{\perp}+1}}\right)\right] && \text{(B.12)}\\
&= \frac{2\rho_s r_s}{x_{\perp}^2 - 1}\left[1 - \frac{2}{\sqrt{x_{\perp}-1}}\arctan\left(\frac{\sqrt{x_{\perp}-1}}{\sqrt{x_{\perp}+1}}\right)\right] && \text{(B.13)}
\end{aligned}$$

This is exactly the same as in Wright & Brainerd (1999, eq. 11) and Bartelmann (1996). Note that Wright & Brainerd (1999) say that the convergence $\kappa_{NFW} = \Sigma_{NFW}(r_{\perp})/\Sigma_{crit}$. However in order to calculate shear, they say one must calculate the mean density within R, $\bar{\Sigma}(r_{\perp} < R)$.

Projected 2D halo density profile - integrated over the line of sight up to the virial radius

The above substitution is less useful if we set the limits of the integral to be the virial radius of the halo, as (see B.6) then we get $\theta_{limit} = \arctan\sqrt{\frac{x_v^2}{x_\perp^2} - 1}$ and so, must calculate the $\tan\left(\arctan\frac{\sqrt{\frac{x_v^2}{x_\perp^2}-1}}{2}\right)$. Also this way it is hard to account for possible poles in the integration.

For this reason we do the integral directly, with the limit becoming $x_\parallel^{limit} = \sqrt{c^2 - x_\perp^2}$, since $r_\parallel^{limit} = \sqrt{r_v^2 - r_\perp^2}$ and $c = r_v/r_s$:

$$\Sigma(x_\perp) = \rho_s r_s \int_0^{\sqrt{c^2-x_\perp^2}} \frac{dx_\parallel}{\sqrt{x_\perp^2 + x_\parallel^2}\left(1 + \sqrt{x_\perp^2 + x_\parallel^2}\right)^2} \tag{B.14}$$

In order to be able to solve this one needs to assume that $\{c, x_\parallel, x_\perp\} \in \mathbb{R}$, $c > 0$, $0 \le x_\parallel \le c$ and $0 \le x_\perp < c$ (since $x_\perp = c$ makes the integral go to 0). There are 5 different cases of solution to this integral: $x_\perp > 1$, $x_\perp = 1$, $x_\perp < 1$ with $c \le 1$, $x_\perp < 1$ with $c > 1$ and $x_\perp = 0$ (the last case diverges and is impossible to solve?).

Case 1: $1 < x_\perp < c$

Note here the identity: $\arctan(-x) = -\arctan(x)$. As well as:

$$\arctan(x) = \frac{i}{2}\ln\left(\frac{i+x}{i-x}\right) = \frac{i}{2}\ln\left(\frac{1+x/i}{1-x/i}\right) = \frac{i}{2}\ln\left(\frac{1-ix}{1+ix}\right) \tag{B.15}$$

Then,

$$\Sigma(x_\perp > 1) = \frac{2\rho_s r_s}{(1+c)(x_\perp^2-1)^{3/2}} F(x_\perp > 1) \tag{B.16}$$

Mathematica gives:

$$F(x_\perp > 1 \vee c \le 1) = \sqrt{(c^2 - x_\perp^2)(-1 + x_\perp^2)} - (1+c)\arctan\left(\frac{\sqrt{c^2 - x_\perp^2}}{\sqrt{-1 + x_\perp^2}}\right) + G(x_\perp > 1) \tag{B.17}$$

where

$$G(x_\perp > 1) = \frac{i(1+c)}{2}\ln\left(\frac{c - i\sqrt{\frac{c^2-x_\perp^2}{x_\perp^2-1}}}{c + i\sqrt{\frac{c^2-x_\perp^2}{x_\perp^2-1}}}\right) = (1+c)\frac{i}{2}\ln\left(\frac{1 - \frac{i}{c}\sqrt{\frac{c^2-x_\perp^2}{x_\perp^2-1}}}{1 + \frac{i}{c}\sqrt{\frac{c^2-x_\perp^2}{x_\perp^2-1}}}\right) \quad , \tag{B.18}$$

which simplifies to:

$$F(x_\perp > 1) = \sqrt{(x_\perp^2 - 1)(c^2 - x_\perp^2)} - (1+c)\arctan\left(\frac{\sqrt{c^2 - x_\perp^2}}{\sqrt{x_\perp^2 - 1}}\right) + (1+c)\arctan\left(\frac{\sqrt{c^2 - x_\perp^2}}{c\sqrt{x_\perp^2 - 1}}\right) \tag{B.19}$$

Case 2: $x_\perp = 1$

This means $r_\parallel = r_s$. Need to calculate this separately, since need to avoid zeros in denominators!

$$\Sigma(x_\perp = 1) = \frac{2\rho_s r_s (c+2)\sqrt{c-1}}{3(c+1)^{3/2}} \tag{B.20}$$

Case 3: $x_\perp < 1$

Here the solution is

$$\Sigma(x_\perp < 1) = \frac{-2\rho_s r_s}{(1+c)(1-x_\perp^2)^{3/2}} F(x_\perp < 1) \tag{B.21}$$

where for the case, where $c > 1$, Mathematica gives:

$$\begin{align}
F(x_\perp < 1) &= \frac{1}{2i}\left[2i\sqrt{(c^2-x_\perp^2)(1-x_\perp^2)} + (1+c)\pi + \right. \tag{B.22}\\
&+ \left. i(1+c)\ln\left(-\frac{1+\sqrt{\frac{c^2-x_\perp^2}{1-x_\perp^2}}}{1-\sqrt{\frac{c^2-x_\perp^2}{1-x_\perp^2}}}\right) + i(1+c)\ln\left(\frac{c-\sqrt{\frac{c^2-x_\perp^2}{1-x_\perp^2}}}{c+\sqrt{\frac{c^2-x_\perp^2}{1-x_\perp^2}}}\right)\right] \tag{B.23}\\
&= \sqrt{(c^2-x_\perp^2)(1-x_\perp^2)} - \frac{i}{2}(1+c)\pi + \frac{i}{2}(1+c)\ln(-1) + \tag{B.24}\\
&+ \frac{1}{2}(1+c)\ln\left(\frac{1+\frac{\sqrt{c^2-x_\perp^2}}{\sqrt{1-x_\perp^2}}}{1-\frac{\sqrt{c^2-x_\perp^2}}{\sqrt{1-x_\perp^2}}}\right) - \frac{1}{2}(1+c)\ln\left(\frac{1+\frac{\sqrt{c^2-x_\perp^2}}{c\sqrt{1-x_\perp^2}}}{1-\frac{\sqrt{c^2-x_\perp^2}}{c\sqrt{1-x_\perp^2}}}\right) \tag{B.25}\\
&= \sqrt{(c^2-x_\perp^2)(1-x_\perp^2)} - \frac{i}{2}(1+c)\pi + \frac{i}{2}(1+c)\pi + \tag{B.26}\\
&+ (1+c)\text{arctanh}\left(\frac{\sqrt{c^2-x_\perp^2}}{\sqrt{1-x_\perp^2}}\right) - (1+c)\text{arctanh}\left(\frac{\sqrt{c^2-x_\perp^2}}{c\sqrt{1-x_\perp^2}}\right) \tag{B.27}
\end{align}$$

Note that

$$\text{arctanh}(x) = \frac{1}{2}\ln\left(\frac{1+x}{1-x}\right) \tag{B.28}$$

as well as the fact that $\ln(-a) = \ln(-1) + \ln(a) = i\pi + \ln(a)$.
For the case, where $c < 1$, the result is equivalent to Case 1, but is here written in a format that avoids imaginary intermediate results. Note also that we know that $\mathcal{X} \equiv \sqrt{\frac{c^2-x_\perp^2}{1-x_\perp^2}} < c \leq 1$ in the this case.
Therefore,

$$F(x_\perp < 1) = \begin{cases} \sqrt{(1-x_\perp^2)(c^2-x_\perp^2)} + (1+c)\text{atanh}\left(\mathcal{X}\right) - (1+c)\text{atanh}\left(\frac{\mathcal{X}}{c}\right) & \text{if } c < 1 \\ \sqrt{(1-x_\perp^2)(c^2-x_\perp^2)} + (1+c)\text{atanh}\left(\frac{1}{\mathcal{X}}\right) - (1+c)\text{atanh}\left(\frac{c}{\mathcal{X}}\right) & \text{if } c > 1 \end{cases} \tag{B.29}$$

As for $c = 1$:

$$\Sigma(x_\perp < 1, c = 1) = \frac{-\rho_s r_s \left(1 - x_\perp^2 + \ln(x_\perp^2)\right)}{(1-x_\perp^2)^{3/2}} \tag{B.30}$$

since $\lim_{x\to 1} \operatorname{arctanh}(x) = \infty$.

Case 4: $x_\perp = 0$

The solution to this case is undefined as the integral diverges at the lower limit of $x_\parallel = 0$ & $x_\perp = 0$. As we can safely assume that the infinite density at the centre of a halo would be unphysical, we can assume it is somehow smoothened. Fortunately the entire 3D integral of the NFW density converges as we integrate over $\sim \rho_{nfw}(r) r^2 dr$. So in the integral over $\theta = x_\perp r_s/d$ for the Fourier transformation of $\kappa(\theta)$ converges at 0:

$$\kappa_l = \int_0^{\theta_v} \theta d\theta \kappa(\theta) J_0\left(\left(\frac{1}{2} + l\right)\theta\right) \tag{B.31}$$

These results are exactly the same as eq. (27) in Takada & Jain (2003), but I haven't yet managed to show it analytically. However I have plotted them and they look exactly the same.

Books and Reviews

Alcubierre M. (2008). *Introduction to 3+1 Numerical Relativity.* International Series of Monographs on Physics (OUP Oxford). ISBN 9780199205677. URL `http://books.google.de/books?id=4hDvRvVJeEIC`.

Arnowitt R.L., Deser S. & Misner C.W. (1962). *The dynamics of general relativity.* ArXiv e-prints arXiv:gr-qc/0405109.

Bardeen W.A. (1985). *Gauge anomalies, gravitational anomalies and superstrings.* NASA STI/Recon Technical Report N 86:p. 32383.

Bartelmann M. & Schneider P. (2001). *Weak gravitational lensing.* Phys.Rept. 340:pp. 291–472. arXiv:astro-ph/9912508.

Bergström L. & Goobar A. (2006). *Cosmology and Particle Astrophysics.* Springer-Praxis books in astronomy and planetary science (Springer). ISBN 9783540329244. URL `http://books.google.de/books?id=CQYu_sutWAoC`.

Börner G. (2004). *The Early Universe: Facts and Fiction.* Astronomy and Astrophysics Library (Springer). ISBN 9783540441977. URL `http://books.google.de/books?id=cDJw3dWjw_UC`.

Bullock J.S. (2010). *Notes on the Missing Satellites Problem.* ArXiv e-prints arXiv:1009.4505.

Carroll S.M. (2003). *Why is the universe accelerating?* eConf C0307282:p. TTH09. arXiv:astro-ph/0310342.

Challinor A. (2009). *Cosmology Lecture Notes, Part III: Large-scale Structure Formation.* University of Cambridge, DAMPT. URL `http://camd05.ast.cam.ac.uk/Cosmology/COSMOLOGY_files/Structure_formation.pdf`.

Dodelson S. (2003). *Modern Cosmology* (Academic Press). ISBN 9780122191411. URL `http://books.google.de/books?id=3oPRxdXJexcC`.

Hogg D.W. (1999). *Distance measures in cosmology.* ArXiv e-prints arXiv:astro-ph/9905116.

Kay D. (1988). *Schaum's Outline of Tensor Calculus.* Schaum's Outline Series (McGraw-Hill). ISBN 9780070334847. URL `http://books.google.de/books?id=6tUU3KruG14C`.

Kodama H. & Sasaki M. (1984). *Cosmological Perturbation Theory.* Prog.Theor.Phys.Suppl. 78:pp. 1–166.

Kolb E. & Turner M. (1994). *The Early Universe*. Frontiers in Physics (Westview Press). ISBN 9780201626742. URL http://books.google.de/books?id=Qwijr-HsvMMC.

Landau L. & Lifshits E. (1975). *The Classical Theory of Fields*. No. v. 2 in Course of Theoretical Physics (Butterworth-Heinemann). ISBN 9780750627689. URL http://books.google.de/books?id=X18PF4oKyrUC.

Liddle A.R. & Lyth D.H. (1993). *The cold dark matter density perturbation*. Phys.Rept. 231:pp. 1–105. arXiv:astro-ph/9303019.

Lyth D. & Liddle A. (2009). *The Primordial Density Perturbation: Cosmology, Inflation and the Origin of Structure* (Cambridge University Press). ISBN 9780521828499. URL http://books.google.de/books?id=Mor_ehlYc4QC.

Ma C.P. & Bertschinger E. (1995). *Cosmological perturbation theory in the synchronous and conformal Newtonian gauges*. Astrophys.J. 455:pp. 7–25. arXiv:astro-ph/9506072.

Maggiore M. (2007). *Gravitational Waves: Volume 1: Theory and Experiments*. Gravitational Waves (Oxford University Press, USA). ISBN 9780198570745. URL http://books.google.de/books?id=AqVpQgAACAAJ.

Misner C., Thorne K. & Wheeler J. (1973). *Gravitation*. No. pt. 3 in Physics Series (W. H. Freeman). ISBN 9780716703440. URL http://books.google.de/books?id=w4Gigq3tY1kC.

Mukhanov V. (2005). *Physical Foundations of Cosmology* (Cambridge University Press). ISBN 9780521563987. URL http://books.google.de/books?id=1TXO7GmwZFgC.

Mukhanov V.F., Feldman H. & Brandenberger R.H. (1992). *Theory of cosmological perturbations. Part 1. Classical perturbations. Part 2. Quantum theory of perturbations. Part 3. Extensions*. Phys.Rept. 215:pp. 203–333.

Padmanabhan T. (2008). *Dark energy and gravity*. Gen.Rel.Grav. 40:pp. 529–564. arXiv:0705.2533.

Peacock J. (1998). *Cosmological Physics*. Cambridge Astrophysics Series (Cambridge University Press). ISBN 9780521422703. URL http://books.google.de/books?id=t8O-yylU0j0C.

Peebles P. (1993). *Principles of Physical Cosmology*. Princeton Series in Physics (Princeton University Press). ISBN 9780691019338. URL http://books.google.de/books?id=AmlEt6TJ6jAC.

Rosswog S. (2009). *Astrophysical smooth particle hydrodynamics*. New A Rev.53:pp. 78–104. arXiv:0903.5075.

Weinberg S. (1972). *Gravitation and cosmology: principles and applications of the general theory of relativity* (Wiley). ISBN 9780471925675. URL http://books.google.de/books?id=XLbvAAAAMAAJ.

Weinberg S. (2008). *Cosmology* (OUP Oxford). ISBN 9780198526827. URL http://books.google.de/books?id=nqQZdg020fsC.

Bibliography

Abazajian K.N. et al. (2009). *The Seventh Data Release of the Sloan Digital Sky Survey.* ApJS182:543. arXiv:0812.0649.

Ade P. et al. (Planck Collaboration) (2011). *Planck Early Results. I. The Planck mission.* Astron.Astrophys. 536:p. 16464. arXiv:1101.2022.

Alam S.K., Bullock J.S. & Weinberg D.H. (2002). *Dark matter properties and halo central densities.* Astrophys. J. 572:pp. 34–40. arXiv:astro-ph/0109392.

Albrecht A. et al. (2006). *Report of the Dark Energy Task Force.* ArXiv e-prints arXiv:astro-ph/0609591.

Amara A. & Refregier A. (2007). *Optimal Surveys for Weak Lensing Tomography.* Mon.Not.Roy.Astron.Soc. 381:pp. 1018–1026. arXiv:astro-ph/0610127.

Amendola L. et al. (2012). *Cosmology and fundamental physics with the Euclid satellite.* ArXiv e-prints arXiv:1206.1225.

Appel A. (1985). *An efficient program for many-body simulation.* SIAM Journal on Scientific and Statistical Computing 6(1):pp. 85–103.

Astier P. et al. (2006). *The Supernova Legacy Survey: measurement of Ω_m, Ω_Λ and w from the first year data set.* A&A447:pp. 31–48. arXiv:astro-ph/0510447.

Audren B., Lesgourgues J., Bird S., Haehnelt M.G. & Viel M. (2012). *Neutrino masses and cosmological parameters from a Euclid-like survey: Markov Chain Monte Carlo forecasts including theoretical errors.* ArXiv e-prints arXiv:1210.2194.

Avila-Reese V., Colin P., Valenzuela O., D'Onghia E. & Firmani C. (2001). *Formation and structure of halos in a warm dark matter cosmology.* Astrophys.J. 559:pp. 516–530. arXiv:astro-ph/0010525.

Bacon D., Amara A. & Read J. (2009). *Measuring Dark Matter Substructure with Galaxy-Galaxy Flexion Statistics.* ArXiv e-prints arXiv:0909.5133.

Bagla J. & Ray S. (2003). *Performance characteristics of TreePM codes.* New Astron. 8:pp. 665–677. arXiv:astro-ph/0212129.

Baldi M., Pettorino V., Robbers G. & Springel V. (2010). *Hydrodynamical N-body simulations of coupled dark energy cosmologies.* MNRAS403:pp. 1684–1702. arXiv:0812.3901.

Barkana R., Haiman Z. & Ostriker J.P. (2001). *Constraints on warm dark matter from cosmological reionization.* ArXiv e-prints arXiv:astro-ph/0102304.

Barnes J. & Hut P. (1986). *A Hierarchical O(NlogN) Force Calculation Algorithm.* Nature 324:pp. 446–449.

Bartelmann M. (1996). *Arcs from a universal dark-matter halo profile.* A&A313:pp. 697–702. arXiv:arXiv:astro-ph/9602053.

Benitez-Llambay A. et al. (2012). *Dwarf Galaxies and the Cosmic Web.* ArXiv e-prints arXiv:1211.0536.

Benson A.J. et al. (2012). *Dark Matter Halo Merger Histories Beyond Cold Dark Matter: I - Methods and Application to Warm Dark Matter.* ArXiv e-prints arXiv:1209.3018.

Bertone G., Hooper D. & Silk J. (2005). *Particle dark matter: evidence, candidates and constraints.* Phys.Rept. 405:pp. 279–390. arXiv:hep-ph/0404175.

Bird S., Viel M. & Haehnelt M.G. (2012). *Massive neutrinos and the non-linear matter power spectrum.* MNRAS420:pp. 2551–2561. arXiv:1109.4416.

Blas D., Lesgourgues J. & Tram T. (2011). *The Cosmic Linear Anisotropy Solving System (CLASS) II: approximation schemes.* JCAP 1107:p. 034. arXiv:1104.2933.

Bode P., Ostriker J.P. & Turok N. (2001). *Halo formation in warm dark matter models.* Astrophys.J. 556:pp. 93–107. arXiv:astro-ph/0010389.

Boehm C., Mathis H., Devriendt J. & Silk J. (2005). *Non-linear evolution of suppressed dark matter primordial power spectra.* Mon. Not. R. Astron. Soc. 360:p. 282.

Bond J., Efstathiou G. & Silk J. (1980). *Massive Neutrinos and the Large Scale Structure of the Universe.* Phys.Rev.Lett. 45:pp. 1980–1984.

Bond J. & Szalay A. (1983). *The Collisionless Damping of Density Fluctuations in an Expanding Universe.* Astrophys.J. 274:pp. 443–468.

Boyanovsky D., de Vega H. & Sanchez N. (2008). *The dark matter transfer function: free streaming, particle statistics and memory of gravitational clustering.* Phys.Rev. D78:p. 063546. arXiv:0807.0622.

Boyarsky A., Lesgourgues J., Ruchayskiy O. & Viel M. (2009). *Lyman-α constraints on warm and on warm-plus-cold dark matter models.* JCAP 0905:p. 012. arXiv:0812.0010.

Boyarsky A., Neronov A., Ruchayskiy O. & Shaposhnikov M. (2006). *The masses of active neutrinos in the νMSM from X-ray astronomy.* JETP Lett. 83:pp. 133–135. arXiv:hep-ph/0601098.

Brooks A.M., Kuhlen M., Zolotov A. & Hooper D. (2012). *A Baryonic Solution to the Missing Satellites Problem.* ArXiv e-prints arXiv:1209.5394.

Bryan G. & Norman M. (1997). *Simulating X-ray clusters with adaptive mesh refinement.* ArXiv e-prints arXiv:astro-ph/9710186.

Bullock J.S. et al. (2001). *Profiles of dark haloes. Evolution, scatter, and environment.* Mon.Not.Roy.Astron.Soc. 321:pp. 559–575. arXiv:astro-ph/9908159.

Carroll S.M. (2001). *The cosmological constant.* Living Rev.Rel. 4:p. 1. arXiv:astro-ph/0004075.

Casarini L., La Vacca G., Amendola L., Bonometto S.A. & Maccio A.V. (2011). *Non–linear weak lensing forecasts.* JCAP 1103:p. 026. arXiv:1102.3877.

Colin P., Avila-Reese V. & Valenzuela O. (2000). *Substructure and halo density profiles in a warm dark matter cosmology.* Astrophys.J. 542:pp. 622–630. arXiv:astro-ph/0004115.

Collister A.A. & Lahav O. (2004). *ANNz: Estimating Photometric Redshifts Using Artificial Neural Networks.* PASP116:pp. 345–351. arXiv:astro-ph/0311058.

Colombi S., Jaffe A.H., Novikov D. & Pichon C. (2008). *Accurate estimators of power spectra in N-body simulations.* ArXiv e-prints arXiv:0811.0313.

Colombo L., Pierpaoli E. & Pritchard J. (2009). *Cosmological parameters after WMAP5: forecasts for Planck and future galaxy surveys.* Mon.Not.Roy.Astron.Soc. 398:p. 1621. arXiv:0811.2622.

Cooray A. & Hu W. (2001). *Power spectrum covariance of weak gravitational lensing.* Astrophys.J. 554:pp. 56–66. arXiv:astro-ph/0012087.

Cooray A., Hu W. & Miralda-Escude J. (2000). *Weak lensing by large scale structure: a dark matter halo approach.* Astrophys.J. 535:pp. L9–L12. arXiv:astro-ph/0003205.

Cooray A. & Sheth R.K. (2002). *Halo models of large scale structure.* Phys.Rept. 372:pp. 1–129. arXiv:astro-ph/0206508.

Csabai I. et al. (SDSS Collaboration) (2003). *The application of photometric redshifts to the SDSS Early Data Release.* Astron.J. 125:p. 580. arXiv:astro-ph/0211080.

Dicke R.H., Peebles P.J.E., Roll P.G. & Wilkinson D.T. (1965). *Cosmic Black-Body Radiation.* Astrophys.J. 142:pp. 414–419.

Donato F. et al. (2009). *A constant dark matter halo surface density in galaxies.* Mon.Not.Roy.Astron.Soc 397:pp. 1169–1176. arXiv:0904.4054.

Dunkley J. et al. (WMAP Collaboration) (2009). *Five-Year Wilkinson Microwave Anisotropy Probe (WMAP) Observations: Likelihoods and Parameters from the WMAP data.* Astrophys.J.Suppl. 180:pp. 306–329. arXiv:0803.0586.

Dunstan R.M., Abazajian K.N., Polisensky E. & Ricotti M. (2011). *The halo model of large scale structure for warm dark matter.* ArXiv e-prints arXiv:1109.6291.

Einstein A. (1905). *On the electrodynamics of moving bodies.* Annalen Phys. 17:pp. 891–921.

Einstein A. (1916). *Die Grundlage der allgemeinen Relativitätstheorie.* Annalen der Physik 354:pp. 769–822. URL `http://en.wikisource.org/wiki/The_Foundation_of_the_Generalised_Theory_of_Relativity`.

EISENSTEIN D.J., HU W. & TEGMARK M. (1998). *Cosmic complementarity: H(0) and Ω(m) from combining CMB experiments and redshift surveys.* Astrophys.J. 504:pp. L57–L61. arXiv:astro-ph/9805239.

FRIEDMANN A. (1924). *Über die Möglichkeit einer Welt mit konstanter negativer Krümmung des Raumes.* Zeitschrift für Physik A Hadrons and Nuclei 21(1):pp. 326–332.

FRIGO M. (1999). *A fast Fourier transform compiler.* SIGPLAN Not. 34(5):pp. 169–180. ISSN 0362-1340. URL `http://www.fftw.org/`.

FRY J.N. & GAZTANAGA E. (1993). *Biasing and hierarchical statistics in large scale structure.* Astrophys.J. 413:pp. 447–452. arXiv:astro-ph/9302009.

GAO L. & THEUNS T. (2007). *Lighting the universe with filaments.* Science 317:p. 1527. arXiv:0709.2165.

GUTH A.H. (1981). *Inflationary universe: A possible solution to the horizon and flatness problems.* Phys.Rev.D 23:pp. 347–356.

HAMANA T., OUCHI M., SHIMASAKU K., KAYO I. & SUTO Y. (2004). *Properties of host haloes of Lyman-break galaxies and Lyman-α emitters from their number densities and angular clustering.* MNRAS347:pp. 813–823. arXiv:astro-ph/0307207.

HAMANN J., LESGOURGUES J. & MANGANO G. (2008). *Using BBN in cosmological parameter extraction from CMB: A Forecast for PLANCK.* JCAP 0803:p. 004. arXiv:0712.2826.

HANSEN S.H., LESGOURGUES J., PASTOR S. & SILK J. (2002). *Constraining the window on sterile neutrinos as warm dark matter.* Mon.Not.Roy.Astron.Soc. 333:pp. 544–546. arXiv:astro-ph/0106108.

HENRY J.P. (2000). *Measuring cosmological parameters from the evolution of cluster X-ray temperatures.* Astrophys.J. 534:pp. 565–580. arXiv:astro-ph/0002365.

HU W. & KRAVTSOV A.V. (2003). *Sample variance considerations for cluster surveys.* Astrophys.J. 584:pp. 702–715. arXiv:astro-ph/0203169.

IVEZIC Z., TYSON J., ALLSMAN R., ANDREW J. & ANGEL R. (LSST Collaboration) (2008). *LSST: from Science Drivers to Reference Design and Anticipated Data Products.* ArXiv e-prints arXiv:0805.2366.

JENKINS A. et al. (Virgo Consortium) (1998). *Evolution of structure in cold dark matter universes.* Astrophys.J. 499:p. 20. arXiv:astro-ph/9709010.

JENKINS A. et al. (2001). *The mass function of dark matter halos.* Mon.Not.Roy.Astron.Soc. 321:p. 372. arXiv:astro-ph/0005260.

KATZ N., WEINBERG D.H. & HERNQUIST L. (1996). *Cosmological simulations with TreeSPH.* Astrophys.J.Suppl. 105:p. 19. arXiv:astro-ph/9509107.

KILBINGER M., BENABED K., COUPON J., MCCRACKEN H.J. & FU L. (2009). *NumerIcal Cosmology And lEnsing cAlculations (nicaea).* URL `http://www2.iap.fr/users/kilbinge/nicaea/`.

KLYPIN A., KRAVTSOV A.V., VALENZUELA O. & PRADA F. (1999). *Where Are the Missing Galactic Satellites?* ApJ522:pp. 82–92. arXiv:astro-ph/9901240.

KNEBE A., DEVRIENDT J.E., GIBSON B.K. & SILK J. (2003). *Top-down fragmentation of a warm dark matter filament.* Mon.Not.Roy.Astron.Soc. 345:p. 1285. arXiv:astro-ph/0302443.

KOMATSU E. et al. (WMAP Collaboration) (2011). *Seven-Year Wilkinson Microwave Anisotropy Probe (WMAP) Observations: Cosmological Interpretation.* Astrophys.J.Suppl. 192:p. 18. arXiv:1001.4538.

LARSON D. et al. (2011). *Seven-Year Wilkinson Microwave Anisotropy Probe (WMAP) Observations: Power Spectra and WMAP-Derived Parameters.* Astrophys.J.Suppl. 192:p. 16. arXiv:1001.4635.

LEE K.G. (2012). *Systematic Continuum Errors in the Lyman-α Forest and The Measured Temperature-Density Relation.* Astrophys.J. 753:p. 136. arXiv:1103.2780.

LEMAITRE G. (1927). *A homogeneous universe of constant mass and growing radius accounting for the radial velocity of extragalactic nebulae.* Annals of the Scientific Society of Brussels 47:p. 49.

LESGOURGUES J. (2011). *The Cosmic Linear Anisotropy Solving System (CLASS) III: Comparision with CAMB for ΛCDM.* ArXiv e-prints arXiv:1104.2934.

LEVI-CIVITA T. (1999). *Mechanics: On the analytic expression that must be given to the gravitational tensor in Einstein's theory.* ArXiv e-prints arXiv:physics/9906004.

LEWIS A. & BRIDLE S. (2002). *Cosmological parameters from CMB and other data: A Monte Carlo approach.* Phys.Rev. D66:p. 103511. arXiv:astro-ph/0205436.

LEWIS A. & CHALLINOR A. (2006). *Weak gravitational lensing of the CMB.* Phys.Rept. 429:pp. 1–65. arXiv:astro-ph/0601594.

LEWIS A., CHALLINOR A. & LASENBY A. (2000). *Efficient computation of CMB anisotropies in closed FRW models.* Astrophys.J. 538:pp. 473–476. arXiv:astro-ph/9911177.

LI M., LI X.D., WANG S. & WANG Y. (2012). *Dark Energy: a Brief Review.* ArXiv e-prints arXiv:1209.0922.

LIFSHITZ E. (1946). *On the gravitational stability of the expanding universe.* J. Phys.(USSR) 10:p. 116.

LIMBER D.N. (1953). *The Analysis of Counts of the Extragalactic Nebulae in Terms of a Fluctuating Density Field.* Astrophys.J. 117:p. 134.

LOVELL M.R. et al. (2012). *The Haloes of Bright Satellite Galaxies in a Warm Dark Matter Universe.* Mon.Not.Roy.Astron.Soc. 420:pp. 2318–2324. arXiv:1104.2929.

LOVELOCK D. (1972). *The Four-Dimensionality of Space and the Einstein Tensor.* Journal of Mathematical Physics 13(6):pp. 874–876.

LOVERDE M. & AFSHORDI N. (2008). *Extended Limber Approximation.* Phys.Rev. D78:p. 123506. arXiv:0809.5112.

Ma C.P. (1996). *Linear power spectra in cold + hot dark matter models: Analytical approximations and applications.* Astrophys.J. 471:pp. 13–23. arXiv:astro-ph/9605198.

Maccio A.V., Paduroiu S., Anderhalden D., Schneider A. & Moore B. (2012). *Cores in warm dark matter haloes: a Catch 22 problem.* ArXiv e-prints arXiv:1202.1282.

Markovič K. (2009). *Part III Applied Mathematics Essay: Constraining Cosmological Inflation.* Master's thesis, University of Cambridge, Darwin College. URL `http://www.usm.uni-muenchen.de/people/markovic/docs.html`.

Markovič K., Bridle S., Slosar A. & Weller J. (2011). *Constraining warm dark matter with cosmic shear power spectra.* JCAP 1101:p. 022. arXiv:1009.0218.

Mather J.C. et al. (1991). *Early results from the Cosmic Background Explorer (COBE).* Advances in Space Research 11:pp. 181–191.

Mather J.C. et al. (1994). *Measurement of the cosmic microwave background spectrum by the COBE FIRAS instrument.* Astrophys.J. 420:pp. 439–444.

Mo H. & White S.D. (1996). *An analytic model for the spatial clustering of dark matter halos.* Mon.Not.Roy.Astron.Soc. 282:p. 347. arXiv:astro-ph/9512127.

Navarro J.F., Frenk C.S. & White S.D. (1997). *A universal density profile from hierarchical clustering.* Astrophys.J. 490:pp. 493–508. arXiv:astro-ph/9611107.

Overbye D. (1991). *Lonely hearts of the cosmos: the scientific quest for the secret of the universe* (HarperCollins). ISBN 9780060159641. URL `http://books.google.de/books?id=682xAAAAIAAJ`.

Peacock J. & Dodds S. (1996). *Nonlinear evolution of cosmological power spectra.* Mon.Not.Roy.Astron.Soc. 280:p. L19. arXiv:astro-ph/9603031.

Peebles P.J.E. (1965). *The Black-Body Radiation Content of the Universe and the Formation of Galaxies.* Astrophys.J. 142:p. 1317.

Peiris H. (2009). *Cosmology Lecture Notes, Part I: The Unperturbed Universe.* University of Cambridge, DAMPT. URL `http://nefertiti.hpc.phys.ucl.ac.uk/cosmology/COSMOLOGY_files/Cosmology.pdf`.

Penzias A.A. & Wilson R.W. (1965). *A Measurement of Excess Antenna Temperature at 4080 Mc/s.* Astrophys.J. 142:pp. 419–421.

Percival W.J. et al. (2007). *Measuring the Baryon Acoustic Oscillation scale using the Sloan Digital Sky Survey and 2dF Galaxy Redshift Survey.* MNRAS381:pp. 1053–1066. arXiv:0705.3323.

Perlmutter S. et al. (Supernova Cosmology Project) (1999). *Measurements of* Ω *and* Λ *from 42 high redshift supernovae.* Astrophys.J. 517:pp. 565–586. arXiv:astro-ph/9812133.

Pfitzner D.W., Salmon J.K. & Sterling T. (1997). *Halo World: Tools for Parallel Cluster Finding in Astrophysical N-body Simulations.* Data Mining and Knowledge Discovery 1:pp. 419–438. ISSN 1384-5810. URL `http://dx.doi.org/10.1023/A%3A1009729602855`.

POLISENSKY E. & RICOTTI M. (2010). *Constraints on the dark matter particle mass from the number of milky way satellites. In American Astronomical Society Meeting Abstracts #215*, vol. 42 of *Bulletin of the American Astronomical Society*, p. 408.02.

PRESS W.H. & SCHECHTER P. (1974). *Formation of galaxies and clusters of galaxies by selfsimilar gravitational condensation.* Astrophys.J. 187:pp. 425–438.

RASSAT A. et al. (2008). *Deconstructing Baryon Acoustic Oscillations: A Comparison of Methods.* ArXiv e-prints arXiv:0810.0003.

REFREGIER A. et al. (2010). *Euclid Imaging Consortium Science Book.* ArXiv e-prints arXiv:1001.0061.

RICCI G. & LEVI-CIVITA T. (1901). *Mèthodes de calcul diffèrentiel absolu et leurs applications.* Mathematische Annalen 54:pp. 125–201. URL `http://eudml.org/doc/157997`.

RIESS A.G. et al. (Supernova Search Team) (1998). *Observational evidence from supernovae for an accelerating universe and a cosmological constant.* Astron.J. 116:pp. 1009–1038. arXiv:astro-ph/9805201.

RIESS A.G. et al. (2009). *A Redetermination of the Hubble Constant with the Hubble Space Telescope from a Differential Distance Ladder.* ApJ699:pp. 539–563. arXiv:0905.0695.

ROBERTSON H. (1935). *Kinematics and world-structure.* The Astrophysical Journal 82:p. 284.

SCHAYE J. et al. (2010). *The physics driving the cosmic star formation history.* Mon.Not.Roy.Astron.Soc. 402:p. 1536. arXiv:0909.5196.

SCHNEIDER A., SMITH R.E., MACCIO A.V. & MOORE B. (2012). *Nonlinear Evolution of Cosmological Structures in Warm Dark Matter Models.* Mon.Not.Roy.Astron.Soc 424:pp. 684–698. arXiv:1112.0330.

SCHWARZSCHILD K. (1916). *On the Gravitational Field of a Mass Point According to Einstein's Theory.* Abh. Konigl. Preuss. Akad. Wissenschaften Jahre 1906,92, Berlin,1907 pp. 189–196.

SELJAK U. (2000). *Analytic model for galaxy and dark matter clustering.* Mon.Not.Roy.Astron.Soc. 318:p. 203. arXiv:astro-ph/0001493.

SELJAK U., SLOSAR A. & MCDONALD P. (2006). *Cosmological parameters from combining the Lyman-α forest with CMB, galaxy clustering and SN constraints.* JCAP 0610:p. 014. arXiv:astro-ph/0604335.

SELJAK U. & ZALDARRIAGA M. (1996). *A line of sight integration approach to cosmic microwave background anisotropies.* Astrophys.J. 469:pp. 437–444. arXiv:astro-ph/9603033.

SEMBOLONI E., HOEKSTRA H., SCHAYE J., VAN DAALEN M.P. & MCCARTHY I.J. (2011). *Quantifying the effect of baryon physics on weak lensing tomography.* Mon. Not. Roy. Astron. Soc. 417:pp. 2020–2035. arXiv:1105.1075.

Sheth R.K. & Tormen G. (1999). *Large scale bias and the peak background split.* Mon.Not.Roy.Astron.Soc. 308:p. 119. arXiv:astro-ph/9901122.

Silk J. (1967). *Fluctuations in the Primordial Fireball.* Nature 215:pp. 1155–1156.

Smail I., Ellis R.S. & Fitchett M.J. (1994). *Gravitational lensing of distant field galaxies by rich clusters: I. - faint galaxy redshift distributions.* ArXiv e-prints arXiv:astro-ph/9402048.

Smith R. et al. (Virgo Consortium) (2003). *Stable clustering, the halo model and nonlinear cosmological power spectra.* Mon.Not.Roy.Astron.Soc. 341:p. 1311. arXiv:astro-ph/0207664.

Smith R.E., Desjacques V. & Marian L. (2011). *Nonlinear clustering in models with primordial non-Gaussianity: the halo model approach.* Phys.Rev. D83:p. 043526. arXiv:1009.5085.

Smith R.E. & Markovič K. (2011). *Testing the warm dark matter paradigm with large-scale structures.* Phys.Rev. D84:p. 063507. arXiv:1103.2134.

Smith R.E., Scoccimarro R. & Sheth R.K. (2007). *The Scale Dependence of Halo and Galaxy Bias: Effects in Real Space.* Phys.Rev. D75:p. 063512. arXiv:astro-ph/0609547.

Smoot G.F. et al. (1991). *Preliminary results from the COBE differential microwave radiometers - Large angular scale isotropy of the cosmic microwave background.* Astrophys.J. Letters 371:pp. L1–L5.

Smoot G.F. et al. (1992). *Structure in the COBE differential microwave radiometer first-year maps.* Astrophys.J. Letters 396:pp. L1–L5.

Sommer-Larsen J. & Dolgov A. (2001). *Formation of disk galaxies: warm dark matter and the angular momentum problem.* Astrophys.J. 551:pp. 608–623. arXiv:astro-ph/9912166.

Springel V. (2005). *The cosmological simulation code GADGET-2.* Mon.Not.Roy.Astron.Soc. 364:pp. 1105–1134. arXiv:astro-ph/0505010, URL `http://www.mpa-garching.mpg.de/gadget/`.

Springel V., Yoshida N. & White S.D. (2001). *GADGET: A code for collisionless and gasdynamical cosmological simulations.* New Astron. 6:p. 79. arXiv:astro-ph/0003162.

Starobinskiĭ A.A. (1979). *Spectrum of relict gravitational radiation and the early state of the universe.* Soviet Journal of Experimental and Theoretical Physics Letters 30:p. 682.

Takada M. & Bridle S. (2007). *Probing dark energy with cluster counts and cosmic shear power spectra: including the full covariance.* New J.Phys. 9:p. 446. arXiv:0705.0163.

Takada M. & Jain B. (2003). *The three-point correlation function in cosmology.* Mon.Not.Roy.Astron.Soc. 340:pp. 580–608. arXiv:astro-ph/0209167.

Takada M. & Jain B. (2004). *Cosmological parameters from lensing power spectrum and bispectrum tomography.* Mon.Not.Roy.Astron.Soc. 348:p. 897. arXiv:astro-ph/0310125.

Thomas S.A., Abdalla F.B. & Lahav O. (2010). *Upper Bound of 0.28eV on the Neutrino Masses from the Largest Photometric Redshift Survey*. Phys.Rev.Lett. 105:p. 031301. arXiv:0911.5291.

Thomas S.A., Abdalla F.B. & Lahav O. (2011). *The angular power spectra of photometric Sloan Digital Sky Survey luminous red galaxies*. MNRAS412:pp. 1669–1685.

Tikhonov A., Gottloeber S., Yepes G. & Hoffman Y. (2009). *The sizes of minivoids in the local universe: an argument in favor of a warm dark matter model?* arXiv arXiv:0904.0175.

Vale A. & Ostriker J. (2004). *Linking halo mass to galaxy luminosity*. Mon.Not.Roy.Astron.Soc. 353:p. 189. arXiv:astro-ph/0402500.

van Daalen M.P., Schaye J., Booth C. & Vecchia C.D. (2011). *The effects of galaxy formation on the matter power spectrum: A challenge for precision cosmology*. Mon.Not.Roy.Astron.Soc. 415:pp. 3649–3665. arXiv:1104.1174.

Vanderveld R.A., Mortonson M.J., Hu W. & Eifler T. (2012). *Testing dark energy paradigms with weak gravitational lensing*. Phys.Rev. D85:p. 103518. arXiv:1203.3195.

Viel M., Bolton J. & Haehnelt M. (2009). *Cosmological and astrophysical constraints from the Lyman-α forest flux probability distribution function*. Mon.Not.Roy.Astron.Soc. 399:pp. L39–L43. arXiv:0907.2927.

Viel M., Haehnelt M.G. & Springel V. (2004). *Inferring the dark matter power spectrum from the Lyman-α forest in high-resolution QSO absorption spectra*. Mon.Not.Roy.Astron.Soc. 354:p. 684. arXiv:astro-ph/0404600.

Viel M., Haehnelt M.G. & Springel V. (2010). *The effect of neutrinos on the matter distribution as probed by the intergalactic medium*. JCAP 1006:p. 015. arXiv:1003.2422.

Viel M., Lesgourgues J., Haehnelt M.G., Matarrese S. & Riotto A. (2005). *Constraining warm dark matter candidates including sterile neutrinos and light gravitinos with WMAP and the Lyman-α forest*. Phys.Rev. D71:p. 063534. arXiv:astro-ph/0501562.

Viel M., Markovič K., Baldi M. & Weller J. (2012). *The Non-Linear Matter Power Spectrum in Warm Dark Matter Cosmologies*. Mon.Not.Roy.Astron.Soc. 421:pp. 50–62. arXiv:1107.4094.

Viel M. et al. (2008). *How cold is cold dark matter? Small scales constraints from the flux power spectrum of the high-redshift Lyman-α forest*. Phys.Rev.Lett. 100:p. 041304. arXiv:0709.0131.

Vinas J., Salvador-Sole E. & Manrique A. (2012). *Typical density profile for warm dark matter haloes*. Mon.Not.Roy.Astron.Soc. 424:p. L6. arXiv:1202.2860.

Walker A. (1935). *On the formal comparison of Milne's kinematical system with the systems of general relativity*. Monthly Notices of the Royal Astronomical Society 95:pp. 263–269.

Wang J. & White S.D. (2007). *Discreteness effects in simulations of hot/warm dark matter*. Mon.Not.Roy.Astron.Soc. arXiv:astro-ph/0702575.

WHITE . Martin J. (2002). *The mass function.* Astrophys.J.Suppl. 143:p. 241. arXiv:astro-ph/0207185.

WHITE S.D.M. & FRENK C.S. (1991). *Galaxy formation through hierarchical clustering.* Astrophys.J. 379:pp. 52–79.

WHITE S.D.M., FRENK C.S., DAVIS M. & EFSTATHIOU G. (1987). *Clusters, filaments, and voids in a universe dominated by cold dark matter.* Astrophys.J. 313:pp. 505–516.

WRIGHT C.O. & BRAINERD T.G. (1999). *Gravitational Lensing by NFW Halos.* ArXiv e-prints arXiv:astro-ph/9908213.

XIA J.Q. et al. (2012). *Constraints on massive neutrinos from the CFHTLS angular power spectrum.* J. Cosmology Astropart. Phys.6:010. arXiv:1203.5105.

ZAVALA J., OKAMOTO T. & FRENK C.S. (2008). *Bulges versus disks: The evolution of angular momentum in cosmological simulations of galaxy formation.* Mon.Not.Roy.Astron.Soc. 387:p. 364. arXiv:0710.2901.

ZAVALA J. et al. (2009). *The velocity function in the local environment from* Λ*CDM and* Λ*WDM constrained simulations.* Astrophys.J. 700:pp. 1779–1793. arXiv:0906.0585.

ZENTNER A.R. & BULLOCK J.S. (2003). *Halo substructure and the power spectrum.* Astrophys.J. 598:p. 49. arXiv:astro-ph/0304292.

ZHAO G.B. et al. (2012). *The clustering of galaxies in the SDSS-III Baryon Oscillation Spectroscopic Survey: weighing the neutrino mass using the galaxy power spectrum of the CMASS sample.* ArXiv e-prints arXiv:1211.3741.

ZWICKY F. (1933). *Die Rotverschiebung von extragalaktischen Nebeln.* Helvetica Physica Acta 6:pp. 110–127.

Index

An Acknowledgment

My gratitude goes first to my supervisor - Jochen Weller, who tolerated my unpredictable bouts of incompetence, to Martin Kilbinger, Marco Baldi, Stephen Appleby and Tommaso Giannantonio for many many massively interesting and educational discussions as well as much much help with everyday physics problems. In particular, I am extremely grateful to Michael Kopp, for many fascinating discussions, countless explanations of the physics and mathematics of General Relativity and for faithfully and bravely pointing out my errors and stupidities, in conversations and in this thesis!

Thanks to Christa Ingram, the Excellence Custer & USM secretaries, Andi Weiss and Tadziu Hoffmann for the unconditional and good-willed technical support. Thanks to Wikipedia for directing, reassuring & explaining, thanks to Zaz Magic, Rob Yates, Chervin Laporte, Tomek Rembiasz and of course Francesca Ianuzzi for theatrical and normal life, thanks to Ana Kusar for sticking with me and making me feel normal if only every once in a while. Thanks to my parents and my sisters for all their encouragement and their unlimited interest in my work!

Finally, thanks to Milan Kreuschitz, who sacrificed so much to be here for me, for all the emotional support and for the numerous times he has made things easier and better for me while writing this thesis!